Characterisation of Cold Atmospheric Plasma Afterglow for Decontamination

Meike Müller

München 2019

Characterisation of Cold Atmospheric Plasma Afterglow for Decontamination

Meike Müller

Dissertation
an der Fakultät für Physik
der Ludwig–Maximilians–Universität
München

vorgelegt von
Meike Müller
aus Ottweiler

München, den 19. Juni 2019

Erstgutachter: Prof. Dr. Dr. h.c. Gregor Morfill

Zweitgutachter: Prof. Dr. Markus Thoma

Tag der mündlichen Prüfung: 24.09.2019

Zusammenfassung

Die Erkundungsmissionen des Weltraums und die damit verbundene Suche nach außerirdischen Lebensformen erfordern die Einhaltung der internationalen Regeln zum Planetenschutz (COSPAR). Heutzutage stellen die Methoden zur Verwendung von trockener Hitze (DHMR) und verdampftem Wasserstoffperoxid (VHP) validierte Sterilisationsmethoden für Weltraummissionen dar. Die Tatsache, dass diese Methoden empfindliche Materialien negativ beeinflussen können, erhöht jedoch die Nachfrage nach alternativen Dekontaminationsmethoden für die Weltraumforschung. Kaltes atmosphärisches Plasma (KAP) bietet eine der vielversprechendsten Dekontaminationsmethoden bei niedrigen Temperaturen und umfasst verschiedene Vorteile wie beispielsweise niedrige Kosten, einfaches Design und komfortable Verwendung.

In der vorliegenden Arbeit wird ein neu entwickelter Plasma-Afterglow-Zirkulationsapparat (PACA), basierend auf der Oberflächen-Mikroentladungstechnologie, untersucht. Um die wichtigen chemischen Reaktionsprozesse zu verstehen und den präsentierten PACA als alternative Dekontaminationsmethode für den Planetenschutz zu evaluieren, kombiniert die vorliegende Arbeit interdisziplinäre Forschungsgebiete aus Physik, Biologie und Chemie. Insbesondere werden die chemischen Reaktionsprozesse, die mikrobiologische Inaktivierung und die Materialverträglichkeit der Plasmabehandlung untersucht.

Zu diesem Zweck wird eine umfassende Analyse der Afterglow-Zusammensetzung mittels Fourier-Transformations-Infrarotspektroskopie (FTIR) und UV-Absorptionsspektroskopie vorgenommen. Die Erzeugung von O_3, N_2O, NO_2, HCHO und HNO_3 wird in Abhängigkeit von verschiedenen Parametern wie Feuchtigkeit, Gasfluss, Plasmaleistung und Gaszusammensetzung bestimmt. Für die verwendete Plasmaleistung und Umgebungsluft, arbeitet der PACA in einem ozonreichen Bereich, wechselt jedoch zu einem NO_x dominierten Bereich für Stickstoff und Argon als Trägergase. Darüber hinaus verändert die Zunahme der Luftfeuchtigkeit die chemischen Reaktionswege und das Vorhandensein von NO_x Molekülen beeinflusst die Afterglow Zusammensetzung. Infolgedessen empfehlen die Untersuchungsergebnisse die Überwachung der Afterglow Zusammensetzung, um eine reproduzierbare Plasmabehandlung zu ermöglichen.

Mikrobielle Untersuchungen zeigen die Funktionalität und Skalierbarkeit des PACA durch die effektive Inaktivierung des Bioindikators *Bacillus atrophaeus* in verschiedenen Behand-

lungsvolumina. Darüber hinaus zeigen die Ergebnisse die erfolgreiche Inaktivierung der Endosporen, unter Verwendung von 3D- und Diffusionsbarrieren, durch Anpassung der Behandlungszeit oder Verwendung eines direkten Gasstroms.

Die Materialverträglichkeit der PACA Behandlung bei unterschiedlichen Feuchtigkeitsbedingungen wird durch die Analyse der visuellen Veränderung, Benetzbarkeit und chemischen Oberflächenzusammensetzung verschiedener plasmabehandelter Proben bestimmt. Die Materialien reagieren unterschiedlich auf die Plasmabehandlung und zeigen eine Abhängigkeit von der plasmainduzierten Veränderung zur verwendeten Luftfeuchte. Kupfer, Messing und Aluminium sind stark durch die Afterglow Behandlung beeinflusst, wohingegen PTFE, POM, Silizium, Epoxid, Polymid und Edelstahl nur geringe Reaktionen auf die Behandlung zeigen.

Zusammenfassend liefert diese Arbeit eine detaillierte Charakterisierung der Afterglow Zusammensetzung des PACA für verschiedene Bedingungen und zeigt die erfolgreiche Inaktivierung von bakteriellen Endosporen in unterschiedlichen Behandlungsvolumina und in komplexen Objekten. Die Untersuchungen an plasmabehandelten Materialien zeigen die höchste Materialverträglichkeit für eine hohe Luftfeuchtigkeit, die sich auch positiv auf die sporizide Wirksamkeit der Plasmabehandlung auswirkt. Die Ergebnisse dieser Arbeit liefern neue Erkenntnisse und zeigen ideale Bedingungen und Voraussetzungen für eine erfolgreiche Plasmabehandlung und Hochskalierung, sowie für die Evaluierung des PACA als alternative Dekontaminationsmethode für den Planetenschutz.

Abstact

The exploration missions of outer space and the associated search for extra-terrestrial lifeforms require to fulfill the international planetary protection policies of COSPAR. Today, dry heat microbial reduction (DHMR) and vapor phase bioburden reduction using hydrogen peroxide (VHP) are validated sterilisation methods for space missions. However, the fact that these methods could negatively influence sensitive materials increases the demand of alternative decontamination methods for space research. Cold atmospheric plasma (CAP) provides one of the most promising low-temperature decontamination methods and comprises various benefits such as low cost, simple design and comfortable usage.

In the presented work, a newly developed plasma afterglow circulation apparatus (PACA) based on the surface micro-discharge (SMD) technology is investigated. To understand the important chemical reaction processes and to evaluate the presented PACA as a useful alternative decontamination method for planetary protection, this thesis combines interdisciplinary research fields of physics, biology and chemistry. In particular, the chemical reaction processes, the microbial inactivation and the material compatibility of the plasma treatment are investigated.

For this purpose, extensive analysis of the afterglow composition using Fourier Transform Infrared (FTIR) spectroscopy and UV absorption spectroscopy are performed. The generation of O_3, N_2O, NO_2, HCHO and HNO_3 are determined as a function of various conditions, such as humidity, gas flow, power consumption and carrier gas. For the used plasma power and ambient air, the PACA operates in an ozone rich regime, but changes to a NO_x dominated regime for nitrogen and argon as carrier gases. Furthermore, the increase of the humidity changes the chemical pathways and the presence of NO_x molecules influences the afterglow composition. In consequence, the findings recommend the monitoring of the afterglow to enable a reproducible plasma treatment.

Microbial investigations show the functionality and scalability of the PACA, by the effective inactivation of the bioindicator *Bacillus atrophaeus* in different treatment volumes. In addition, the results show the inactivation of the endospores using 3D and diffusion barriers by adapting the treatment time or applying a direct gas flow.

The material compatibility of the PACA treatment for different humidity conditions is characterised by the analysis of the visual alteration, wettability and chemical surface com-

position of various plasma treated samples. The materials react differently to the plasma treatment and show a dependency on the plasma induced alteration to the humidity conditions. Copper, brass and aluminium are strongly affected by the afterglow, whereas PTFE, POM, silicon, epoxy, polymide and stainless steel show minor reactions to the treatment.

In conclusion, this work provides a detailed characterisation of the afterglow composition of the PACA for various conditions and show the successful inactivation of bacterial endospores in different treatment volumes and in complex objects. The investigations of plasma treated materials show the highest compatibility for high humidity conditions, which are also beneficial for the sporicidal efficiency of the plasma treatment. The results of this work provide new findings and show ideal conditions and prerequisites for a successful plasma treatment and up-scaling, as well as for the evaluation of the PACA as an alternative decontamination method for planetary protection.

Contents

Chapter 1

Introduction

1.1 Planetary Protection

In space research the exploration of the outer space and the search for extra-terrestrial life are of great interest. In the late 1950s, the International Council of Scientific Unions (ICSU) founded the Committee on Space Research (COSPAR) as an interdisciplinary scientific committee with the aim to avoid that missions to moon or other extra-terrestrial bodies compromise their future exploration [1].

In order to protect the explored extra-terrestrial bodies from terrestrial organisms and to prevent backward contamination in the case of earth return missions [1–3], the COSPAR created planetary protection policies. Therefore, COSPAR provides an international standard for spacefaring nations and defines five categories of missions [1, 4]. Following the planetary protection policies is crucial for the search for extra-terrestrial life to avoid false positive answers by the contamination of the investigated regions. Table 1.1 shows the different mission categories depending on the target body (e.g. planet, moon, comet or asteroid) and the type of interaction of the spacecraft with the target (e.g. flyby, orbiter and lander) [6]. Missions in Category I are related to extra-terrestrial bodies where no microbial life-forms are supported. Here, no special planetary protection requirements are needed. For Categories II to V, the requirements become increasingly stringent depending on the particular mission and on the astrobiological relevance of their individual mission target [7]. For example, Category IV is associated with missions, where a spacecraft has to land in a region of special interest and a contamination by terrestrial life-forms is possible. Special regions are regions of interest, which are associated to investigations for the search of extra-terrestrial lifeforms [6]. A detailed description about the different categories for target body/mission type combinations and their requirements are described in more detail in *COSPAR's Planetary Protection Policy* which was updated in 2017 [1].

Previous publications demonstrated that a microbial diversity inhabit spacecraft assembly clean rooms despite their extreme environment [8, 9]. In particular, spore forming bacteria

Mission Category	Mission Type	Planetary Target
I	flyby, orbiter, lander	Undifferentiated, metamorphosed asteroids; Io; others TBD (to be defined)
II	flyby, orbiter, lander	Venus; Earths Moon; Comets; non-Category I Asteroids; Jupiter; Jovian Satellites (except Io and Europa); Saturn; Saturnian Satellites (except Titan and Enceladus); Uranus; Uranian Satellites; Neptune; Neptunian Satellites (except Triton); Kuiper-Belt Objects ($< 1/2$ the size of Pluto); others TBD
II[a]	flyby, orbiter, lander	Ganymede (Jupiter); Titan (Saturn); Triton, Pluto and Charon (Neptune); others TBD
III	flyby, orbiter	Mars; Europa; Enceladus; others TBD
IV (a-c)	lander, probe	IVa is for lander systems not investigating extant martian life or special regions[b]. IVb is for lander systems investigating extant martian life. IVc is for missions investigating martian special regions.
V	earth-return	Restricted Earth-Return: (Mars; Europa; Enceladus; others TBD) Unrestricted Earth-Return: (Venus, Moon; others TBD)

Table 1.1: Planetary protection categories [5, 6].

[a] The mission-specific assignment to Category II needs an analysis of a possible contamination of potential liquid water environments [1].

[b] A Special Region is defined as a region within which terrestrial organisms are likely to replicates [1].

Mission Category	Surface Bioburden
IVa	Surface bioburden level $\leq 3 \times 10^5$ with an average of ≤ 300 spores/m^2.
IVb	The entire landed system is restricted to ≤ 30 spores.
IVc	The entire landed system is restricted to ≤ 30 spores. For missions with a risk of hard landing, the total bioburden level (surface, mated, encapsulated) is $\leq 30 + (2 \times 10^5)$ spores.

Table 1.2: Planetary protection Category IV for Mars is subdivided into IV a-c [1].

like *Bacillus* species can outlast nutrient poor conditions, and germinate when favourable conditions are restored, which is described in more detail in chapter 1.2. Some of these species were observed in spacecraft associated environments [3, 8] and could become a potential risk for planetary protection [10–14]. For this reason, spores are used as a proxy for the total bioburden on a spacecraft and as model organisms to test the effectivity of different inactivation methods [15].

For example, a bioburden level of spacecraft equipment in dependence on a mission of Category IV is presented in Table 1.2. For Category IVa, where no special region is investigated, a surface bioburden level $\leq 3 \times 10^5$ spores is acceptable. Missions of Category IVb investigate extant martian life and allow a surface bioburden of ≤ 30 spores. In addition, for the exploration of special regions the surface bioburden has to be below ≤ 30 spores and the total bioburden including encapsulated components has to be below $\leq 30 + (2 \times 10^5)$ spores. In order to decontaminate spacecraft equipment, validated inactivation methods are needed. Validated methods for the decontamination of spacecraft equipment are described in chapter 1.3.

1.2 Bacterial Endospores

Bacterial endospores are permanent stages formed by different vegetative bacteria of the type *Bacillus* and *Clostridium* under nutrient limitations and have been recognised as one of the most resistant known life-forms on earth [16]. In this stadium, the dormant endospores are able to survive for decades in extreme terrestrial and extra-terrestrial conditions and show a high resistance against chemical components, desiccation, dry/wet heat and UV/gamma radiations [17–20]. The high resistance of spore-forming bacteria allows them to survive many space-related extremes. Under the presence of appropriate nutrients the dormant spores germinates again [21, 22]. This morphological changes are caused by changes of the gene expressions [23].

Consecutively, *Bacillus* spores could survive outer space conditions in Low Earth Orbits (LEO) [24]. In addition, these resistant microorganisms were already detected in spacecraft

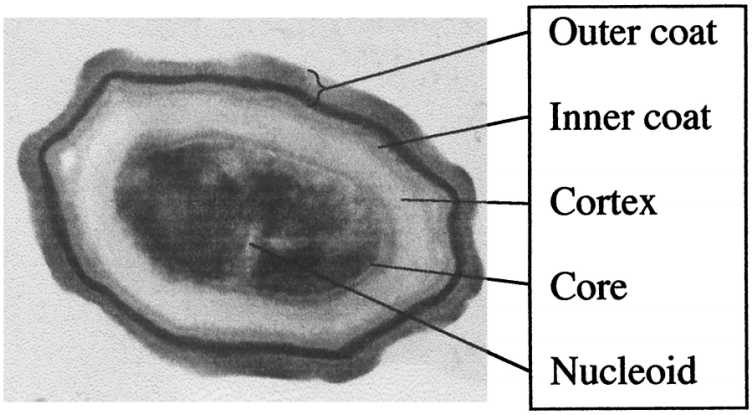

Figure 1.1: Cross-section of a spore of *B. subtilis*. The long axis of the spore is 1.2 mm and the the core area has the size of 0.25 mm^2 (extracted from Nicholson *et al.*[18]).

associated facilities [25]. Therefore, it is important to avoid contaminated spacecraft equipment to prevent forward contamination of extra-terrestrial bodies by terrestrial lifeforms [15]. Furthermore, the bacterial endospores (for example *Bacillus atrophaeus*) are widely used as bioindicators to monitor the dry heat, ethylene oxide, and plasma sterilisation processes [26, 27].

The high resistance of *Bacillus* spores are caused by a morphology, which prevents damage of the spore and by the possibility of DNA repair [24]. The endospores consist of a dehydrated mineralised core with a protective envelope, the cortex and coat layers [16, 28]. Fig. 1.1 shows a cross-section of a spore (*B. subtilis*) with its core, cortex and different coat layers [18]. The cortex consists of peptidoglycan and is important for the reduction of the water contend of the core, which increases the resistance against wet heat and peroxide sterilisation processes [20, 29]. The saturation of the spore DNA with acid-soluble proteins change the chemical enzymatic reactivity of the DNA [30]. Thus, the spores are protected from genotoxic chemicals, desiccation, dry and wet heat, as well as UV and gamma radiation [24, 31].

The increasing interest in space research to inactivate *Bacillus* species and the fact that this microorganisms are widely used as biological indicators, *B. atrophaeus* are used as a test organism to analyse the inactivation efficiency of the plasma treatment in the presented work.

1.3 Validated Sterilisation Techniques for Spacecraft Components

In general, various cleaning and sterilisation methods exist, but the most common ones are biocleaning with isopropylic alcohol (IPA) or sporicides, dry- and wet-heat, hydrogen peroxide, gamma or beta radiation. To fulfill the planetary protection policy requirements, the procedures have to reach the defined decontamination levels for the missions (described in

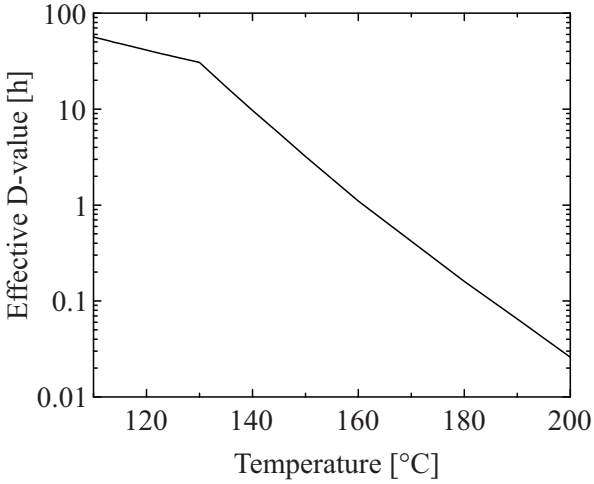

Figure 1.2: Effective D-values for 4 to 6 orders of magnitude surface reduction using DHMR [34].

chapter 1.1) and have to be compatible with the spacecraft hardware. Therefore, validation tests are needed [2, 32].

The European Cooperation for Space Standardisation (ECSS) is a normative system which was created by European space agencies and companies [32]. In detail, ECSS provides standard requirements in respect to COSPARs planetary protection policies. Nowadays, dry heat microbial reduction (DHMR) and vapour phase bioburden reduction using hydrogen peroxide (VHP) are validated sterilisation methods for planetary protection missions by the ECSS [33, 34]. In the following, the validated sterilisation methods for spacecraft equipment are discussed.

1.3.1 Dry Heat Microbial Reduction (DHMR)

Dry heat microbial reduction (DHMR) provides an evaluated sterilisation technique for missions, where a bioburden control is required to follow the planetary protection policies. The sterilisation efficiency depends on temperature, humidity and treatment time. For the application of dry heat, the humidity level has to be below $1.2\,\mathrm{g/m^3}$. A typical test organism to investigate the sterilisation efficiency of DHMR is *B. atrophaeus*, which was used as a test organism in the present work [35].

NASA and ESA have approved processes for the sterilisation with dry heat [36]. The validated decontamination process of DHMR was already used in the Viking lander missions in 1975. For DHMR, D-values were developed for temperatures between $T = 110 - 200\,^{\circ}\mathrm{C}$ while NASA invested since 1960 in DHMR friendly hardware. The D-value defines the required time to achieve an inactivation of 90 % of the test microorganism population [34]. In Fig. 1.2 the effective D-values depending on the temperature are illustrated for DHMR (data from ECSS standard [34]). For temperatures of $T = 110\,^{\circ}\mathrm{C}$ a D-value of 56 h is achieved, while for

a temperature of $T = 200\,°C$ a D-value of 0.027 h is possible. Thus, for the decontamination process using $T = 110\,°C$, the spacecraft equipment is heated in a sealed and dry oven for long periods of time [2]. In addition to the surface reduction using DHMR, the D-value of the treatment of mated bioburden (surfaces joined by fasteners rather than by adhesives) needs to multiply the effective D-value of Fig. 1.2 with a factor of 2. The D-value for the treatment of encapsulated bioburden (bioburden inside bulk nonmetallic materials) require a multiplication using a factor 10. Typical bioburden levels before applying a bioburden reduction process are in the range of 3×10^2 spores/m^2 to 1×10^5 spores/m^2 [34].

More detailed information about the use of dry heat could be found in reference [34].

1.3.2 Vapour Hydrogen Peroxide (VHP)

The European Space Agency evaluated a standard process for the use of Vapour Hydrogen Peroxide (VHP), which is also accepted by NASA [36]. This method has a high compatibility by treating surfaces of high tech medical and surgical devices and instruments. According to ECSS [35], the typical parameters for VHP are the following:

- Temperature: $40 - 60\,°C$
- Gas concentration: $4 - 10\,g/m^3$ H_2O_2 in gas phase.
- Pressure: Ambient or mixed (vacuum/ambient) circles
- Duration 1 h per cycle

For the bioburden reduction for flight hardware, the ECSS propose a standard for ambient and vacuum condition and for the overkill procedure. To achieve a $2-6$ order of magnitude surface bioburden reduction under ambient conditions, the H_2O_2 concentration has to be > 1.1 mg/L with a D-value of 200 (mg/L)s. For a controlled vacuum environment (T: $25 - 45°C$, p: $1.3 - 13.3$ hPa), the H_2O_2 concentration shall be between $0.5 - 1.1$ mg/L, with an D-value of 200 (mg/L)s. To achieve a $2 - 6$ order of magnitude reduction, the respective D-value is multiplied by a factor of $2-6$ respectively. The application of an overkill procedure (equivalent to a 12 order of magnitude bioburden reduction), uses a H_2O_2 concentration of $6 - 8.6$ mg/L with a time integrated H_2O_2 concentration of 1400 (mg/L)sec. After the application of an overkill procedure, the bioburden is supposed to be zero. A typical test organism to investigate the sterilisation efficiency of VHP is *B. stearothermophilus* [33].

More detailed information about the use of VHP could be found in reference [33].

1.3.3 Alternative Sterilisation Methods

The already validated sterilisation methods DHMR and VHP have a severe disadvantage: The sensitivity of modern instruments prohibits a complete sterilisation of the spacecraft

equipment [3]. In detail, ECSS reported in their standard [35], that high temperatures could negatively affect heat sensitive materials and high concentrations of H_2O_2 could alter different materials (epoxy, silver, cellulose etc.) [35]. In addition, copper, silver and manganese can lead to a catalytic decomposition of H_2O_2. Hence, new low-temperature sterilisation technologies in addition to VHP and DHMR are required to treat various spacecraft components without damaging the surface. Furthermore the low-temperature sterilisation technology should be compatible with materials used in space industry, and should provide an adequate microbial reduction [2, 14].

1.4 What is Plasma?

Irving Langmuir used the Greek word *plasma* in the year 1927 to describe the charge-neutral part of a gas discharge [37, 38]. Langmuir choose the word plasma based on the word blood plasma. Mott-Smith explained [37] that Langmuir compared the acting of the discharge with a substratum carrying special kinds of particles, which reminds him to the way blood plasma carries around red and white corpuscles and germs [38].

The term plasma is used for a fully or partly ionised gas and is often described as the *fourth state of matter*, in addition to the solid, liquid and gaseous state [39]. With an increase of the energy input, the state of the matter changes from solid to liquid, to the gaseous states and will be finally transformed into the state of a plasma. In a plasma, the number of free electrons is equal to the number of positive charges of the ions in the gas, so that the plasma is called electrically neutral or quasi-neutral. The ratio of the charged particle density n_i to the neutral particle density n_n is called as the ionisation degree n_i/n_n. The ionisation degree in a conventional system is between 10^{-7} and 10^{-4} [39]. When the plasma contains no neutral molecules anymore, it is called a *completely ionised plasma* which is conventional for thermonuclear plasma systems [39]. In the present work, I am working with a weakly ionised plasma.

It is assumed that over 99 % of the visible universe exists as a plasma. The free electric charges in a plasma makes it conductive, internally interactive and strongly responsive to electromagnetic fields [39]. The universe contains plasma such as solar wind, solar corona, nebular and earth ionosphere [40]. On earth, lightning and *aurora borealis* are the most common natural plasmas [39, 41]. For example, the observable phenomenon of *aurora borealis* is caused by the interaction of the solar wind with the earth atmosphere close to the earth poles. Different plasmas are present under different conditions in terms of pressure, electron temperatures and electron densities. Most of the plasmas have electron temperatures of $1 - 20\,\mathrm{eV}$ and electron densities in the range of $10^6 - 10^{18}\,\mathrm{cm}^{-1}$ [39].

1.5 Plasma Categorisation

1.5.1 Ideal Plasma

Most of the used plasmas in the lab and in the nature are ideal plasmas. The term ideal plasma is used when the potential Energy $E_{pot} = \mathrm{e}^2/(4\pi\epsilon_0)n^{1/3}$, could be neglected compared to the thermal energy $E_T = 3/2\mathrm{k_B}T$ of the particles, $E_T \gg E_{pot}$ [41]. Here, $1/n^{1/3}$ is the mean distance of the particles and e the elementary charge.

The states solid, liquid and gaseous of neutral matter could be described by the degree of coupling (coupling parameter) between the atoms. The coupling parameter Γ_c is calculated by the relation of kinetic and potential energy and is given by the following equation [38]:

$$\Gamma_c = \frac{\mathrm{e}^2}{4\pi\epsilon_0}\frac{n^{1/3}}{T}. \tag{1.1}$$

For an ideal plasma, the coupling parameter is $\Gamma_c \ll 1$.

1.5.2 Thermal and Non-Thermal Plasma

All of the studied plasma systems can be divided into two major categories: thermal and non-thermal plasmas [42]. When the temperature of electrons T_e, ions T_i and neutrals T_n, approach each other ($T_\mathrm{e} \approx T_\mathrm{i} \approx T_\mathrm{n}$), they are in a thermal equilibrium. For this case, the plasma is called a *thermal plasma* [39]. These kinds of plasmas often operate with high gas temperatures and are associated with Joule heating and thermal ionisation [42]. Thermal equilibrium conditions in nature are often found in the interior of stars. But also laboratory systems generate thermal plasmas like electric arc discharges or inductively coupled plasma torches and are often used for welding, application in metallurgy, high temperature chemistry and thermal spraying [38, 43, 44].

Many plasmas are not acting in a thermal equilibrium. In this case the electrons have a significant higher kinetic energy than the heavy particles ($T_\mathrm{e} \gg T_i \approx T_n$). The collision of the electrons with heavy ions and neutrals leads to a small transfer of energy. This non-equilibrium plasma is called *non-thermal* plasma [39, 45]. In some of the non-thermal plasmas, the electron temperature is $T_\mathrm{e} \approx 1\,\mathrm{eV}$ (10 000 K), while the ion temperature has room temperature, due to the energy exange of ions with the surrounding gas. These non thermal plasmas are also called *cold* plasmas. In nature, *aurora borealis* is an example for a non-thermal plasma. In most laboratory conditions, a gas discharge is used as a plasma source like corona discharge, glow discharge and dielectric barrier discharge [39, 43, 45]. These discharges are also the most common ones, used against biological contaminants [46].

1.5.3 Low Pressure and Atmospheric Pressure Plasma

Non-thermal plasmas are used under different pressure conditions depending on the application. With an increase of the gas pressure, the collision frequency increases, which increases the probability that the particles reach a steady state energy equilibrium [44]. Plasmas under low pressure are widely used for material processing and manufacturing of semiconductor devices, as well as in treatment of polymer materials [39, 47]. The use of low pressure plasmas enables a precise treatment due to the fact that the operation is working with a low particle density, which leads to a small number of collisions [47]. The operation in vacuum chambers is indispensable, which leads to several drawbacks, like high costs and limited size. In addition, the treated materials have to be vacuum compatible. In the presented work, an atmospheric pressure plasma source is used. Under atmospheric pressure, higher voltages are required for a gas breakdown [47], but atmospheric pressure plasmas overcome the drawback of the use of a vacuum chamber. In particular, the operation in atmospheric pressure allows the treatment of vacuum sensitive materials like human skin [39]. The independence to a vacuum chamber enables to adapt the atmospheric plasma source to even complex devices and conventional processes [46]. Various plasma sources have already been used for plasma decontamination [48]: Shimizu *et al.* [15], Stapelmann *et al.* [49] and Cooper *et al.* [50] demonstrated that low pressure plasmas, as well as atmospheric pressure plasmas are both able to inactivate bacterial endospores.

1.6 CAP Inactivation of Microorganisms

Cold plasma at atmospheric pressure (CAP) is a non-thermal plasma operating at ambient pressure. In this case *cold* means, that the temperature of the plasma is below 40°C or the use of a pulsed plasma allows a treatment without heating the target [51]. The plasma remains cold, if the number of high energy electrons is limited by short times or if the heavy particles are cooled [51]. For the ionisation procedure, different kinds of processes can be used, like thermal, optical (UV) and X-ray ionisation. However, the most common widely used method is to apply electric or electromagnetic fields. In addition, the plasma properties depend on the power (DC, AC, pulsed, frequency) and on the type of the gas [44].

Plasma technologies are already applied in various fields, for example for treatment of medical equipment, implants, and in the food industry [52]. Sterilisation using CAP comprises a plurality of benefits such as low cost, simple design and comfortable usage without organic residues after the treatment [53]. CAP is one of the most promising low-temperature sterilisation technologies [54, 55]. It is often generated with helium and argon combined with a molecular gas like oxygen, but also ambient air can be used [56, 57]. In detail, the electrons in the plasma generates exited atoms and molecules, which leads to an initiation of chemical reactions. The energy, which is stored in exited molecules could lead to a formation of long

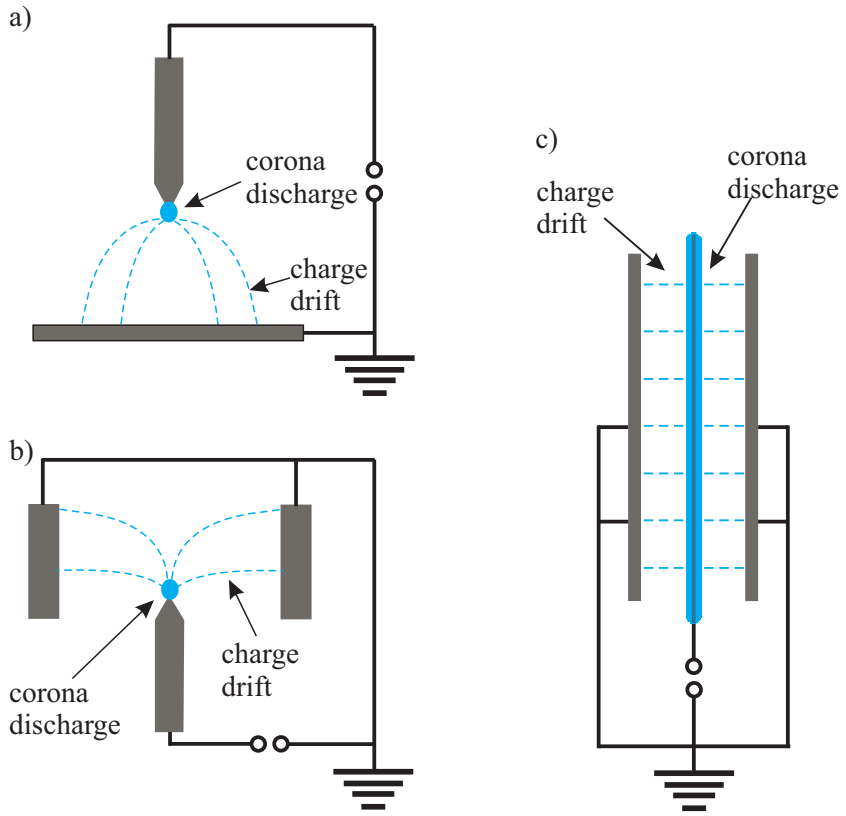

Figure 1.3: Schematic view of different corona discharge arrangements. a) point to plate b) needle to cylinder c) wire to cylinder (adapted from [20]).

living species (like ozone) or the release of photons (eximer) [58].

Investigations using different sources of CAP already showed properties to inactivate different microorganisms. These used plasma sources vary in geometry, plasma chemistry and mechanisms of actions.

An overview of atmospheric pressure plasma sources with a focus on geometry and concepts of plasma ignition are given by Ehlbeck *et al.* [46]. In the following, an overview of different plasma sources for a microbial decontamination processes is given.

1.6.1 Corona Discharge

In general, non-thermal corona discharges are observable under ambient pressure in regions with non-uniform electric fields, for example near edges or sharp points, needles and small diameter wires [39, 59]. Different types of corona discharges exist, depending on geometrical configurations of the electrode and the polarity [59]. For example, the needle-plate, wire-plate and needle-cylinder are possible configuration for corona discharges [59, 60]. Fig. 1.3 shows different arrangements of corona discharges. Furthermore, corona reactors can be driven by direct current (DC), alternating current (AC) and in pulsed modes [59, 61]. For the

application of microbial inactivation, in most of the cases negative DC corona discharges are used, but also pulsed modes [46, 62].

Nowadays, the corona discharges are used for different industrial applications as the treatment of surfaces, the removal of volatile organic compounds (VOC), water disinfection and also for biological decontamination [42, 46, 63].

Scholtz *et al.* [46, 64] used a negative DC corona in ambient air for the inactivation of yeasts, vegetative bacteria and bacterial spores. Therefore they used a pin to plate arrangement with $U = 10\,\mathrm{kV}$ and $I = 0.5\,\mathrm{mA}$, while the treatment time varied between $5 - 30\,\mathrm{min}$. Furthermore, Bussiahn *et al.* [65] used a negative DC corona discharge with 10 ns pulses for the inactivation of *Escherichia coli*. They suggest the application of the plasma filaments in dentistry to treat a human tooth canal. Joubert *et al.* [66] used corona discharges in water to inactivate vegetative bacteria and spores of *Bacillus subtilis* and *Bacillus atrophaeus*. The study showed that a combination of H_2O_2 and shock waves could be responsible for the inactivation effect. In addition, Dobrynin *et al.* [67] reported that the presence of charged particles increases the inactivation efficiency using corona discharges. Recently, corona discharges have also been employed for the disinfection of different food packaging and to reduce microorganisms on food [68, 69]. The summarised inactivation studies presented here, could be found in the appendix A.

1.6.2 Glow Discharge

Glow discharges provide uniform discharges for high voltages and low currents [39, 70]. Under low pressure, the glow discharge is a self maintained discharge formed by ion bombardment on a cold cathode, while the increase of the pressure leads to the transformation from a glow to an arc discharge [70–72]. The transformation is caused by an increase of the cathode temperature by the ion bombardment. Under atmospheric pressure, the generation of a glow discharge could be obtained by the adaption of an appropriate frequency of the applied voltage to trap the ions but not the electrons between the electrodes [70, 73]. Furthermore, the application of radio frequency (RF) discharge instead of DC reduces sputtering and erosion of the electrodes, contamination of the plasma and stabilise the plasma against the glow-to-arc transition [73]. The use of a dielectric plate on at least one of the electrodes additionally suppress the glow-to-arc transformation further [73]. It was introduced by Roth *et al.* in 1995 as an one atmosphere uniform glow discharge plasma (OAUGDP) [74]. Fig. 1.4 shows a schematic illustration of an atmospheric pressure glow discharge. The glow discharge is generated between two parallel electrodes which are covered by a dielectric barrier, while the distance between the electrodes is typically a few millimetres [72]. Laroussi presented the use of this technology for the sterilisation of contaminated matter in 1996 [75]. In detail, he used a uniform steady-state glow discharge at atmospheric pressure and supposed that in addition to UV radiation, charged particles and radicals are responsible for the inactivation of the mi-

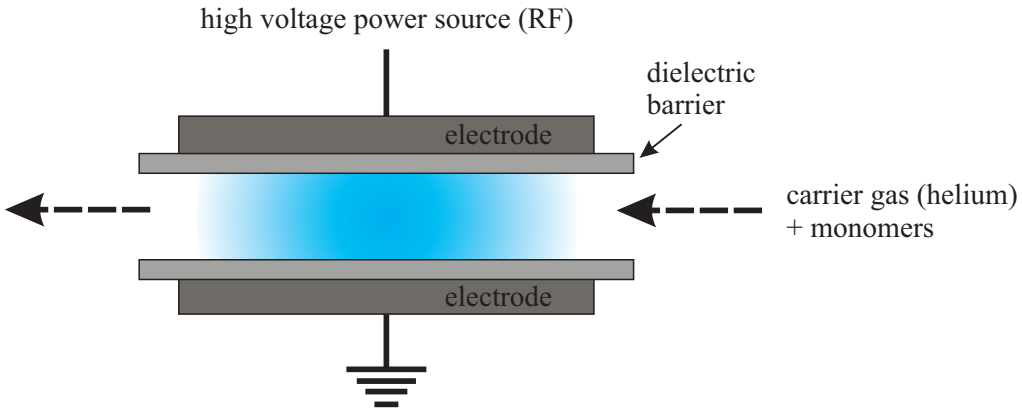

Figure 1.4: Schematic view of an atmospheric pressure glow discharge with electrode distances of a few mm and the use of dielectric barriers and RF voltage (adapted from [72]).

croorganisms [75]. In addition, Montie *et al.* used the OAUGDP to reduce bacteria, bacterial endospores, yeast and bacterial viruses on different surfaces [76]. But also additional studies showed that glow discharges could be used for the inactivation of various microorganisms [77–79].

The glow discharge at atmospheric pressure can be realised as atmospheric pressure plasma jets (APPJs) using noble gases like helium [39, 80, 81]. Furthermore, the APPJ is often used in particular for plasma-enhanced chemical vapor deposition of silicon dioxide and silicon nitrite thin films. The APPJ can consist of a planar and coaxial system using a discharge gap in the order of 11.6 mm and an operation frequency in the megahertz range, for example 13.56 MHz or 27.12 MHz [39, 46, 51, 80]. Note, that the exposure distance to the target is in the centimeter range [46]. The ignition voltages depends on the used process gas and the electrode gap and reach from 100 V to kV. This leads to a power consumption of about 500 W [46]. The predominant temperature is connected to the gas flow (in the range of slm) and to the power consumption, but with special electrical working modes (alternating plasma-on/plasma-off phases) the temperature can be decreased to approximately room temperature [46, 82]. In plasma jets, the plasma discharge is ignited inside a nozzle and transported outside using a gas flow [83]. A scheme of two different types of plasma jets are illustrated in Fig. 1.5. Note, that the exited feed gas reacts outside the APPJ with the ambient air or the target, which leads to chemical reaction processes for the microbial inactivation [86].

In general, APPJs are widely used for biomedical applications. For example, the successful inactivation of *Demodex folliculorum* of patients with *rosacea* skin disease [87]. The studies of Lim *et al.* [88] demonstrated the inactivation of *Bacillus atrophaeus* using an Ar/O_2 plasma jet. They observed D-values in the range of $5-57$ s with an exposure distance of $0.5-1.5$ cm. Weltmann *et al.* [83, 89] showed that APPJs are useful in decontamination of sensitive materials inactivating *E. coli* and *B. atrophaeus*. The application of plasma jets requires a scanning process for the complete area as well as cavities because the plasma radiation

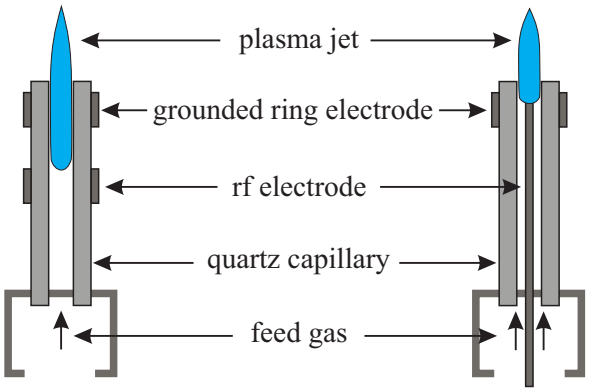

Figure 1.5: Schematic drawings of two different types of a plasma jet using a feed gas and RF electrodes. The left device uses two ring electrodes and the right device uses one ring and a centrally introduced rod electrode (adapted from [84, 85]).

area is often limited to only a few millimeters [52]. A more detailed overview about the microbiological inactivation using APPJs can be found from Ehlbeck *et al.* and Lackmann *et al.* [46, 90]. In addition Laroussi [91] presented a review in which he described that APPJs can successfully inactivate bacteria, pathogenic proteins and destroy cancer cells *in vitro*. A summary of some inactivation studies using glow discharges, corona discharges and DBDs could be found in the appendix A.

1.6.3 Dielectric Barrier Discharge (DBD)

The dielectric barrier discharge (DBD) provides a possibility to prevent the spark formation under ambient pressure by using a dielectric barrier in the discharge region to inhibit currents [39]. Due to the absence of sparks, the DBD is also called a silent discharge. The use of a dielectric barrier prevents the application of DC currents so that the DBD is operated with an alternating current using frequencies between $0.05 - 500\,\mathrm{kHz}$ and high voltages in the kilo-volt range [39, 42, 92]. Fig. 1.6 shows configurations of common planar and cylindrical DBDs with at least one dielectric layer between the electrodes. Note, that Fig. 1.4 and Fig. 1.6 c) show a similar electrode configuration. A glow discharge can be obtained with the same electrode as used for a DBD, by either lowering the pressure, by using a pulsed discharge or by using large amounts of helium or neon [39, 43, 92, 94]. Typical dielectric materials are glass, quartz, ceramics and polymers with a discharge gap between 0.1 mm and several centimeters [95, 96]. The amount of the current which passes the dielectric depends on several parameters, like the dielectric constant, the thickness and the applied voltage. Furthermore, the electrical field has to be high to reach a breakdown in the gas [40, 58, 92].

The DBDs are closely related to glow discharges. However, where glow discharges are homogeneous across the electrodes, the breakdown of the DBD results in a formation of streamers or micro-discharges with a duration of nanoseconds [72, 94].

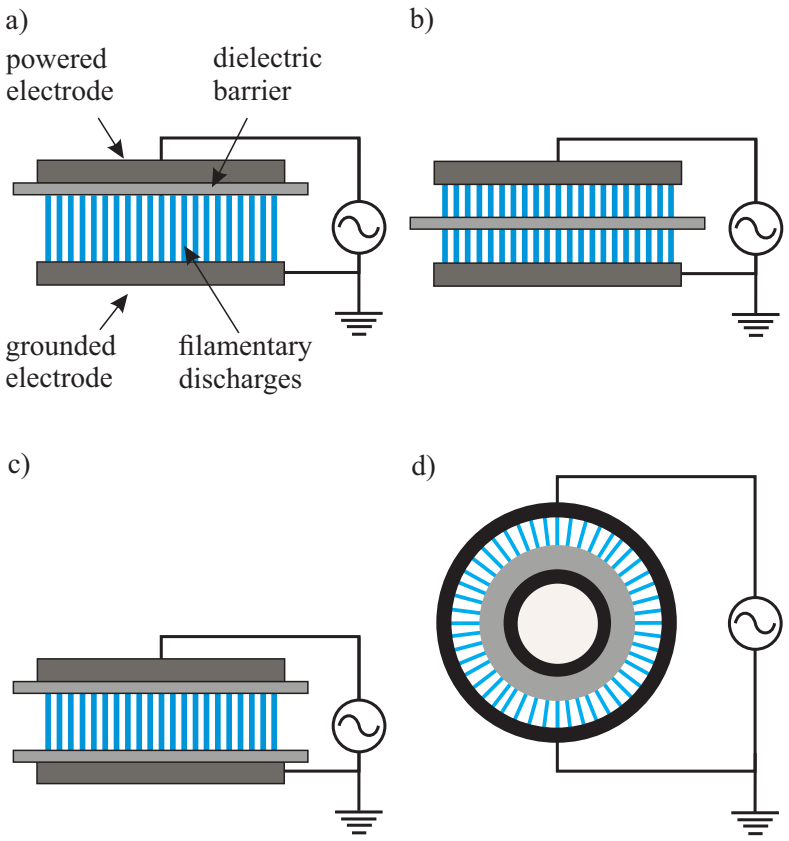

Figure 1.6: Schematic view of typical DBD arrangements with filamentary discharges and with planar a), b), c) and cylindrical d) configurations, with at least one dielectric layer between the electrodes using AC currents (adapted from [20, 39, 93]).

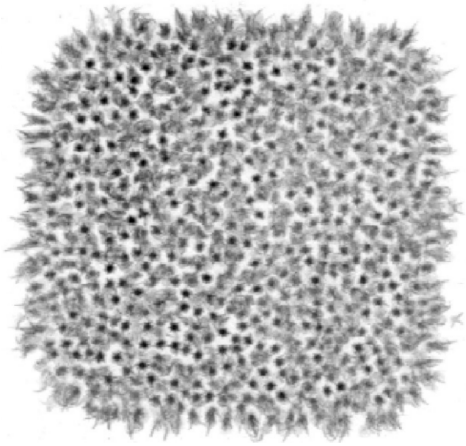

Figure 1.7: The storage phosphor image of filaments in a 0.762 mm discharge gab in air of a DBD with 5 cm × 5 cm discharge area [42].

In a DBD, the short duration of micro-discharges avoids overheating and obtains $T_e > T_i$ [42]. Fig. 1.7 shows a photograph of DBD micro-discharges, taken through a transparent electrode. The image shows, that the discharges are spread uniformly over the DBD [42]. The micro-discharges and the breakdown mechanism are described in more detail in chapter 1.6.5. Due to the fact, that DBDs can operate in non-equilibrium conditions under ambient pressure without the use of pulsed power supplies, the DBD is useful for many industrial applications [42, 46].

The DBD plasma technology allows direct and indirect ways of treatment. For the direct treatment, the visible plasma region is in contact with the target. As a result, UV light and short lifetime species with a high chemical activity, such as electrons and ions reach the target. Direct application allows the treatment of large surfaces, but the surface has to be flat to avoid inhomogeneous plasma discharges [52]. For the indirect plasma treatment, only stable species with a long lifetime, like O_3, H_2O_2, and NO_2, are able to reach the target. This cocktail of long-lifetime plasma species is called *plasma afterglow* and is predominant for the treatment of targets located at a certain distance from the plasma source [14, 50, 97]. The plasma technologies, which are working with a direct treatment and UV-light, have difficulties to access narrow cavities or complex geometries. The afterglow plasma operates like a reactive gas and can penetrate these areas by diffusion and convection.

Nowadays, numerous studies exist about the application of DBD to inactivate various microorganisms. At first, Siemens introduced the DBD in 1857 to create ozone [39, 98]. A DBD configuration shown in Fig. 1.6 a) was used by Trompeter *et al.* to inactivate [99] *Bacillus subtilis* and *Aspergillus niger* spores on polyethylene (PET), polystyrene and glass plates. In addition, Fridman *et al.* [56, 100] invented a DBD plasma source using a floating electrode (FE-DBD), which uses the target as a counterelectrode, while the current continues mostly in the form of displacement current through the target. In detail, the FE-DBD was

used to sterilise skin flora (*Staphylococci*, *Streptococci*, and *Candida* species of yeast) [97], for the inactivation of *Escherichia coli* [101], for blood coagulation [56] and for the destruction of Melanoma skin cancer cells [100]. Cooper *et al.* [50] porposed the application of CAP for planetary protection and used a similar DBD in a direct mode to inactivate *Deinococcus radiodurans* on a dry surface showing a 6 log reduction after 30 min. When the microorganisms were suspended in distilled water, a 4 log reduction was observed already after 15 s. They assumed that the water chemistry leads to a phospholipid peroxidation of the bacteria. Gallagher *et al.* [102] showed the inactivation of *Escherichia coli* using a dielectric barrier grating discharge (DBGD) for air-decontamination experiments. The DBGD was realised using a plane of wires, which were shielded by quartz capillaries. Furthermore, Kuzminova *et al.* [103] used a direct DBD application at ambient air to investigate etching effects of polymers, bovine serum albumin (BSA) and *Bacillus subtilis* spores. They observed a 2.7 log reduction after a treatment time of 180 s and a spore etching rate of 0.1 nm/s. Note, that Kuzminova *et al.* used low ozone concentrations (~ 0.3 ppm). A detailed review of DBD applications could be found by Brandenburg *et al.* [104]. They reported about the applications of DBD devices for life-science application, such as cleaning and sterilisation of medical equipment and therapeutic application as skin decontamination and blood coagulation. Another review by Liao *et al.* [105] shows the application of non-thermal plasmas as DBD for the microbial reduction of food products. They reported that DBDs were used to inactivate *G. stearothermophilus* on wheat grains and polypropylene [106] or to inactivate microorganisms on sliced cheese [107], celery, radicchio and deionised water [108]. In addition, Lu *et al.* showed the inactivation of *Escherichia coli* and *Listeria monocytogenes* in sterile phosphate buffered saline (PBS) using a DBD device [109]. Note, an overview of the inactivation studies using DBD, glow and corona discharges could be found in the appendix A.

1.6.4 Surface Micro-Discharge (SMD)

In this work, a non-thermal plasma source based on a surface micro-discharge (SMD) electrode is used, which was presented by Shimizu and Morfill *et al.* [20, 53, 57]. The SMD electrode provides a contact free plasma treatment, without the use of the treated sample as a counterelectrode [110]. The non-thermal SMD plasma allows an indirect way of treatment, where the discharge region and the charged species are spatially separated from the treatment area. When ambient air is used as a treatment gas, the dominant reaction processes lead to a formation of reactive oxygen and nitrogen species (RONS) [111]. The SMD is a combination of the DBD and corona discharge technology. In contrast to the DBD electrode, which operates with a volumetric plasma, the SMD configuration uses a surface plasma with a filamentous discharge. This design leads to a formation of plasma channels along the edges of the mesh and the dielectric barrier surface [40]. The micro-discharges are individual discharge steps in a thin layer on the insulator surface and are considered to be uniform over

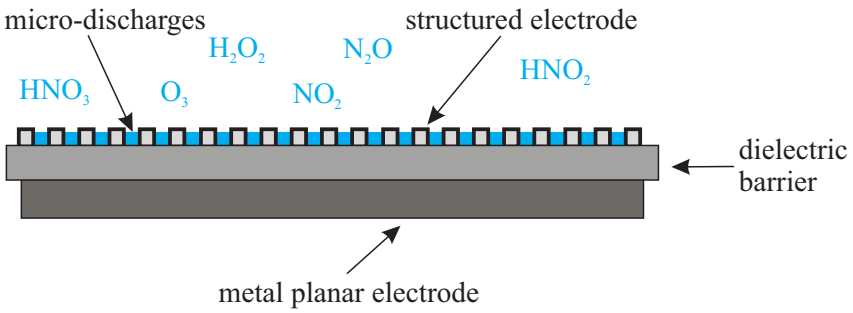

Figure 1.8: Schematic view of the surface micro-discharge electrode, consisting of a planar and structured electrode with a dielectric barrier. In most of the cases, the planar metal electrode is used as the driven electrode and the structured electrode as the grounded electrode. For the use of ambient air, reactive oxygen and nitrogen species are present in a distance to the discharge region (adapted from [53]).

a certain distance [72]. An AC or pulsed voltage is used for the plasma ignition, while the dielectric surface leads to a decrease of the breakdown voltage due to non-uniformities of the electric field and local overvoltage [39]. Fig. 1.8 shows a schematic view of a SMD using a planar arrangement consisting of a planar metal electrode, an insulator and a structured grid electrode. In most of the cases, the planar metal electrode is used as the driven electrode and the mesh grid as the grounded electrode [20]. However, typical parameters are $U = 1 - 10\,\mathrm{kV}$ and $f = 0.1 - 20\,\mathrm{kHz}$ [20], while the discharge area is proportional to the applied voltage [72, 112].

In the following, studies based on the surface DBD technology are described and are additionally listed in Table 1.3. Mastanaiah *et al.* presented a direct "surface" DBD treatment of vegetative bacteria and endospores and received a 6 log reduction of *Geobacillus stearothermophilus* spores after 20 min treatment time. For vegetative bacteria and yeast cells, a 6 log reduction was observable after a treatment time of 4 min [113]. Oehmingen *et al.* [114] introduced a surface DBD treatment of liquids containing different microorganisms. In their study they showed a successful inactivation of suspensions with *Escherichia coli* and *Staphylococcus aureus* with concentrations of $10^6 - 10^8$ cfu/ml after treatment times of $5 - 15$ min. In addition, the treatment of *B. atrophaeus* showed only a 2.5 log reduction after 30 min plasma treatment. In total, the authors found a dependency of the inactivation efficiency to the acidification of the liquids, which was also reported elsewhere [121]. Hähnel *et al.* [115] presented a surface-DBD as a useful tool to inactivate *B. atrophaeus* endospores which were placed in a distance of 0.6 mm to the dielectric barrier. They observed a 5 log reduction of the endospores after 7.5 min plasma treatment with relative humidity conditions $< 50\,\%$. Furthermore, they concluded that OH radicals play an important role for the inactivation efficiency under high humidity conditions. A surface micro-discharge (SMD) electrode at ambient air was used by Klämpfl *et al.* [116] to successful inactivate *B. subtilis*, *B. pumilus*, *B. atrophaeus*, and *G. stearothermophilus* with D-values of 0.3 min, 0.5 min, 0.6 min, and 0.9 min, respectively.

Plasma	Target	Efficiency	Reference
direct surface DBD	*G. stearothermophilus,* vegetative bacteria, yeast cells	6 log for $t = 20$ min 6 log for $t = 4$ min	Mastanaiah *et al.* [113] 2013
surface DBD	microorganisms in liquid *E. coli*, *Staphylococcus B. atrophaeus*	$6 - 8$ log for $t = 5 - 15$ min 2.5 log for $t = 30$ min	Oehmingen *et al.* [114] 2010
direct surface DBD	*B.atrophaeus*	5 log for $t = 7.5$ min	Hähnel *et al.* [115] 2010
SMD	*B. subtilis, B. pumilus, B. atrophaeus* and *G. stearothermophilus*	1 log for $t = 0.3$, 0.5, 0.6 and 0.9 min respectively	Klämpfl *et al.* [116] 2012
SMD	*D. radiodurans* and MRSA	6 log for $t = 20$ s	Maisch *et al.* [110] 2012
SMD	*E. mundtii E. coli*	6 log for $t = 60$ s	Shimizu *et al.* [53] 2011
SMD	*G. stearothermophilus*	$0.5 - 3.5$ log after $t = 5$ min	Jeon *et al.* [117] 2014
indirect SMD	*B. atrophaeus, B. safensis B. megaterium, B. thuringiensis*	3, 6, 6 and 3 log after $t = 90$ min	Shimizu *et al.* [15] 2014
SMD	adenovirus	$5 - 6$ log after $t = 60 - 120$ s	Zimmermann *et al.* [118] 2011
SMD	*E. coli* through textiles	$5 - 6$ log after $t = 60 - 120$ s	Zimmermann *et al.* [119] 2012
SMD	*E. mundtii*	5 log after $t = 15$ min	Mandler *et al.* [120] 2017

Table 1.3: Overview of some studies for inactivation of microorganisms using surface DBDs.

Similar to the previous described studies for this setup, the samples were placed close to the discharge region. Using a similar SMD plasma source, Maisch *et al.* [110] showed a 6 log reduction of *Deinococcus radiodurans* and methicillin-resistant *S. aureus* (MRSA) on dried agar plates after 20 s plasma treatment at ambient air. Timmons *et al.* [122] used a surface discharge to inactivate *Listeria monocytogenes*, *Salmonella enterica* and *E. coli*. Jeon *et al.* [117] showed the inactivation of *G. stearothermophilus* using a SMD for different humidity conditions. The investigation to create a safe therapeutic window for wound treatment is described by Shimizu *et al.* [123]. They also reported about the dependency of ozone production to power input and humidity contend of the ambient air.

Shimizu *et al.* [53] also reported the inactivation of Gram-positive *Enterococcus mundtii* and Gram-negative *E. coli* for different humidity conditions between 20 % and 80 % relative humidity. They did not find a dependency of the inactivation efficiency to the humidity, but they observed a 5 log reduction of the microorganisms after 60 s treatment time using a 6 mm distance of the samples to the plasma ignition. They also investigated the dependency of the ozone production to the power consumption of the SMD electrode. Furthermore, they observed a correlation of the ozone concentration to the inactivation efficiency for *E. coli* [111]. This study indicates, that ozone is one of the major inactivation agents in the afterglow. Zimmermann *et al.* [118] described the inactivation of adenovirus using a SMD at air and achieving a 6 log after 240 s treatment time. They also showed in an other study the disinfection efficiency through different textiles [119]. In detail, they observed a $5-6$ log reduction of *E. coli* on agar plates within 60-120 s. Furthermore, Mandler *et al.* [120] used a similar apparatus, as presented here, to inactivate *E. mundtii* on stainless steel and dental equipment.

This thesis continues the former work by Shimizu *et al.* [15] regarding the use of SMD for the decontamination of spacecraft components. Shimizu *et al.* [15] used an open system where the bacterial samples were treated with CAP afterglow, transported by convection and diffusion without plasma boosting by the circulation of the reactive species. To increase the inactivation efficiency I used an indirect plasma treatment method by introducing a closed CAP afterglow circulation apparatus.

1.6.5 Breakdown Mechanisms

There are differences in the electric breakdown of the plasma devices. In the following, the electric breakdown mechanism based on a streamer formation of a DBD is explained in more detail, as it is mostly applicable to the SMD plasma generation. Although breakdown mechanisms can be very complex, most breakdowns start with an electron avalanche. [42]. In detail, the application of a high voltage between two planar electrodes enables a homogeneous electric field which creates some primary electrons on the side of the cathode. After the electron generation, the primary electron is accelerated to the anode and produces secondary elec-

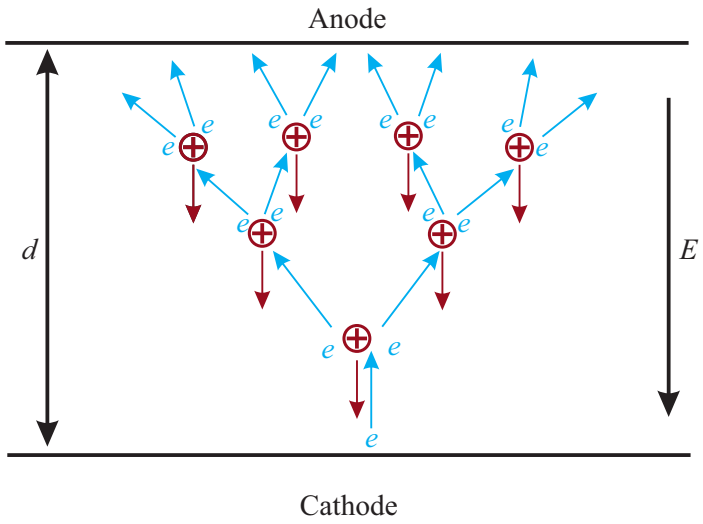

Figure 1.9: Illustration of the Townsend breakdown gap. The primary electron is accelerated to the anode and produces secondary electrons by ionisation of the gas (adapted from [42]).

trons by ionisation of the gas, which generates an avalanche. The ionization in the avalanche is often described using the first Townsend ionization coefficient α, which is defined by the number of electrons produced over a distance of 1 cm by a single electron in the direction of the applied field [42, 124].

The number n of produced ion-electron pairs after the avalanche has passed a distance x is given by [124, 125]

$$n = \exp(\alpha x). \tag{1.2}$$

The electrons lead to positive ions in the electrode gap, which move back to the cathode and create secondary electron emissions. Note, that the ions move much slower than the electrons in the electrode gap [126]. The secondary-electron-emission coefficient γ describes the probability of a secondary electron generation by an ion impact [41, 127]. In detail, γ depends on the cathode material, the state of the surface, type of gas and reduced electric field. When the electric field and thus the Townsend ionization coefficient α exceed a certain value, a transition to a self-sustained discharge by secondary electron emission from the cathode takes place. This process is also named as the Townsend breakdown [42]. In Fig. 1.9 the Townsend breakdown with an electron avalanche is illustrated in a discharge gap. Note that the Townsend breakdown mechanism is only applied for relatively low pressures and short gaps ($pd < 4000\,\mathrm{Torr{\cdot}cm}$).

DBDs consist of numerous micro-discharges, which are distributed in the discharge gap. Furthermore, a micro-discharge is a group of local processes in the discharge gap, which are initiated by an avalanche and developed until the electron current terminated [42]. In detail, micro-discharges are build from so-called streamers, which could be described as weakly ionized plasma channels with a production of fast electrons and ions [39, 58]. The understanding

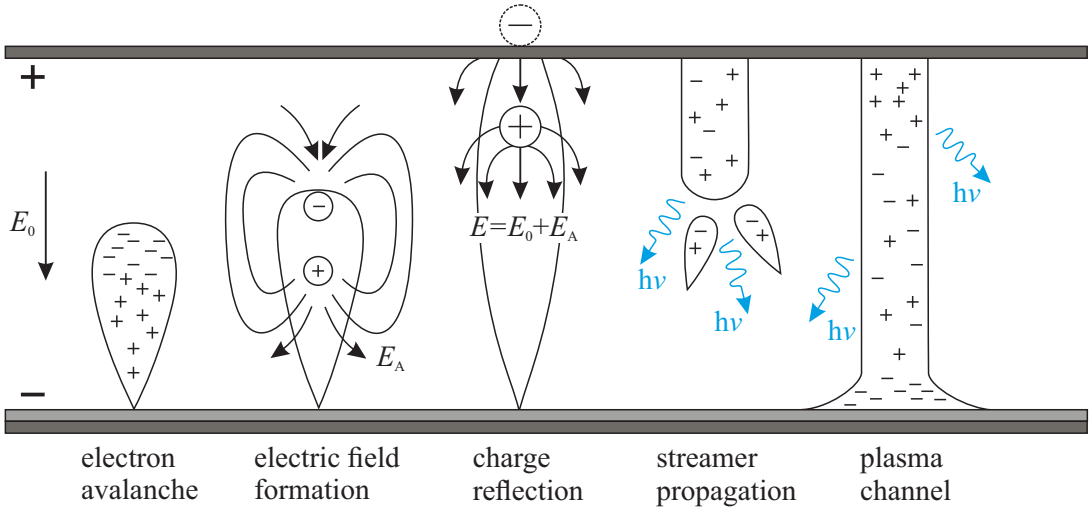

Figure 1.10: Illustration of the mechanism of a cathode-directed streamer, starting with an electron avalanche and an external electric field distortion (adapted from [39, 40]).

of streamer breakdown mechanism originates from the observation of spark discharges. The concept of streamers was originally developed by Raether [128, 129], Loeb [130] and Meek and Craggs [42, 125]. In contrast to the Townsend breakdown, the spark/streamer breakdown mechanism is found in larger gaps and under a higher pressure [39]. Similar to the Townsend breakdown, the streamer are related to a formation of avalanches. The streamer formation of high pd and overvoltage develops faster than the needed time for ions to cause secondary electron emission from the cathode due to the low mean free path for ions under ambient pressure [42].

The streamer formation is described in the following and is illustrated in Fig. 1.10. The formation of a streamer starts with an electron avalanche to the anode. Due to the different velocities and velocity directions of electrons and ions, the electrons are found in the front of the avalanche which leads to a formation of space charges which also introduce an electric field resulting in an external electric field distortion. As can be seen in Fig. 1.10, the electric field distortion leads to an increase of the electric field at the front of the avalanche which accelerates the ionization [131]. Note, that the electric field inside the avalanche is reduced [39]. When the avalanche reaches the anode, the positive tail remains in the gap and still causes an electric field distortion. When the avalanche is strong enough, a cathode-directed streamer is formed due to the high electric field on the side of the anode, because the positive charge and electric field are maximal at this point. In particular, a streamer happens when the electric field of the space charge of an avalanche is in the range of the external field. Afterwards, the streamer propagates along the positively charged tail of the primary avalanche [42]. The streamer formations leads to the generation of photons, which also generates secondary avalanches, while the electrons of these avalanches are pulled in the positively charged tail in

	Duration	Charge transferred
Micro-discharge (0.2 mm radius)	40 ns	10^{-9} C
• Electron avalanche	10 ns	10^{-11} C
• Cathode-directed streamer	1 ns	10^{-10} C
• Plasma channel	30 ns	10^{-9} C
Microdischarge remnant	1 ms	$\geq 10^{-9}$ C

Table 1.4: Mico-discharge characteristics of a DBD using ambient air and pressure for 1 mm gab [42].

the avalanche. This creates a quasi-neutral, conducting plasma channel for electrons which bridges the gap [130, 132]. A streamer which starts from the anode to the cathode is called a cathode-directed or positive streamer. An anode-directed or negative streamer grows in both directions and is not shown here. They occur in large gaps with high voltages, where a transformation of an avalanche to streamer is possible. More information about anode-directed streamer could be found in the literature [39].

The charge accumulation on the dielectric barrier compensates the external electric field which avoids the formation of new avalanches and streamers until the voltage on the electrodes is reversed [43]. The charge accumulation leads to a lateral spreading [133], which is visible in Fig. 1.10. After the discharge collapses, the left ionic charges in the volume and deposit on the surface are called a micro-discharge remnant. This remnant facilitate the formation of new micro-discharges at the same location after the polarity of the applied voltage is reverted [39].

For the used electrode system in this thesis, the literature [39, 93] suggests an electron density of $10^{14} - 10^{15}\,\mathrm{cm}^{-3}$, an electron energy of $E_\mathrm{e} = 1 - 10\,\mathrm{eV}$ and an ionisation degree of $10^{-7} - 10^{-4}$ for the micro-discharges. Furthermore, Kogelschatz *et al.* reported that at atmospheric pressure, current densities in the range of 100 to $1000\,\mathrm{A/cm}^2$ are reached. Furthermore, the diameter of the micro-discharge filaments are about of some 100 µm [58, 133]. In general, the electrons which are established by the streamer, dissipate from the gap in about 40 ns, while the ions can be found for several microseconds in the gap [42]. Table 1.4 shows the calculated duration for the micro-discharge processes. The short duration of the micro-discharges avoid an overheating of the streamer channel [39].

The discharge patterns of surface discharges are comparable to those in dielectric barrier discharge arrangements with a dielectric cathode [112]. In the case of a surface discharge, the charge transfer takes place in a thin layer on the dielectric surface, while the discharge area on the dielectric increases by an increase of the applied voltage [134]. Note, that an observation of glow discharges under ambient pressure conditions could be observed when a sufficient overlap of simultaneously propagating electron avalanches is given. This condition is observable in helium with its relatively wide streamer channels [133].

1.7 Plasma Chemistry

In this work, the afterglow of a SMD device is used with ambient air for different humidity conditions. In general, the chemical reactions of air plasma in humid conditions are complex [40, 135, 136]. In the presented apparatus, the afterglow is circulating and the long-living reactive species are acting in a treatment chamber with the target, which is placed in a distance to the discharge region. Thus, the reactions with UV light and charged particles are prevented. In order to use reasonable parameters for the plasma treatment and to understand the mechanism of action with the treated surfaces and endospores, it is crucial to investigate the long-living reactive species in the afterglow.

In general, the production of the reactive species of the plasma depends on the used plasma source and the operating conditions [137]. The interaction of electrons in the plasma discharge region initiates a cascade of dissociation, excitation and ionisation processes with other particles and is responsible for the unique variety of the plasma chemical cocktail. Due to that, the electron energy influences the plasma chemistry in the plasma discharge [39, 40] The operation of a SMD in air leads to a production of various oxygen and nitrogen species close to the discharge region. Furthermore, these species react in the afterglow region, next to the discharge region, while the detailed mechanisms of the coupled and dynamic processes are relatively poor understood for SMD devices [137]. Numerical simulations of Sakiyama *et al.* [138] predict, that O_3, NO_2, N_2O, N_2O_5, HNO_2, HNO_3 and H_2O_2 are reactive species produced by SMD using humid air. For the simulations, they used a model including over 50 species and 600 elementary reactions with a differentiation of two regions namely a discharge layer with both charged and neutral species and an afterglow region consisting only of neutral species [138].

The device in the present work operates in an ozone rich mode. Ozone is a strong bactericidal and oxidising agent, while nitric oxide (NO) is often transformed into nitrites and nitrates, which are important signalling molecules in aerobic biology [111, 139]. In the past, many ozone generating DBD devices were analysed in order to optimise the ozone production for different applications like treatment of drinking water, bleaching, disinfection, food processing [140–146]. Note, that in general ozone is mainly produced by electrical discharges like corona and DBDs [141].

In the following, some important chemical reactions in air are described, which are used later to explain the experimental findings in this work. The production of ozone originates from the dissociation of O_2 into O atoms [133, 144]. Afterwards, O_3 molecules are formed by a three-body reaction:

$$O + O_2 + M \rightarrow O_3^* + M \rightarrow O_3 + M \tag{1.3}$$

with M as a third collision partner (for example O_2, O_3, O, N_2) and O_3^* as a transient excited state [133]. In addition, the following side reactions compete with the ozone production when

the feed gas would only be O_2:

$$O + O + M \rightarrow O_2 + M \tag{1.4}$$
$$O + O_3 + M \rightarrow 2O_2 + M \tag{1.5}$$
$$O + O_3^* \rightarrow 2O_2 + M. \tag{1.6}$$

In discharges in the presence of air, various reactive oxygen and nitrogen species (RONS), like NO, N_2O, NO_2, NO_3 and N_2O_5 are generated, due to the excitation and dissociation of nitrogen molecules. The presence of nitrogen leads to the following reaction paths, which are responsible for half of the O_3 production in air discharges [133, 142, 147]

$$N + O_2 \rightarrow NO + O \tag{1.7}$$
$$N + NO \rightarrow N_2 + O \tag{1.8}$$
$$N_2^* + O_2 \rightarrow N_2O + O \tag{1.9}$$
$$N_2^* + O_2 \rightarrow N_2 + 2O. \tag{1.10}$$

Note, that N_2^* represents an exited nitrogen state. Under the presence of nitrogen, the formation of ozone takes 100 µs instead of 10 µs when only ozone is present. By a variation of the plasma parameters like an increase of the power consumption or reduction of the mass flow, the production of NO and NO_2 reaches a level at which the ozone generation breaks down, which is called *discharge poisoning* [148, 149]. For these plasma parameters, O_3 and N_2O_5 are not measurable, while NO, NO_2 and N_2O are detectable, as NO_x molecules are consuming the oxygen atoms faster than O_2 molecules, which causes a catalytic recombination of O atoms [58]

$$O + NO + M \rightarrow NO_2 + M \tag{1.11}$$
$$O + NO_2 \rightarrow NO + O_2 \tag{1.12}$$

$$O + O \rightarrow O_2. \tag{1.13}$$

Additionally, remaining O_3 molecules are dissociated via catalytic processes of NO and NO_2 [58, 133]

$$NO + O_3 \rightarrow NO_2 + O_2 \tag{1.14}$$
$$O + NO_2 \rightarrow NO + O_2 \tag{1.15}$$

$$O + O_3 \rightarrow 2O_2. \tag{1.16}$$

Note, that equation 3.1 and 3.2 are the same. Previous publications reported an absence of NO and NO_2 in a gas mixture [148], when O_3 is present, which is explained by the fast reaction rates of NO, NO_2 with O_3. The main responsible reactions in addition to equation 1.14 are:

$$NO_2 + O_3 \rightarrow NO_3 + O_2 \tag{1.17}$$

$$NO_2 + NO_3 \rightarrow N_2O_5 \tag{1.18}$$

$$2NO + 3O_3 \rightarrow N_2O_5 + 3O_2. \tag{1.19}$$

Shimizu *et al.* [111] reported that the transition from the ozone mode to the nitrogen mode for a SMD is different to classical ozone reactors. They showed, that a SMD operates in the ozone rich regime for an input power below $0.1\,W/cm^2$ and in a NO_x rich regime when the power is higher than $0.1\,W/cm^2$. They described that the reaction of N atoms with O_2/O_3 is not fast enough to generate NO and propose an alternative model of reactions between vibrationally excited nitrogen molecules ($N_2(v)$) and oxygen atoms [111, 138]. The significant difference of SMD to former ozone generators is, that the mode transition is observed over time using a constant input power of the plasma.

The presence of humidity during the micro-discharge leads to the generation of H, OH and HO_2 molecules which influences the production processes and chemical pathways of ozone [133, 144]. In addition, molecular oxygen reacts fast with water vapour and forms H_2O_2 which also decomposes into OH radicals [147]

$$O^* + H_2O \rightarrow H_2O_2^* \rightarrow 2OH. \tag{1.20}$$

In addition, NO and NO_2 rapidly react with OH molecules and form HNO_2 and HNO_3. HNO_2 is also consumed by the reaction with OH to form NO_2 and HNO_3 by the reaction with OH to form NO_3 [150, 151]. Some of the reactive neutral species like (N, O, OH, NO and HO_2) are confined in the discharge layer (around 1 ppm), while their density is low in the afterglow [138, 152]. In addition, N_2O_5 reacts together with H_2O to HNO_3 [147].

Due to the complexity of the plasma chemistry at ambient air under different humidity conditions, the presented section provides only some of the possible reactions. More detailed discussions about chemical reactions could be found in the literature [111, 137, 138, 150].

1.8 Objectives of the Thesis

Inactivation of microorganisms using cold atmospheric plasma has a plurality of benefits such as low cost, simple design and comfortable usage without organic residues after the treatment [53]. Furthermore, the utilisation of long-lifetime plasma species allows an homogeneous and gentle treatment of space relevant materials, as no vacuum chambers are required [116, 153]. The main focus of this work is the presentation of a new CAP apparatus for the

inactivation of bacterial endospores on sensitive materials to provide a useful alternative for the decontamination of spacecraft equipment for planetary protection.

In chapter 2.1, the plasma afterglow circulation apparatus (PACA) and the SMD electrode are introduced, operating with ambient air under different humidity conditions and various treatment chambers. In addition the used investigation methods like UV absorption spectroscopy in gas and liquid, Fourier Transformation Infrared (FTIR) spectroscopy and the power monitoring are summarised.

In chapter 3 a detailed spectroscopic characterisation and analysis of the plasma afterglow composition is discussed. At first, the distribution of the ozone concentration within the apparatus and the influence of the humidifier water and the humidifier position were investigated. Furthermore, the plasma chemistry in dependence on different parameters was analysed. In detail, measurements show the dependency of the plasma composition to the flow rate, gas humidity and power consumption. Some of the important findings are, that the detection of HNO_3 increases by the reduction of the gas humidity. In addition, the ozone concentration correlates with the power consumption and shows an inverse proportionality to the gas flow rate. The formation of HNO_3 and NO_2 and the quenching of O_3 were observed and discussed. Finally, the afterglow composition was varied by the use of different gases like synthetic air, nitrogen and argon in te PACA.

In addition to the spectroscopic analysis of the afterglow composition, in chapter 4 the PACA was investigated to inactivate bacterial endospores of *Bacillus atrophaeus* to analyse the inactivation efficiency. In detail, the inactivation efficiency in different treatment chamber volumes and the inactivation homogeneity within the largest treatment chamber was examined. Furthermore, the inactivation efficiency using 3D barriers (cylinders and Tyvek packages) was analysed plus the influence of an additional gas flow. In conclusion, it was possible to inactivate bacterial endospores by adapting the treatment time for all settings. The analysis using scanning electron microscopy (SEM) allowed to observe the influence of the plasma treatment to the bacterial endospores samples and to reveal the differences in the manufacturing process of the spore samples.

In chapter 5 the compatibility of the plasma afterglow treatment to different materials were examined in order to complete the investigations to introduce the PACA as a useful inactivation method for planetary protection. Therefore, microscopic analysis, contact angle and X-ray photoelectron spectroscopy (XPS) measurements were executed and discussed. In the investigations, the plasma afterglow treatment shows an increased material compatibility for high humidity conditions and an enhanced treatment compatibility of plastic materials compared to some metals like copper, brass and aluminium.

In total, the combination of the various examinations improved the understanding of the cold atmospheric plasma technology and provides a big contribution to the evaluation of this promising technology for the application of CAP for planetary protection.

Chapter 2

Experimental Setup and Methods

The presented chapter introduces the plasma afterglow circulation apparatus (PACA) using the surface micro-discharge technology for the inactivation of bacterial endospores. In addition, the chapter gives an overview about the used investigation methods, like UV absorption spectroscopy, FTIR spectroscopy and power monitoring to analyse the PACA and the afterglow composition.

2.1 SMD Electrode and Circulation Setup

In order to inactivate bacterial endospores on large components, the plasma afterglow circulation apparatus (PACA) was build up in cooperation with terraplasma GmbH. The PACA consists of 1) a humidifier for the circulating ambient air, 2) a membrane pump to create a circulating gas flow, 3) a plasma source of two cylindrical electrodes to generate the CAP, 4) a treatment chamber, 5) a UV absorption spectrometer to analyse the O_3 concentration, 6) a flow meter and 7) a FTIR to investigate the composition of the afterglow species, as shown in Fig. 2.1. As demonstrated in Fig.2.1, the air passes through the water (bubbling) and becomes humid. The humidified air is transported to the electrode system by a membrane pump (NMP 850.1.2 and N86KT.18, KNF Neuberger GmbH, Germany) with a velocity of $1.5 - 7.0\,\mathrm{l/min}$. When the circulating air passes the electrode tubes (terraplasma GmbH, Germany), reactive oxygen and nitrogen species (RONS) are produced as long-living species by micro-discharges of the plasma. These species are forming the plasma afterglow, which is transported to the treatment chamber and through a UV-absorption-measurement-box and a heating pipe to the FTIR spectrometer (CX 4000, Gasmet Ansyco, Germany) to analyse the afterglow composition. The heating pipe of 1 m length and 60 °C is crucial to avoid condensation on the spectrometer mirrors. This leads to a temperature increase less than 2 °C in the treatment chamber over the treatment time of 30 min, so that the afterglow composition is not affected. Finally, the afterglow gas returns into the humidifier and runs through the closed circuit again. Using a circulating gas flow in a closed apparatus causes an accumulation of the

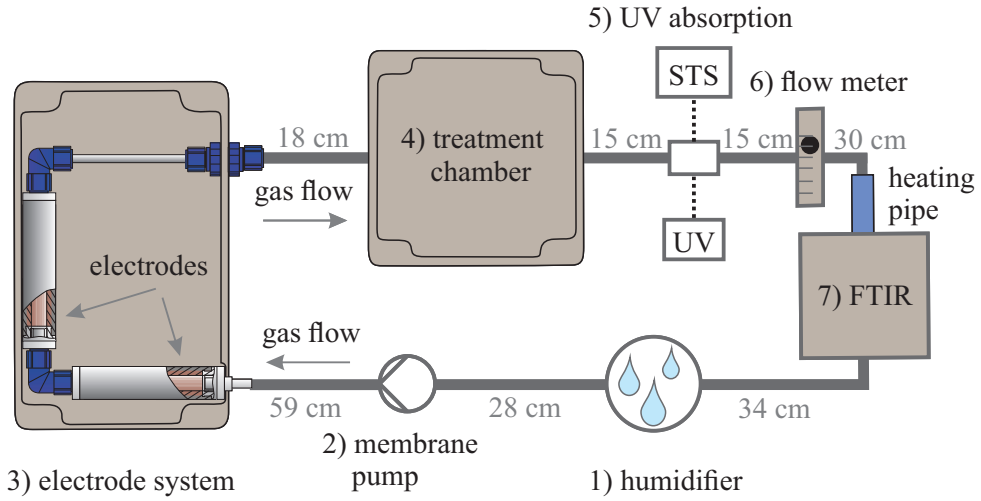

Figure 2.1: Plasma afterglow circulation apparatus consisting of 1) a humidifier, 2) a membrane pump, 3) an electrode box with two SMD electrodes, 4) a treatment chamber, 5) a UV spectrometer, 6) a gas flow meter, and 7) a FTIR.

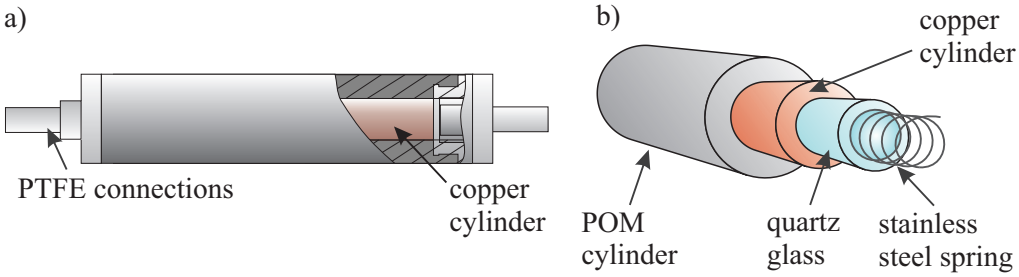

Figure 2.2: Surface micro discharge electrode for the plasma production. a) Top view of the cylindrical electrode with PTFE connections. b) Cross-section electrode with copper cylinder, quartz glass and a stainless steel spring with cylindrical shape, surrounded by a POM casing (adapted from [14]).

reactive afterglow species in the PACA, which is called plasma boosting. Note, that Fig. 2.1 shows the UV-absorption-measurement-box for the UV aborption spectroscopy to analyse the ozone concentration. The O_3 measurement is described in chapter 2.2 in more detail. Furthermore, the design of the PACA allowed to install the UV-absorption-measurement-box at different measurement points or to position the UV spectrometer at the treatment chamber itself.

Fig. 2.2 shows a sketch of the electrodes for the plasma production based on the surface micro-discharge (SMD) plasma technology [53, 57]. The used SMD plasma electrodes have a coaxial structure, with an inner diameter of 10.7 mm and a length of 8.25 cm. One SMD electrode consists of a grounded stainless steel electrode with spring shape, which is separated by a quartz glass tube covered by a driven copper electrode. The detailed description of the used materials and measures for the SMD electrode are listed in Table 2.1. The SMD electrodes are

	Material	Thickness	Length & Inner Diameter
dielectric	quartz glass	1 mm	103 mm & 12 mm
grounded electrode	stainless steel	0.63 mm	82.5 mm & 10.7 mm
driven electrode	copper	2 mm	82.5mm & 14 mm

Table 2.1: Materials and measures of the SMD electrode.

enclosed in a sealed Polyoxymethylene (POM) cylinder with Polytetrafluorethylen (PTFE) connections. For the plasma generation, a high voltage amplifier (Trek, 10/10B HS, Acal BFi Germany GmbH, Germany) and a function generator (Hameg, HM8150, Hameg Industries, Germany) are used to apply a high sinusoidal voltage ($6 - 10\,\mathrm{kHz}$, $4.5 - 6.4\,\mathrm{kV_{pp}}$) to the electrodes. The applied high voltage generates numerous micro-discharges on the side of the stainless-steel spring, which partly ionize the circulating gas. The activated gas molecules react and form the long-living reactive species of the plasma afterglow, which is used for the sporicidal inactivation.

The components of the PACA are connected by 6.35 mm (0.25") tube fittings (Swagelok, Germany) and corresponding Perfluoroalkoxy alkanes (PFA) tubes (Swagelok, Germany) of 6.35 mm outer diameter and ~ 4 mm inner diameter. In addition, the connection to the humidifier was achieved by silicone tubes of 6.3 mm inner diameter (VWR International GmbH, Germany). In general, the apparatus is operated in ambient air at room temperature and under ambient pressure. For the circulating gas, different humidity conditions are used. The humidification is achieved by a 500 ml gas washing bottle (Carl Roth GmbH, Germany), filled with 400 ml distilled water.

Using the PACA, it is easily possible to change the treatment chamber size. In detail, for some of the measurements three different volumes (0.54 l, 1.80 l and 2.6 l) of air-tight aluminium boxes were used as treatment chambers. The samples were placed at the bottom of the treatment chamber, so that they were not in the direct line of the afterglow flow. The reactive gas entered the treatment chamber in the middle of the sidewall (in a height of 36 mm/41 mm/46 mm for the treatment volumes 0.54 l/1.8 l/2.6 l) through a round opening with 4 mm diameter. The maximal residual system volume was estimated with 250 ml without FTIR and 700 ml with FTIR, respectively. Note, that for the use of the FTIR, there is no need to remove gas from the system, but the spectrometer increases the total volume of the apparatus about 450 ml, because the gas has to fill up the measuring cell of the FTIR.

In the following chapters, the PACA was operated in most of the measurements with 2.6 l treatment volume, $Q = 3.5\,\mathrm{l}$ gas flow, $f = 10\,\mathrm{kHz}$ and $U = 6.0\,\mathrm{kV_{pp}}$. If some of the parameters were changed for the investigations, it is mentioned separately in the description of the measurements.

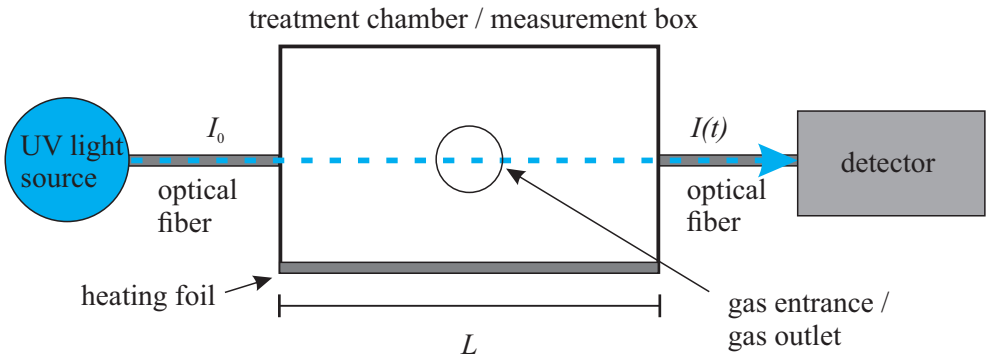

Figure 2.3: UV absorption spectroscopy for the ozone measurement using a treatment chamber or measurement box. The intensity of the UV light I_0 is reduced by passing the measurement cell with absorbing ozone molecules.

2.2 UV Absorption Spectroscopy

Ozone is one of the dominant species produced by SMD at ambient air and is a known oxidizing and bactericidal agent [111, 138]. Ultraviolet (UV) absorption spectroscopy was used to analyse the ozone concentration in the presented plasma afterglow circulation apparatus in chapter 3 and chapter 4. Note, that it was not possible to use the FTIR spectrometer for the qualitative ozone analysis, as the measured concentration range of O_3 exceeds the measurement range of the FTIR (see chapter 3). Fig. 2.3 illustrates the UV absorption measurement. In general, UV light enters a volume with an initial intensity I_0, while the intensity is reduced by passing a volume with an absorbing gas and an optical path length of L. Afterwards, the remaining intensity of the UV light $I(t)$ is detected.

For the measurement, a spectrometer (STS-UV, Ocean Optics, Germany) and a UV lamp (Hg/Ar, HG-1, Ocean Optics, Germany) were used. For this purpose, optical fibers with collimating lenses were installed in the middle of the side walls of the treatment chambers (0.54 l, 1.8 l and 2.6 l) or the measurement box. Furthermore, one of the fibers was connected to the spectrometer and the other one to the light source. As already mentioned in chapter 2.1, the use of a small measurement box (with $V = 34$ ml) for the UV absorption spectroscopy enables to analyse the ozone concentration at different positions within the apparatus. In addition, the PACA could be analysed with the UV-measurement-box only and without treatment chamber in the circle. To avoid condensation on the UV spectrometer lenses by the moisturised gas, the UV-measurement-box is heated with a 50 °C warm heating foil (thermo Technologies, Germany).

In the presented apparatus, the O_3 concentration is monitored by UV absorption at approximately 254 nm wavelength [154–156]. For the measurement, the measured intensity was integrated from 253.5 to 254.5 nm. The integration time of the signal was adjusted between $50 - 200$ ms and a data point was recorded every 500 ms.

Treatment Chamber [l]	Optical Path Length L [mm]
0.54	86
1.8	146
2.6	180
0.034	32

Table 2.2: Optical path length for UV absorption spectroscopy. The value 0.034 l refers to the use of the UV-measurement-box.

In detail, the O_3 density N_{O_3} [m^{-3}] is calculated using Lambert-Beer's law [157]:

$$I(t) = I_0 e^{-N_{O_3,m^{-3}}(t)\sigma L} \tag{2.1}$$

$$N_{O_3,m^{-3}}(t) = -\left(\frac{1}{\sigma L}\right) \ln\left(\frac{I(t)}{I_0}\right). \tag{2.2}$$

$I(t)$ is the measured UV intensity at the time t, L is the optical path length and σ is the absorption cross-section of O_3 at $\lambda = 254\,\text{nm}$, with $\sigma = 1.147$ x $10^{-17}\,\text{cm}^2$ [158]. Table 2.2 summarises the used optical path lengths for the measurement in the treatment chambers and in the UV-measurement-box.

To convert the ozone concentration to the unit ppm (parts per million), an ideal gas is assumed. In this case, the number of 6.02×10^{23} particles are present in a volume of 22.4 l, which corresponds to a particle density of $N = 2.69 \times 10^{25}\,\text{m}^{-3}$. The ozone concentration using ppm is then given by

$$N_{O_3,\text{ppm}} = \frac{N_{O_3,\text{m}^{-3}}}{N} \times 10^6. \tag{2.3}$$

Note that the presented ozone concentration in this work is always the mean value of at least three measurements with the corresponding standard deviation.

2.3 UV Spectroscopy in Liquids

The PACA was operated under various humidity conditions for the investigations. To investigate the chemical reactions within the circulating gas, it is crucial to understand the interaction of the RONS with the water of the humidifier.

The solubility of gas molecules in liquids underlies Henry's law, which says that the equilibrium ratio of a molecule concentration in the gas phase and in aqueous phase is constant [159]. The Henry solubility H^{cp} is often defined as

$$H^{cp} = \frac{c_a}{p_g} \sim \frac{c_a}{c_g}, \tag{2.4}$$

where c_a is the concentration of the species in the aqueous phase, p_g the partial pressure

Species	Henry's Constant [M/atm]
O_3	1.1×10^{-2}
NO_2	1.2×10^{-4}
N_2O	2.4×10^{-4}
NO	1.9×10^{-5}
H_2O_2	7.0×10^{2}
HNO_3	2.1×10^{3}

Table 2.3: Henry's constant for different afterglow components [159].

of the same species in the gas phase with the gas phase concentration c_g. Different Henry solubilities for the expected reactive molecules of the afterglow are displayed in Table 2.3.

In this work, a UV/VIS spectrometer (Lambda 35, PerkinElmer, Germany) was used for the investigation of the dissolved molecules in the water of the wash bottle. For the measurement, a reference sample of untreated water and plasma treated water was analysed. Afterwards, the UV/VIS spectrometer software calculated the resulting absorbance A based on Lambert-Beer's law [157]:

$$A = \log(I_0/I) = c\varepsilon L. \tag{2.5}$$

Here, c describes the molar concentration, ε the molar absorption coefficient and L the optical path length. The optical path length of the UV/VIS spectrometer for the liquid was 1 cm. The absorbance for nitrate was analysed at 205 nm with $\varepsilon = 38750\,\mathrm{M^{-1}cm^{-1}}$ [160] and for O_3 at 260 nm with $\varepsilon = 3300\,\mathrm{M^{-1}cm^{-1}}$ [161] using common molar absorption coefficients for ozone and nitrate.

2.4 FTIR Spectroscopy

This chapter summarises the general fundamentals of the FTIR spectroscopy and the used methods for the afterglow analysis in the PACA. For a quantitative and qualitative multi-component analysis of the plasma afterglow composition, a Fourier Transform Infrared spectrometer (FTIR) was used. The technology is based on the analysis of vibrational and rotational molecule states, caused by the interaction of electromagnetic radiation in the infrared range with molecules. Infrared radiation is divided into three wavelength regions, far-infrared ($\tilde{\nu} = 10 - 200\,\mathrm{cm^{-1}}$), mid-infrared ($\tilde{\nu} = 200 - 4000\,\mathrm{cm^{-1}}$) and near-infrared ($\tilde{\nu} = 4000 - 12800\,\mathrm{cm^{-1}}$). If a molecule absorbs a photon in the far-infrared to microwave range, molecular rotations can be excited. However, if a photon from the near-infrared regime is absorbed, mainly molecular vibrations are excited [162]. The infrared absorption spectrum of an infrared active molecule has an unique shape. This allows to identify multiple components in an unknown gas.

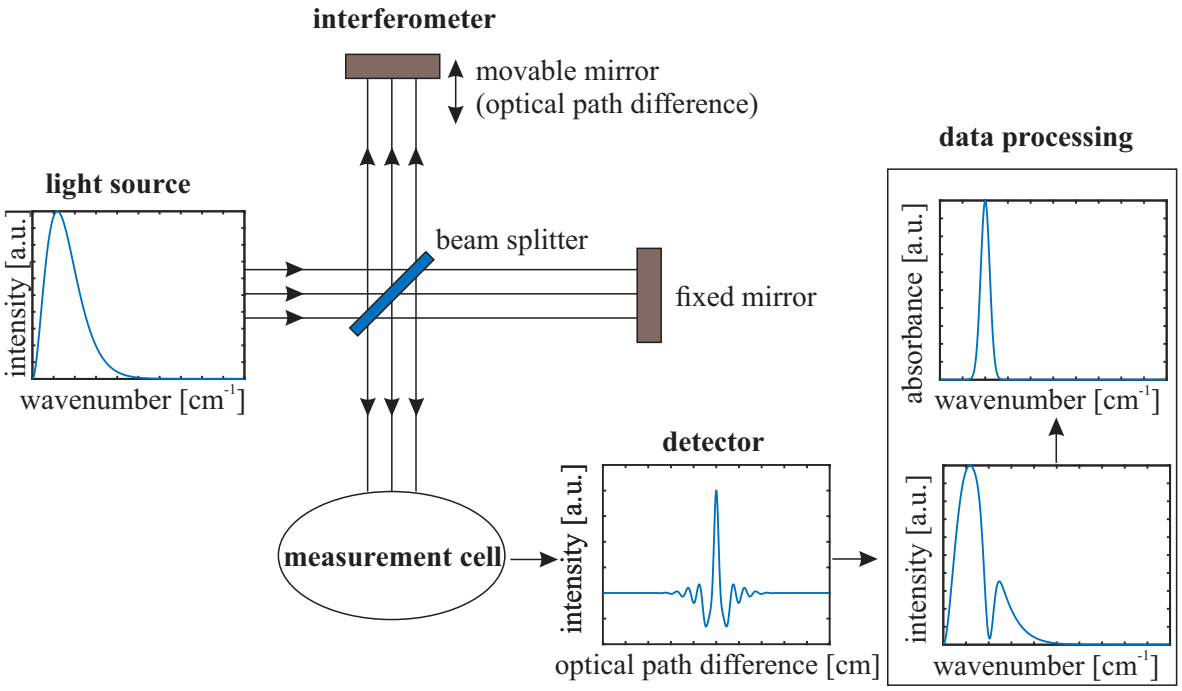

Figure 2.4: Schematic view of the components of a FTIR spectrometer (light source, interferometer, measurement cell, detector and data processing).

The FTIR spectrometer is a non-dispersive spectrometer which works with a polychromatic radiation source and therefore allows the detection of the IR absorption spectrum with a single measurement. The components of the FTIR spectrometer are illustrated in Fig. 2.4. In detail, the generated infrared beam is modulated by a Michelson interferometer and passes the measuring cell, containing the sample gas and finally reach the detector. In detail, the detector measures the resulting interferogram, which shows the detection intensity in dependence to the position of the movable mirror (optical path difference resulted from the spectrometer). The data processing uses the Fourier transformation to convert the detected interferogram into the frequency dependent infrared absorption spectrum of the sample gas [163].

The qualitative analysis of the component concentration is based on Lambert Beer's law, which is already described in chapter 2.2 and 2.3 for the UV absorption spectroscopy [164, 165]. To calculate the absorbance $A = \log(I_0/I) = \varepsilon cL$ using Lambert Beer's law, a background spectrum $I_0(\nu)$ is measured using a reference gas without infrared activity (for example N_2). Afterwards, the ratio of the background spectrum and the sample spectrum is used to calculate the absorbance A as a function of the wavenumber $\tilde{\nu}$. According to Lambert Beer's law the absorbance is proportional to the concentration c and the absorptivity ε of a molecule when the optical path length is constant. Note, that the absorptivity $\varepsilon(\tilde{\nu})$ varies with the wavenumber $\tilde{\nu}$, but is independent of the sample concentration. If the sample concentration varies in a

wide range, the absorptivity ε is not constant anymore, which causes a non-linear dependency of the concentration c to the absorbance A. In addition, the variation of temperature and pressure have an influence to the absorption line shape of the absorption spectrum [163]. In total, the measured absorption spectrum is the sum of the absorption spectra of each gas component. To receive a correct quantitative and qualitative analysis, the spectrometer has to be calibrated for the used temperature, pressure and the expected concentration range of the molecules.

To analyse the afterglow composition in the present work, a commercial FTIR spectrometer (CX4000, Gasmet Technologies, Finland) was included in the PACA. The FTIR is working with an Silicon Carbide light source in the mid-infrared region and detects an absorption spectrum in the range of $850 - 4200\,\mathrm{cm}^{-1}$ with an spectral resolution of $8\,\mathrm{cm}^{-1}$ and an optical path length of $L = 5\,\mathrm{m}$. According to the manufacturer Gasmet, it is possible to analyse up to 50 gas components at once [163]. To avoid condensation of reactive substances in the spectrometer, the operation temperature of the measurement cell was set to 60 °C and the reactive gas had to pass a 1 m heating pipe of 60 °C before it entered the FTIR (as already mentioned in chapter 2.1). During the investigations, the scan rate was 0.5 scan/s for an absorption spectrum of the reactive gas. For the detection of the background spectrum, the spectrometer was flushed with nitrogen gas (N_2 5.0 Linde: $O_2 \leq 3\,\mathrm{ppm}$, $H_2O \leq 5\,\mathrm{ppm}$). The processing of the data was done by the FTIR spectrometer software Calcmet, which uses reference spectra for each expected gas component. To calculate the concentration of a gas component, Calcmet uses multipliers of the individual gas spectra [163]. In general, if the calculated spectrum diverges from the measured spectrum, the difference of these spectra are shown in a rest spectrum in the Calcmet software. The used reference spectra of the individual gas components are listed in the appendix B.

In the present work, the time evolution of the calculated concentrations for N_2O, HCHO, H_2O, HNO_3, NO_2 and NO are discussed. Note, that the absolute humidity concentration of H_2O was calculated by the Calcmet software (1 vol % corresponds to ~ 30 % relative humidity at room temperature [138]). The absorption spectra itself were analysed to identify additional reactive species, for which no reference spectra were available. In the following, an exemplary absorption spectrum during the afterglow circulation is presented to illustrate the spectral analysis in chapter 3. Fig. 2.5 a) shows typical FTIR absorption spectra of the afterglow plasma for a relative humidity (RH) of ~ 33 % (blue line) and ~ 90 % RH (red line) as a function of the wavenumber $\tilde{\nu}$ in a range of $4200\,\mathrm{cm}^{-1} - 850\,\mathrm{cm}^{-1}$. The black line shows the absorption spectrum of ambient air without plasma. Note, that Fig. 2.5 is shown for decreasing wavenumbers. The spectra were detected after 9.5 min plasma ignition, as an exemplary time point and without treatment chamber in the circle of Fig. 2.1. Note, that the examination using 33 % RH, was measured without humidifier in the system. The afterglow spectrum for 90 % RH indicates that CO_2, H_2O and N_2O are present in the treatment setup

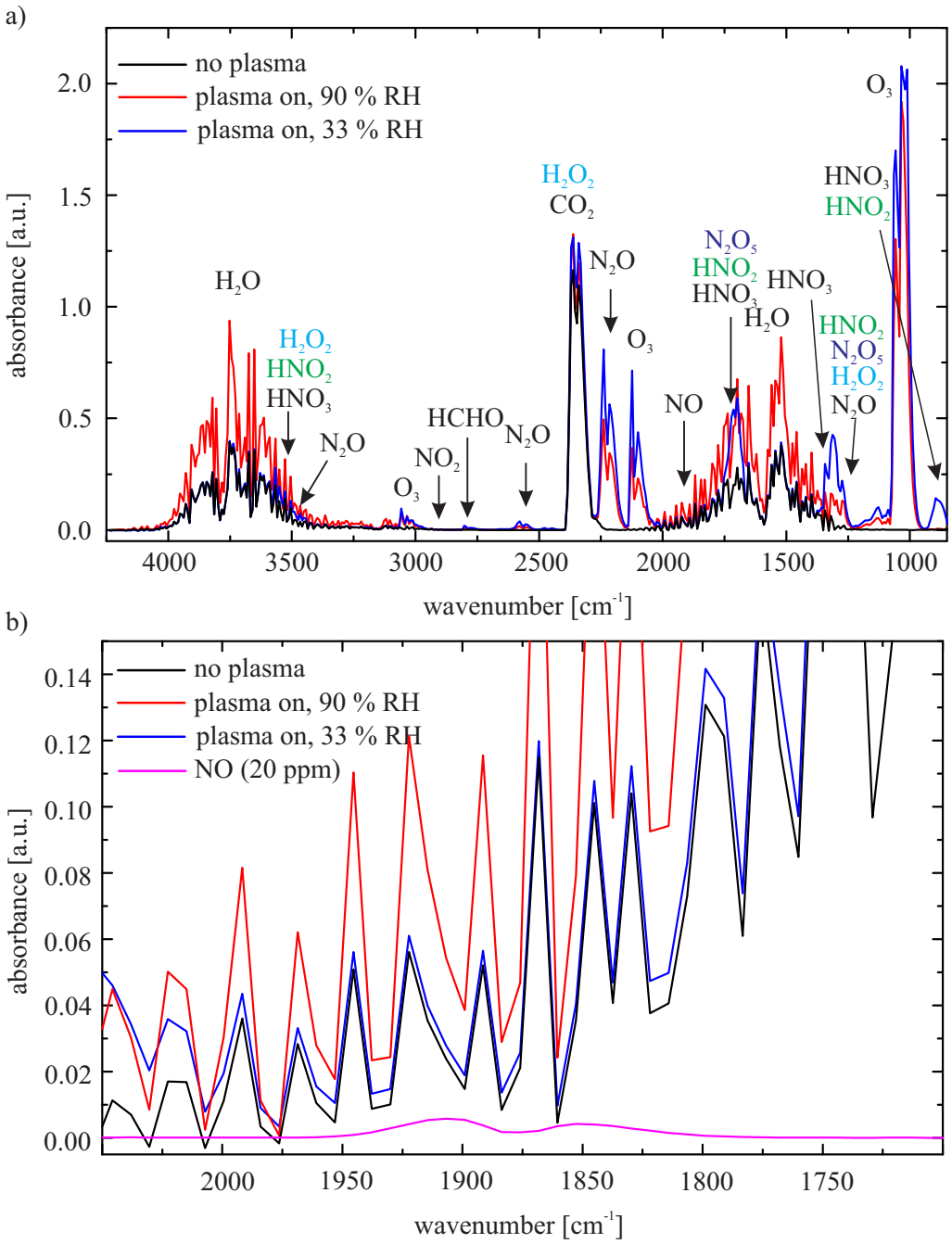

Figure 2.5: FTIR absorption spectra: a) Absorption spectra before plasma ignition (black line) and during plasma ignition with high humidity conditions ∼90 % RH (red line) and ambient humidity condition ∼33 % RH (blue line) (adapted from [14]). b) Magnification of Figure a) with an additional library spectrum for 20 ppm NO.

together with O_3, while CO_2 and H_2O are components of the ambient air. The absorbance by H_2O is increased under high humidity conditions. For 33 % RH, N_2O and O_3 are visible in the spectrum - similar to 90 % RH - but in addition HNO_3 is detectable with the FTIR. Furthermore, the concentrations of the species are slightly higher than during high humidity conditions. For both conditions, NO_2 and NO cannot be clearly identified in the absorption spectra. The detection of NO is difficult in the presence of water, since the small NO absorption peaks appear in the region of the H_2O absorption bonds. Fig. 2.5 b) illustrates a magnification of a) with a reference spectrum of NO for 20 ppm. The diagram points out, that the identification of NO is not possible in the absorption spectrum for low NO concentrations. The FTIR software Calcmet calculates the NO concentration by the superposition of the used library spectra of all components but the procedure is error-prone in the presence of water.

However, numerical simulations of Sakiyama *el al.* predict, that O_3, NO_2, N_2O, N_2O_5, HNO_2, HNO_3 and H_2O_2 are long-living reactive species produced by SMD [111, 138]. For the reactive species of N_2O_5, HNO_2 and H_2O_2 exist no usable reference spectra of the FTIR spectrometer for $L = 5\,\mathrm{m}$ and $T = 60\,^{\circ}\mathrm{C}$. Due to the missing reference spectra, a qualitative analysis of these species is not possible.

To investigate the presence of HNO_2 and H_2O_2, additional Gasmet reference spectra for different conditions were analysed and compared with the measured absorption spectrum. This reference spectra are presented in the appendix B. For the identification of N_2O_5 the report of Cantrell *el al.* identified important absorption cross-sections for the wavenumbers $\tilde{\nu} \sim 1250\,\mathrm{cm}^{-1}$ and $\tilde{\nu} \sim 1700\,\mathrm{cm}^{-1}$ [166]. The wavenumber position of the absorption peaks for H_2O_2 (blue), HNO_2 (green) and N_2O_5 (purple) are shown in Fig. 2.5 a). Unfortunately, the absorption peaks of these molecules are overlapping with the dominating molecules CO_2, H_2O, HNO_3 and N_2O, which hinders the clear identification of these species. Nevertheless, N_2O_5 and HNO_2 are absent under high humidity conditions (similar to HNO_3). The low absorbance of H_2O_2 molecule does not allow to prove the presence or absence of this species for both humidity conditions.

As stated before, the ozone concentration exceeds the detection limit of the FTIR, as the available reference spectrum was measured for 50 ppm. Therefore, the ozone concentration was monitored by UV absorption spectroscopy, which is described in chapter 2.2.

2.5 Dissipated Plasma Power

To measure the reproducibility of the afterglow generation, the dissipated plasma power was monitored. The dissipated plasma power is given by [167]:

$$P = \frac{1}{T} \int_T U \cdot I \mathrm{d}t. \tag{2.6}$$

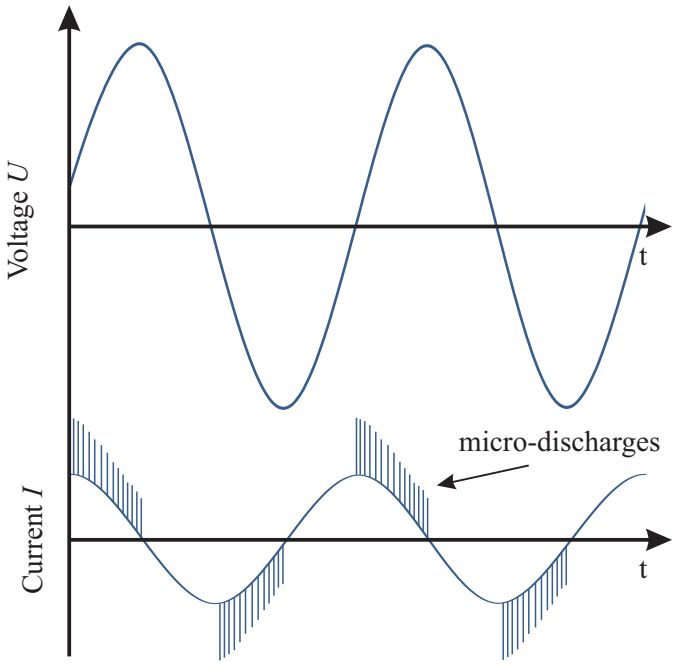

Figure 2.6: Illustration of the voltage and current with micro-discharges as a function of time (adapted from [133]).

For a detailed measurement of the current I the consideration of all filamentary discharges in a discharge period is necessary, as shown in Fig. 2.6. Therefore, the use of high frequency oscilloscopes and high bandwidth current sensors is required [167].

An alternative method to analyse the plasma power provides the use of voltage-charge-cyclograms, which was firstly described by T. C. Manley in 1943 [167, 168]. This is a widely used method and is described in more detail in the literature by Kogelschatz *et al.* [133] and Kostov *et al.* [169]. A sketch of a lissajous figure is shown in Fig. 2.7a). The dissipated electrical energy E_k per cycle k is given by the enclosed cyclogram area [40, 168]. For the calculation of the power consumption, a capacitance C with 0.1 µF was placed in series with the electrode system, shown in Fig. 2.7b). The voltage $U_C(t)$ across the capacitor C correlates with the charge Q. The charge Q is equal to the integrated current, which comprises all discharge pulses [170]. E_k is given by

$$E_k = \oint_k Q(t)\mathrm{d}U = \oint_k C U_C(t)\mathrm{d}U \tag{2.7}$$

with the applied voltage $U(t)$, the capacitance C, the capacitance voltage $U_C(t)$ and the charge Q. The consumed electrical power is $P = fE_k$, with the frequency f of the applied sinusoidal voltage $U(t)$ [171].

For the investigations in this work, the applied voltage $U(t)$ and the capacitance voltage $U_C(t)$ were detected with an oscilloscope (DSOX2004A, Keysight Technologies Deutschland

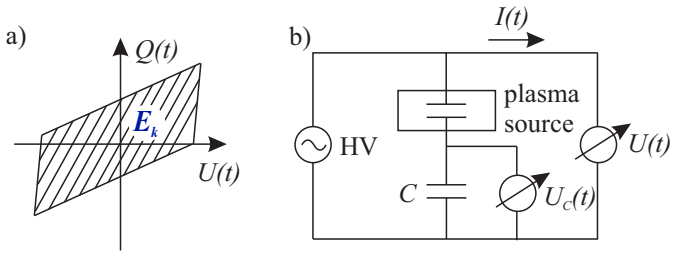

Figure 2.7: a) Sketch of a voltage-charge-cyclogram to calculate the plasma power consumption (adapted from [133]). b) Circuit for plasma power measurement with an additional capacitance C.

GmbH) for $f = 6 - 10\,\mathrm{kHz}$ and $U = 4.5 - 6.4\,\mathrm{kV}$. A measurement software of terraplamsa GmbH was used to calculate the power consumption of the electrode. The software measured the power consumption every $1 - 2\,\mathrm{s}$, which allowed to monitor the power during the complete plasma on phase. The presented power consumption in this work shows mean values of at least three measurements with the corresponding standard deviations.

Chapter 3

Spectroscopic Characterisation of the Plasma Afterglow Composition

In order to develop an apparatus for the decontamination of spacecraft equipment, it is necessary to understand the fundamental effects, which contribute to the inactivation of microorganisms. In detail, the composition of the afterglow has to be investigated to estimate possible interactions with the treated materials. Numerical simulations predict that O_3, NO_2, N_2O, N_2O_5, HNO_2, HNO_3 and H_2O_2 are long-living reactive species produced by SMD [111, 138]. In addition, the detailed mechanisms of the coupled, dynamic processes in the SMD plasma are poorly understood [138]. Pavlovich *et al.* [172] identified ozone O_3, nitrous oxide N_2O, nitric oxide NO and nitrogen dioxide NO_2 as prominent components in SMD air plasma chemistry [14]. In addition, previous studies [115] showed that the inactivation efficacy for microorganisms using cold plasma improves by increasing air humidity. However, different electrode properties, plasma parameter and environmental influences require the spectroscopic measurements of the afterglow composition in addition to theoretical analysis. In this work, the gas composition of the PACA was analysed by UV absorption and FTIR spectroscopy. The FTIR investigations reveal, that it is necessary to evaluate standard parameters for the plasma afterglow circulation apparatus (PACA), which enable a reproducible decontamination procedure for microorganisms on various material surfaces. To identify the dependence of the gas composition to different plasma parameters, the influence of the FTIR measurement, humidifier, gas flow rate, power consumption and humidity was analysed. In addition, the formation of NO_2 and HNO_3, as well as the observation of ozone quenching is described. Finally, FTIR investigations are presented with the use of artificial carrier gases to identify the influence of the neutral gas composition to the afterglow composition.

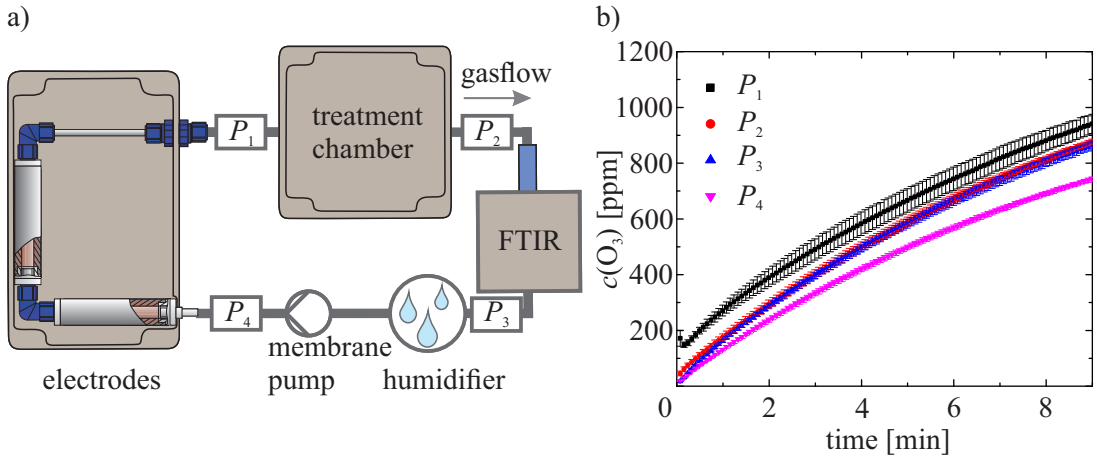

Figure 3.1: a) Setup for the measurement of the O_3 concentration at different measurement positions P_1, P_2, P_3 and P_4 using UV absorption spectroscopy and with FTIR in the PACA. b) O_3 concentration for different positions P_1, P_2, P_3 and P_4.

3.1 Characterisation of the Ozone Distribution

Ozone (O_3) presents one of the important molecules of the cold atmospheric plasma treatment for the inactivation of microorganisms [111, 141, 173, 174]. To gain insights into the PACA, it is important to understand the influence of the gas circulation to the concentration of the circulating species. Since ozone is mainly produced by the PACA and represents one of the major players of the inactivation process, the ozone concentration is measured at different positions in the apparatus using UV absorption spectroscopy.

Therefore, a small UV-absorption-measurement-box with 32 mm path length was used to analyse the O_3 concentration, as described in chapter 2.2. The UV-measurement-box was positioned at three to four examination points (marked in Fig. 3.1 a) and Fig. 3.2 a)). Experiments with and without FTIR in the circle allowed to determine, if the FTIR spectrometer has an influence to the ozone concentration or not.

In the first experiment, the electrode system, the treatment chamber with 2.6 l volume, the FTIR, the humidifier and the membrane pump were included in the setup as shown in Fig. 3.1 a). The figure illustrates the different positions P_1, P_2, P_3 and P_4 of the measurement box. Fig. 3.1b) shows the O_3 concentration for the different positions as a function of time. The illustrated data represent the mean value of three successive measurements and the error bars depict the corresponding standard deviation. The O_3 measurement at P_1 (directly behind the electrode system) shows the highest concentration of ozone in the setup. Immediate after the plasma and the gas flow are switched on, the O_3 concentration shows higher values than for the other positions. This observation was only observable using the humidifier wash bottle in the apparatus, because the gas flow was switched on $2\,\mathrm{s} - 5\,\mathrm{s}$ after the plasma was ignited to avoid a water film on the electrode surface. Thus, the ozone concentration accumulated

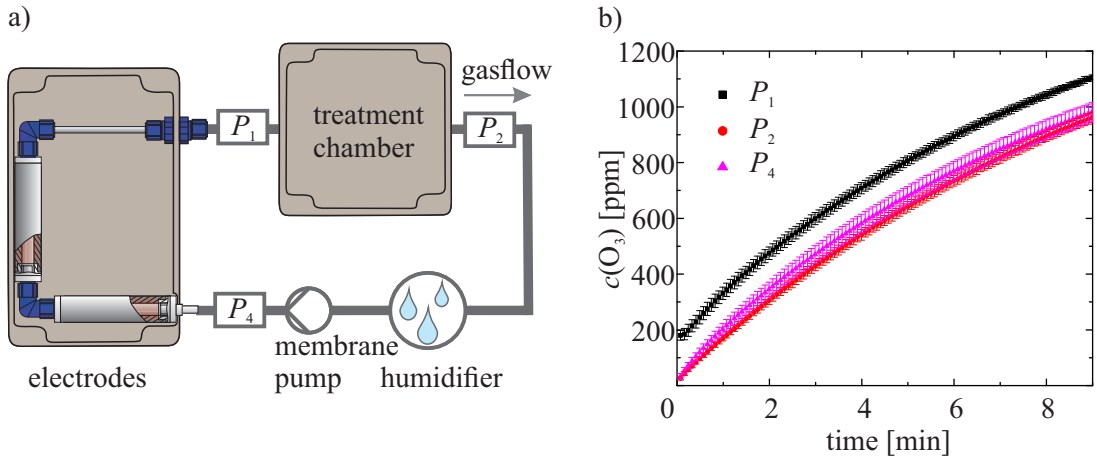

Figure 3.2: a) Setup for the measurement of the O_3 concentration at different measurement positions P_1, P_2 and P_4 using UV absorption spectroscopy and without FTIR in the PACA. b) O_3 concentration for different positions P_1, P_2 and P_4.

in the electrode for a few seconds, and the molecules moved further, after the gas flow was switched on. This effect is only observable for P_1 right after the electrode outlet, because the O_3 molecules distributes in the remaining volume (e.g. treatment chamber). In Fig. 3.1b), the ozone distribution present the same concentration for P_2 and P_3 (before and after the FTIR spectrometer) and ends up with a concentration of 870 ppm after 9 min. Finally, the O_3 concentration was measured between the humidifier and electrode entrance at P_4. The data reveal a lower ozone concentration for this point which reaches a concentration value of 740 ppm after 9 min. This results indicate that ozone is dissolved in the water of the humidifier.

To analyse if the FTIR spectrometer - which is heated up to 60 °C - has an influence to the overall O_3 formation, the experiment is repeated without the FTIR in the circulation apparatus. Fig. 3.2 a), shows the UV measurement positions without the FTIR spectrometer in the circle. As I stick to the same enumeration, P_3 is not present in Fig. 3.2 a). Fig. 3.2 b) displays the distribution of the O_3 concentration at P_1, P_2 and P_4 for a time interval of 9 min. The illustrated data represent the mean value of three measurements and the error bars depict the corresponding standard deviation. The concentration which is measured at P_1 in Fig. 3.2 b) is similar to P_1 in Fig. 3.1 b) with respect to the upwards shift of the values. In addition, the concentration at P_2 and P_4 equals and reveals a concentration of $\sim$970 ppm. In contrast to the use of the FTIR, these results show no loss of O_3 molecules by passing the water of the wash bottle. The result suggests, that the gas temperature increases when the gas passes the FTIR heating pipe and measurement cell, so that the water of the humidifier can take up more of the reactive gas and may increase the dissociation of O_3 molecules.

The comparison of the measurements with (Fig. 3.1b)) and without (Fig. 3.2 b)) FTIR shows, that $c(O_3)$ is $\sim$100 ppm higher for P_1 and P_2 when no FTIR is included. The higher

concentrations of ~ 100 ppm are caused by the difference of the total volume of the apparatus, since the use of the FTIR increases the volume about 450 ml. This increase of the total volume leads to an decrease of the reactive species concentration in the setup, as the production rate of the plasma stays constant. The analysis of P_4 depict ~ 230 ppm higher concentrations for O_3 when no FTIR is included. I assume that the raise of the gas temperature by the FTIR leads to an increase of the partial pressure for ozone, so that more O_3 molecules are dissolved in the water of the wash bottle. The increase of the partial pressure by the temperature is given by the ideal gas equation ($pV = nRT$) [175].

In conclusion, the time dependency of $c(O_3)$ demonstrates an increase of ozone for all measurement positions. The investigations indicate that a high ozone concentration is present at different positions in the apparatus. Furthermore, the results reveal, that the use of the FTIR does not have an effect on the ozone concentration, since the concentration does not change by passing the FTIR. Nevertheless, the dissociation of O_3 by passing the humidifier is increased when the FTIR is included in the setup. In general, it is reasonable to position the treatment chamber between electrode and humidifier, to exclude that the reactive species react with the water, before they enter the treatment chamber. Detailed investigations of the humidifier position are presented in chapter 3.3.

3.2 Characterisation of the Humidifier Water

This section presents the results of the UV/VIS spectroscopy (described in chapter 2.3) and analysis of the dissolved afterglow molecules in the water of the humidifier, which are partially published in AIP Advances [14]. For the measurement, the treatment chamber $V = 1.8$ l and the FTIR were included in the PACA circle. Note, that the O_3 concentration was monitored at the treatment chamber and no additional UV-measurement-box was used. For the detection of the UV absorption spectrum of the humidifier water, the water was treated with plasma for 65 min. The plasma treatment was interrupted for ~ 5 min at the time points 20 min, 35 min and 50 min to detect the absorption spectrum. The detection of the spectrum was repeated after 1 min for each time point.

Fig. 3.3 a) shows the concentration of ozone O_3 and nitrate NO_3 in the humidifier water for different treatment times and Fig. 3.3 b) the detected UV absorption spectrum of the water. The analysis indicates that ozone and nitrate were dissolved in the water of the wash bottle. The ozone concentration does not increase over the observed time span. Furthermore, the repetition of the measurement after ~ 1 min indicates that the ozone concentration decreases fast in the water after the plasma treatment, while NO_3 is more stable and increases over time [14]. The presence of NO_3 indicates that in addition to O_3 also NO_x molecules are present in the afterglow, which leads to a formation of NO_3 in the humidifier water.

The presented data reveal that O_3 is dissolved in water, but shows no high stability, which

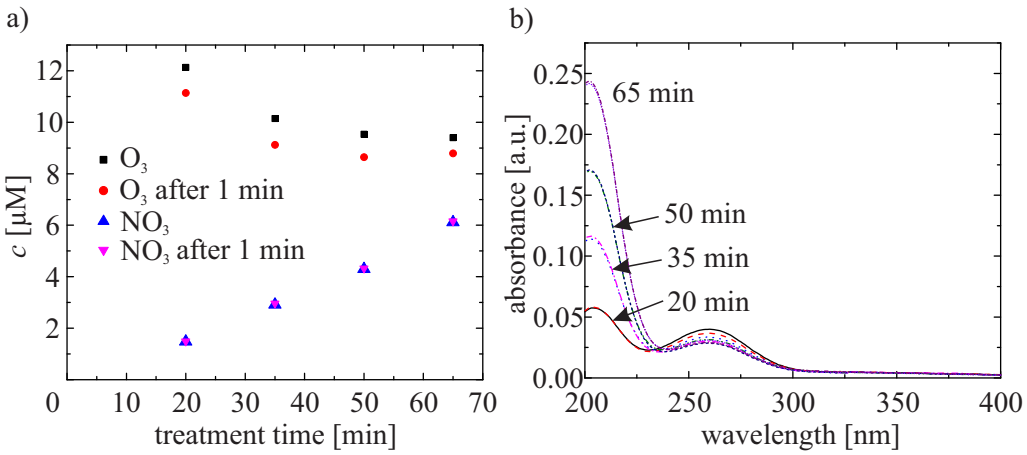

Figure 3.3: a) Concentrations of O_3 and NO_3 which are solved in water in the gas washing bottle for different treatment times. The repetition of the measurements after 1 min demonstrates the fast decay of O_3 in water. b) UV/Vis absorption spectrum of the water in the gas washing bottle after different treatment times [14].

is already known from the literature [176]. The concentration of the molecules in the aqueous phase c_a could be calculated by Henry's law (see chapter 2.3, equation 2.4). The detected $c(O_3)$ in the gaseous phase during these measurements has a maximum ozone concentration of ~ 1100 ppm, which refers to a partial pressure of $p_g[O_3] = 1100 \times 10^{-6}$ atm. The use of Henry's constant of 1.1×10^{-2} M/atm for O_3 (see chapter 2.3, Table 2.3) allows the calculation of ozone in the aqueous phase: $c_a[O_3] = H^{cp} \times p_g \sim 12$ µM. This result is in agreement with the data in Fig. 3.3 a) which reveal an ozone concentration of ~ 10 µM in the solution. The fact, that the detected ozone concentration is lower than the calculated ozone concentration can be explained with the instability of the O_3 molecule in water. Nevertheless, the solubility of ozone in water is relatively low.

3.3 Characterisation of the Humidifier Position

Previous investigations already demonstrated that the humidity condition could have a dramatic effect to the afterglow composition [115]. Furthermore, the results in chapter 3.2 illustrate, that reactive species are solved in the water of the wash bottle. In this section, the influence of the humidifier position in the PACA is analysed to identify the influence of the humidity concentration and the humidifier position to the reactive gas composition. The experiments were executed for two different humidifier positions (P_1^h and P_2^h) and without the use of a humidifier (P_0^h).

For the investigations, the circulation system of the PACA was opened, so that the electrode operated with fresh air and the reactive species could not reenter the electrode after the FTIR analysis. This setup enables to investigate the influence of the humid air to the

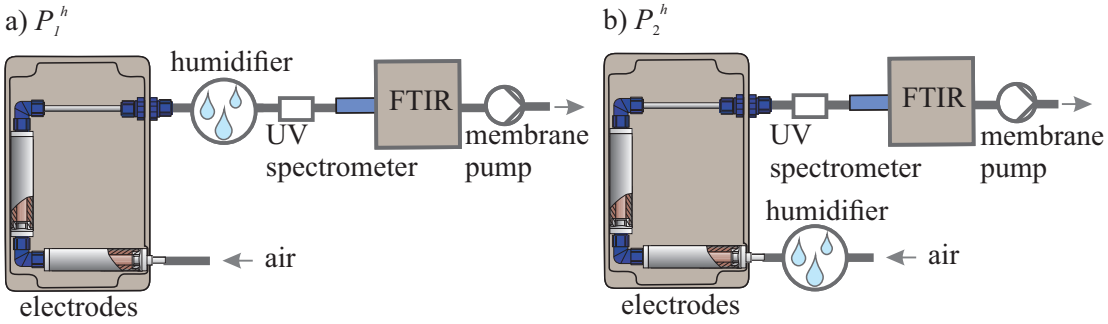

Figure 3.4: Setup for the investigations of two different humidifier positions P_1^h and P_2^h in the open PACA with a gas flow in one direction. a) P_1^h: humidifier is placed between electrode outlet and UV spectrometer. b) P_2^h: humidifier is placed in front of the electrode entrance.

plasma production and the influence of the humidifier as a possible filter of reactive species.

Fig. 3.4 depicts the open afterglow setup with different humidifier positions P_1^h and P_2^h, in a) and b), respectively. The membrane pump is positioned at the outlet of the FTIR spectrometer to transport fresh air into the apparatus and the reactive gas out, using a gas flow velocity of 3.5 l/min. One part of the measurements was done using the humidifier at position P_1^h (shown in Fig. 3.4 a)). Therefore the humidifier was installed between the outlet of the electrode system and the entrance of the UV-measurement-box. In this case, the fresh air passed the electrode system before the gas travelled through the water of the wash bottle and was analysed by UV absorption and FTIR spectroscopy. Further measurements were executed with the humidifier installed at the gas entrance of the electrode system (P_2^h), as demonstrated in Fig. 3.4 b). The fresh air was humidified before it passed the plasma region of the electrode system and was then analysed by the UV and FTIR spectrometer.

Fig. 3.5 a) displays the ozone concentration ($c(O_3)$) for P_0^h, P_1^h and P_2^h as a function of time. The data represent the mean value of three different measurements. The error bars are not shown in Fig. 3.5 a) to enable a better clearance. The average standard deviation of the mean values was 4 ppm. The analysis reveals a clear difference between P_1^h and P_2^h, whereas the ozone concentration for P_0^h is similar to P_1^h. P_1^h and P_0^h show a higher ozone concentration than the detected concentration for P_2^h. It can be seen from the data that $c(O_3)$ of P_0^h and P_1^h reaches a plateau after a few seconds. The ozone concentration for P_2^h peaks in the first seconds, but then decreases again until a lower plateau is reached. The behaviour is caused by the accumulation of reactive species in the switch-on procedure. In total, the ozone concentration increases slowly within the 5 min observation time for P_2^h.

A solving of the O_3 in the water (which refer to a lower concentration of P_1^h compared to P_0^h), could not be observed in the investigations. However, the concentration of O_3 is slightly higher (~ 20 ppm) for P_1^h than for P_0^h.

Furthermore, the power consumption p of the apparatus was analysed for the investigations. Fig. 3.5 b) depicts the power consumption for the different humidifier positions P_0^h, P_1^h

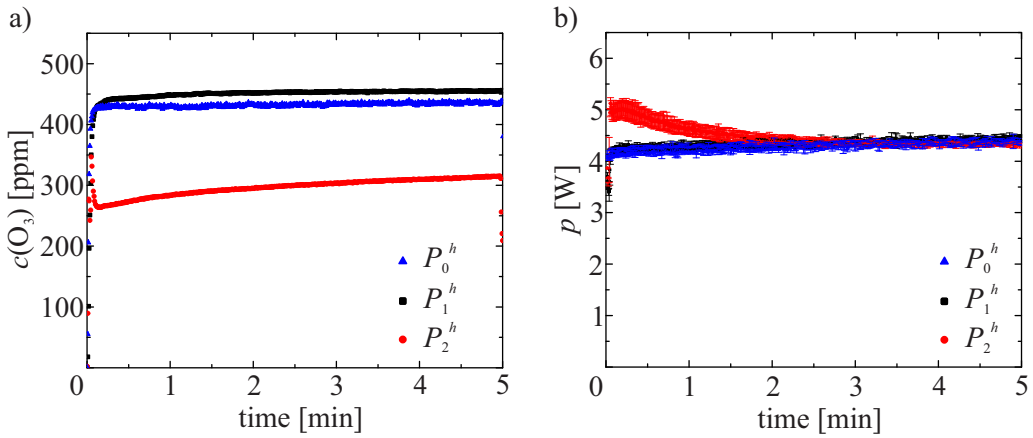

Figure 3.5: a) Investigations of the ozone concentration for P_0^h, P_1^h and P_2^h (error bars are not shown). b) Investigations of the power consumption for P_0^h, P_1^h and P_2^h.

and P_2^h, within the observation time of 5 min. Similar to the trend of the ozone concentration, the calculated power for P_0^h and P_1^h appears constant and shows a slight tendency to increase after 2.5 min plasma ignition to a value of 4.4 W. For P_2^h, the power consumption peaks at 5.0 W at $t = 0.2$ min and decreases slowly within 5 min to a constant value of $p = 4.3$ W, which is in the range of p for P_1^h and P_0^h.

The peak of the power consumption is explained by the condensation of a water film on the cold electrode surface. This water film leads to an increase of the surface conductivity of the dielectric, which causes stronger micro-discharges [133]. The ignition of the discharge vaporises the deposit water on the surface and leads to a reduction of the power consumption of the electrode. Since the power consumption approaches the same value for all conditions, the different ozone concentrations cannot be explained by a changed plasma ignition in the presence of high humidity. From the literature [144, 150] it is known, that the increased amount of H_2O changes the chemical pathways so that O_3 is produced in a lower concentration in the plasma region. When the energy deposition remains constant and the amount of H_2O molecules raises, more energy is consumed by the H_2O decomposition and the production of OH increases, while the amount of O atoms decreases. This results in a decrease of the ozone production and is also reported by theoretical models in previous publications [144, 150].

The investigations of the afterglow composition using the FTIR enable a further insight in the chemical reactions which occurs for the use of the gas wash bottle as an humidifier. In general, a detailed explanation of the FTIR spectrometer analysis using a exemplary absorption spectrum is described in chapter 2.4. The investigations of the molecules (HCHO, NO_2, N_2O, HNO_3 and H_2O) using a FTIR spectrometer are displayed in Fig. 3.6. The data is averaged over three measurements and the error bars show the corresponding standard deviation.

Fig. 3.6 a) presents the concentration of formaldehyde (HCHO) for different humidifier

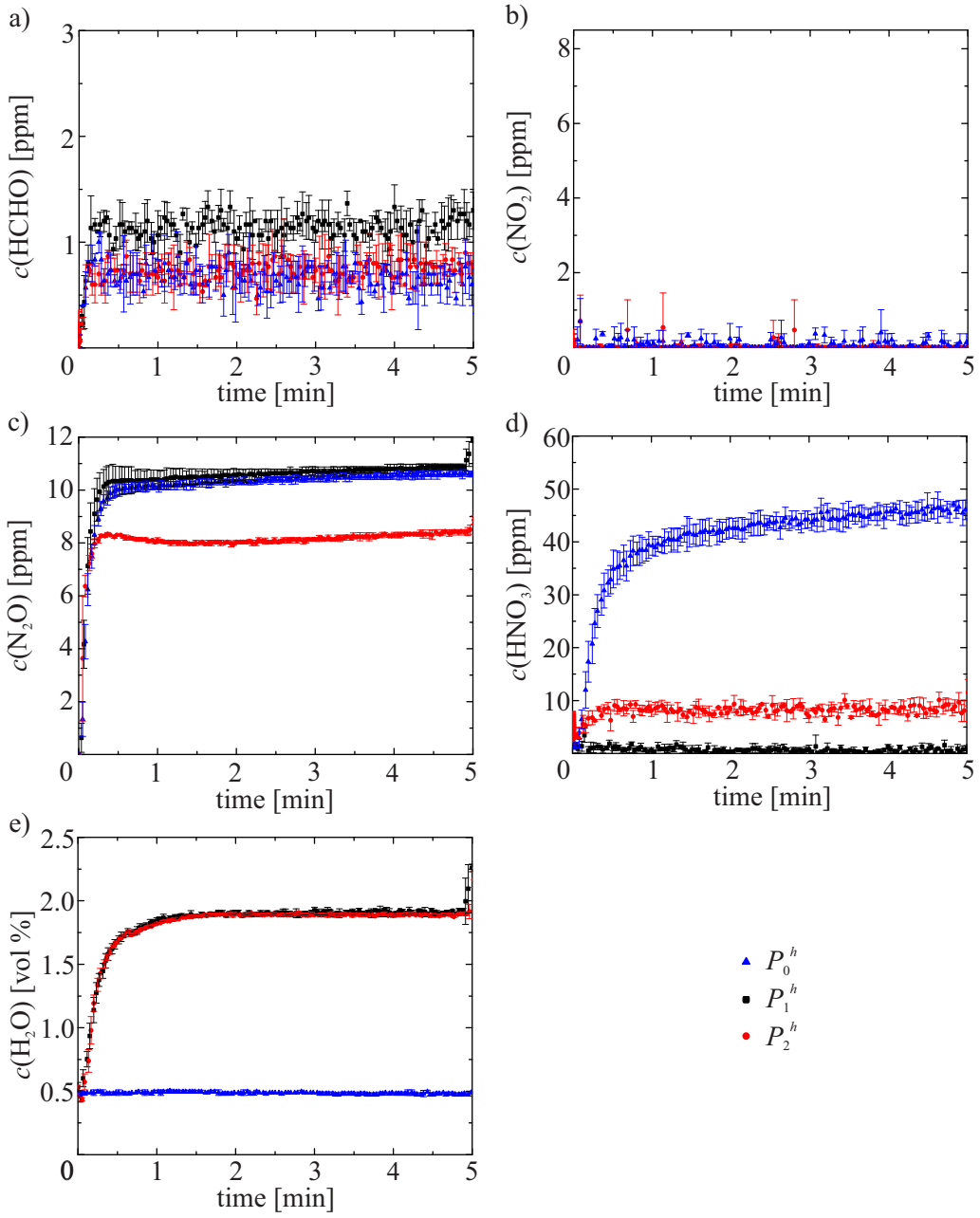

Figure 3.6: FTIR analysis for P_0^h, P_1^h and P_2^h in the open afterglow apparatus. a) HCHO concentration. b) NO_2 concentration. c) N_2O concentration. d) HNO_3 concnetration. e) H_2O concentration.

position in the open apparatus. The concentration of HCHO is constant for P_0^h, P_1^h and P_2^h, while the concentration of P_1^h tends to be higher than for the other conditions. The detection of HCHO in relation with plasma is not described in detail in the literature. But several publications mention the increase of HCHO in the presence of VOC (volatile organic compounds) and O_3 [177–179]. The examination of NO_2 is displayed in Fig. 3.6 b). The detected concentration of NO_2 remains zero for P_1^h, while $c(NO_2)$ for P_2^h and P_0^h fluctuates below a threshold of 1 ppm. The data displays, that NO_2 is produced in the plasma. I assume, that the dominant O_3 and OH molecules react fast with NO_2 molecules, so that only a negligible concentration of NO_2 is detectable (see chapter 1.7). In addition, when the reactive gas has to pass the water of the gas wash bottle, the NO_2 molecules are solved in the water and could form HNO_3 (see chapter 1.7). This theory is consistent with the observation, that no NO_2 fluctuation is observed when the wash bottle is installed at P_1^h. Fig. 3.6 c) shows the N_2O concentration ($c(N_2O)$) for the different conditions as a function of time. According to the diagram, the concentrations increase within ~ 0.8 min and remain on a constant level. In addition, the $c(N_2O)$ is higher for P_1^h and P_0^h and ends up to a value of $10.6 - 10.8$ ppm while the concentration for P_2^h reaches a value of 8.4 ppm. The data indicate that the production conditions for N_2O depend on the H_2O concentration in the plasma ignition region, similar to O_3. Dorai *el at.* [150] presented in their theoretical analysis of the plasma afterglow, that N_2O decreases when the amount of OH molecules increases. They describe that the major formation process of N_2O are reactions of NO_2 with N ($NO_2 + N \rightarrow N_2O + O$). Under high humidity conditions NO_2 is preferentially consumed by reactions with OH, so that the production of N_2O decreases. The measurement of the HNO_3 concentration $c(HNO_3)$ in Fig. 3.6 d) shows different trends for the different humidifier conditions. The highest HNO_3 concentration was measured for P_0^h and the lowest for P_1^h. When the humidifier is installed at P_1^h, $c(HNO_3)$ fluctuates between $0 - 1$ ppm. For P_2^h, the concentration of HNO_3 increases in the first 30 s and stays on a constant level. The investigations of P_0^h depict that HNO_3 increases rapidly within the first minute and shows a slower raise of the concentration afterwards. HNO_3 is an expected molecule by the afterglow plasma, which is created by reactions of NO, NO_2, OH and H_2O [150]. These expectations lead to the assumption, that nitric acid (HNO_3) is produced under high humidity conditions and should show a high concentration for P_2^h. Since $c(HNO_3)$ is low for P_2^h, HNO_3 is probably produced by the plasma, but is captured in the condensed water within the apparatus. The condensation of nitric acid within the apparatus leads to a lower detection by the FTIR for high humidity conditions. The results for P_1^h show, that only a low concentration of HNO_3 is detected. In the case for P_1^h the reactive gas has to pass the water of the gas wash bottle before it is analysed by the FTIR. Since the FTIR only detects a small amount of HNO_3 and the HNO_3 is observed when the dry air enters the electrode, the molecules have to be captured in the water of the gas wash bottle. The theory agrees with the results in chapter 3.2, that NO_3

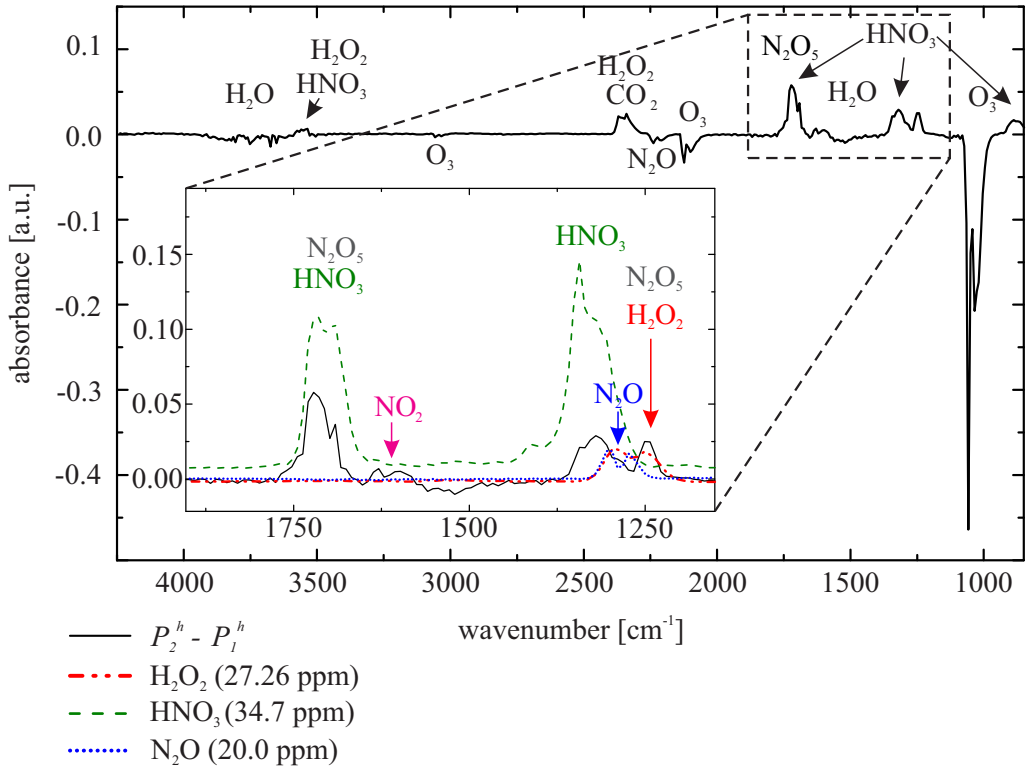

Figure 3.7: Difference absorption spectrum ($P_2^h - P_1^h$) to identify additional reactive species. Inset: Magnification of absorption spectrum ($P_2^h - P_1^h$) and library spectra of H_2O_2, HNO_3 an N_2O.

is present in the water of the gas washing bottle, which is used for high humidity conditions. The detection of HNO_3 under different humidity conditions will be discussed in chapter 3.5 in more detail. In Fig. 3.6 e) the trend of the H_2O concentration within the observed time span is identical for both humidifier positions. The H_2O concentration reaches a constant value of 1.9 vol % after 1 min plasma ignition and remains constant. The H_2O concentration without humidifier displays a constant value of $\sim$ 0.49 vol %.

For a detailed analysis of the difference between P_2^h and P_1^h, the absorption spectra after 4.5 min plasma ignition were subtracted. The difference-absorption spectrum of $P_2^h - P_1^h$ is illustrated in Fig. 3.7. The analysis of the spectrum in Fig. 3.7 allows the confirmation of afterglow species HCHO, N_2O, O_3 and HNO_3, which were analysed in Fig. 3.6. The negative absorption peaks show O_3 and N_2O which are produced in higher concentrations for P_1^h, when the humidifier is installed behind the electrode. Furthermore, the data show positive peaks for HNO_3, which indicate that HNO_3 is dissolved in the water of the wash bottle. In chapter 2.4 it is discussed that HNO_2 could not be measured qualitatively with the FTIR, but shows absorption peaks at the same positions as HNO_3. Thus, the measurements indicate that in the case, that HNO_2 would be present in the afterglow, it is also dissolved in the water of the wash bottle like HNO_3. The inset in Fig. 3.7 shows reference spectra of HNO_3, N_2O

and H_2O_2. The reference spectra show that the HNO_3 absorption peak is higher at 1700 cm^{-1} than at 1330 ,cm^{-1} and shows an additional peak at 1250 cm^{-1}. According to the description in chapter 2.4, the increased absorption at 1700 cm^{-1} and 1250 cm^{-1} could be due to the presence of N_2O_5, whereas the increase of the absorption at 1250 cm^{-1} could also origin from H_2O_2 and HNO_2. In addition, the inset shows a small absorption peak which is attributed to the absorption of NO_2. Consecutively, I assume that small amounts of NO_2, H_2O_2, HNO_2 and N_2O_5 are produced for P_2^h, when humidified air interacts with the micro-discharges. Due to the lack of appropriate reference spectra a detailed analysis of N_2O_5, HNO_2 and H_2O_5 is not possible.

The investigations of the humidifier position illustrate, that the composition of the plasma afterglow highly depends on the humidity content of the gas which enters the electrode system. The use of high humidity conditions affect the formation of the reactive species in the electrode region. Furthermore, the results demonstrate that already generated molecules of O_3, HCHO and N_2O, negligible interact with the water of the humidifier in the PACA. In addition, I found, that HNO_3 (and probably HNO_2) and NO_2 are solved in the water of the wash bottle, which was already discussed in chapter 3.2. The investigations emphasise that some of the afterglow species could not pass the humidifier. For all of the measurements, the humidifier was positioned in front of the electrode entrance, so that the UV and FTIR spectroscopy of the afterglow composition were not influenced.

3.4 Characterisation of the Flow Rate

The developed plasma afterglow circulation apparatus (PACA) is working with a circulating gas flow. To understand, if this gas flow has an effect to the afterglow formation, the gas composition was analysed for different flow rates.

In a first experiment the gas flow Q was varied between 2.0 l/min, 3.5 l/min and 4.9 l/min under low humidity conditions. For the investigations, the described setup in Fig. 2.1 was used without treatment chamber. Fig. 3.8 displays the O_3 concentration $c(O_3)$, the detected power consumption p and the H_2O concentration $c(H_2O)$ for 10 min plasma ignition of different flow rates. The presented data demonstrate the mean value of three measurements and the standard deviation gives the corresponding error bars. The detected $c(O_3)$ in Fig 3.8 a) shows a different behavior for the chosen flow rates, while $c(O_3)$ has a similar slope within the first minute of plasma ignition. In detail, the highest concentration was detected for the lowest flow rate ($Q = 2.0$ l/min, $c(O_3) \sim 4880$ ppm for $t = 10$ min) and the lowest concentration for the highest flow rate ($Q = 4.9$ l/min, $c(O_3) \sim 3930$ ppm for $t = 10$ min). Thus, the results indicate a similar production rate of O_3, while $c(O_3)$ saturates at different concentrations for different Q. This observation leads to the conclusion that the balance of the production and recombination rates are reached for different concentrations of O_3. According to the data,

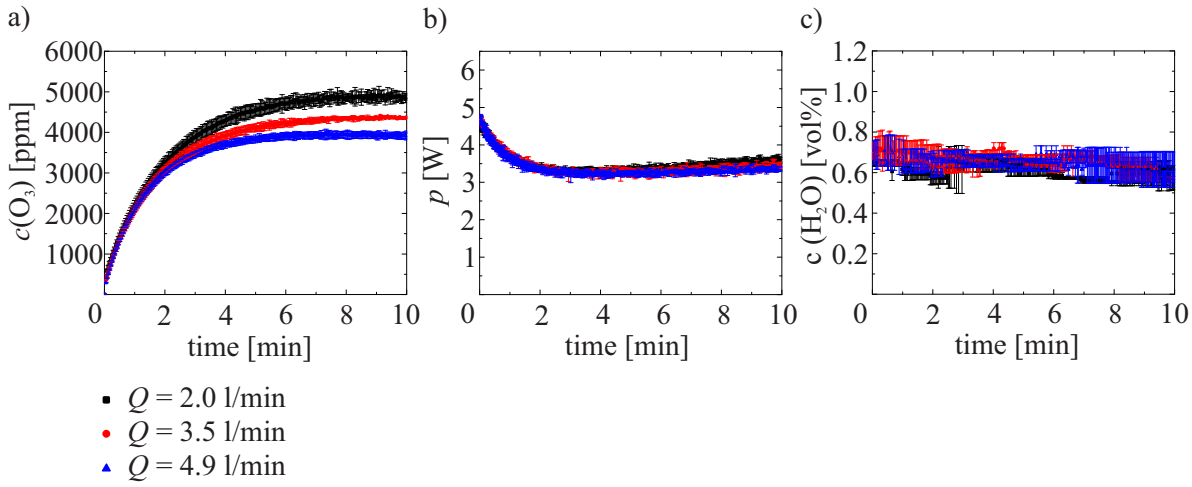

Figure 3.8: a) O_3 concentration for different gas flow rates for an observation time of 10 min under low humidity conditions. b) Power consumption for different gas flow rates under low humidity conditions. c) H_2O concentration for the low humidity condition.

the higher gas flow increases the recombination of O_3 molecules. This theory fits to previous reports, that the half-life time of O_3 decreases with an increase of the gas flow rate [180]. The increase of the gas flow rate causes, that the gas molecules disperse and interact faster which leads to a reduction of the O_3 concentration. To investigate the influence of the gas flow rate Q to the power consumption p of the circulation apparatus, the power measurement is shown in Fig. 3.8 b). The data reveals, that Q has no significant influence to the power consumption, but shows a decrease of p in the beginning and a slight increase after 4 min, while the slope is inversely proportional to the flow rate. Furthermore, the power consumption shows a different behavior for the closed setup here, than for the open apparatus in chapter 3.3, which showed a constant power consumption over the observed time. The measurement agrees with the notion, that the conditions of the circulating gas have an impact to the power consumption. I assume, that the temperature of the electrode is increased for the closed PACA including FTIR, which influences the measured power consumption of the electrode. Furthermore, reactive species enters the apparatus, which could lead to a change of the plasma ignition compared to ambient air. Fig. 3.8 c) displays the H_2O concentration detected by the FTIR as a function of time. The humidity is similar for the different flow rates but shows a small decrease during the plasma ignition from ~ 0.70 vol % to ~ 0.58 vol %. Probably, the plasma dissociates a small amount of H_2O to form OH. Furthermore, additional absorption peaks of plasma generated species in the water bonds could influence the calculation of the spectrometer software, so that lower concentrations for H_2O are measured.

In addition, Fig. 3.9 illustrates the FTIR measurements for the concentrations of NO_2, HCHO, HNO_3 and N_2O. The diagram for NO is not shown, since no NO was detected during the measurements. Fig. 3.9 a) shows the data for NO_2, where no significant difference for the

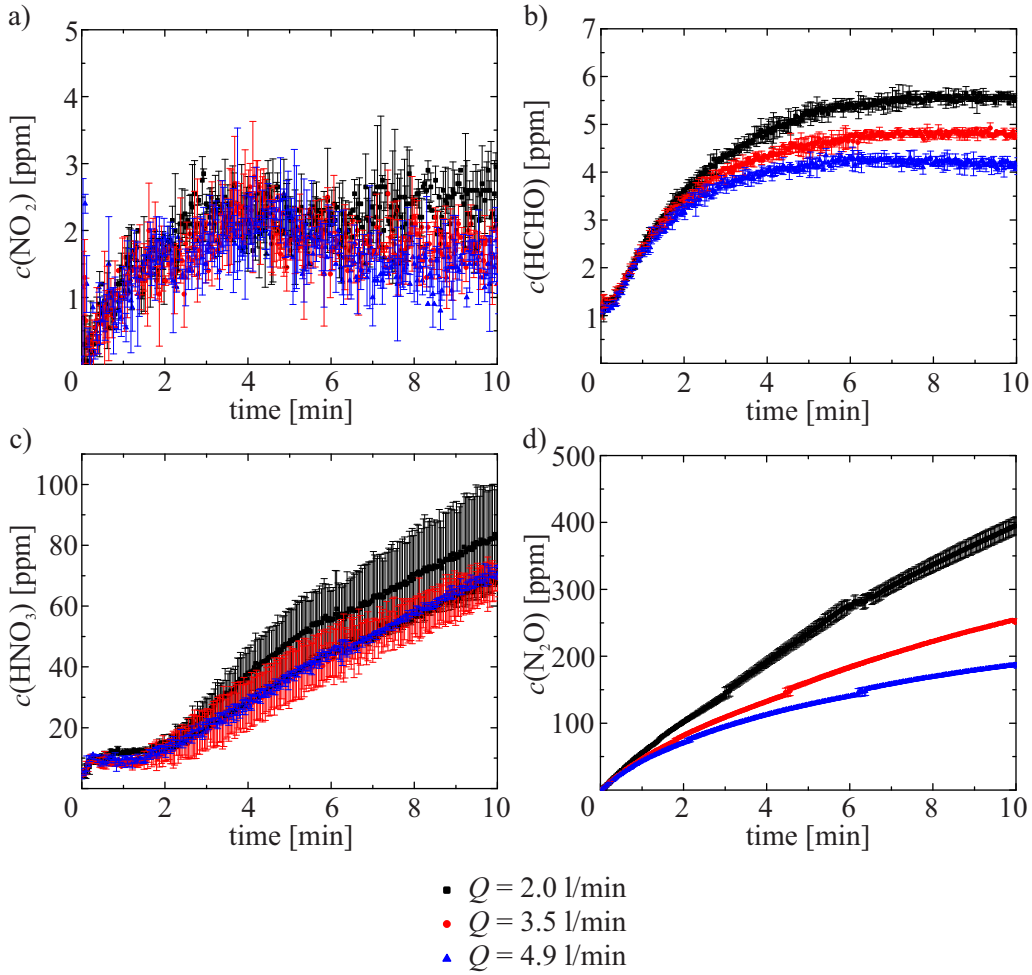

Figure 3.9: FTIR analysis of the afterglow composition using three different gas flow rates Q (2.0 l/min, 3.5 l/min and 4.9 l/min) under low humidity conditions. a) NO_2 concentration. b) HCHO concentration. c) HNO_3 concentration. d) N_2O concentration.

gas flow rates were detected for $t < 6\,\mathrm{min}$. For $t > 6\,\mathrm{min}$, the concentration for $Q = 2.0\,\mathrm{l/min}$ tends to be higher but the calculated error bars overlap with the measured values of the different flow rates. In total, no significant dependence of $c(NO_2)$ to Q could be found, which is explained by the fact, that the electrodes mainly produces O_3, so that the change in the gas flow has a minor influence to the detected NO_x molecules. The analysed HCHO concentration is shown in Fig. 3.9 b) and shows the same trend as the $c(O_3)$ distribution for different flow rates. For the different flow rates, the HCHO concentrations increase with the same slope in the first minute, but diverge inverse proportional to Q afterwards. This observation stays in conclusion to the notion in chapter 3.3, that the formation of HCHO relates to the presence of O_3 together with VOC (volatile organic compounds) [177–179]. The concentration of HNO_3 ($c(HNO_3)$) is displayed in Fig. 3.9 c) and shows a linear increase for all gas flow rates. According to the data, I find that $c(HNO_3)$ is similar for 3.5 l/min and 4.9 l/min and shows slightly higher concentrations for 2.0 l/min. Since HNO_3 is produced mainly by reactions of NO_2 with OH and the behavior of NO_2 showed no dependency to Q, I do not expect a strong dependency of HNO_3 to Q. Furthermore, the N_2O concentration $c(N_2O)$ for different flow rates is demonstrated in Fig. 3.9 d), which shows different concentration slopes for all flow rates. Similar to $c(O_3)$ and c(HCHO), the concentration increases faster for a smaller flow rate. This observation was also reported in previous work [181, 182]. I assume, that the lower gas flow allows the air molecules a longer residence time in the plasma region which leads to a higher energy density in the gas and thus a higher production of the N_2O molecules. This theory would also lead to an increase of NO_x molecules by a reduced gas flow. In the PACA no increase of NO_x was detected, since the apparatus favourable produces O_3 which reacts with NO_x. In contrast to $c(O_3)$ and c(HCHO), the concentrations of N_2O and HNO_3 do not saturate within the observed time span. In Fig. 3.9 d) concentration jumps are visible at the same concentration for all flow rates. This is an side effect of the FTIR Calcmet software when an other reference spectrum is used for the calculation of the concentration.

In addition to the previous section, the influence of the gas flow rate to the plasma composition is analysed for 2.0 l/min, 3.5 l/min and 4.9 l/min under high humidity conditions. Fig. 3.10 displays the O_3 concentration $c(O_3)$, the detected power consumption p and the H_2O concentration $c(H_2O)$ as a function of time for different Q. The detected O_3 concentration, in Fig 3.10 a) reveals different trends of $c(O_3)$ for different Q, similar to the observations under low humidity conditions. The ozone concentrations follow the same trend for $t < 2\,\mathrm{min}$ and diverge for $t > 2\,\mathrm{min}$. The highest concentration was detected for the lowest flow rate ($Q = 2.0\,\mathrm{l/min}$, $c(O_3) \sim 1970\,\mathrm{ppm}$ for $t = 10\,\mathrm{min}$) and the lowest concentration for the highest flow rate ($Q = 4.9\,\mathrm{l/min}$, $c(O_3) \sim 1727\,\mathrm{ppm}$ for $t = 10\,\mathrm{min}$). This effect was already reported for low humidity conditions and is explained by the recombination of O_3 molecules in dependence to the gas flow rate. As in the case of low humidity conditions, the power consumption was detected during plasma ignition, which is illustrated in Fig. 3.10 b). The use

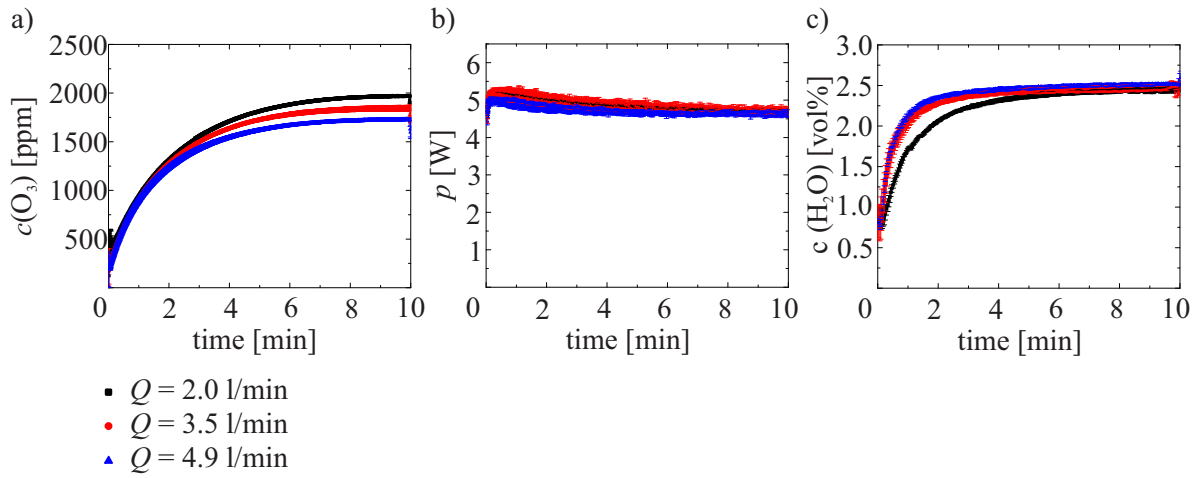

Figure 3.10: a) O_3 concentration for different gas flow rates for an observation time of 10 min for high humidity conditions. b) Power consumption for different gas flow rates for high humidity conditions. c) H_2O concentration for the 10 min observation time for high humidity conditions.

of different gas flow rates reveals no influence to the power consumption under high humidity conditions. The power increases to a maximum value of ~ 5.1 W within a few seconds and decreases afterwards to a constant value. A value of ~ 4.7 W was detected after a plasma ignition of 10 min. Compared to the power consumption under low humidity conditions, the detected power is higher for high humidity conditions which is caused by the changed plasma ignition due to the high humidity. In chapter 3.3 no dependency of the power consumption to the humidity was reported. Nevertheless, the humidity in the closed circle is higher and could influence the power consumption. As already mentioned before, high humidity conditions could lead to an increase of the surface conductivity of the dielectric which causes stronger micro-discharges [133]. Fig. 3.10 c) illustrates the H_2O concentrations for different gas flow rates under high humidity conditions as a function of time. The H_2O concentration reaches the same level for the different flow rates after 6 minutes. The distribution of 3.5 l/min and 4.9 l/min is similar. The increase of the H_2O concentration is slower for a 2.0 l/min gas flow and reaches the plateau after ~ 6 min. This observation agrees with the notion that a smaller amount of gas passes the humidifier per time, which causes a slower saturation of the humidity.

Fig. 3.11 illustrates the FTIR measurements for the concentrations of HCHO, NO_2 and N_2O. The diagram for HNO_3 is not shown, since HNO_3 is not visible under high humidity conditions. This effect is discussed in detail in chapter 3.5. Note, that the clear identification of NO was not possible in the measurements (see chapter 2.4). Fig. 3.11 a) depicts the NO_2 concentration for different flow rates. According to the diagram, the NO_2 concentration is fluctuating below a value of 1 ppm, thus no dependence to the gas flow rate is observable. Fig. 3.11 b) displays different distributions for the HCHO concentration as a function of time, depending on the gas flow rate. The trend shows a similar slope for c(HCHO) for $t < 2$ min

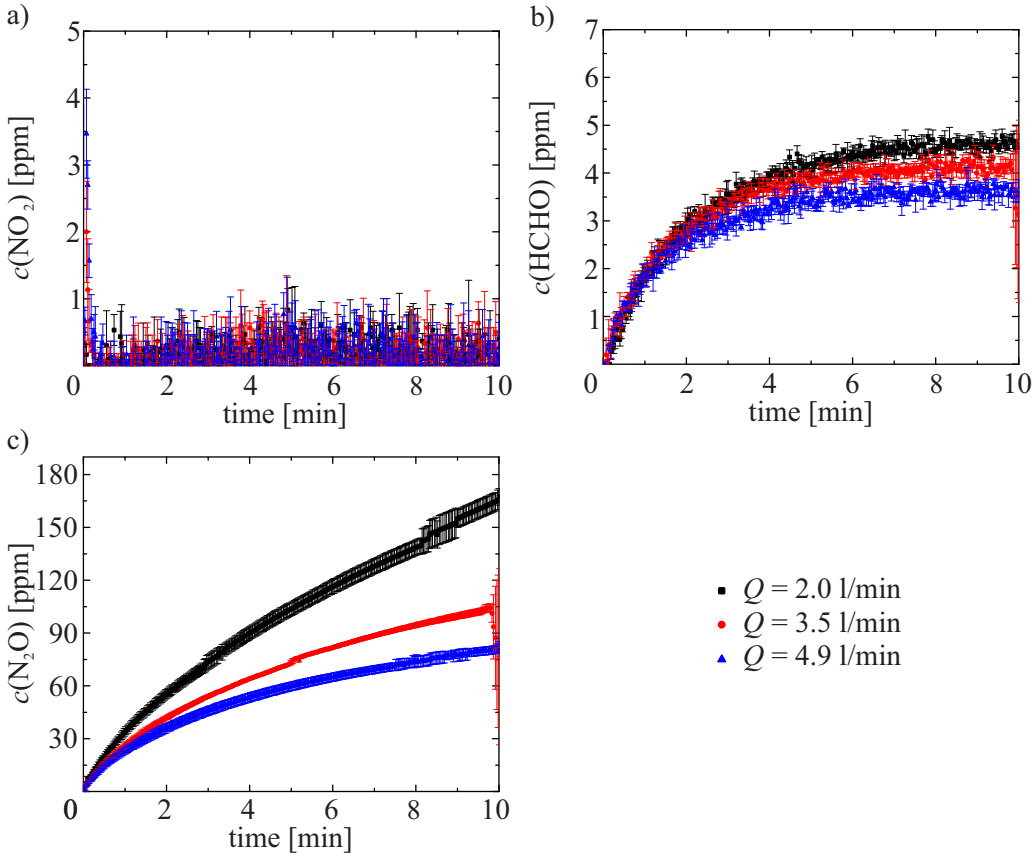

Figure 3.11: FTIR analysis of the afterglow composition using three different gas flow rates Q (2.0 l/min, 3.5 l/min and 4.9 l/min) under high humidity conditions. a) NO_2 concentration. b) HCHO concentration. c) N_2O concentration.

and saturates at different concentrations, while $c(\mathrm{HCHO})$ shows an inverse proportionality to Q. This trend is comparable to $c(O_3)$ as already described for the measurements under low humidity conditions. The concentration of N_2O is displayed in Fig. 3.11 c) and shows the same trend as using low humidity conditions. The concentrations of the different flow rates diverge from the beginning and show an inverse proportionality to the flow rate. As already mentioned before, I assume, that the smaller gas flow allows the air molecules a longer residence time in the plasma region which leads to a higher energy density in the gas and thus a higher production of N_2O molecules. Similar to low humidity conditions the concentration of N_2O does not approach to a constant value within the observed time span in contrast to $c(O_3)$ and $c(\mathrm{HCHO})$. This shows, that the production rate for N_2O is still higher than its recombination rate. Compared to the spectroscopic investigations under low humidity conditions, the concentrations for O_3, HCHO, HNO_3 and N_2O are significant lower for high humidity conditions. The change of the afterglow composition by the variation of the humidity is explained by a change in the chemical pathways [117], which is discussed in more detail in the following chapter.

In conclusion, the measurements of the O_3, N_2O and HCHO concentrations reveal that the concentration is influenced by the flow rate for both humidity conditions. In detail, the concentrations of O_3, N_2O and HCHO decrease with the increase of the gas flow. Furthermore, HNO_3 and NO_2 show no dependency to the gas flow. These investigations emphasise, that the plasma afterglow could be manipulated by the gas flow. To avoid a variation of the afterglow by the gas flow, a fix value of $Q = 3.5\,\mathrm{l/min}$ was used for the microbiological, material compatibility and spectroscopic investigations in this work. The gas flow of 3.5 l/min allows a fast exchange of the reactive species in the treatment chamber, while the concentrations of O_3, N_2O and HCHO remains high. A sufficient exchange of the reactive species within the treatment chamber is crucial for the decontamination of 3D objects.

3.5 Characterisation of Different Humidity Conditions

Previous measurements already demonstrated that the H_2O concentration of the fresh air has an influence to the composition of the afterglow generation. Therefore, different humidity conditions were used to examine the afterglow composition by FTIR and UV absorption spectroscopy.

For the investigations, the described setup in Fig. 2.1 was used without treatment chamber. To adjust the H_2O content of the fresh air, the air was circulating with the installed humidifier in the PACA until the desired H_2O concentration was reached. To avoid a further increase of the humidity concentrations, the wash bottle was removed when $c(H_2O)$ was high enough. If $c(H_2O)$ became to high, the PACA was flushed with fresh air, to minimise the humidity content again. This procedure allowed to adjust the humidity to a stable value for the

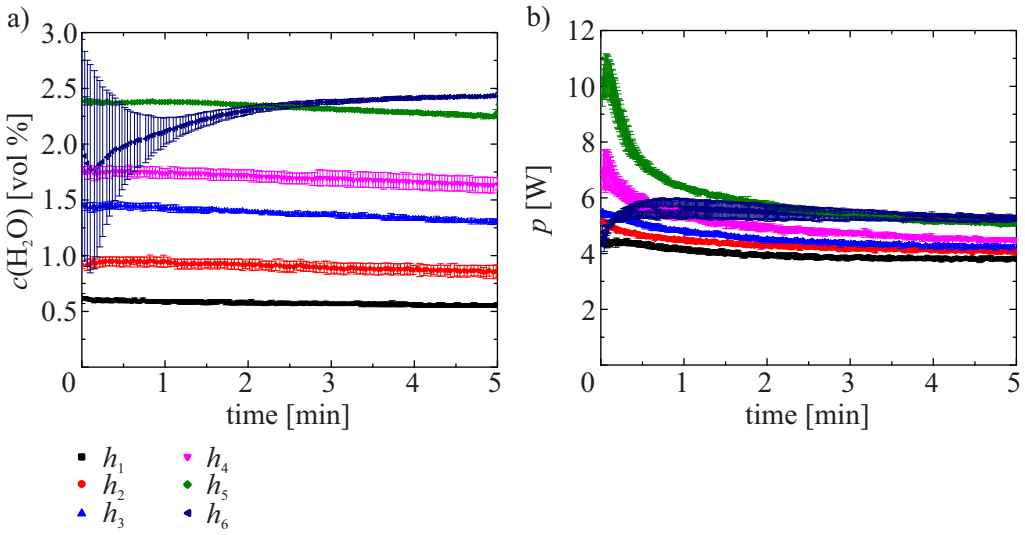

Figure 3.12: a) FTIR measurement of different humidity conditions during plasma ignition. b) Power consumption for different humidity conditions during plasma ignition.

measurement time with a precision of ±0.1 vol %.

The investigations were executed for six different humidity conditions $h_1 - h_6$. Fig. 3.12 a) shows the H_2O concentrations for different humidity conditions (h_1, h_2, h_3, h_4, h_5 and h_6) as a function of time. For the measurements of $h_1 - h_5$ the gas was already circulating before the plasma was ignited. In case of the h_1 condition, no humidifier was used. For h_6, the humidifier was included during the measurement, so that the humidity starts to increase with the start of the plasma ignition. Thus, the humidity in Fig. 3.12 a) shows a stable behavior for $h_1 - h_5$, while the humidity increases for h_6. For h_6 the gas flow was switched-on a few seconds after the plasma was ignited to prevent condensations on the electrode surface by the water. This switch-on process causes variations at the beginning of the H_2O detection. Furthermore, a slow decrease of the H_2O amount was observed for $h_1 - h_6$. The decrease of $c(H_2O)$ for $h_2 - h_6$ could be caused by a possible condensation of humidity on the surfaces of the apparatus (which are not heated) or by a possible leakage of the setup. Nevertheless, a decrease is also observed for h_1 (using ambient humidity), where no decrease by leakage is possible. Because of this observation, H_2O is probably dissociated by the plasma or reactive species which are created from the plasma. After 5 min measurement, $c(H_2O)$ reached the following values for the different conditions: $h_1 = 0.6$ vol %, $h_2 = 0.9$ vol %, $h_3 = 1.3$ vol %, $h_4 = 1.6$ vol %, $h_5 = 2.3$ vol % and $h_6 = 2.4$ vol %. Relating to the adjusted H_2O concentrations of Fig. 3.12 a), Fig. 3.12 b) displays the detected power consumption p during 5 min plasma ignition using different humidity conditions $h_1 - h_6$. For $h_1 = 0.6$ vol % the power consumption shows the lowest value and decreases within the time span of 5 min. The distribution of the power consumption is shifted to higher power levels by increasing the operation humidity. The conditions of h_4 and h_5 show an increase of the power maximum in the beginning of the

plasma ignition. The increase of the power consumption could be explained by the fact, that the humidifier was used to adjust the humidity level before the plasma was ignited. In case of high humidity concentrations, the water was condensed on the electrode surface and probably built a water film on the surface which evaporates when the plasma is ignited.

In contrast to $h_1 - h_5$, the distribution of p for h_6 demonstrates an increase of the power up to 5.5 W and deceases to a value of 5.3 W within the observation time. As already mentioned for h_6 (with the humidifier installed in the setup), the gas flow was switched on $2 - 3$ s after the plasma was ignited. In this case, no water film was present in the beginning of the plasma ignition, so that no maximum of p is visible. The shift to a higher power consumption with an increase of the humidity, indicates that c(H_2O) of the circulating gas influences the plasma ignition. This observation could not be approved using an open system in chapter 3.3, but for this investigations the humidity concentrations were lower than for h_5 and h_6, presented here. Kogelschatz *et al.* reported, that the humidity increases the surface conductivity of the dielectric which causes stronger micro-discharges [133]. The formation of stronger micro-discharges would explain the increase of the power consumption in the first minute due to a thin water layer on the electrode surface. Furthermore, the ignition of the discharge vaporise the deposited water on the surface which leads to a reduction of the power consumption of the electrode.

The results of the spectroscopic analysis using FTIR and UV absorption spectroscopy are presented in Fig. 3.13. Fig. 3.13 a) illustrates the detected O_3 concentration for the different humidity conditions as a function of time. The ozone concentration shows a dependency to different humidity conditions $h_1 - h_6$ with an increase of $c(O_3)$ as the $c(H_2O)$ decreases. This divergence is detectable from the beginning of the plasma ignition. The increase of O_3 supports the results of chapter 3.3 that the increase of the H_2O content changes the chemical reaction pathways. With an increase of the humidity, a part of the discharge energy is consumed by the H_2O molecules to form OH and OH_2 [117].

As already mentioned before, the presence of NO could not be measured with the present apparatus, due to the significant H_2O absorption bonds in the region of the NO absorption peak. Dorai *et al.* reported in their investigations, that one of the dominant production processes of NO is proportional to the amount of OH (OH+N→NO+H)[181]. Furthermore, they described in their theoretical model that NO and NO_2 increases with the relative humidity [150]. Fig. 3.13 b) shows the NO_2 concentration $c(NO_2)$, measured with the FTIR. The investigations show no dependence of the NO_2 concentration on the air humidity since the concentration values of NO_2 are fluctuating below 1.3 ppm between $t = 0.5 - 5.0$ min. A remarkable observation is, that the NO_2 concentration increases in the first seconds and decays between $t = 0.1 - 0.5$ min. The highest NO_2 maximum could be observed for $h_5 = 2.3$ vol %, which also showed the highest power consumption in the beginning. This results fits to the assumption (see chapter 1.7), that the production of NO and NO_2 increases with the power

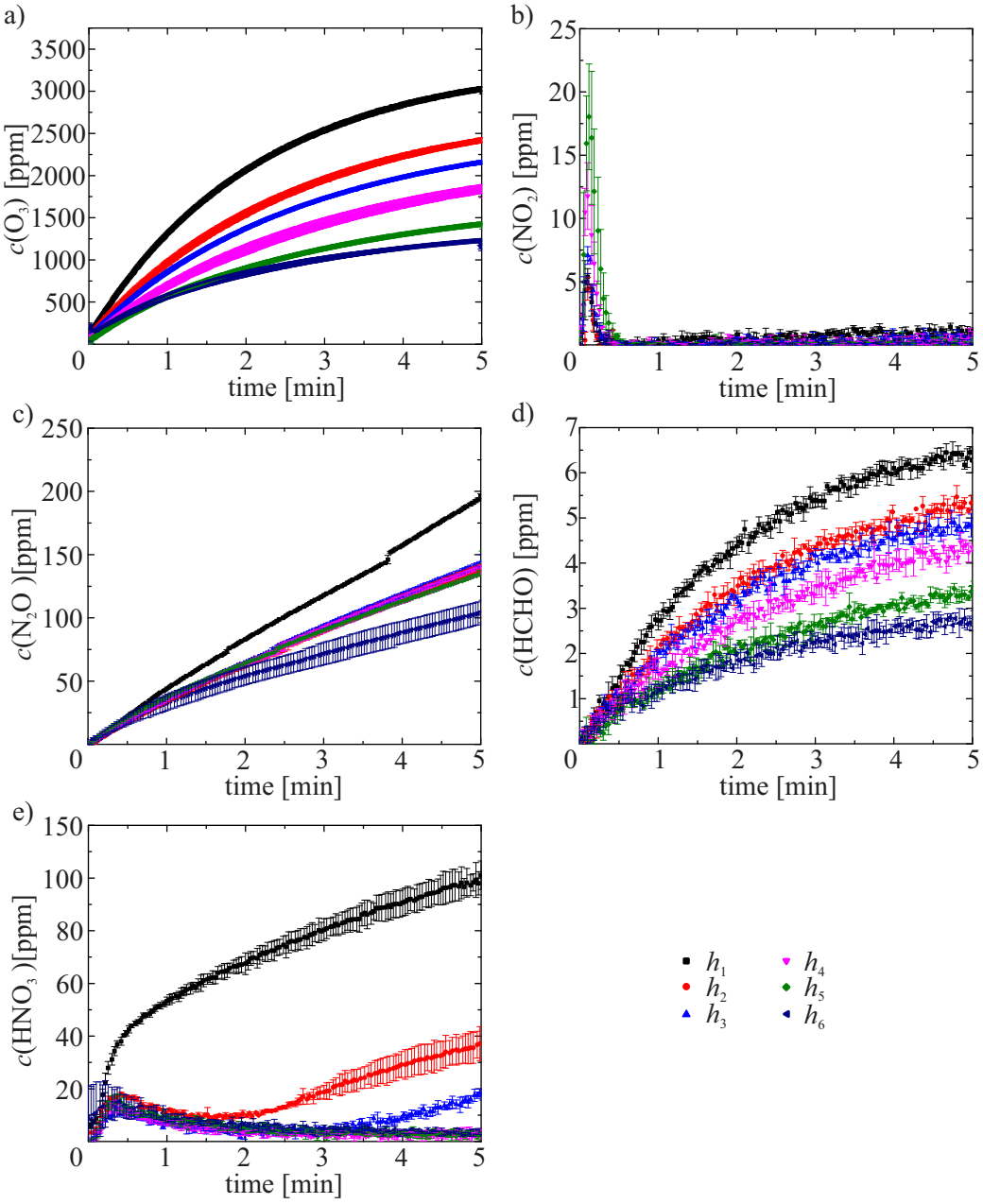

Figure 3.13: Analysis of the plasma afterglow composition for different humidity conditions of $h_1 = 0.6\,\text{vol}\,\%$, $h_2 = 0.9\,\text{vol}\,\%$, $h_3 = 1.3\,\text{vol}\,\%$, $h_4 = 1.6\,\text{vol}\,\%$, $h_5 = 2.3\,\text{vol}\,\%$ and $h_6 = 2.4\,\text{vol}\,\%$ a) O_3 concentration. b) NO_2 concentration. c) N_2O concentration. d) HCHO concentration. e) HNO_3 concentration.

consumption of the micro-discharge. From the data can be concluded that the NO_2 production is increased by the raise of the power consumption at the beginning of a measurement. Since the apparatus mainly generates ozone, the O_3 molecules react with NO_2 which leads to a reduction of the NO_2 concentration. In addition to O_3, NO_2 molecules react with OH molecules to form HNO_3 [150]. These reactions lead to low concentrations of NO_2.

Furthermore, the concentration of N_2O is displayed in Fig. 3.13 c) for different humidity conditions. The trend of $c(N_2O)$ is similar for h_2, h_3, h_4 and h_5, which ends up to 138 ppm after $t = 5$ min. In case of h_1 the N_2O concentration is maximal and for h_6, the concentration for N_2O is minimal. Note, that for h_6 the humidifier was included in the circulation, which increased the total volume from $\sim$ 540 ml to $\sim$ 740 ml. The increase of the total volume explains the lower concentration for N_2O. The results in chapter 3.3, indicate that no N_2O was dissolved by passing the water in the wash bottle. Thus I assume that the reduction of $c(N_2O)$ is not caused by the dissolving of N_2O in the humidifier water. The results in the present section suggests that the loss processes of N_2O are stronger in the closed circulation apparatus using high humidity conditions. Dorai *et al.*[150] reported that N_2O is dominantly produced by $NO_2 + N \rightarrow N_2O + O$. On the one hand, the production of NO_2 increases by an increase of the relative humidity, but on the other hand NO_2 reacts with OH molecules to HNO_3 so that it is not available for the formation of N_2O. Probably, the solving of NO_2 in the humidifier water for h_6 leads to a further decrease of the N_2O formation.

Fig. 3.13 d) presents the measured HCHO concentration for different humidity conditions. The diagram shows the same trend for HCHO concentration as for the trend of $c(O_3)$ in a). After a plasma ignition time of 5 minutes, the values of HCHO reached concentrations between 2.7 and 6.5 ppm. The investigations reveal an increasing trend for O_3 and HCHO, while the H_2O level decreases. Furthermore, the production processes of O_3 and HCHO seems to be interdependent. As already mentioned in chapter 3.3 the occurrence of HCHO molecules together with VOC (volatile organic compounds) and O_3 was also reported in previous work [177–179].

A high dependence to the humidity conditions is shown by the HNO_3 measurement in Fig. 3.13 e). The HNO_3 concentration shows a decrease of the concentration for $t > 0.4$ min and $h_4 - h_6$. Here, the $c(HNO_3)$ decreases from a value of $\sim$15 ppm to 3 ppm. The HNO_3 concentrations for h_2 and h_3, follow the same trend in the first two minutes as for h_4, h_5 and h_6 with an higher humidity. However, the HNO_3 concentration later starts to increase linearly for h_2 ($t > 2$ min) and for h_3 ($t > 3.2$ min). The highest HNO_3 concentration is observed for h_1 without additional humidity in the setup. The HNO_3 concentration increases rapidly within the first 0.5 min and goes into a smaller increase afterwards. The investigations illustrate, that HNO_3 is strongly dependent on the humidity concentration in the circulation apparatus and that the $c(HNO_3)$ shows a maximum concentration when no additional humidification of the ambient air is used. It is feasible, that HNO_3 is still produced under high humidity conditions

due to the increase of NO_2 and OH molecules but condensate under high humidity conditions. This leads to the absence of HNO_3 in the gas phase and thus, in the FTIR spectrometer. In addition, Fig. 3.13 e) demonstrates, that the slope of $c(HNO_3)$ for $t > 3\,\text{min}$ seems to be similar for h_1, h_2 and h_3. This observation indicates, that the HNO_3 concentration starts to increase in the gas phase, when enough HNO_3 is already dissolved in the water, which supports the observations in this work. A fluctuation of HNO_3 in the afterglow composition was also reported by Pavlovich *et al.* [172]. Their explanation for this observation is that HNO_3 is sensitive to ambient water vapour concentrations.

The results emphasise, that the humidity conditions influence the formation of the reactive species, due to the increase of possible chemical reactions with H_2O molecules. The observation of the $c(O_3)$ decrease indicates that the formation of OH molecules is increased by the increasing humidity. This OH molecules are suspected to be involved in the microbiological processes for the bacterial inactivation by the plasma treatment. Due to the fact, that the inactivation efficiency is increased for high humidity, the microbiological investigations in chapter 4 were executed under high humidity conditions.

3.6 Characterisation of the Plasma Power

In addition to the previous experiments, the plasma afterglow composition was analysed in dependence of the power consumption p. In particular, I varied the applied voltage U between $6.0\,\text{kV}_\text{pp}$, $5.5\,\text{kV}_\text{pp}$, $5.0\,\text{kV}_\text{pp}$ and $4.5\,\text{kV}_\text{pp}$ and the applied frequency f between 10 kHz, 8 kHz and 6 kHz. The analysis of the plasma afterglow for different plasma parameters were executed under low and high humidity conditions. For the investigations, the setup in Fig. 2.1 was used without treatment chamber. To minimise variations due to environmental influences, the investigations were executed within one day and the illustrated data represents a mean value of three measurements per plasma condition. The presented error bars are calculations of the standard deviation of the measurements.

At first, the investigations under low humidity conditions were executed. Fig. 3.14 a) displays the detected power consumption of the PACA for ten different voltage and frequency conditions. The power consumption was detected for 3 min and shows an increasing behaviour with an increase of the voltage and frequency. The parameters of $4.5\,\text{kV}_\text{pp}$ and 10 kHz show the lowest power consumption. A further decrease of the frequency or voltage leads to an expiration of the plasma ignition. In Fig. 3.14 a), the power consumption decreases within the first minute with an applied voltage of $6.0\,\text{kV}_\text{pp}$ and $5.5\,\text{kV}_\text{pp}$ and approaches a constant value afterwards. The measured power for $5.0\,\text{kV}_\text{pp}$ and $4.5\,\text{kV}_\text{pp}$ is constant for the complete time span of 3 min.

For the low humidity condition, the decrease of p is explained by the increase of the temperature for a high power consumption. Thus, a reduced power consumption (with a

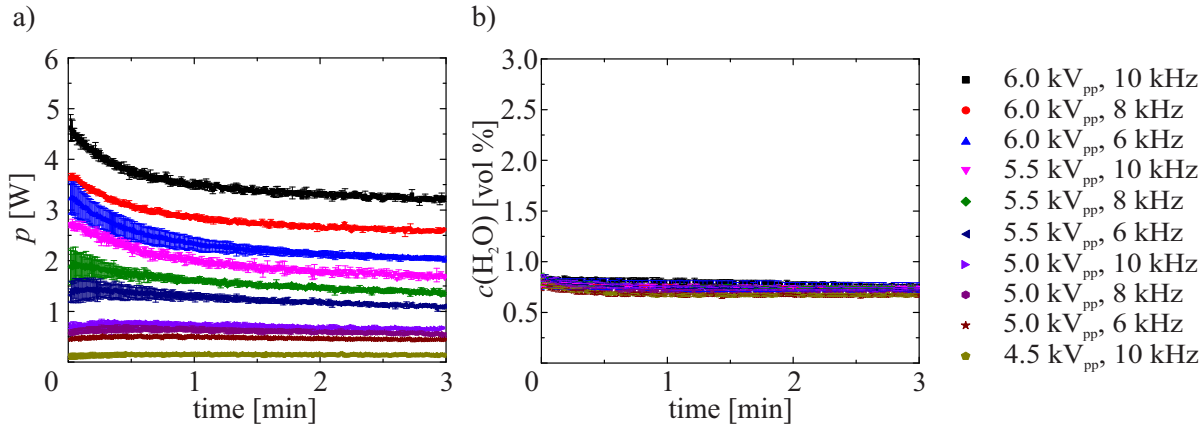

Figure 3.14: Analysis of the plasma afterglow composition for different voltages and frequencies for low humidity conditions. a) Power consumption. b) H_2O concentration.

low temperature increase) shows a lower decrease of p within the observed time span. For the sake of completeness, Fig. 3.14 b) shows the H_2O concentration as a function of time, using the FTIR. As described before (see chapter 3.4), the detailed observation of the H_2O concentration depict a decrease of $\sim 0.08\,\mathrm{vol\,\%}$ within the observed the time span.

The plasma afterglow composition for low humidity conditions and different plasma parameters was analysed using FTIR and UV absorption spectroscopy. Fig. 3.15 reveals the analysed concentration of the components O_3, NO_2, N_2O, HCHO and HNO_3 as a function of time. The ozone concentration was detected using the UV absorption spectroscopy and is presented in Fig. 3.15 a). In detail, the O_3 concentration decreases with a reduction of the power consumption. The highest $c(O_3)$, was reached for $6.0\,\mathrm{kV_{pp}}$ and 10 kHz and the lowest $c(O_3)$ for $4.5\,\mathrm{kV_{pp}}$ and 10 kHz. As previously observed, the results for HCHO in Fig. 3.15 d) show a similar course as $c(O_3)$ in a). The data show a diverging increase from the beginning on for both concentrations of O_3 and HCHO. The similar trend of HCHO and O_3 is already mentioned in previous chapters (see chapter 3.3). I assume, that HCHO is produced by reactions of VOC (volatile organic compounds) and O_3 [177–179].

The detected NO_2 concentration in dependence of the plasma power consumption is presented in Fig. 3.15 b). From the figure it is visible that the NO_2 concentration is fluctuating below 3 ppm within the observed time span and shows no dependence to the power consumption. Fig. 3.15 c) illustrates the N_2O concentration for different plasma power conditions as a function of time. According to the diagram, the N_2O concentration increases linearly for the observed time interval. As already observed for the concentration of O_3 and HCHO, the concentration of N_2O is maximal ($\sim$168 ppm) for $6.0\,\mathrm{kV_{pp}}$ and 10 kHz and decreases with a reduction of the power consumption down to $\sim$15 ppm for $4.5\,\mathrm{kV_{pp}}$ and 10 kHz.

The analysis under low humidity conditions for the components of O_3, HCHO and N_2O depict the same trend. For these molecules, the observed concentrations are proportional to

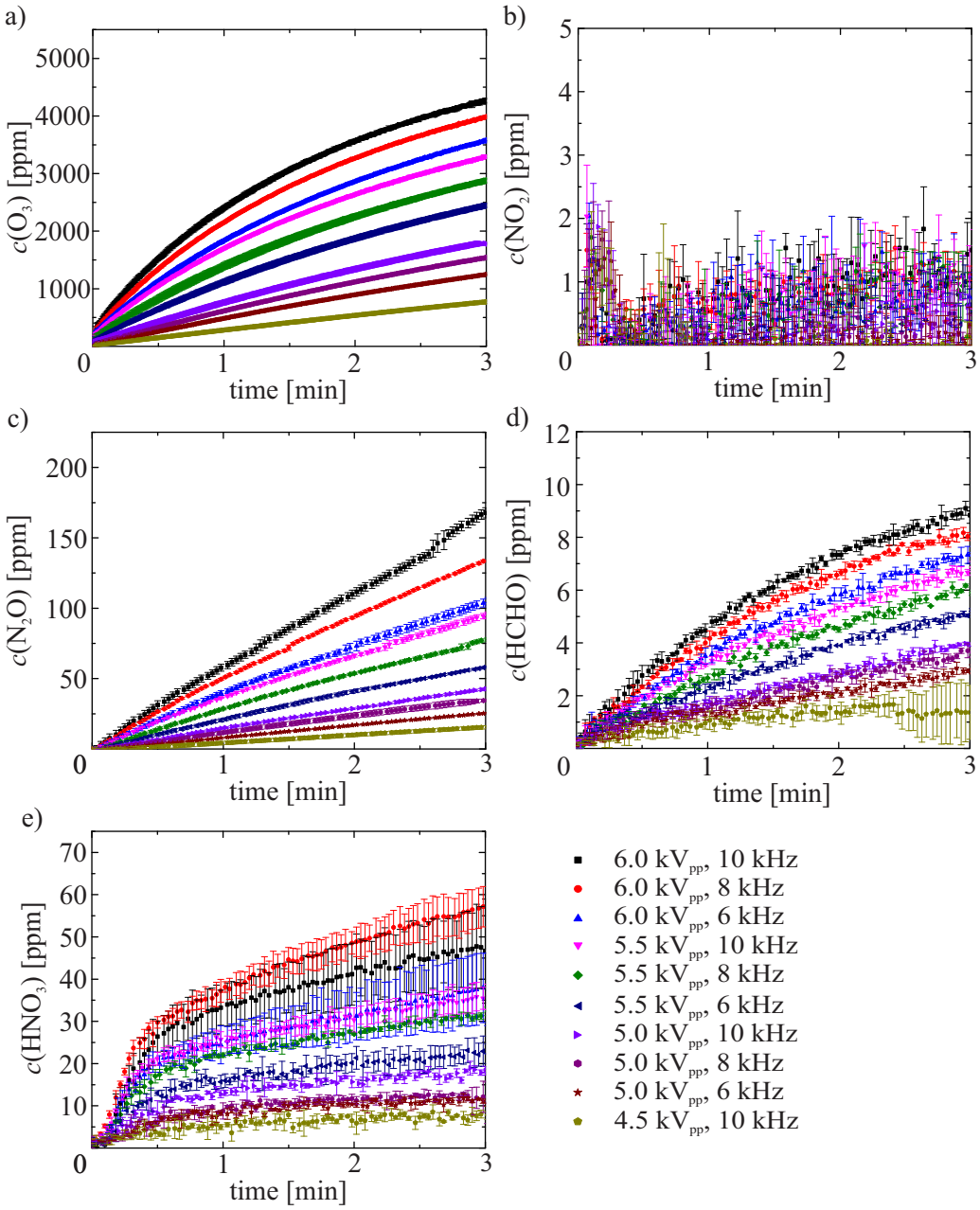

Figure 3.15: Analysis of the plasma afterglow composition for different voltages and frequencies for low humidity conditions. a) O_3 concentration. b) NO_2 concentration. c) N_2O concentration. d) HCHO concentration. e) HNO_3 concentration.

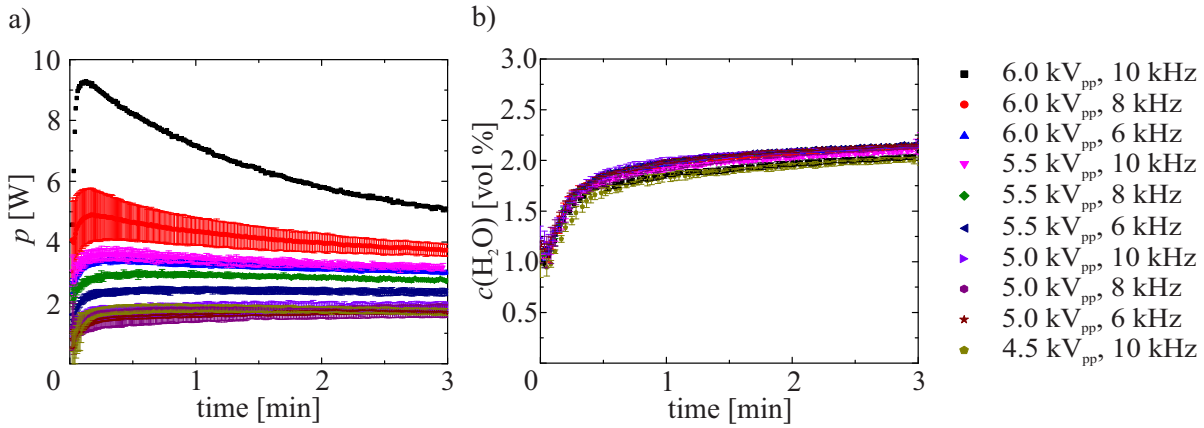

Figure 3.16: Analysis of the plasma afterglow composition for different voltages and frequencies for high humidity conditions. a) Power consumption. b) H_2O concentration.

the power input on the electrode. The increase of the power input, increases the electron density in the field of the micro-discharge which leads to an increased production of atomic oxygen and nitrogen, which are responsible for the formation of O_3 and N_2O. In addition, HCHO is strongly coupled to the amount of ozone production.

The detected HNO_3 concentration is presented in Fig. 3.15 e). The diagram shows that the HNO_3 concentration increases with increasing power consumption. The values for $6.0\,kV_{pp}$ and 8 kHz reaches the maximum concentration for the measurement within the observed time span. The measured data of $c(HNO_3)$ show high standard deviations for $U = 6.0\,kV_{pp}$ (8 kHz and 10 kHz) due to the sensitivity of HNO_3 to the environmental conditions. The concentration of NO_2 reveals no clear dependency to p but the measurement of HNO_3 increases over time with an increase of the power consumption. Since NO_2 is mainly responsible for the HNO_3 production, it is assumed that NO_2 is produced in the afterglow, but reacts immediately further to HNO_3 [150, 183]. Due to the increase of HNO_3 with an increase of the power consumption, I assume an increase of the OH production and a possible increase of NO and NO_2 which are also attributed to the increase of the electron density in the region of the micro-discharges.

In addition to the investigations for low humidity conditions, the afterglow composition was analysed for high humidity conditions to gain insights into the afterglow formation process. Fig. 3.16 a) shows the power consumption as a function of time for different voltages and frequencies. Similar to Fig. 3.14 a) the power is higher for high values of the applied voltage and frequency. In contrast to low humidity conditions, the power consumption increases in the first $0.1 - 0.2$ min and decreases afterwards for voltages of $U > 5.5\,kV_{pp}$. The data for $U = 6.0\,kV_{pp}$ (8 kHz, 6 kHz) and $U = 5.5\,kV_{pp}$ (10 kHz, 8 kHz) approach to a constant value within the observed time interval of 3 min, whereas the trend for $U = 6.0\,kV_{pp}$ and $f = 10$ kHz does not reach a constant value within the measurement. The remain-

ing data depict a constant behavior for $t > 0.2\,\mathrm{min}$ while the values for $U = 5.0\,\mathrm{kV_{pp}}$ and $U = 4.5\,\mathrm{kV_{pp}}$ are overlapping. At $t = 3\,\mathrm{min}$, the minimal power consumption was detected for $U = 4.5\,\mathrm{kV_{pp}}$ and $f = 10\,\mathrm{kHz}$ ($p = 1.7\,\mathrm{W}$) and the maximum power consumption was observed for $U = 6.0\,\mathrm{kV_{pp}}$ and $f = 10\,\mathrm{kHz}$ ($p = 5.1\,\mathrm{W}$). The presented data reveal a shift of the power consumption to higher values when the humidity is high. Probably, the presence of high humidity in the closed circulation apparatus leads to a formation of a water film, which changes the micro-discharges [133]. The decrease ot the power maximum for $U = 6.0\,\mathrm{kV_{pp}}$ could be explained by the increase of the electrode temperature, which leads to a reduction of the water film and the power consumption on the electrode. Fig. 3.16 b) displays the detected H_2O concentration of the investigations under high humidity conditions, using the FTIR spectrometer. For all measurements, the H_2O concentration shows a fast increase in the first 30 s and a nearly constant trend afterwards. After 3 min of measurement, the H_2O concentration reaches a value between 2.0 vol % and 2.2 vol %.

The detailed analysis of the afterglow composition using UV absorption and FTIR spectroscopy is illustrated in Fig. 3.17. The investigated O_3 concentration is depicted in Fig. 3.17 a) and shows a similar dependency on the power consumption as under low humidity conditions, with the exception, that the O_3 concentration is higher for $5.5\,\mathrm{kV_{pp}}$ and 10 kHz than for $6.0\,\mathrm{kV_{pp}}$ and 6 kHz. As already observed in chapter 3.5 the O_3 concentration is lower for high humidity conditions (Fig. 3.17 a)) than for low humidity conditions (Fig. 3.15 a)). In addition, the temporal evolution shows a small maximum in the first seconds, which is an effect of the use of the humidifier (see chapter 3.1). The maximum concentration of 2707 ppm after 3 min is depicted for $6.0\,\mathrm{kV_{pp}}$ and 10 kHz and the minimal concentration of 760 ppm after 3 min is given for $4.5\,\mathrm{kV_{pp}}$ and 10 kHz. The HCHO concentrations in Fig. 3.17 d) behaves similar to the recorded data for $c(O_3)$. The measurement of NO_2 in Fig. 3.17 b) demonstrates no clear trend of $c(NO_2)$ depending on the plasma parameter. In the time span of 1−2 min, the concentration is fluctuating close to zero. Furthermore, the NO_2 concentration shows again a maximum peak for $5.5\,\mathrm{kV_{pp}}$ and 8 kHz in the first minute of plasma ignition, but shows no dependence to the power consumption. The concentration maximum in the first minute reveals, that NO_2 is produced during plasma ignition. I propose that the NO_2 molecule reacts fast with other afterglow components (especially OH and O_3 molecules) and are not visible in the detected time span. This consideration agrees with the assumption that the high humidity increases the OH amount in the afterglow. The investigations of $c(N_2O)$ are presented in Fig. 3.17 c) and reveal a similar dependency to the power consumption like the O_3 and HCHO concentrations. The concentrations of N_2O, O_3 and HCHO for $5.5\,\mathrm{kV_{pp}}$ and 10 kHz depict higher concentrations for the molecules than for the parameters $6.0\,\mathrm{kV_{pp}}$ and 6 kHz. This observation agrees with the power consumption, which is slightly higher for $5.5\,\mathrm{kV_{pp}}$ and 10 kHz than for $6.0\,\mathrm{kV_{pp}}$ and 6 kHz. In addition, the power consumption shows a similar distribution for the parameters of $5.0\,\mathrm{kV_{pp}}$ and $4.5\,\mathrm{kV_{pp}}$. The presence of water changes the

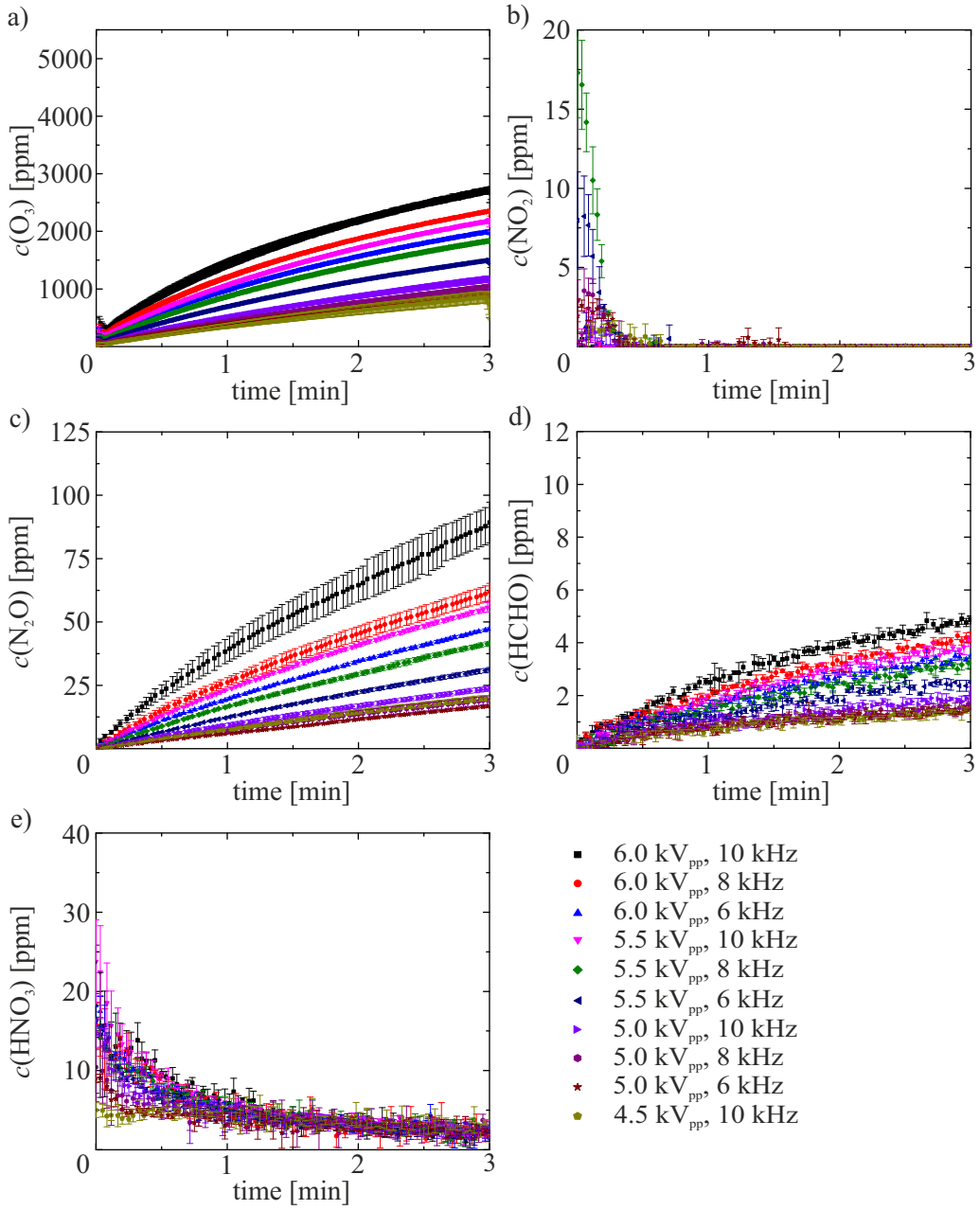

Figure 3.17: Analysis of the plasma afterglow composition for different voltages and frequencies for high humidity conditions. a) O_3 concentration. b) NO_2 concentration. c) N_2O concentration. d) HCHO concentration. e) HNO_3 concentration.

micro-discharge within the electrode so that the consumption power is shifted to other values than under low humidity conditions. Furthermore, the HNO_3 concentration was detected under high humidity conditions for different plasma power conditions and is presented in Fig. 3.17 e). Analog to the investigations of NO_2, the HNO_3 concentration reveals no clear dependence to the plasma power. The concentration decreases over the observed time span and ends up in a fluctuation below 4.5 ppm after 3 min plasma ignition. It is assumed, that HNO_3 is generated within the plasma ignition but reacts with the water in the humidified air. Probably, the HNO_3 is not visible in the FTIR measurement due to condensation in the apparatus. This assumption is discussed in more detail in the following chapter 3.7.

The results show, that the concentrations of O_3, N_2O and HCHO increase with the increase of the power consumption for low and high humidity conditions. For low humidity conditions, the dependence of the HNO_3 formation to the power consumption is also detected, while $c(HNO_3)$ is low for high humidity conditions. In addition, the NO_2 concentrations is low for all conditions. These investigations reveal, that for the used plasma parameter of U and f, the PACA operates in a ozone dominated mode. That means, that ozone is mainly produced by the plasma ignition. It is reported by several publications, that an increase to a higher power consumption could lead to an increase of the NO_x formation, which causes a decrease of the detected ozone concentration (ozone quenching) [58, 111]. The formation of NO_x due to the increase of the power consumption is explained in more detail in chapter 1.7. This quenching effect could not be observed for the different power consumption, but is separately discussed in chapter 3.8. The investigations of the power consumption show an increase of the reactive species, by an increase of the power consumption. To operate with high concentrations of the reactive species, the parameters $U = 6.0\,kV_{pp}$ and $f = 10\,kHz$ were used for the investigations in this work.

3.7 HNO_3 and NO_2 Formation

In the previous characterisation of the PACA, the reactive species were analysed during the plasma ignition. These investigations provided insights into the plasma composition for different conditions. Nevertheless, it is difficult to explain all observations of the experiments for sure, for example the absence of HNO_3 for high humidity conditions. In the present section, the analysis of the afterglow composition, after the plasma was switched-off, is analysed and provides additional information to understand the chemical processes in the PACA.

3.7.1 HNO_3 Formation for High Humidity Conditions

Previous investigations already show a variation in the HNO_3 production and measurement in the presence of high humidity (as already discussed in chapter 3.5). The results for different humidity conditions ($h_1 - h_6$) depict that HNO_3 strongly depends on the H_2O content of the

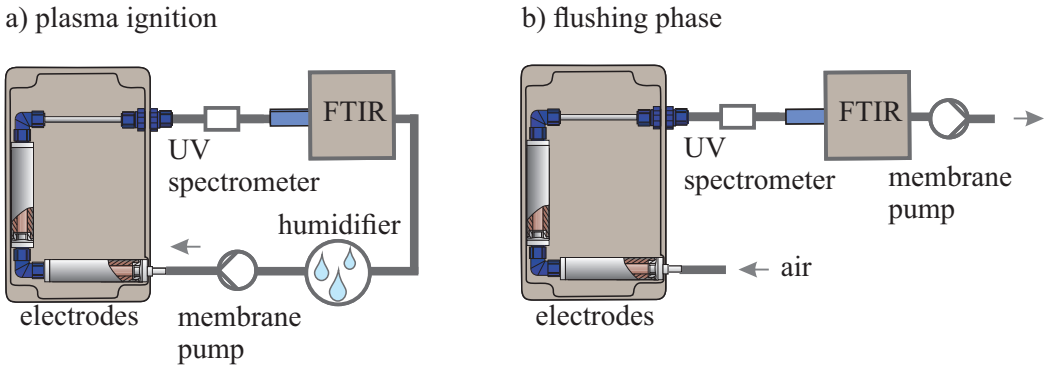

Figure 3.18: a) Setup of the PACA for the plasma afterglow analysis during plasma ignition for different humidity conditions. b) Setup during the flushing phase after the plasma is switched-off.

gas mixture. In detail, HNO_3 shows lower concentrations for increasing H_2O concentrations. I assume that an increase of H_2O molecules leads to an increase of OH formation, which reacts together with NO_2 to form HNO_3 [150]. This notion predict an increase of HNO_3 by the increase of humidity in the PACA. However, the detected amount of HNO_3 is low for high humidity conditions in chapter 3.5 (Fig. 3.13 e)). In addition to the analysis during the plasma ignition phase, the gas was analysed after the plasma was switched-off. In detail the gas mixture was analysed, when the apparatus was flushed with ambient air.

The setup during the plasma ignition and during the flushing phase is illustrated in Fig. 3.18 a) and b), respectively. After the plasma is switched-off, the gas flow is interrupted for less than 2 min. Afterwards, the closed apparatus was opened between the pump and the electrodes (and the humidifier was removed for h_6) to flush the apparatus with ambient air (see Fig. 3.18 b)). The fresh air entered the electrode system and passed the UV-measurement-box and FTIR spectrometer before it left the apparatus again. The FTIR detection was continued during this flushing phase.

Fig. 3.19 a) illustrates the HNO_3 concentration for the plasma ignition phase ($t < 5$ min) - as already shown in Fig. 3.13 e) - and the flushing phase ($t > 5$ min) for the conditions of $h_1 - h_5$ (with humidities of 0.6, 0.9, 1.3, 1.6 and 2.3 vol %). The data represent the calculated mean values of three measurements. For a better overview, the error bars are not included in the diagram and the trend is illustrated using a solid line. For a single measurement of h_6 (~ 2.4 vol %), the trend of the H_2O and the HNO_3 concentration is presented in Fig. 3.19 b). According to the Fig. 3.19 a), the HNO_3 concentration depends on the humidity during the plasma ignition. When the plasma is switched-off and the apparatus is flushed with fresh air, the HNO_3 concentration shows an expected decrease for condition h_1. The investigations of $h_2 - h_5$ depict an increase of HNO_3 when the apparatus is flushed with fresh air (with a lower humidity). In this case, the HNO_3 amount increases up to 80 ppm in Fig. 3.19 a). For condition h_6, Fig. 3.19 b) shows the behaviour of $c(H_2O)$ and $c(HNO_3)$ during the flushing

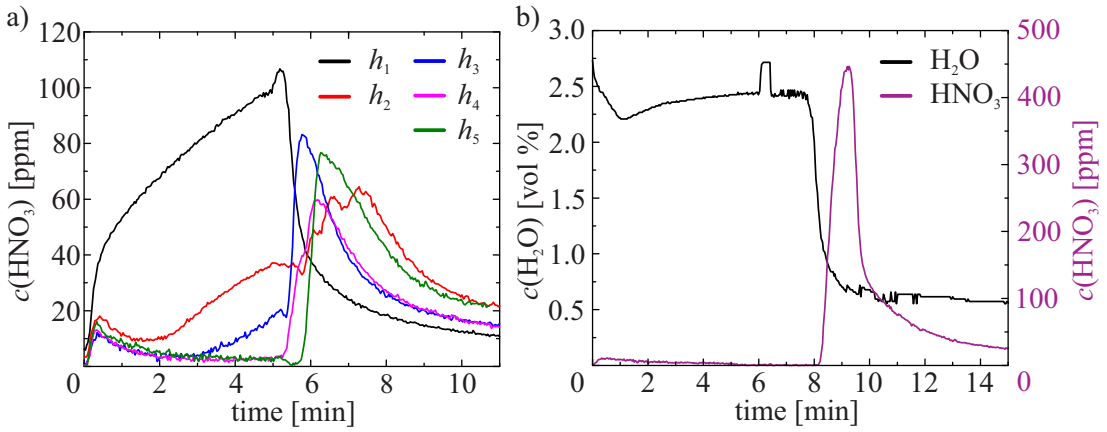

Figure 3.19: Analysis of the HNO_3 concentration under different humidity conditions ($h_1 - h_6$). a) HNO_3 concentration for different humidity conditions ($h_1 - h_5$) during the plasma ignition phase ($t < 5$min) and during the flushing phase with ambient air ($t > 5$min). b) HNO_3 and H_2O distribution for h_6 during the plasma ignition phase ($t < 5$min) and during the flushing phase with ambient air ($t > 5$min).

phase. The plasma ignition and the gas flow were stopped after 5 min to remove the humidifier and to open the apparatus circle (as shown in Fig. 3.18 b)). The interruption of the gas flow at $t = 5$ min is visible in the peak of the H_2O concentration in Fig. 3.19 b), because the FTIR measurement is influenced by the interruption. Afterwards, the gas flow was switched on again and the fresh air entered the apparatus. The data demonstrate that the humidity remains constant on a high level for ~ 1 min and decreases afterwards within 2 min and stays on a constant level. The HNO_3 concentration was minimal for h_6 during the plasma ignition phase and starts to increase when the amount of humidity decreases. The maximum of the HNO_3 concentration reaches a value of 447 ppm.

The presented data supports the assumption, that HNO_3 is produced, but solved in the water of the circulating gas or maybe condensed on the inner surface of the apparatus. This observation was already mentioned in chapter 3.3 and 3.5. If HNO_3 would be present in water droplets in the circulating gas, it should be measurable by the FTIR spectrometer. I assume, that HNO_3 condensates on the inner surface in the PACA and goes into the gaseous and detectable state when the apparatus is flushed by air with a lower humidity. A remarkable result of the HNO_3 production in the flushing phase is, that HNO_3 increases fast in the beginning and decays slowly afterwards. This points out, that a certain amount of HNO_3 enters the gaseous state fast, but some molecules are still in the liquid phase and transforms slowly. Furthermore, it can not be said with certainty that HNO_3 is completely removed from the apparatus after the flushing phase. These results emphasise, that the observation of the afterglow after the plasma is switched-off, shows additional insights in the chemical processes during the plasma ignition.

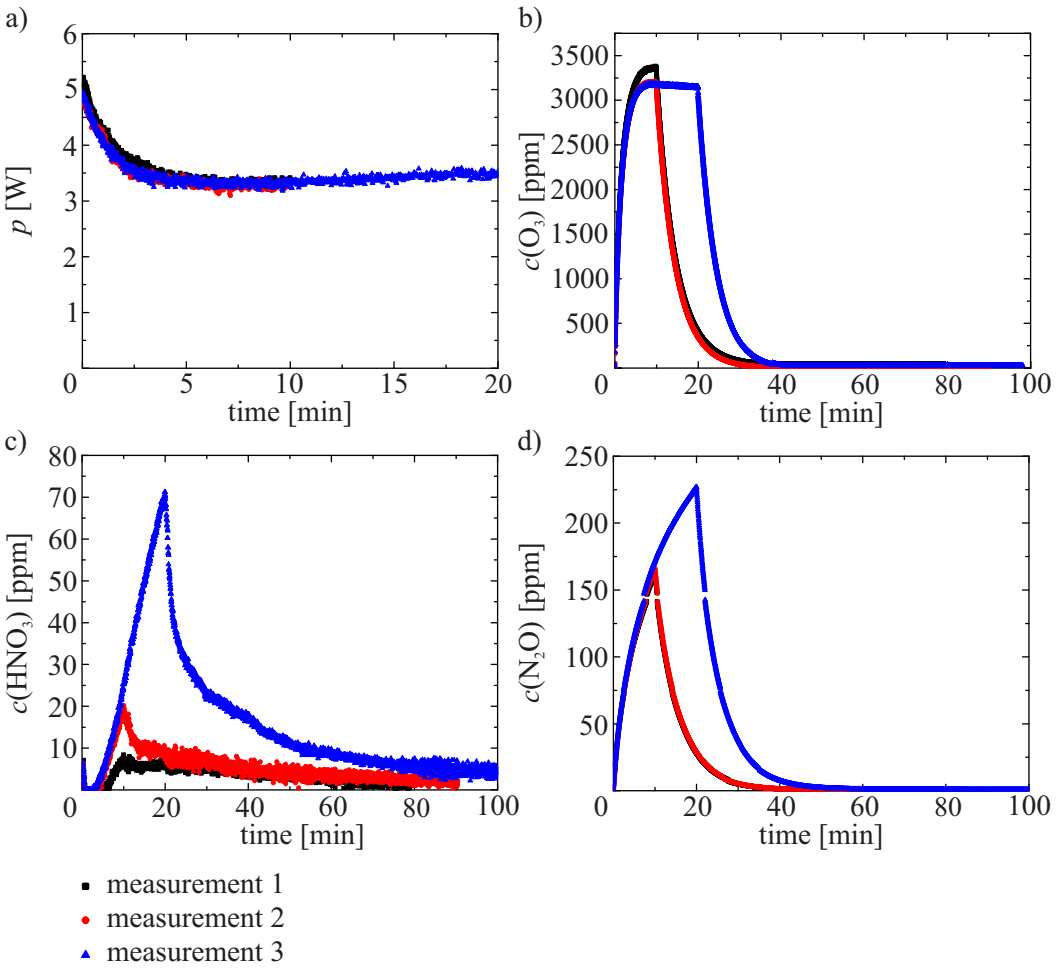

Figure 3.20: Analysis of the plasma afterglow composition for three consecutive measurements (measurement 1: 10 min plasma ignition, measurement 2: 10 min plasma ignition, measurement 3: 20 min plasma ignition). a) Power consumption p. b) O_3 concentration. c) HNO_3 concentration. d) N_2O concentration.

3.7.2 NO_2 Formation

For some experiments, the investigations of the decay phase showed a NO_2 formation after the plasma ignition. In the following, the observation of NO_2 formation is discussed for experiments under low humidity conditions. Fig. 3.20 illustrates the composition of the afterglow using low humidity conditions of ~ 0.7 vol % for three consecutive measurements. Since no humidifier was used, the circulation of the gas flow was not interrupted after the plasma ignition and the circulation of the reactive gas continued for more than one hour, after the plasma was switched-off. The power consumption is displayed in Fig. 3.20 a) and shows a similar distribution for the three measurements, so that I assume that the plasma ignition is equal. The plasma ignition for measurement 1 and 2 were executed for 10 min, while the plasma ignition of measurement 3 took 20 min in total. The detected ozone concentration

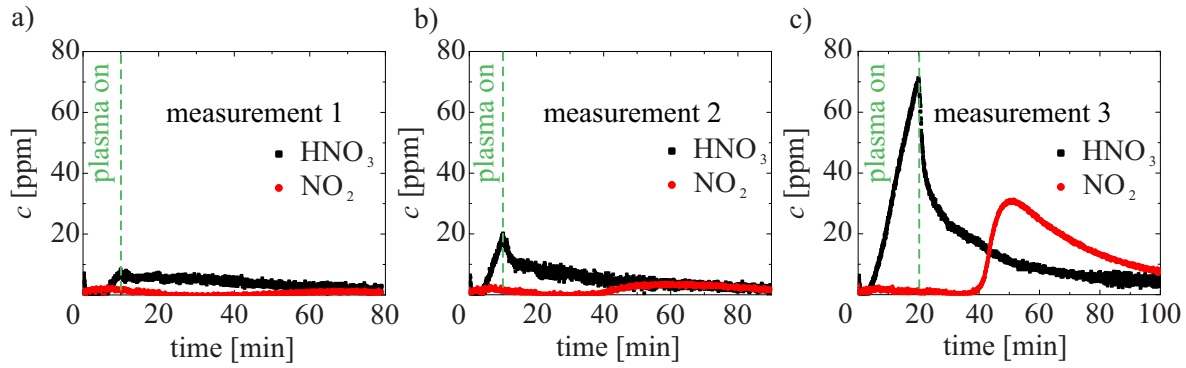

Figure 3.21: Analysis of the HNO_3 and NO_2 concentration for three consecutive measurements. a) Measurement 1: 10 min plasma ignition. b) Measurement 2: 10 min plasma ignition. c) Measurement. 3: 20 min plasma ignition.

is illustrated in Fig. 3.20 b) and reveals a similar trend for measurement 2 and 3. The O_3 concentration of measurement 1 shows a slightly higher concentration. After the plasma was switched-off, the ozone concentration decreased for all measurements. Fig. 3.20 c) presents the detected HNO_3 concentration. Measurement 1 depicts an increase for HNO_3 to a maximum of $\sim$ 8 ppm during plasma ignition and shows a slow decrease of the concentration afterwards. The HNO_3 concentration of measurement 2 and 3 increases up to $\sim$ 20 ppm within 10 min. After 20 min plasma ignition for measurement 3, the HNO_3 concentration reaches the maximum value of $\sim$ 70 ppm. The trends of measurement 2 and measurement 3 show a fast decrease of the HNO_3 concentration, followed by a slow decrease. The detection of N_2O in Fig. 3.20 d) reveals a similar concentration within the first 10 min for all measurements and shows a fast decrease of the molecules after the plasma ignition. In contrast to HNO_3, the detected concentration of O_3 and N_2O is negligible after $\sim$ 40 min. The data reveal that HNO_3 is more stable than N_2O and O_3 and shows a trend of accumulation with the repetition of measurements. In total, the dissociation of the reactive afterglow components reveals no extraordinary behavior after the plasma ignition.

In addition to O_3, HNO_3 and N_2O, the concentration for NO_2 was detected after the plasma ignition. Fig. 3.21 a), b) and c) illustrate the data for measurement 1, 2 and 3 for the concentrations of HNO_3 and NO_2, respectively. During plasma ignition, NO_2 is fluctuating below 2 ppm for all measurements and demonstrates a trend of decrease when the plasma is switched-off. Against the expectations, the NO_2 concentration starts to increase again, when the plasma is switched-off for $20 - 30$ min. This effect increases from measurement 1 to measurement 3. Especially for measurement 3, the concentration of NO_2 rises up to 31 ppm and shows a decrease afterwards. The highest concentration of HNO_3 was detected for this measurement. To date, the production source of the NO_2 molecules is unclear. The main production process of NO_2 during plasma ignition is caused by NO and OH in the following

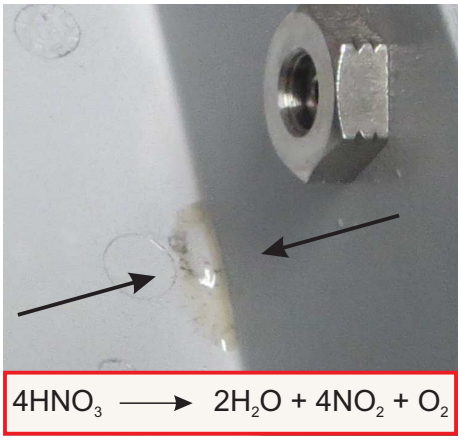

Figure 3.22: Observation of orange/red droplets in the treatment chamber.

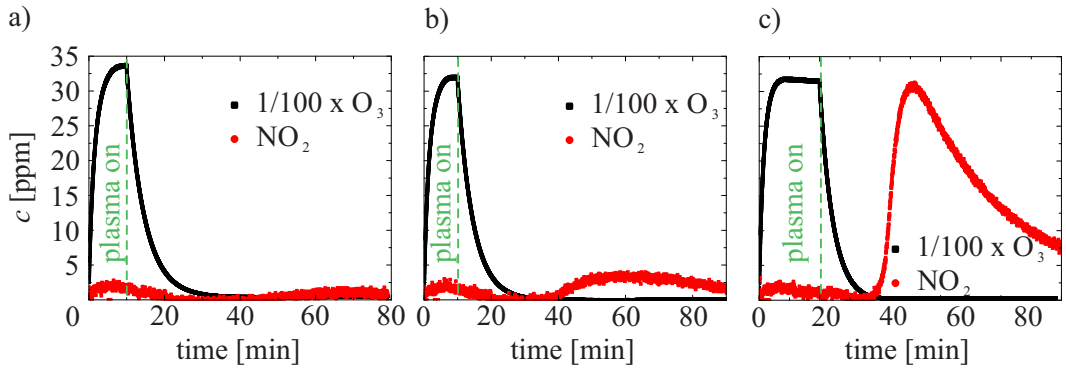

Figure 3.23: Analysis of the O_3 and NO_2 distribution for three consecutive measurements. a) Measurement 1: 10 min plasma ignition. b) Measurement 2: 10 min plasma ignition. c) Measurement 3: 20 min plasma ignition.

reactions [150]:

$$NO + O_3 \rightarrow NO_2 + O_2 \tag{3.1}$$

$$NO + HO_2 \rightarrow NO_2 + OH \tag{3.2}$$

$$OH + HNO_2 \rightarrow NO_2 + H_2O. \tag{3.3}$$

When the plasma is switched-off, it is assumed that HO_2 and OH are not present in the circulating gas. In addition, the production of NO_2 still increases when O_3 is dissociated. Thus, equations (3.1) – (3.3) could not explain the increase of NO_2. The formation of NO_2 is probably due to the deposit of nitric acid (HNO_3) in the apparatus. For high HNO_3 concentration NO_2 is formed in the nitric acid which is visible in an orange/red colour of the liquid [184, 185]. During some of the measurements, droplets with an orange/red colour occurred in the treatment chamber, shown in Fig. 3.22.

To find the reason of the unexpected NO_2 detection after the plasma ignition phase,

Fig. 3.23 compares the NO_2 and the O_3 concentration as a function of time. The illustrated O_3 is divided by a factor of 100, to compare the O_3 concentration with the other molecule concentrations. The data reveal, that the NO_2 concentration starts to increase when the O_3 concentration is close to zero. It was also reported in previous measurements of Kogelschatz *et al.* [148], that in presence of ozone, neither NO nor NO_2 could be detected due to fast reaction rates - described in chapter 1.7.

To analyse the dissociation of O_3, N_2O, and HNO_3 and the production of NO and NO_2, I analysed the FTIR absorption spectra for different time points for measurement 3. Fig. 3.24 presents the absorption spectra of the time points $t_1 = 10.0\,\text{min}$, $t_2 = 19.9\,\text{min}$, $t_3 = 30.0\,\text{min}$, $t_4 = 39.0\,\text{min}$, $t_5 = 45.0\,\text{min}$ and $t_6 = 50.1\,\text{min}$ of measurement 3 in a range of $4250-850\,\text{cm}^{-1}$. Time point t_1 was measured during the plasma ignition phase, while t_2 is detected right before the plasma is extincted. The time point t_3 depicts the dissociation phase with an decrease of O_3, N_2O, HNO_3 and NO_2. For $t > t_4$, the NO_2 concentration starts to increase until the maximum is reached for t_6. The time point of t_5 presents the phase, when the NO_2 concentration is raising. The presence of H_2O leads to a challenge for the interpretation of the absorption spectra, using FTIR. Therefore the spectrum for $t = 0\,\text{min}$ (before the plasma ignition), is subtracted from the spectral data for the chosen time points of measurement 3. The visible absorption peaks could be allocated to the expected molecules of the reactive gas composition. In this illustration, no additional afterglow species could be identified (for example NO), which could explain the formation of NO_2. The magnification in Fig. 3.24 presents a detailed illustration of the time points h_4, h_5 and h_6, but also this declination reveals no additional absorption peaks. In total, the absorption spectra confirm the calculation of the spectrometer software. The O_3, N_2O and HNO_3 peaks decrease, while the NO_2 absorption peak appears after the plasma is switched-off. In addition, HNO_3 is still detectable when O_3 and N_2O were completely dissociated. Due to its low intensity, the NO peak could not be detected in Fig. 3.24. Note, that the absorption intensities of $\sim 1700\,\text{cm}^{-1}$ and $1330\,\text{cm}^{-1}$ have a similar intensity (compared to Fig. 3.7), so that I conclude that N_2O_5 is not present in the afterglow composition. Furthermore, the behavior of the absorption peak at $\sim 2300\,\text{cm}^{-1}$ is observed. The absorption intensity demonstrates an increase during plasma ignition, while the peak shows a negative direction in the transition phase, after the plasma is switched-off. The negative absorption peak is caused by the subtraction of the absorption spectrum of time point $t = 0\,\text{min}$ for measurement 3. The absorption peak could relate to CO_2, H_2O_2 and HCHO. Since the increase of the absorption peak is remarkable and the HCHO absorption relatively low, the observation cannot be explained with an increase of HCHO only. In addition an increase of CO_2 and H_2O_2 is possible, while H_2O_2 cannot be identified clearly, as the other absorption peaks are overlapping with HNO_3. Furthermore, the results indicate, that the amount of CO_2 is increased, which means, that C molecules are produced during the plasma ignition phase. A possible raise of CO_2 could be due to etching effects of polymers,

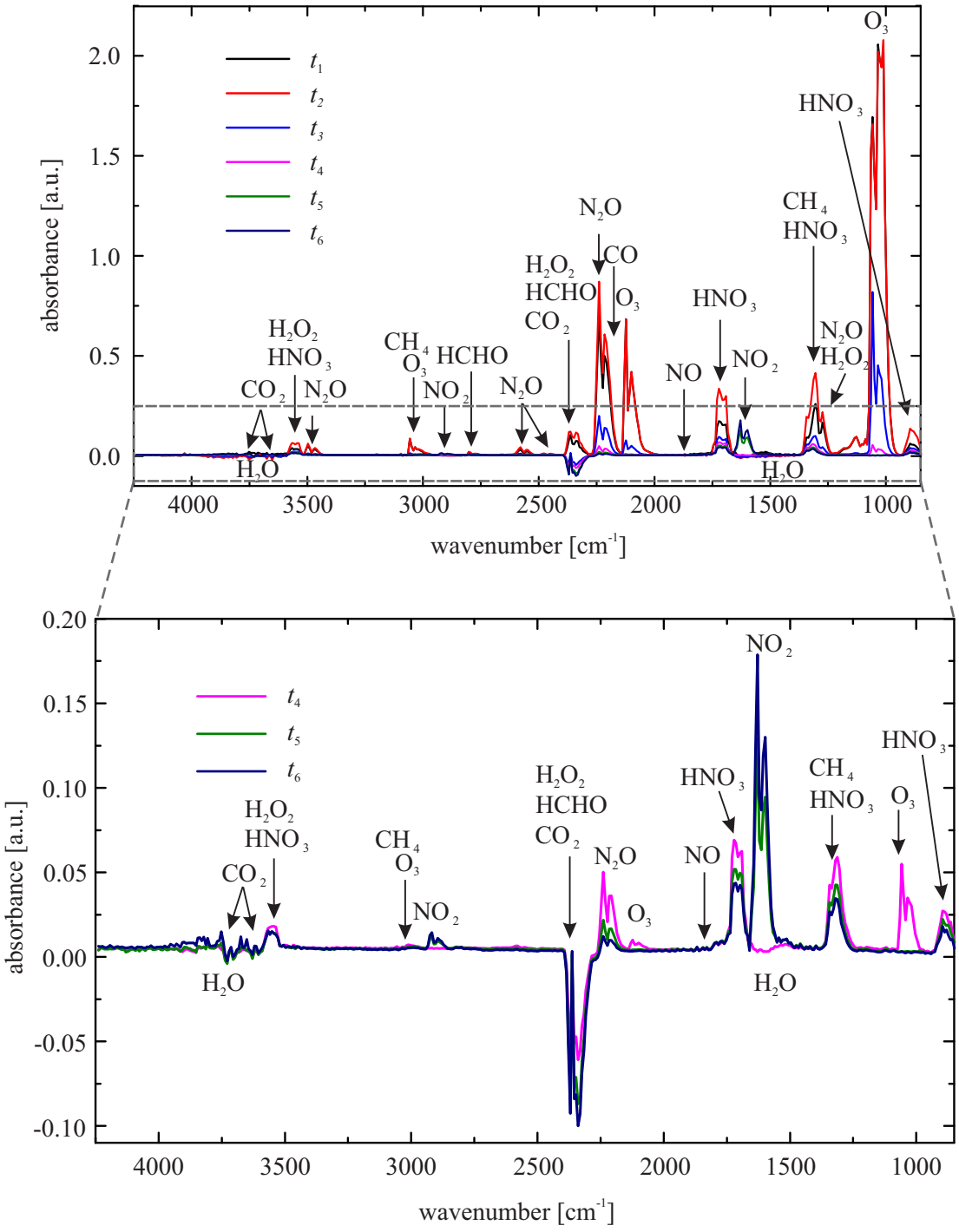

Figure 3.24: Absorption spectra of measurement 3 for the time points of $t_1 = 10.0\,\text{min}$, $t_2 = 19.9\,\text{min}$, $t_3 = 30.0\,\text{min}$, $t_4 = 39.0\,\text{min}$, $t_5 = 45.0\,\text{min}$, and $t_6 = 50.1\,\text{min}$ with a magnification of t_4, t_5 and t_6.

which occurs in the presence of atomic oxygen [186]. The influence of the plasma treatment to different materials is discussed in more detail in chapter 5. Hansen *et al.* [187] already reported an emission of CO_2 from polymers like polyethylene, polypropylene, polyimide and polysulfide under the influence of O atoms. Since the apparatus consists of PTFE and PFA (Perfluoroalkoxy alkanes) fittings and tubing, it could not be excluded that this materials were etched during the plasma ignition. Previous work from Pipa *et al.* [188] reported an increase of CO_2 during the operation of a atmospheric pressure plasma jet (APPJ). They assumed, that the additional amount of CO_2 is produced by the contact of the plasma with the plastic holder of the APPJ. Nevertheless, I assume that the presence of CO_2 could not explain the formation of NO_2. Furthermore, the data allows no identification of NO due to its low intensity and the presence of water in the apparatus (see chapter 2.4). The analysis of the subtracted spectra indicates, that HNO_3 is the only present long-living molecule when NO_2 was measured after the other reactive species were dissociated. Thus, the results suggest, that the presence of HNO_3 leads to a release of NO_2.

In conclusion, the investigations in this section emphasise, that the examination of the gas mixture after the plasma is switched-off, gives additional information. The results for different humidity conditions indicate, that HNO_3 is also generated for high humidity conditions and becomes detectable, when the humidity is decreased. Furthermore, the presence of HNO_3 is involved in the formation of NO_2, which is not detectable for high O_3 concentrations.

3.8 Quenching

The examination of the plasma afterglow composition shows, that the plasma afterglow circulation apparatus (PACA) operates in an ozone rich regime for the applied voltages and frequencies. In the following the reduction of the ozone concentration during plasma ignition (quenching) is described, which was detected for high ambient humidity conditions in the lab ($\sim 1.5\,\mathrm{vol\,\%}$). In previous studies, the observation of ozone quenching is often connected to the presence of NO_x molecules [15, 111, 133]. In the present work, the detected NO_x concentrations were low during the plasma ignition (for example in chapter 3.6). The following discussion of the ozone quenching contributes to the understanding of the involved chemical processes in the PACA.

The investigations were executed under high humidity conditions, using the humidifier and the treatment chamber of 2.6 l in the circulation system (see setup in Fig. 2.1). Furthermore, the plasma was ignited for seven consecutive measurements (m_i) with different treatment times t, named $m_1 - m_4$ ($t = 20\,\mathrm{min}$) and $m_5 - m_7$ ($t = 1\,\mathrm{h}$) using $U = 6,0\,\mathrm{kV_{pp}}$ and $f = 10\,\mathrm{kHz}$. The apparatus was not flushed by fresh air between the measurements, but the treatment chamber was opened for $2 - 5\,\mathrm{minutes}$. Consequently, the reactive species were exchanged by fresh air within the treatment chamber but remained present in the residual

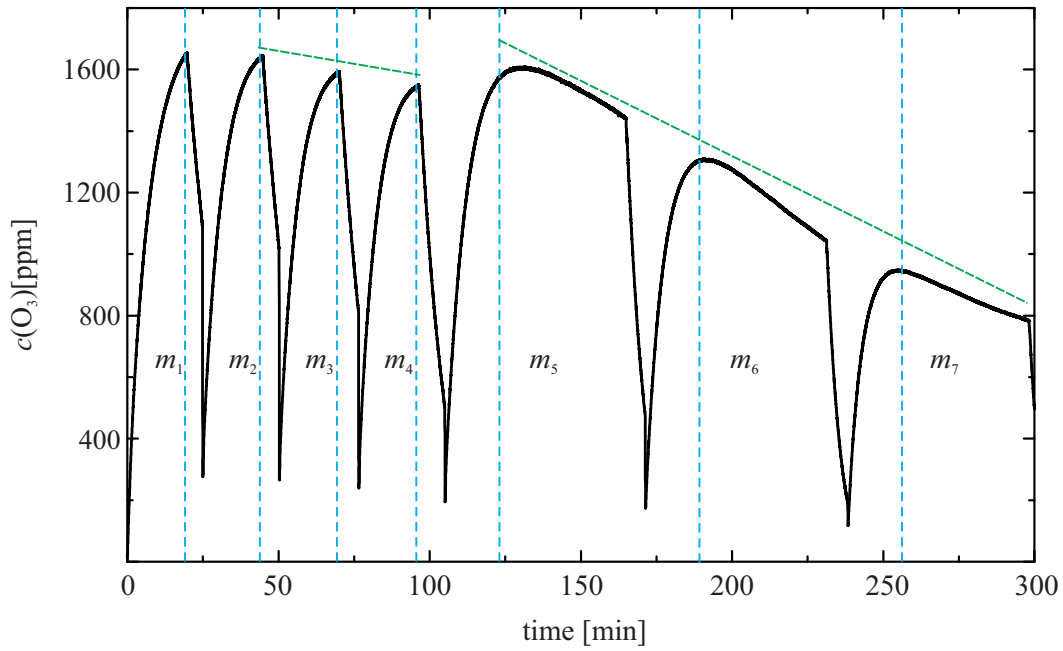

Figure 3.25: Illustration of an ozone quenching measured by UV absorption spectroscopy for seven consecutive measurements m_1 (20 min), m_2 (20 min), m_3 (20 min), m_4 (20 min), m_5 (60 min), m_6 (60 min) and m_7 (60 min).

volume. Fig. 3.25 illustrates the O_3 concentration for the seven consecutive measurements as a function of time. According to the diagram, the O_3 concentration is produced during plasma ignition, but shows an overall decease of the maximum ozone concentration (illustrated with green lines) for consecutive measurements ($m_1 - m_7$). In addition to the decrease of the maximal ozone production, $m_5 - m_7$ show a reduction of $c(O_3)$ during the plasma ignition, after the maximum was reached. Furthermore, the maximum of $c(O_3)$ for m_6 is below the minimal concentration for m_5 and the maximum for m_7 is below the minimal value of m_6. However, the observation of a strong decrease of the ozone production during plasma ignition contradicts the previous observations.

In former publications, the reduction of ozone (quenching) is often observed for an increased power consumption with a consequential increase of NO_x molecules [39, 111, 133]. The results in chapter 3.6 show, that the PACA operates in a power range, where mainly O_3 is produced and no reduction of ozone by an increase of the power is observed.

In the following, I thus discuss the power consumption and FTIR measurements to unambiguously identify the effect of ozone quenching. The monitored power consumption p of the circulation apparatus is displayed in Fig. 3.26 a) as a function of time. The diagram shows a different time axis as Fig. 3.25 to enable a better comparability of the consecutive measurements. Here, for $m_1 - m_7$ the time starts at $t = 0$ min. The data reveal a power maximum of 9.8 W for the first measurement m_1 which is explained by the removing of remaining precip-

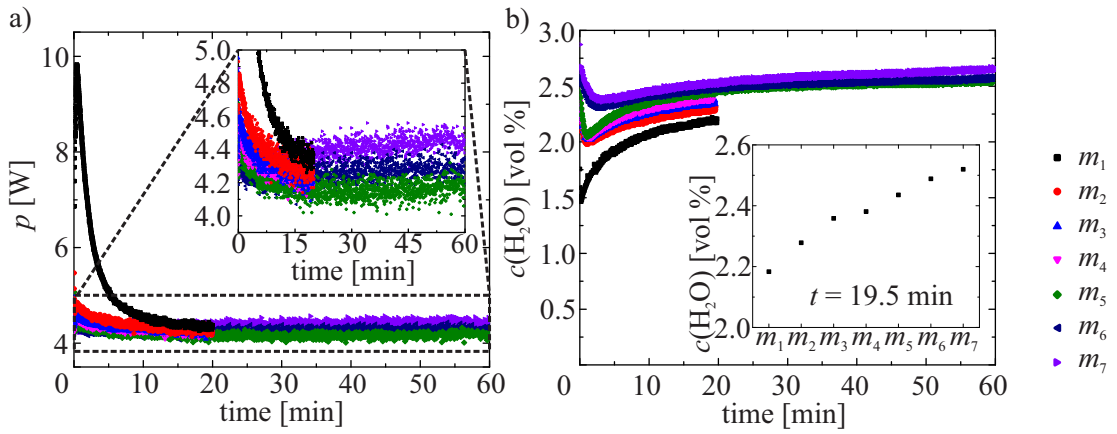

Figure 3.26: a) Power consumption during ozone quenching for seven consecutive measurements. b) FTIR measurement of the H_2O concentration during ozone quenching for seven consecutive measurements. Inset: Dependency of $m_1 - m_7$ to the H_2O condensation at $t = 19.5\,\text{min}$.

itates and water on the surface of the electrodes at the first ignition. This is also mentioned in chapter 3.6. The measurements $m_2 - m_7$ show a similar trend in the first minutes, while the power consumption varies between $p = 4.1 - 4.4\,\text{W}$ (at $t = 19.5\,\text{min}$) for $m_1 - m_7$. The inset in Fig. 3.26 a) depicts a slight deviation of the power measurement for m_5, m_6 and m_7 of maximal 0.2 W, while m_7 shows the highest and m_5 the lowest power consumption. This deviation of the power consumption for $m_5 - m_7$ could be explained by the increase of the humidity concentration for the consecutive measurements, which is discussed in Fig. 3.26 b). In conclusion, the power consumption is comparable for all measurements $m_1 - m_7$, but the ozone concentrations shows significant differences. This stays in contrast to the results of chapter 4.1.2, where $c(O_3) \sim p$. Consequently, the reduction of ozone could not be explained by the power consumption.

Fig. 3.26 b) depicts the detected H_2O concentration which was present during the investigations as a function of time. As can be seen from the inset in Fig. 3.26 b) for $t = 19.5\,\text{min}$, the H_2O concentration increases with the consecutive measurements. The increase of the absolute humidity is caused by an increase of the temperature in the lab (24.8 °C – 27.1°C), which leads to a rise of the temperature in the plasma apparatus and enables the circulating gas to take up more water molecules. The high temperatures in the lab leads to a maximum H_2O concentration of 2.65 vol % in the last measurement. The variation of the ozone production for measurements $m_1 - m_4$ is small and could be explained by the increasing amount of water in the circulating gas (see chapter 3.3 and 3.5). However, the trend of the ozone concentration of measurements $m_5 - m_7$ cannot be explained by the raise of the absolute humidity concentration, as the H_2O trend shows a similar distribution for $m_5 - m_7$. Additional FTIR observations of the time dependency for NO_2, N_2O and HNO_3 give no further insight to the O_3 quenching (time dependencies not shown). In detail, the concentrations of NO_2

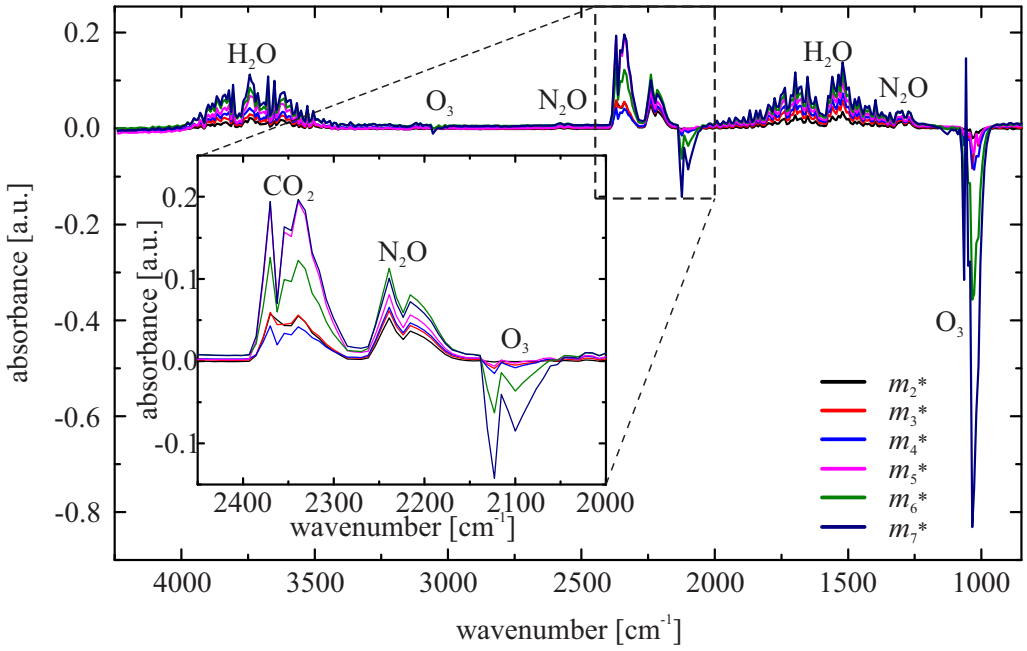

Figure 3.27: Subtracted FTIR absorption spectra, detected 19.5 min after the beginning of the plasma ignition (m_2^*, m_3^*, m_4^*, m_5^*, m_6^*, m_7^*). Inset: Magnification to analyse the CO_2, N_2O and O_3 absorption peaks.

and HNO_3 fluctuates below 1 ppm. The concentration of HCHO follows the same trend as O_3 and is explained by the assumption, that the formation of HCHO depends on the O_3 amount (see chapter 3.3).

The reduction of the ozone concentration shows an unexpected behavior, which cannot be explained by the variations of the humidity and the power consumption. Consequently, I investigate the FTIR absorption spectra to identify the production of reactive molecules which may reacts with ozone during the plasma ignition. Therefore, I analyse FTIR absorption spectra after 19.5 min (dotted line in Fig. 3.25) plasma ignition for each measurement. The absorption spectrum of m_1 after 19.5 min plasma ignition is used as a reference spectrum as no quenching effect is present in the first measurement. This reference spectrum is subtracted by the absorption spectra of m_2 to m_7, which are named m_2^* to m_7^*. This subtraction enables to identify changes in the FTIR spectra compared to the m_1 spectrum at $t = 19.5$ min, when no quenching was observable. The subtracted absorption spectra for $t = 19.5$ min are illustrated in Fig. 3.27. As already reported in Fig. 3.26 b), the absorption spectra illustrate an increase of H_2O for the consecutive measurements. This complicates the identification of additional species in this area. The inset of Fig. 3.27 and the absorption peak at ~ 1030 ppm illustrate the decreasing O_3 concentration for m_2^* to m_7^*. The N_2O peak shows a slight increase for all spectra, which is explained by the fact that m_1 was the initial plasma ignition, where lower N_2O values are possible. The increase of N_2O may occur due to the increased production of

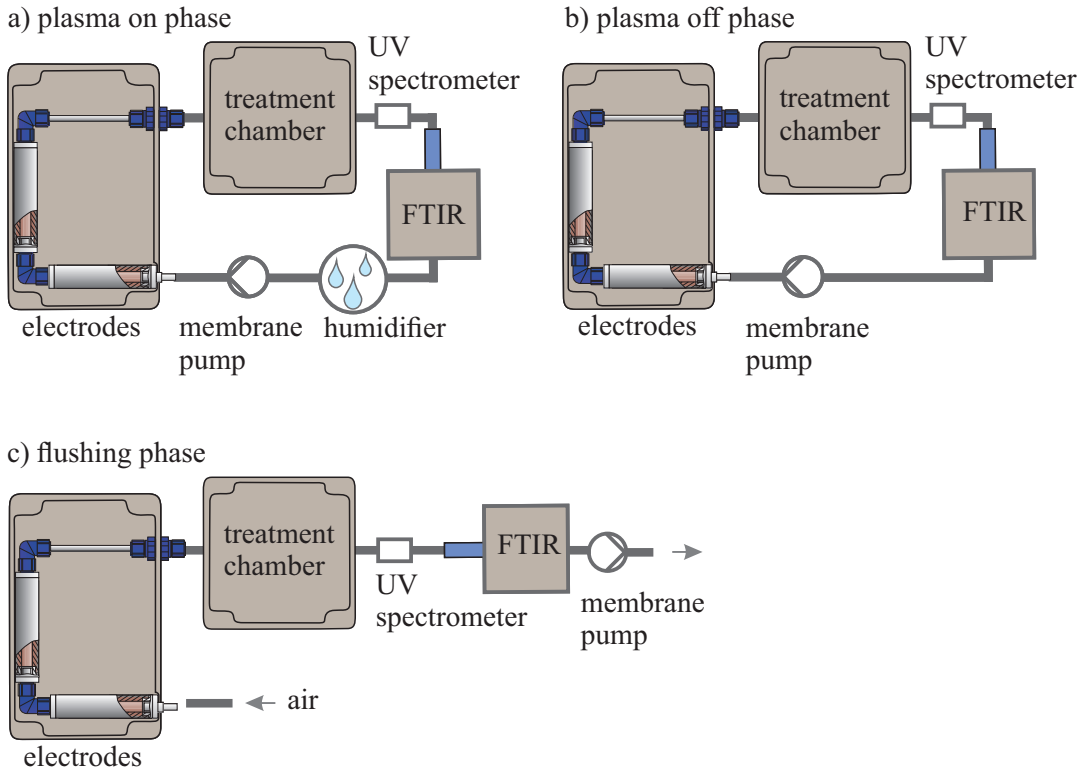

Figure 3.28: a) Closed setup of PACA during the plasma on phase, including humidifier. b) Closed setup of the plasma off phase after the plasma is switched-off and the humidifier is removed. c) Open PACA setup in the flushing phase with fresh air.

NO_2, as one major production process of N_2O is the reaction of NO_2 with N [150]

$$NO_2 + N \rightarrow N_2O + O. \tag{3.4}$$

Nevertheless, no NO_2 peak was visible during the plasma ignition, which could be due to the presence of ozone, as already reported in chapter 3.7. An additional variation is observed for the absorption peak in the region of $2300 - 2400\,\mathrm{cm}^{-1}$ but shows no significant dependency to the observed quenching process. As already mentioned in chapter 3.7, CO_2 can be observed in this wavenumber range. A possible raise of CO_2 could occur due to etching effects of polymers in the presence of atomic oxygen [186]. Furthermore, no additional afterglow components compared to m_1 ($t = 19.5\,\mathrm{min}$) could be identified, especially NO_2, NO and HNO_3 were not detected in the analysed spectra during the plasma on phase.

The measurements of the circulating afterglow composition during the plasma on phase show no clarifying trend to identify the reason for the ozone decrease. Because of this result, the plasma afterglow is analysed for m_7 for the time after the plasma is switched-off. After the measurement m_7 of the *plasma on* phase (see Fig. 3.28 a)), the setup was opened for $\sim 4\,\mathrm{min}$ to evacuate the treatment chamber. Afterwards, the treatment chamber was closed

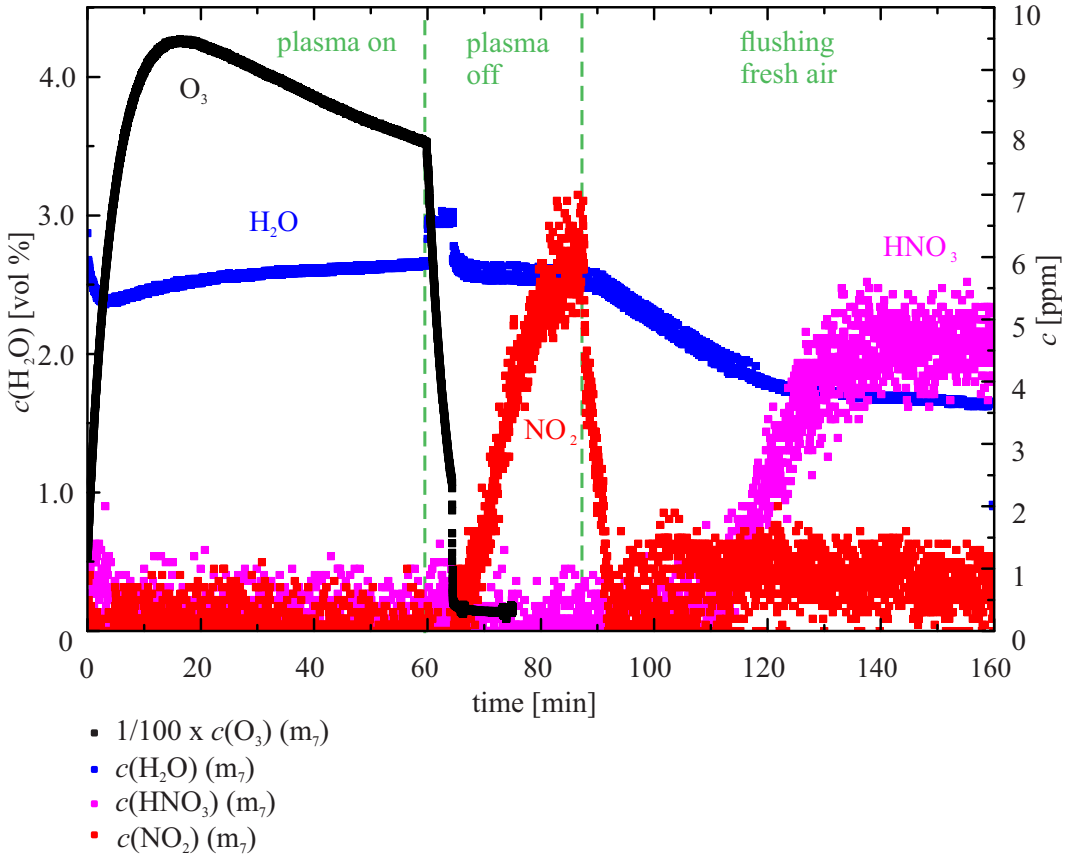

Figure 3.29: Analysis of the O_3, NO_2, H_2O and HNO_3 distribution during the phases of plasma on, plasma off and flushing phase for the measurement m_7. Note, that the O_3 concentration is divided by a factor of 100 to compare the O_3 concentration with the other components.

and the humidifier was removed to avoid additional humidity and the circulation of the gas was continued until $t = 88$ min. This phase is called *plasma off* phase (see Fig. 3.28 b)). At the time point of $t = 88$ min the apparatus was opened and flushed with fresh air until the end of the measurement. This phase is called *flushing phase* (see Fig. 3.28 c)).

Fig. 3.29 shows the H_2O, O_3, NO_2 and HNO_3 concentrations for measurement m_7 during the plasma on, plasma off and flushing phase. The data depict a NO_2 increase in the plasma off phase until the apparatus was flushed with fresh air at $t = 88$ min. The decrease in the flushing phase was detected because the reactive molecules were transported to the outside of the apparatus. Furthermore, the production of NO_2 is low, so that no increase of NO_2 could be detected in the flushing phase, when the apparatus is open. Fig. 3.29 indicates - as described in chapter 3.7 - that NO_2 becomes detectable, when the ozone concentration is negligible. The absence of NO_2 molecules by the presence of O_3 was already reported in previous work [148]. NO_2 is an important molecule which could lead to a reduction of O_3 (see chapter 1.7). The presence of NO_2 during the measurements explains the observed quenching of ozone. The presence of NO_2 in connection to HNO_3 is already described in chapter 3.7.

I assume that the increase of NO_2 after the plasma is switched-off is caused by remaining HNO_3, which is not detectable during the plasma on phase in m_7 and the plasma off phase. In Fig. 3.29, the observation of the humidity shows, that the H_2O concentration increases for the first 60 min when the humidifier was included in the setup. The increase of the humidity is caused by the adjustment to a state of equilibrium. Furthermore the temperature increases $\sim 1-2\,°C$ within 60 min resulting in an increased water capacity of the circulating gas. After $t = 60$ min the gas flow was switched-off and the treatment chamber was opened. The visible increase of H_2O for this time span of 4 min is a result of the interruption of the gas flow. It is remarkable, that the H_2O concentration remains at the high humidity level despite the fact that the treatment chamber was opened for 4 minutes. I assume, that the humidity in the apparatus was so high that the exchange of fresh air - in the opening procedure of the treatment chamber - was not enough to reduce the humidity in the setup. Finally, the humidity reduced to the value of ~ 1.6 vol % when the apparatus was flushed with fresh air. As the humidity decreases in the flushing phase, the concentration of HNO_3 starts to increase (up to $c(HNO_3) \sim 5$ ppm). This observation indicates that HNO_3 is condensed on the surface within the apparatus and released by reducing the humidity. Compared to chapter 3.7 ($c(HNO_3) > 60$ ppm), the detected HNO_3 concentration of 5 ppm was low. I assume that a lower amount of HNO_3 was released, because the humidity (~ 1.5 vol %) of the flushing air was higher than in the previous measurement. This leads to a reduced release of the HNO_3, so that a part of the molecules remained in the apparatus in the liquid phase.

In conclusion, the plasma afterglow analysis during the plasma on phase reveals no additional insights to explain the observed ozone quenching. In addition, the observation of the power consumption and humidity concentration showed no significant variations. However, the analysis of the plasma off phase point out, that a NO_2 source exists in the apparatus. The increase of NO_2 during plasma ignition increases the dissociation of O_3 (quenching). This NO_2 increase cannot be detected directly during plasma ignition, as NO_2 reacts fast and is not detectable when O_3 is present in the apparatus [148]. The increase of NO_2 after plasma ignition is explained by an accumulation of HNO_3 which is condensed on the surface within the apparatus and is not detectable in this condition. This theory is supported by the results of the flushing phase, which showed an increase of HNO_3 when the apparatus was flushed by ambient air. Thus, the HNO_3 amount is accumulated with each plasma ignition, which also increases the NO_2 molecules in the condensed water-acid film, which causes the reduction of O_3. The solved HNO_3 cannot be removed by flushing with ambient air, since the humidity was to high to release HNO_3 in the gaseous state.

These results emphasise, that the circulation of reactive molecules under high humidity conditions could lead to residual components within the plasma apparatus. To some extent, these residuals could influence the plasma composition itself, therefore an appropriate cleaning of the circulation apparatus is necessary (for example with dry gases). Furthermore the control

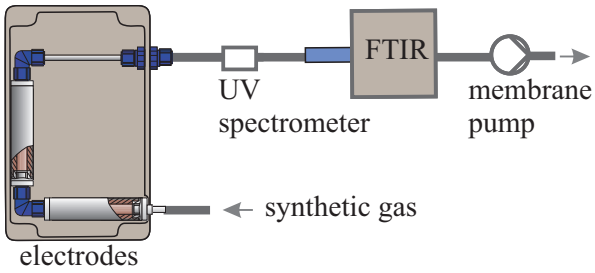

Figure 3.30: Flushing of the open PACA using synthetic gas.

of the power consumption and a monitoring of the plasma components is necessary to screen the status of the apparatus.

3.9 FTIR Measurements with Artificial Gases

In the previous chapters, the afterglow composition was analysed for ambient air under ambient or high humidity conditions. The presence of the water bonds prohibits the identification of small absorption peaks in the regions of the water bonds. Since the PACA is a closed apparatus, the design allows the use of different gas mixtures in addition to ambient air. In this chapter, synthetic air (Linde: $O_2 = 20\,\%$, $N_2 = 80\,\%$ N_2, $H_2O \leq 2\,\text{ppm}$ $CO_2 \leq 1\,\text{ppm}$, $CO \leq 1\,\text{ppm}$), is used to measure the afterglow composition for minimal humidity conditions and to reduce the water bonds in the spectrum. Previous studies already showed, that the reactive species of the afterglow depend on the carrier gas and the chosen gas mixture for the plasma ignition [189, 190]. In order to gain insights into the plasma chemistry, investigations with different synthetic gases were executed. In addition to synthetic air, the apparatus was flushed by nitrogen (N_2 5.0 Linde: $O_2 \leq 3\,\text{ppm}$, $H_2O \leq 5\,\text{ppm}$) and argon (Ar 5.0 Linde: $N_2 \leq 5\,\text{ppm}$, $O_2 \leq 2\,\text{ppm}$, $H_2O \leq 3\,\text{ppm}$).

3.9.1 Synthetic Air

The first investigations were executed with synthetic air and without treatment chamber in the setup. For these measurements, the plasma parameters $U = 6.0\,\text{kV}_\text{pp}$ and $f = 10\,\text{kHz}$ were used. To avoid the detection of residual components which are caused by former plasma treatments (discussed in chapter 3.8), the apparatus was rebuilt with clean components. Afterwards, the apparatus was flushed by synthetic air until the H_2O concentration decreased to a minimal level ($\sim 0.05\,\text{vol}\,\%$). Fig. 3.30 illustrates the flushing of the apparatus with an artificial gas. The open system enables the synthetic gas to enter the apparatus on the side of the electrode and to flow through all components until the gas is released afterwards. After the humidity in the PACA decreased to a minimum, the apparatus was closed and the gas flow and plasma were switched-on.

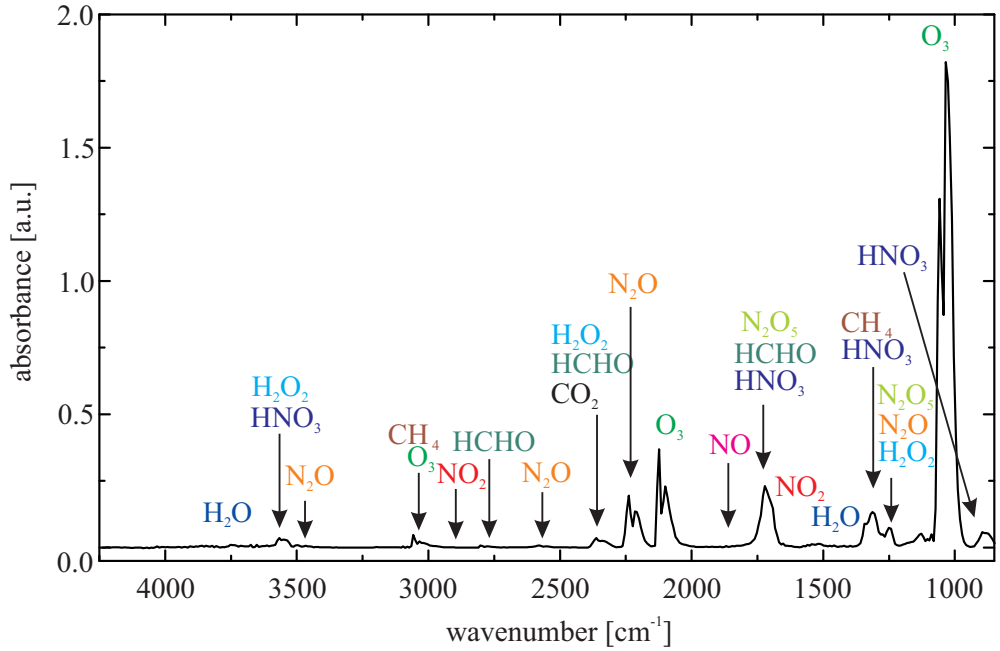

Figure 3.31: FTIR absorption spectrum of the afterglow composition using synthetic air (80 % N_2, 20 % O_2) after 0.5 min plasma ignition.

For synthetic air, the measurement were repeated three times. Fig. 3.31 illustrates an exemplary absorption spectrum of one of the measurements using synthetic air after 0.5 min plasma ignition. To further decrease the H_2O absorption peaks the spectrum was subtracted by a reference spectrum of $t = 0$ min. According to the diagram, no additional reactive species could be identified by the software Calcmet compared to the absorption spectra of the afterglow for ambient air conditions (see Fig. 2.5 in chapter 2.4). The increased absorption peak at 1700 cm^{-1} and the absorption peak at 1250 cm^{-1} could be a sign for the formation of N_2O_5 and H_2O_2. Due to the reduction of H_2O by the use of synthetic gas I assume that H_2O_2 plays a minor role.

The time dependency of an exemplary measurement with synthetic air is illustrated in Fig. 3.32. Here, the plasma was ignited for 1.7 min and the gas flow was continued afterwards. The diagram shows the concentrations of NO_2, N_2O, HNO_3 and HCHO, which were measured by the FTIR. The illustrated O_3 is divided by a factor of 40, to compare the O_3 concentration with the other molecule concentrations. Fig. 3.32 shows an increase of O_3, N_2O, HNO_3 and HCHO when the plasma is on ($t < 1.7$ min). The production of these reactive molecules is comparable to the results of ambient air (for example in Fig. 3.15). In addition, Fig. 3.32 shows a stable behavior for O_3, HCHO and N_2O after the plasma is switched-off, while HNO_3 decreases fast. Furthermore, the concentration of NO_2 is negligible. A remarkable result is that HNO_3 is still produced for conditions with a small humidity in the apparatus. I assume, that enough H_2O is present to form OH molecules, which are important for the formation of

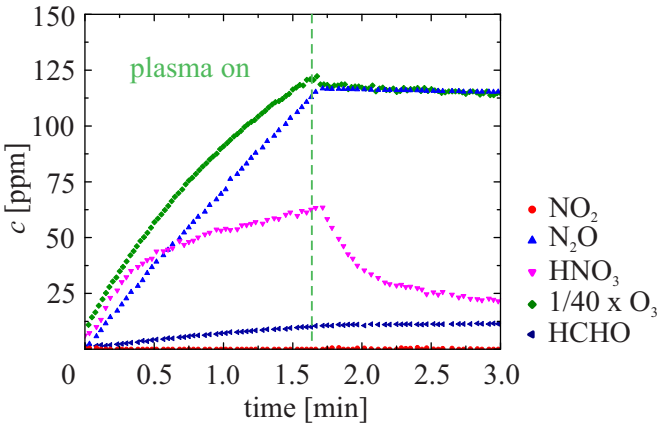

Figure 3.32: Analysis of O_3, NO_2, N_2O, HNO_3 and HCHO for an afterglow measurement after flushing the apparatus with synthetic air, during (< 1.7 min) and after (> 1.7 min) the plasma on phase. The $c(O_3)$ is divided by a factor of 40, to compare the O_3 concentration with the other molecule concentrations.

HNO_3.

3.9.2 Nitrogen

To examine the influence of the variation of the carrier gas composition to the production of the reactive species, the apparatus was flushed with a carrier gas (here N_2 gas) until the humidity decreased to a minimal level (~ 0.05 vol %). The experiments were executed without treatment chamber in the setup. For nitrogen, the parameter for the plasma ignition were $U = 5.9\,\mathrm{kV_{pp}}$ and $f = 10\,\mathrm{kHz}$ and the plasma was ignited for 0.5 min.

Fig. 3.33 shows the absorption spectra after 0.5 min plasma using synthetic air (black), nitrogen (red) and argon (blue). The illustrated spectra were subtracted by a spectrum before the plasma treatment to minimise the H_2O absorption bonds. Note, that the absorption spectrum of argon is discussed in the next section 3.9.3. The analysis of the absorption peaks enables to identify differences in the absorption spectra for the different conditions. The magnified spectra for nitrogen and argon are shown in red and blue, while the absorption spectrum of synthetic air is shown as a dotted black line.

For a high amount of nitrogen as a carrier gas, the diagram reveals the detection of NO_2 and the absence of O_3. This observation is in contrast to the results of synthetic air, where NO_2 is absent and ozone is the dominant molecule. With an increase of N_2 molecules in the gas and thus a reduction of O_2 molecules the production of NO_2 and N_2O becomes more favourable. This results supports the previous investigations from Jeon *et al.* [189], which showed an decrease of the ozone production by the decrease of the O_2 amount in the gas mixture. This trend was explained by the increase of quenching mechanisms when the amount of N_2 is increased. Furthermore, the presence of N_2O and NO_2 supports the

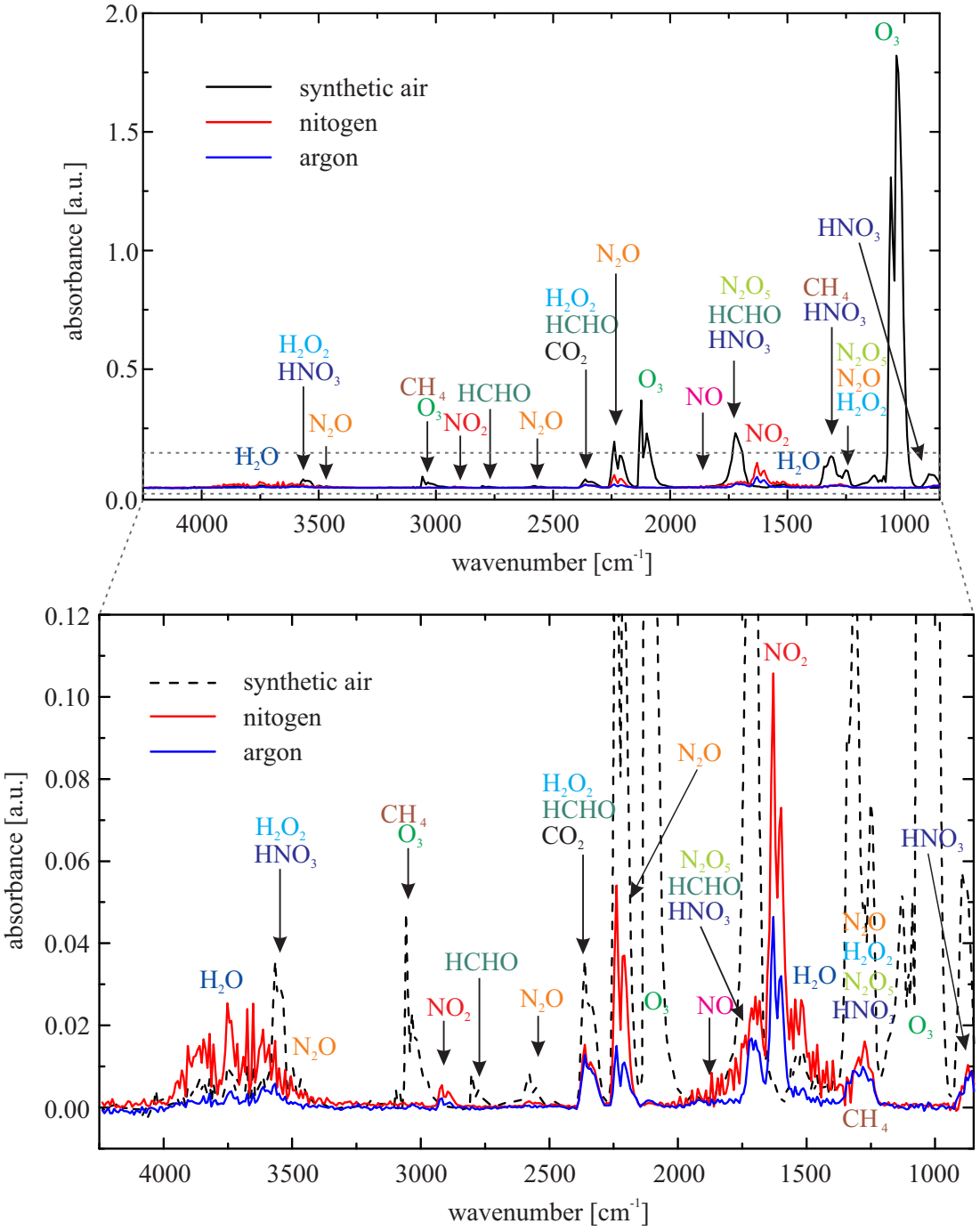

Figure 3.33: FTIR absorption spectra of the afterglow composition for different carrier gases (synthetic air, nitrogen, argon) after 0.5 min plasma ignition.

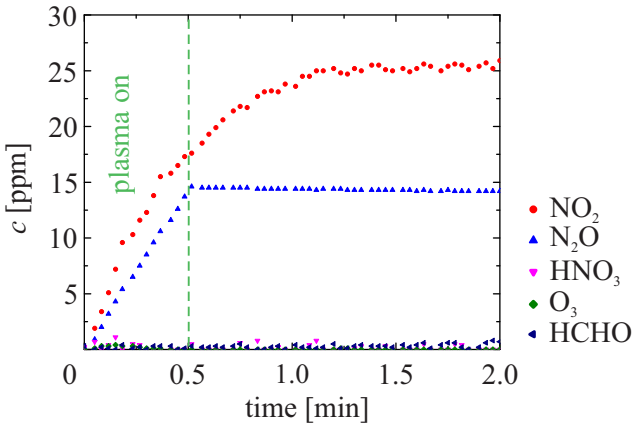

Figure 3.34: Analysis of O_3, NO_2, N_2O, HNO_3 and HCHO for an afterglow measurement after flushing the apparatus with N_2, during (< 0.5 min) and after (> 0.5 min) the plasma on phase.

assumption in chapter 3.5, that the formation N_2O may occur due to the production of NO_2, as one major production process of N_2O is the reaction of NO_2 with N ($NO_2 + N \rightarrow N_2O + O$) [150]. Furthermore, the absorption spectra depict the presence of HNO_3 absorption peaks during the plasma ignition. The presence of HNO_3 is comprehensible, since NO_2 and a small amount of H_2O are present. Similar to the previous measurements, the presence of NO could not be detected. I assume that NO reacts fast with other molecules, so that is could not be measured by the FTIR. The analysis of the afterglow cocktail using a high amount of nitrogen shows, that the composition of the reactive species could be changed by a variation of the carrier gas in the apparatus.

In addition, the time dependency of the reactive species were analysed for three different measurements. Fig. 3.34 shows an exemplary time dependency of the species of one of the measurements using N_2 as a flushing gas. The plasma is on for 0.5 min and the gas flow was continued afterwards. The time dependency of the reactive species demonstrates, that the production of O_3 by the plasma on phase is negligible for a high amount of N_2.

A remarkable observation is, that the concentration of NO_2 increases for $0.2 - 0.5$ min after the plasma is switched-off. Similar to chapter 3.7 and 3.8, there has to be a source for the NO_2 formation after the plasma is switched-off. On the other hand, it is possible that the generation process of NO_2 continue for a certain time after the plasma is switched-off. Due to the absence of O_3, the reaction of NO with O_3 to NO_2 could not explain the observation. It is thinkable, that vibrationally excited nitrogen molecules reacting with O atoms as described by Shimzu *et al.* [111]. To prove this theory, further investigations are needed. In addition, Fig. 3.34 shows that the Calcmet software only calculated a small amount of HNO_3, but HNO_3 is visible in Fig. 3.33. These results indicate, that HNO_3 is present under these conditions, which would explain the formation of NO_2 after the plasma is switched-off. Note, that no ozone is detected in the PACA which would react with NO_2 and may reduces the amount of

NO_2.

Nevertheless, the concentration of HNO_3 compared to NO_2 is low. However, one of the dominant production processes of HNO_3 is [138]

$$NO_2 + OH + M \rightarrow HNO_3 + M. \tag{3.5}$$

Since NO_2 is present in the afterglow, the amount of OH is probably reduced by a reduction of oxygen in the gas. With a reduction of oxygen the following reactions are also reduced [138]

$$O(^1D) + H_2O \rightarrow OH + OH \tag{3.6}$$

$$O_3 + H \rightarrow OH + O_2. \tag{3.7}$$

3.9.3 Argon

In addition to the investigation using synthetic air and nitrogen, the afterglow composition is analysed for the noble gas argon. As described before, the apparatus was flushed by argon gas until the humidity were decreased to a minimal level ($\sim 0.05\,\mathrm{vol}\,\%$). The parameters for the plasma ignition were reduced to $U = 5.0\,\mathrm{kV_{pp}}$ and $f = 6\,\mathrm{kHz}$ and the plasma was ignited for 0.5 min without treatment chamber in the system. This decrease of the parameters was necessary, as the breakdown voltage of argon is lower than for N_2 [39], which could harm the amplifier otherwise.

Fig. 3.33 shows an exemplary absorption spectrum for the use of argon to compare the afterglow composition with the measurements using synthetic gas and nitrogen. As already described for nitrogen and synthetic air, the absorption spectrum was detected after 0.5 min plasma ignition and was subtracted by a reference spectrum for $t = 0\,\mathrm{min}$. Similar to the use of nitrogen, the argon absorption spectrum reveals the observation of NO_2 and the negligible amount of O_3 for argon. The afterglow composition shows mostly reactive nitrogen species and only a low concentration of O_3. Although argon is the major molecule in the circulating gas, NO_2, HNO_3 and N_2O molecules are mainly produced by the plasma ignition. By flushing the apparatus with argon, the concentrations of N_2 and O_2 are both reduced. I thus assume, that the total amount of O_2 is important for the O_3 dominant mode and not only the relation between N_2 and O_2. Another explanation for the absence of O_3 could be the increased electron density under the presence of argon due to the reduction of electron loss processes. The increase of the electron density may lead to a transformation from the O_3 rich to the NO_x dominated mode (see chapter 1.7).

Similar to the investigations using nitrogen, the time dependency of the reactive species was analysed for three different measurements. Fig. 3.35 shows an exemplary time dependency of the species of one of the measurements using argon as a flushing gas. The plasma is ignited

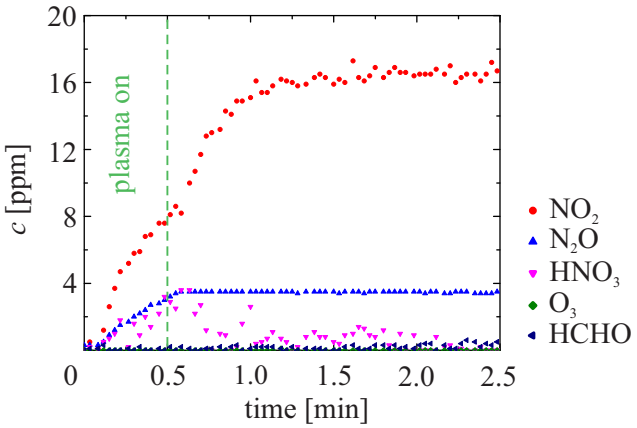

Figure 3.35: Analysis of O_3, NO_2, N_2O, HNO_3 and HCHO for an afterglow measurement after flushing the apparatus with argon, during (< 0.5 min) and after (> 0.5 min) the plasma on phase.

for 0.5 min and the gas flow was continued afterwards. The measured H_2O concentration is not shown, but the H_2O concentration varies between 0.05 vol % and 0.20 vol % within 2.5 min observation time. The time dependency of the afterglow composition shows a linear increase of NO_2, N_2O and HNO_3 during the plasma ignition, while HCHO and O_3 are absent. The N_2O concentration is constant after the plasma is extincted and the HNO_3 concentration decreases. Similar to Fig. 3.34, the NO_2 concentration increases up to $\sim$ 16 ppm after the plasma is switched-off. I assume that the source for the NO_2 production could relate to the presence of HNO_3 in the apparatus as already discussed in chapter 3.7 and 3.8. An other theory is that vibrationally excited nitrogen could cause the formation of NO_2, which could not be measured in our analysis.

3.9.4 Power Consumption for Different Gases

Fig. 3.36 shows the power consumption of the measurements using synthetic air, nitrogen and argon as a function of time. The data present mean values of at least three measurements for 0.5 min. For nitrogen ($U = 5.9\,\mathrm{kV_{pp}}$, $f = 10\,\mathrm{kHz}$), the power consumption starts on a similar value as synthetic air ($U = 6.0\,\mathrm{kV_{pp}}$, $f = 10\,\mathrm{kHz}$), but stays constant during the measurement. In contrast to nitrogen, the power consumption of synthetic air shows a slight decrease during the measurement. The power consumption of argon shows a higher power consumption with a constant trend for $U = 5.0\,\mathrm{kV_{pp}}$ and $f = 6\,\mathrm{kHz}$. The high power consumption is caused by the fact that the breakdown voltage of argon is lower than for N_2. The different gas mixture causes a difference in the plasma ignition, so that the electrode temperature for synthetic air increases during the measurement. This temperature increase could lead to the decrease of the power consumption. An other explanation for the decrease of the power consumption could be the high amounts of O_3 in the PACA, which influences the power consumption of

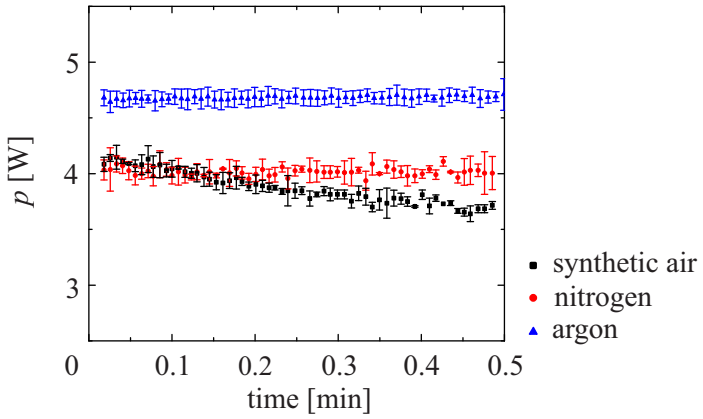

Figure 3.36: Power consumption for different gases (synthetic gas, nitrogen and argon) for 0.5 min plasma ignition.

the electrode. Further investigations have to be executed to understand the interaction of the afterglow composition with the power consumption.

3.9.5 Conclusion of FTIR Measurements with Artificial Gases

The investigations using synthetic air, reveal no additional reactive species in the afterglow during the plasma ignitions. It was not possible to identify NO and NO_2 during plasma ignition, although the absorption bonds of H_2O were smaller than under high humidity conditions. The results demonstrate that HNO_3 is also produced under low humidity conditions. The presence of HNO_3 and N_2O gives a hint, that NO and NO_2 react fast to form other molecules. The experiments with nitrogen and argon depict a negligible ozone production, while NO_2 becomes the major reactive molecule in the afterglow. The investigations using argon in the apparatus decrease the amount of O_2 and N_2 in the same relation. These experiments indicate, that not only the relation of O_2 and N_2 is important for the afterglow production, but also the absolute concentrations of oxygen and nitrogen.

In total, the investigations show, that the plasma composition of the PACA could be controlled by the variation of the carrier gas in the system. This is an important step for future applications of the PACA, where other gas compositions are in the research focus. The microbiological investigations of the inactivation efficiency of the PACA in this work is done for ambient air, as this technology provides a cost efficient treatment without the use of artificial gas mixtures.

3.10 Summary

In the presented chapter, the afterglow composition was characterised by investigating the ozone distribution, the humidifier influence, the gas flow rate, the humidity condition and the

power consumption. Furthermore, the detection of HNO_3, NO_2 molecules and ozone quenching were analysed, as well as the use of different carrier gases. In general, the spectroscopic investigations identify O_3, N_2O, NO_2, HCHO and HNO_3 in the circulating afterglow in dependence on the used condition. The concentrations of H_2O_2, HNO_2, NO and N_2O_5 could not be quantitatively measured by the FTIR. Note, that the generation of CO_2 and HCHO in some measurements indicates a release of C atoms from polymer materials by the plasma.

The analysis of the ozone concentration shows a peak at the electrode outlet and a homogeneous ozone distribution for the remaining PACA. Furthermore, the use of the FTIR reduces the total O_3 concentration by increasing the PACA volume and causes a dissolving of ozone molecules in the humidifier water by an increased gas temperature. In general, the FTIR does not influence the gas composition.

Additional investigations indicate that N_2O, O_3 and HCHO are negligible dissolved, while HNO_3, NO_2 and N_2O_5 are dissolved in the humidifier water. However, H_2O_2 could not be identified in the measurements.

The afterglow composition was analysed in dependence to the gas flow rate for ambient and high humidity conditions. For both humidity conditions, O_3, N_2O and HCHO increase by the reduction of the flow rate, which is explained by the decrease of recombination processes and by the increase of the plasma residence time. NO_2 and HNO_3 show no clear dependency to the gas flow rate.

Further investigations reveal a dependency of the power consumption and the afterglow composition to the humidity conditions. In detail, the O_3, HCHO and N_2O concentrations are inverse proportional to the humidity concentration, due to the change of the chemical pathways. Furthermore, the HNO_3 concentration decreases for an increasing humidity caused by condensation formation. This assumption is supported by the observation of HNO_3 release with a reduction of the gas humidity after the plasma treatment.

The variation ot the power consumption demonstrates the proportionality of the O_3, N_2O, HCHO and HNO_3 concentration to the power consumption for both humidity conditions. The results emphasise that the PACA is operating in the ozone rich regime with a minor production of NO_x molecules. In general, the power consumption shows also a dependency on the ambient conditions. For the microbial and material investigations in chapter 4 and 5, the spectroscopic results suggest the maximal power consumption for the afterglow treatment.

Furthermore, some of the investigations show the increase of NO_2 after the ozone dissociation and plasma extinction. This NO_2 formation cannot origin from NO and OH, but from reactions with long-living HNO_3. Consecutive observations reveal that an accumulation of HNO_3 in the PACA increases the formation of NO_2 to that extend, that a quenching of ozone is observable.

Finally the gas composition was analysed for different carrier gases. The measurements using synthetic air confirm the production of O_3, N_2O, HCHO and HNO_3 and the generation

of N_2O_5. The use of nitrogen and argon leads to a change of the afterglow composition. In detail, the O_3 and HNO_3 formation reduces, while the generation of NO_2 increases.

The results of the spectroscopic analysis provide a detailed characterisation of the PACA and improve the understanding of the time evolution and the interaction processes of the afterglow species for different conditions.

Chapter 4

Inactivation of Bacterial Endospores

To use the plasma afterglow circulation apparatus (PACA) as an alternative sterilisation method for spacecraft equipment, the efficacy of the sporicidal inactivation was analysed. In detail, the inactivation efficiency for different treatment volumes was investigated to treat components of different sizes. Furthermore, the homogeneity of the treatment in the treatment chamber and the use of 3D objects as barriers for the afterglow were performed. Finally, SEM microscopy was used to analyse the shape of the treated and untreated endospores. Some of the figures and parts of the text in this chapter have been published in M. Müller, T. Shimizu, S. Binder, P. Rettberg, J.L. Zimmermann, G.E. Morfill and H.Thomas, *Plasma afterglow circulation apparatus for decontamination of spacecraft equipment*, AIP Advances **8**, 105013 (2018) [14]. In addition, parts of the investigation of homogeneity and 3D objects were performed and supervised in the framework of the Master thesis "*Plasma Sterilization for Space Applications*" by Alisa Schmidt (Justus-Liebig-Universität Giessen) [191].

4.1 Investigations of Different Treatment Volumes

In order to evaluate the PACA as a useful decontamination apparatus for planetary protection applications, it is crucial to enable a treatment of large objects. In this section the PACA inactivation efficiency is investigated for different treatment chamber volumes.

4.1.1 Materials and Methods - SIMICON

In the following investigations, the PACA is used at ambient air with the humidifier and different treatment chamber volumes of 0.54 l, 1,8 l and 2.6 l in the circle, as shown in Fig. 4.1.

For the ozone measurements in different treatment volumes the UV absorption spectrometer was installed at the treatment chamber. Furthermore, the FTIR was not included in

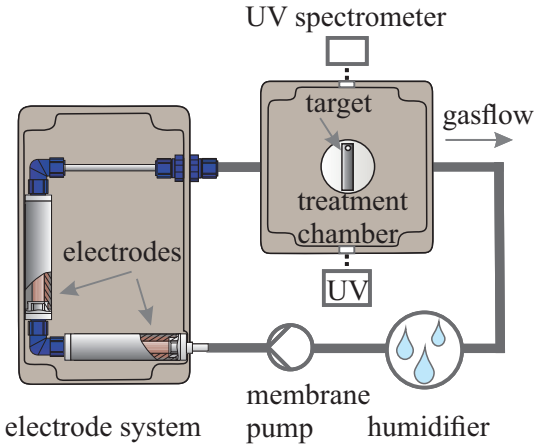

Figure 4.1: Setup of the PACA for the inactivation of bacterial endospores in different treatment volumes of 0.54 l, 1.8 l and 2.6 l.

the circulation system for the investigations. Note, that the investigations in this chapter 4.1 were executed in the laboratories and with an electrode system of terraplasma GmbH. The remaining investigations were executed at the DLR-laboratories with a new build electrode system, made of similar components. For the investigations in this chapter we purchased bacterial endospores *Bacillus atrophaeus* spores ATCC 9372 dried on stainless steel plates (V4A) of 30 x 5 mm^2. These endospores were used as biological indicators with an initial number of spores $N_0 \sim 10^6$ cfu/target (cfu: colony forming units). The biological indicators were produced and packed in Tyvek for storage by SIMICON GmbH (Munich, Germany).

The plasma treatment and the microbiological evaluation protocol are presented as follows:

1. The apparatus was activated for 20 min before the CAP treatment to stabilize the electrode temperature, the concentration of reactive species and humidity in the system. The gas flow rate was 3.5 l/min and the relative humidity in the system about 90 %. Note, that the CAP was already produced in this heat-up preparation of the electrodes.

2. After the heating phase of 20 min, the pump and the plasma were switched-off and the treatment chamber was opened, so that the reactive gas of the treatment chamber exchanged with the environmental air. The residue reactive species remained in the tubes of the apparatus. Afterwards, the biological samples were placed on the bottom in the middle of the treatment chamber before the treatment chamber was closed.

3. The samples were treated by the SMD plasma gas ($f = 10\,\mathrm{kHz}$, $U = 6.4\,\mathrm{kV_{pp}}$) for the chosen treatment time without Tyvek. The treatment times for the 0.54 l treatment chamber were 2.5, 5.0, 7.5 and 10 minutes, for the 1.8 l chamber 2.5, 5.0, 7.5, 15 and 20 minutes and for the 2.6 l chamber 2.5, 5.0, 10, 15, 20 and 30 minutes. When the plasma treatment was started, the pump was switched-on again.

4. After the plasma treatment, plasma and gas flow were switched-off and the samples were transferred into 15 ml centrifuge tubes filled with 5 ml highly purified water (Ampuwa, Fresenius Kabi AG, Germany).

5. The samples were washed out using a vortex mixer for 1 min, an ultra-sonic bath for 30 min, a vortex mixer for 1 min, an ultra-sonic bath for 15 min and again a vortex mixer for 1 min.

6. Another 5 ml of highly purified water was added to the tubes and a dilution series up to $1{:}10^4$ was prepared. 100 µl of each suspension was plated on Müller-Hinton (OXOID, Germany) agar plates and incubated overnight at 37 °C.

7. In parallel to 6., the rest of the suspension was filtered using a membrane filter (0.47 m, Merck KGaA, Germany). The filter was incubated on Müller-Hinton agar plates overnight at 37 °C. By this procedure, the inactivation of spores up to 6 log could be proven.

8. At least nine spore samples were treated to obtain one data point. The measurements for one data point were performed at least on three different days. For each data point, three control samples without any treatment were used to determine the initial number of spores N_0 which were deposited on the stainless steel surface. To determine the number N_0 of cfu of the control samples, three untreated samples were transferred into separate centrifuge tubes and the microbiological protocol was executed (4,5,6,7).

9. By counting cfu on each agar plate, the number of living spores after the plasma treatment N and untreated controls N_0 were estimated. Furthermore, the survival rate is given by N/N_0.

The error bars for the investigation of the inactivation were calculated using error propagation with standard deviations of the measurement series. They are presented only upwards to improve the readability of the semi logarithmic view. For the discussion of some of the results we calculated the log reduction $\log(N_0/N)$, which referred to the inactivation of *Bacillus* in orders of magnitude. A reduction of ~ 6 log corresponds to the complete inactivation of all bacteria within the available measurement range with these spore samples. The treatment time for a 6 log reduction can be used to calculate the treatment time for a 12 log reduction (overkill procedure) [192]. The bioburden on the target is considered zero after applying the overkill procedure [33].

4.1.2 Plasma Power

I already mentioned that the used electrode system to investigate the inactivation efficiency in difference treatment volumes differs slightly from the remaining measurements. This electrode system operated with $U = 6.4\,\mathrm{kV_{pp}}$ instead of $U = 6.0\,\mathrm{kV_{pp}}$. Therefore, the power consumption of the electrode is shown here in addition to the results in chapter 3.

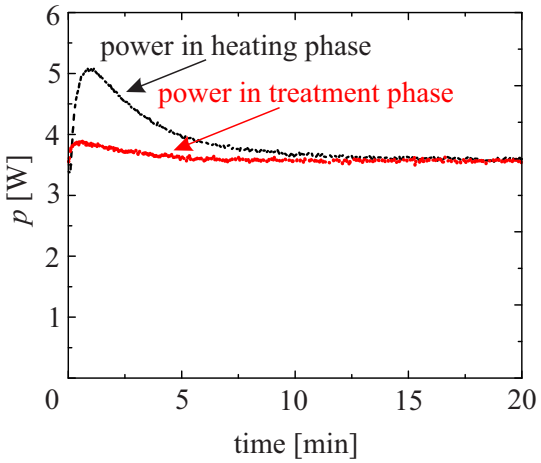

Figure 4.2: Dissipated plasma power in the heating phase (black line). Dissipated plasma power in the treatment phase (red line).

Fig. 4.2 shows the electrodes power consumption measured for a plasma treatment using the 1.8 l treatment chamber as a function of time. The black line shows the heat-up phase, where the plasma ignition removes remaining precipitates and water on the surface of the electrodes. This removal of precipitates leads to a rapid increase of the power consumption in the first minute. The rise of the electrode temperature induces the subsequent decrease of the power consumption after 1 min. Furthermore, Fig. 4.2 shows the power consumption of a treatment phase (red line), when the electrode is already heated up. The plasma is switched-off for $\sim$5 min between the different phases to put in the spore samples. The first increase of the power consumption is lower in the treatment phase than in the heating phase. In both cases, the power consumption reaches the threshold value 3.5 W after 20 min. The results illustrate that it is important to include a 20 min heating phase to achieve reproducible results. Therefore, the electrode system was always heated up for 20 min for all measurements in chapter 4 and 5.

4.1.3 Inactivation Efficiency for Different Humidity Conditions

The design of the PACA allows the plasma afterglow treatment under high humidity conditions, as already mentioned in chapter 2.1. As previous studies [115, 120] showed an increased microbial inactivation for high humidity conditions, this effect was investigated for *B. atrophaeus* in the 2.6 l treatment chamber. For the investigations, SIMICON samples were treated with a reduced number of spores $N_0 \sim 10^5$ cfu/target, which allows a detection limit of $N/N_0 \sim 10^{-5}$. Note, that for these investigations, the microbial evaluation protocol of chapter 4.2.1 was used and the setup of Fig 2.1.

Fig. 4.3 illustrates the survival rates N/N_0 after the treatment times of 10 min and 20 min for relative humidity conditions of 27 % and 90 %. The data show mean values of at least

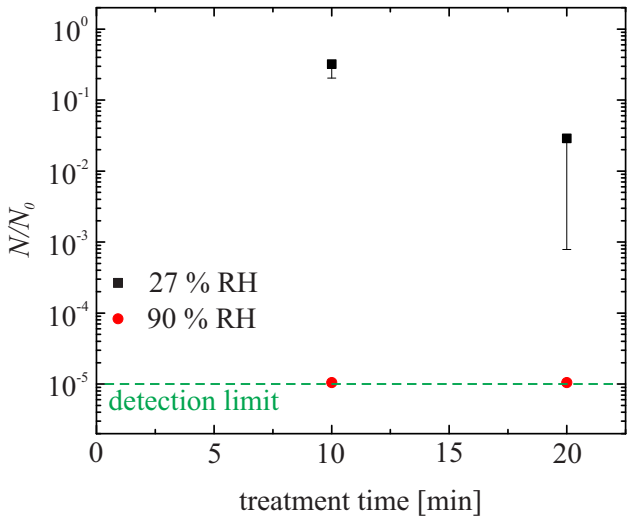

Figure 4.3: Survival rates of *Bacillus atrophaeus* endospores treated for different humidity conditions. The dotted line represents the detection limit.

three treated spore samples and the corresponding standard deviation. For high humidity conditions of 90 % RH, the results reveal a spore reduction to the detection limit, while for low humidity conditions of 27 % RH the suvival rate was $N/N_0 = 2.9 \times 10^{-2}$. These results supports the findings in the literature, that the inactivation efficiency is increased for high humidity conditions, probably by the increase of OH and H_2O_2 molecules. According to these results, the investigations of the microbial inactivation efficiency in this thesis were executed for high humidity conditions.

4.1.4 Inactivation Efficiency in Different Treatment Volumes

Fig. 4.4 shows the mean value of the survival rates N/N_0 over the experiments for different treatment times using three different treatment chambers. At least nine spore samples were treated to obtain one data point. The data show an increase of the inactivation rate of the spores with the increase of exposure time to the CAP afterglow. The investigations illustrate that the inactivation is faster in the smaller volume. A 4.6 log reduction was reached after 10 min treatment in 0.54 l and a 4.4 log reduction was realized after 20 min in 1.8 l treatment volume. In the largest volume of 2.6 l, 30 min were required to observe a log reduction of 4.6. The exponential fits (0.54 l: 0 – 10 min; 1.8 l: 0 – 15 min; 2.6 l: 0 – 20 min) in Fig. 4.4 emphasise the different inactivation efficacies of the used treatment chambers in the first minutes.

The survival rate N/N_0 in Fig. 4.4 demonstrates a fast sporicidal inactivation at the beginning for all treatment volumes, which turns into a slower inactivation after a survival rate of $\sim 10^{-4}$ (4 log). The observation in Fig. 4.4 that the decay of the survival rates is faster with small treatment times could be explained by two facts. Firstly, that the detection limits ends with a survival rate of $\sim 10^{-6}$, due to the fact, that approximately 10^6 spores were incubated

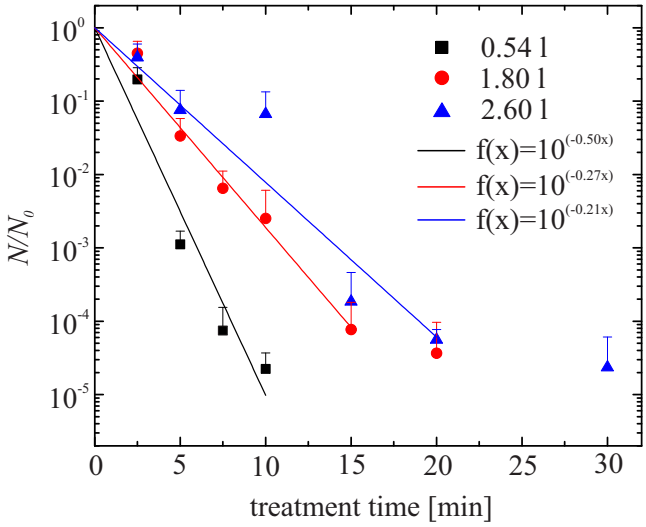

Figure 4.4: Survival rates of *Bacillus atrophaeus* spores treated in different treatment volumes as a function of treatment time (adapted from [14]).

on the stainless steel surface. When the survival rate of $\sim 10^{-6}$ is approached, little deviations of the samples show a large impact. Secondly, the spores exist in multilayers and are not spread homogeneously over the stainless steel plate [193]. By the plasma treatment, the top layer of spores is inactivated first, while the inactivation of the layers below is limited, because they are at least partly covered by other spores [193]. This multi-layer formation leads to a wide variation of inactivation efficacy among different target samples. The presence of spore multilayer is also discussed in chapter 4.3.4.

With a simple calculation we can estimate the number of spores which can be exposed directly to the CAP afterglow. The calculation considers that $P_1 = \sigma_B/A$ (A = surface area of the sample, P_1 = probability of the first spore to be in a certain position of A, σ_B = geometrical cross section of *Bacillus atrophaeus*). $P_2 = 1 - P_1$ describes the probability that a second spore access a region of the unoccupied area and $P_N = (1 - P_1)^{N-1}$ gives the probability that the N^{th} spore access a free area on the sample. Therefore equation 4.1 gives the fraction of the number of covered spores N_c and the number of plated spores N:

$$\frac{N_c}{N} = 1 - \left[1 - \left(1 - \frac{\sigma_B}{A}\right)^N\right] \frac{A}{\sigma_B} \frac{1}{N}. \tag{4.1}$$

Fig. 4.5 shows the number of covered spores N_c (continuous line) as a function of the number of plated spores N. The dashed line shows the number N of possible plated spores starting from the origin. For this calculation a sample area of 5.5 x 30 mm^2 = 1.65 x 10^{-4} m^2 and the geometrical size of *Bacillus subtilis* σ = 1.07 x 0.48 $\mu\mathrm{m}^2$ = 0.51 x 10^{-12} m^2 (described from Carrera *et al.*[194]) were assumed.

This consideration shows that already $\sim$ 1544 spores are covered if 10^6 spores in total are

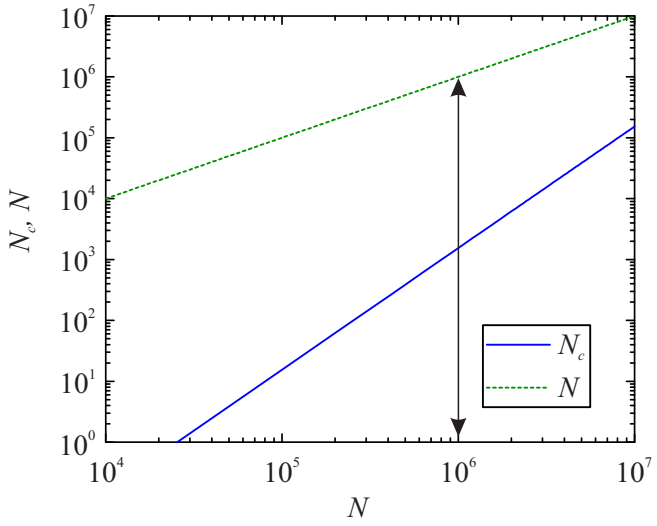

Figure 4.5: N_c: Number of covered spores N_c as a function of number of inoculated spores N. N: Number of inoculated spores N.

inoculated. The calculation of the log reduction $\log(10^6/1544) = 2.8$ illustrates that a log reduction < 2.8 log is caused by superficial CAP impact and an inactivation > 2.8 log due to the penetration of CAP in covered spore multilayers. This penetration is a limitation time factor of the treatment. To avoid this, a lager surface area and another preparation method is needed [195, 196].

To compare the afterglow treatment of the PACA with other sterilisation methods, we calculated the D-values for different treatment volumes using the functions of the exponential fits in Fig. 4.4: D-value = 2.0 min for 0.54 l, D-value = 3.7 min for 1.8 l and D-value = 4.8 min for 2.6 l. As already described in chapter 1.3, the D-value defines the required time to achieve an inactivation of 90 % of the test microorganism population [34].

Table 4.1 summarizes the comparison of the treatment methods of ECSS standard, Shimizu *et al.*[15] and the present work. ECSS propose for > 4 log bioburden reduction a minimum temperature of 125 °C. The VHP treatment time for bioburden reduction depends on the H_2O_2 concentration. For example, with a H_2O_2 concentration of 1 mg/L, the D-value is 3.3 min. The data presented here demonstrate that the new designed apparatus needs less than a 30 min treatment time to achieve a 4.4 log reduction for endospores. In chapter 1.3, the validated sterilisation methods DHMR and VHR are described in more detail.

Additional to the previous mentioned studies of Stapelmann *et al.* [49] and Cooper *et al.* [50] CAP already showed its inactivation effect on microorganisms. Mandler *et al.* [120] already used a similar apparatus, as presented here, to demonstrate the inactivation of *E. mundtii* on stainless steel and dental equipment. In contrast to the work presented here, a small treatment volume was sufficient, and the composition of the reactive species were not analysed in detail. Recent studies also investigated the effect of cold atmospheric air

Method	Temperature [°C]	Treatment time [h]	Log Reduction	Target
DHMR ECSS[33]	125 170	35.4 0.42	4 4	Bioburden reduction
SMD Shimizu *et al.*[15]	25	1.5	3 - 4	*B. atrophaeus*
this work	22	< 0.5	> 4.4	*B. atrophaeus*
VHP (controlled ambient environment)[33] H_2O_2 concentration $> 1.1\,\mathrm{mg/L}$	25 - 45	200 (mg/L)s	1	Bioburden reduction
VHP (controlled vacuum environment)[33] H_2O_2 concentration $0.5 - 1.1\,\mathrm{mg/L}$	25 - 45	200 (mg/L)s	1	Bioburden reduction

Table 4.1: Comparison of the treatment methods of ECSS standard, Shimizu *et al.* [15] and this work [14].

plasma on *Bacillus* spores for different plasma devices. Kuzminova *et al.*[103] reported in their study that *B. subtilis* spores could almost completely be etched by DBD plasma within a few minutes. But they also observed an etching effect of polymers by the DBD plasma. Reineke *et al.*[197] and van Brokhorst-van de Veed *et al.*[198] demonstrated an inactivation of bacterial endospores using an atmospheric pressure plasma jet. In principal, plasma jets are effective devices to inactivate various microorganisms. But the application is limited to a small treatment area which impedes the treatment of large objects. Klämpfl *et al.*[116] used the SMD technology to rapidly inactivate different *Bacillus* species. The SMD electrode was positioned close to the samples and operated in a smaller volume than the presented apparatus. Beside the reactive ROS and RNS, electrical forces could have affected the inactivation process. Since the plasma afterglow could provide a more sensitive surface application, longer treatment times are necessary, but the material compatibility is supposed to be higher. The big advantage is that the reactive afterglow can be used in a defined treatment volume and the afterglow can diffuse into narrow cavities. In chapter 4.3 the inactivation of 3D objects is investigated.

4.1.5 O_3 Concentration in Different Treatment Volumes

Ozone is one of the dominant species produced by SMD plasmas using ambient air (see chapter 3), and it is known as an oxidizing and bactericidal agent[111, 138]. In the experiment the ozone concentrations were measured in the middle of the treatment chambers with three different volume sizes (0.54 l, 1.80 l, 2.60 l) by using UV absorption, as described in chapter 2.2. Fig. 4.6 shows the O_3 concentration in the treatment phase as a function of time. The data points represent the average of six measurements which were recorded on three different

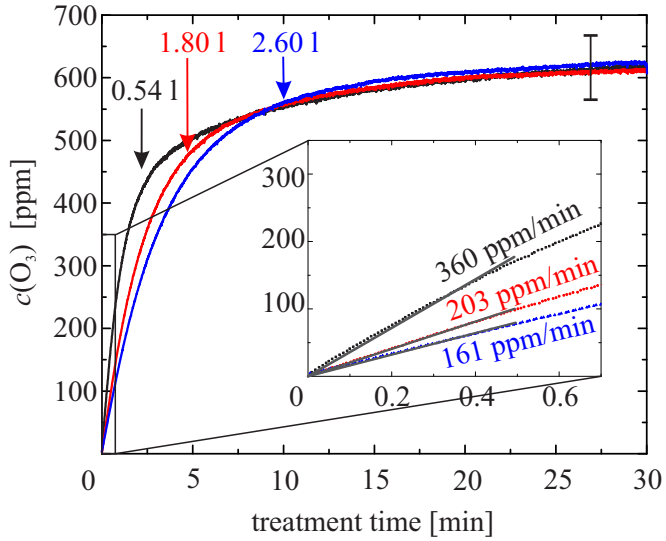

Figure 4.6: Ozone concentrations in three different treatment volumes of 0.54 l, 1.80 l and 2.60 l during the treatment phase (after the heating phase). The error bar represents the maximum standard deviation of the measurements (adapted from [14]).

days to consider possible variations. The error bar in Fig. 4.6 shows the maximum standard deviation of the measurements (approximately 50 ppm) to obtain clearance of the diagram. The data show that the O_3 concentration increases in the three chambers with different rates in the first five minutes. Afterwards, the O_3 concentration saturates in each treatment chamber at values of about 600 ppm. Note, that the ozone concentration of the terraplasma electrode system is lower than for the investigations in chapter 3. In addition the power consumption for $U = 6.4\,\mathrm{kV}$ and $f = 10\,\mathrm{kHz}$ was $\sim 3.5\,\mathrm{W}$. Probably, the electrode used at terraplasma slightly differences from the DLR electrodes which leads to the lower production of reactive species. In addition differences in the sealing of the apparatus' could lead to a variation in the reactive species concentration. However, the dependency of the inactivation efficiency to the treatment volume should be given for both electrode systems.

Fig. 4.6 shows, that the O_3 filling rate in the 0.54 l chamber is higher than for the larger treatment chambers because the ozone production rate by the SMD electrodes is constant. For $t > 10\,\mathrm{min}$, the production of ozone is balanced with the recombination in the setup, so that the concentration reaches a plateau. The filling rates of the apparatus were calculated with linear fits in Fig. 4.6. According to the data, the O_3 concentration increases with the filling rate of 360 ppm/min in the 0.54 l volume, with 203 ppm/min in the 1.8 l volume and with 161 ppm/min in the 2.60 l volume. The filling rates were calculated with the data of the first 30 s, because the recombination rates increase with the concentration of the reactive species which lead to a non-linear development.

Fig. 4.7 shows the survival rate of *Bacillus atrophaeus* as a function of the applied ozone dose (integrated O_3 concentration in Fig. 4.6). The spore survival rates decrease with increas-

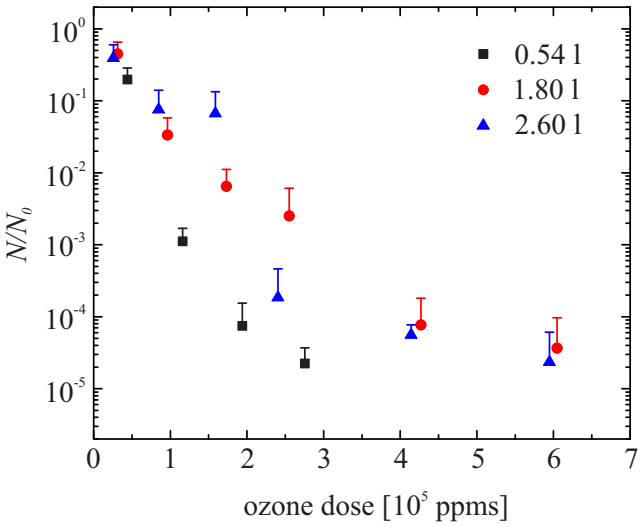

Figure 4.7: Survival rate of *B. atrophaeus* spores as a function of O_3 dose for different treatment volumes [14].

ing ozone dose in all treatment volumes. This supports the hypothesis that the inactivation depends on the present ozone concentration and that ozone is an important inactivation agent in our experiment [111, 141]. Previous studies already reported about the sporicidal effect of gaseous ozone [173, 174]. Aydogan *et al.*[173] reported a 3 log reduction of *Bacillus subtilis* spores for a O_3 concentration of 3 mg/l ($\sim$1500 ppm) after 4 hours exposure time with 90 % relative humidity and an associated D-value of 43 min. Ishizaki *et al.*[174] received a maximum D-value of 20 min for 3 mg/l ($\sim$1500 ppm) and 90 % relative humidity. In addition, Shimizu *et al.* [15] investigated the inactivation rate of *B. atrophaeus* by the plasma afterglow using SMD technology, for different plasma powers. They observed that the inactivation cannot be explained only by the ozone concentration, because the inactivation rate was higher for lower ozone concentrations. These studies indicate that ozone is not the only responsible component for the inactivation of microorganisms using the plasma afterglow.

The analysis in chapter 3 shows the presence of N_2O and HCHO in the afterglow under high humidity conditions. Furthermore, it is assumed that HNO_3 is present in the apparatus under these conditions, but condensed on the surface within the apparatus. Nevertheless, the study of Oehmigen *et al.*[114] reported that no sporicidal effect of HNO_3 could be detected for *B. atrophaeus* after 2 h incubation. Furthermore, Russell *et al.* [199] mentioned that nitrous acid (HNO_2) is a effective agent against coatless but not for normal spores. However, Tennen *et al.* reported that nitrous acid could kill spores through DNA damage. Thus, the role of HNO_3 in the sporicidal inactivation using the plasma afterglow has to be investigated in more detail in the future. The inactivation of microorganisms is more efficient under high humidity than under low humidity, which was also reported from several studies [115, 117]. In addition the results in chapter 3.5 show higher O_3, N_2O and HCHO concentrations for low humidity

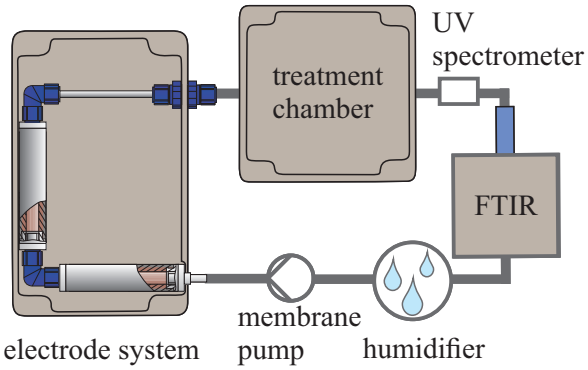

Figure 4.8: Setup of PACA for the investigation of the treatment homogeneity and the investigations with 3D objects.

conditions. These results supports the theory, that molecules in addition to O_3, N_2O and HCHO are responsible for the inactivation process. The increase of humidity changes the chemical pathways, which leads to an increase of OH and may also of H_2O_2 molecules (see chapter 3.5) which could contribute to the inactivation [115].

In future investigations, the treatment volume could exceed the largest tested treatment chamber of 2.6 l by extending the treatment time or using multiple SMD electrodes to fill up the treatment chamber.

4.2 Homogeneity of Inactivation

In order to treat larger objects in the PACA, it is crucial to analyse the spatial homogeneity of the inactivation in the treatment chamber in addition to the treatment in different volumes. Therefore, we executed investigations with bacterial endospores in the largest treatment chamber with and without the use of a fan, to influence the gas flow during the measurement.

4.2.1 Materials and Methods - DLR

In the present chapter, the PACA is used at ambient air with the humidifier, FTIR and the largest treatment chamber of 2.6 l treatment volume, as shown in Fig. 4.8. For these measurements, the UV-measurement-box was positioned between the treatment chamber and the FTIR. The observation of the power, UV and FTIR measurements were used to monitor the plasma conditions and are not shown here. Note that these investigations were executed in the DLR laboratories and that the electrode system was rebuild and is similar to the investigations in chapter 3. Compared to chapter 4.1.4, the applied voltage for the plasma ignition was reduced from 6.4 kV to 6.0 kV in order to prevent the high voltage amplifier from overstressing. For the investigations we used bacterial endospores *Bacillus atrophaeus* ATCC 9372 (DSM 675) suspension from DLR Institute Aerospace Medicine, Cologne, together with

stainless steel discs (V4A, 1.4571, LTO GmbH, Germany) of 10 mm diameter and 1 mm thickness.

In the following chapters, we distinguish between SIMICON samples (used in chapter 4.1) and DLR samples. To manufacture the DLR samples for the inactivation, 100 µl of a spore suspension of $\sim 10^7$ cfu/ml were plated on the stainless steel discs so that we achieved an initial number of spores $N_0 \sim 10^6$ cfu/target.

The microbiological evaluation protocol differ in some points form the protocol in chapter 4.1.1, which was used from terraplasma GmbH for the SIMICON *B. atrophaeus* samples. The plasma treatment and the microbiological evaluation protocol are presented as follows:

1. The apparatus was activated for 20 min before the CAP treatment to stabilize the temperature, the concentration of reactive species and humidity in the system. The gas flow rate was 3.5 l/min and the relative humidity in the system about 90 %. Note that the CAP was already produced in this heat-up procedure.

2. After the heating phase of 20 min, the pump was switched-off and the treatment chamber was opened, so that the reactive gas of the treatment chamber exchanged with the environmental air. The residue reactive species remained in the tubes of the apparatus. Afterwards, the biological samples were placed on the bottom of the treatment chamber before the treatment chamber was closed.

3. The samples were treated by the SMD plasma gas ($f = 10$ kHz, $U = 6.0$ kVpp) for the chosen treatment times between $20 - 120$ min using the 2.6 l treatment chamber. When the plasma treatment was started, the pump was switched-on again.

4. After the plasma treatment, plasma and gas flow were switched-off and the samples were transferred into 5 ml sealable tubes (Eppendorf) filled with 2 ml highly purified water (Ampuwa, Fresenius Kabi AG, Germany).

5. The samples were washed out using a vortex mixer for 1 min, an ultra-sonic bath for 30 min, a vortex mixer for 1 min, an ultra-sonic bath for 15 min and again a vortex mixer for 1 min.

6. Dilution series up to $1{:}10^5$ were prepared. 3×50 µl of each suspension were plated on R2A (VWR International GmbH, Darmstadt, Germany) agar plates and incubated overnight at 32 °C.

7. In parallel to 6., the rest of the undiluted suspension ($\sim$ 1750 ml) was spread on four agar plates (3×500 ml and 1×250 ml) to count the remaining spores in the undiluted solution. By this procedure, the inactivation of spores up to 6 log could be proved.

8. At least three measurements were executed to obtain one data point. For each data point, two to three control samples without any treatment were used to determine the

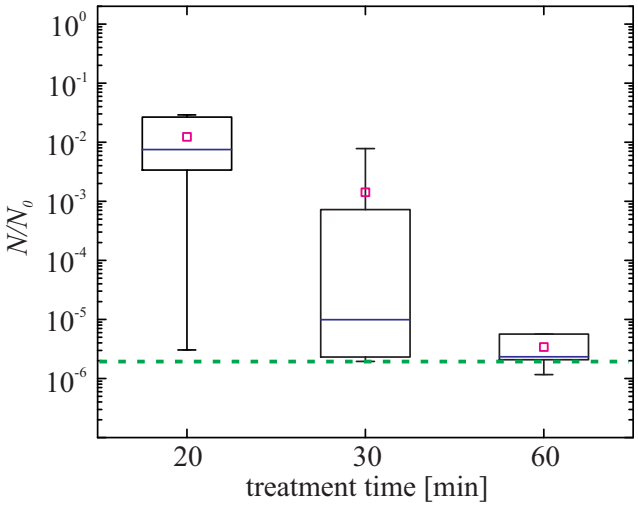

Figure 4.9: Surviving rates of DLR samples after different treatment times of plasma treatment. The dashed line shows the detection limit.

initial number of spores N_0 which were deposited on the stainless steel surface. To determine the number N_0 of cfu of the control samples, the untreated samples were transferred into separate tubes and the microbiological protocol was executed (4,5,6,7).

9. By counting cfu on each plate, the number of survived spores by the plasma treatment N and untreated controls N_0 were estimated. Furthermore, the survival rate is given by N/N_0.

The error bars for the investigation of the inactivation were calculated by the standard deviation of the survival rates for the measurements.

4.2.2 Inactivation of *Bacillus atrophaeus* (DLR Samples)

In the first measurements, we investigated the inactivation efficiency using the DLR samples of *B. atrophaeus*. For the treatment, the samples were placed at the bottom, in the middle of the treatment chamber, similar to chapter 4.1.4. Fig. 4.9 shows the survival rate N/N_0 as a function of time. The data is shown in box plots, where the horizontal line inside the box marks the median and the lower and upper edge of the box present the first and third quartile, respectively. The whiskers cover the interval of all measured values of the survival rate and the coloured small box marks the mean value. In addition, the dashed, green horizontal line shows the detection limit of the survival rate.

The investigations of the inactivation of the *B. atrophaeus* DLR samples show a higher mean value of the survival rate after 20 min and 30 min treatment time as the SIMICON samples in chapter 4.1.4. In addition, the ozone concentration was lower for the treatment of the SIMICON samples, since an other electrode system from terraplasma was used. The

results show that the SIMICON samples are much easier to inactivate than the DLR samples. This could be explained by the differences in the manufacturing process, which is discussed in chapter 4.3.4.

After 60 min treatment time, the survival rate was close to the detection limit. In order to analyse the homogeneity of the plasma treatment inside the treatment chamber we used a treatment time with low inactivation rates to reveal the variations of the plasma treatment. In the following investigations, the treatment time of 20 min is used.

4.2.3 Homogeneity of the Inactivation

To analyse the inactivation efficiency at different regions in the treatment chamber, the spore samples were arranged in a 3×3 pattern and treated for $t = 20$ min. The treatment was done with and without the use of a fan to modify the distribution of the reactive species within the treatment chamber. The used fan was installed in the middle of the lid of the treatment chamber with a distance of 15 mm to the lid. The fan produced a flow velocity of 0.56 m/s, which was measured with an anemometer (TMA10A, Beha-Amprobe, Germany). In total, measurements without fan (M_0), with an upwards adjusted fan direction (M_{up}) and with a downwards adjusted fan direction (M_{down}) were executed. Fig. 4.10 shows the homogeneity of the surviving ratio of *B. atrophaeus* for a) M_0, b) M_{up} and c) M_{down} using a heat map. The data show the calculated mean value of at least three measurements with the corresponding standard deviation. In Fig. 4.10 a) the lowest surviving rate was measured without fan for position B1 with $N/N_0 = 4.6 \times 10^{-6}$, which is close to the detection limit. This is the position, below the outlet of the treatment chamber, so that we assume, that the reactive species are accumulated at this point. In addition, the highest survival rate was measured for B2 in the middle of the treatment chamber with $N/N_0 = 3.9 \times 10^{-3}$. Fig. 4.10 b) shows the distribution of the survival rate for M_{up}. For the upwards adjusted fan position, we find the minimal surviving rate for C1 with $N/N_0 = 3.7 \times 10^{-3}$ and the maximal surviving rate for B1 with $N/N_0 = 5.6 \times 10^{-2}$. Compared to a) the distribution of the surviving rates is even, but shows a lower inactivation efficiency. Fig. 4.10 c) shows the survival rates for M_{down} with a downwards adjusted gas flow. For this measurement condition, the minimal surviving rate was found at point B1 with $N/N_0 = 7.5 \times 10^{-3}$ and the maximal surviving rate at B2 with $N/N_0 = 7.1 \times 10^{-2}$. The investigations for M_{down} show the lowest inactivation efficiency compared to M_0 and M_{up}. The analyse of the ozone concentration, shows no difference between M_0, M_{up} and M_{down}. The spectroscopic data is not presented here, since we do not gain additional insights.

The investigations of the inactivation homogeneity demonstrate, that without additional gas mixing (by a fan) the inactivation efficiency is maximal. In detail, the surviving rate was minimal for B1, which is positioned directly below the outlet of the treatment chamber. We assume, that the reactive gas mixture is accumulated at this point before it is transported

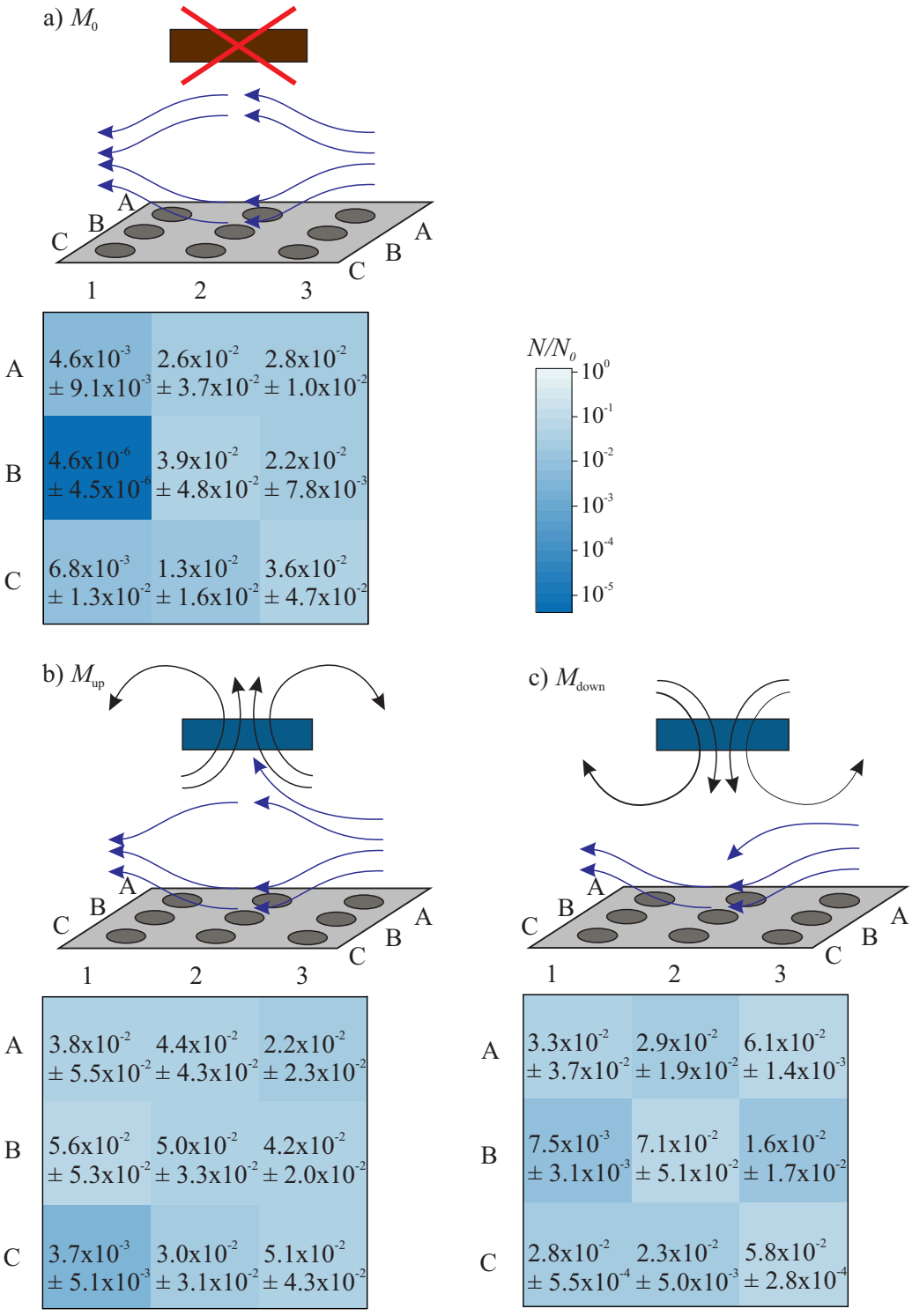

Figure 4.10: Homogeinity of the inactivation in the 2.6 l treatment chamber under different conditions for 3×3 spore samples. The heat maps illustrate the calculated mean value with the corresponding standard deviation. a) Without the use of a fan (M_0). b) Fan with upwards gas flow (M_{up}). c) Fan with downwards gas flow (M_{down}).

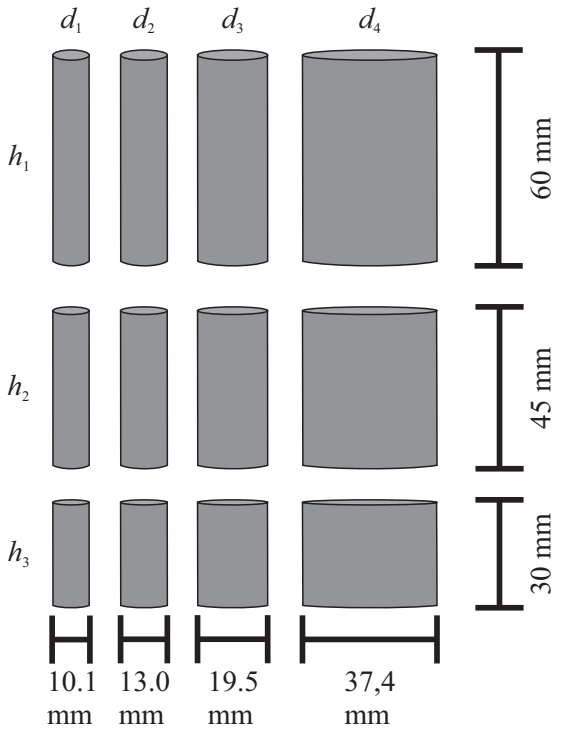

Figure 4.11: Illustration of the used 3D barriers for inactivation of *B. atrophaeus*. The used 3D barriers are stainless steel tubes with different heights $h_1 = 60\,\text{mm}$, $h_2 = 45\,\text{mm}$ and $h_3 = 30\,\text{mm}$ and different diameters $d_1 = 10.1\,\text{mm}$, $d_2 = 13.0\,\text{mm}$, $d_3 = 19.5\,\text{mm}$ and $d_4 = 37.4\,\text{mm}$.

outside the treatment chamber by the gas flow. A homogeneous treatment was achieved with the use of a fan which additionally circulates the reactive gas insight the treatment chamber. The measurement showed slightly higher inactivation rates for M_{up} compared to M_{down}. For the treatment of 3D objects it could be useful to work with an additional gas circulation inside the treatment chamber. Therefore, in the following investigations we analyse the influence of 3D barriers to the plasma treatment with and without the use of a fan.

4.3 Inactivation Using 3D Barriers

In order to decontaminate complex structures, especially spacecraft relevant components, it is necessary to investigate the efficiency of the plasma treatment using 3D barriers. The used setup for the PACA is shown in Fig. 4.8, with 2.6 l treatment volume, UV measurement box, humidifier and FTIR included. For the investigations, we used 12 stainless steel tubes of different heights $h_1 = 60\,\text{mm}$, $h_2 = 45\,\text{mm}$ and $h_3 = 30\,\text{mm}$ and the different diameters $d_1 = 10.1\,\text{mm}$, $d_2 = 13.0\,\text{mm}$, $d_3 = 19.5\,\text{mm}$ and $d_4 = 37.4\,\text{mm}$, illustrated in Fig. 4.11. The size of the stainless steel tubes allows to uprightly place the tubes in the treatment chamber and to place the DLR spore samples inside the tubes on the bottom of the treatment chamber.

For the use of $d_1 = 10.1\,\text{mm}$, the diameter of the spore sample was adjusted to $d = 9.6\,\text{mm}$. Note that the opening for the gas in and outflow is positioned in the middle of the side walls of the treatment chamber in an height of 46 mm (as described in chapter 2.1). The procedure of the plasma treatment is described in chapter 4.2.1. In the following, we present the different measurements using the various tubes as a barrier for the reactive species.

4.3.1 Indirect Treatment Using 3D Barriers

In the first measurements, the stainless steel tubes were used as 3D barriers for the plasma treatment without additional gas circulation in the treatment chamber. The tubes were arranged not directly in the gas steam, which enables an indirect treatment of the spore samples. Fig. 4.12 a) illustrates a schematic drawing of the 3D objects with different diameters and the direction of the gas flow inside the treatment chamber. It was possible to treat two sets of barriers with different heights and different diameters in the treatment chamber (as shown in Fig. 4.12 a)). In total, investigations with an indirect treatment were executed for 20, 60 and 120 min. The mean value of the surviving rates in dependence on the tube diameters are shown in Fig. 4.12 b) for the height $h_1 = 60\,\text{mm}$, in Fig. 4.12 c) for the height $h_2 = 45\,\text{mm}$ and in Fig. 4.12 d) for the height $h_3 = 30\,\text{mm}$. The error bars illustrate the standard deviation of the measurements and are shown upwards to enable a better overview. The black dashed lines illustrate the survival rate after 20 min and the red dashed line the survival rate after 60 min without the use of a barrier (mean values of Fig. 4.9).

The results show, that the inactivation efficiency of the plasma treatment is reduced by the use of 3D barriers. In detail, the increase of the treatment time shows a further decrease of the survival rates for all measurements. Nevertheless, a survival rate close to the detection limit was only observed by the largest diameter $d_4 = 37.4\,\text{mm}$ after 120 min for all heights. In addition, the data show no clear dependence to the barrier height for $t = 20\,\text{min}$ and $t = 60\,\text{min}$ and only a slight dependency on the diameter. For 120 min plasma treatment the inactivation efficiency increases by an increase of the tube diameter and with a reduction of the tube height. The results indicate that with an indirect gas flow, it is still possible to inactivate bacterial endospores, but the treatment time has to be increased.

4.3.2 Indirect Treatment Using 3D Barriers with Fan

The previous measurements analysed the inactivation of spore samples using 3D barriers by an indirect gas flow. To increase the inactivation efficiency, we compared the indirect treatment for 20 min with an additional gas convection by a fan, installed with 15 mm distance to the lid. Fig. 4.13 a) illustrates the use of a fan to support the circulation of the reactive species in the treatment chamber. Therefore, the fan uses an upwards gas flow. The results for $t = 20\,\text{min}$ plasma treatment for the heights h_1, h_2 and h_3 are presented in Fig. 4.13 b), c) and d), respectively. The dashed line presents the survival rate of *B. atrophaeus* without

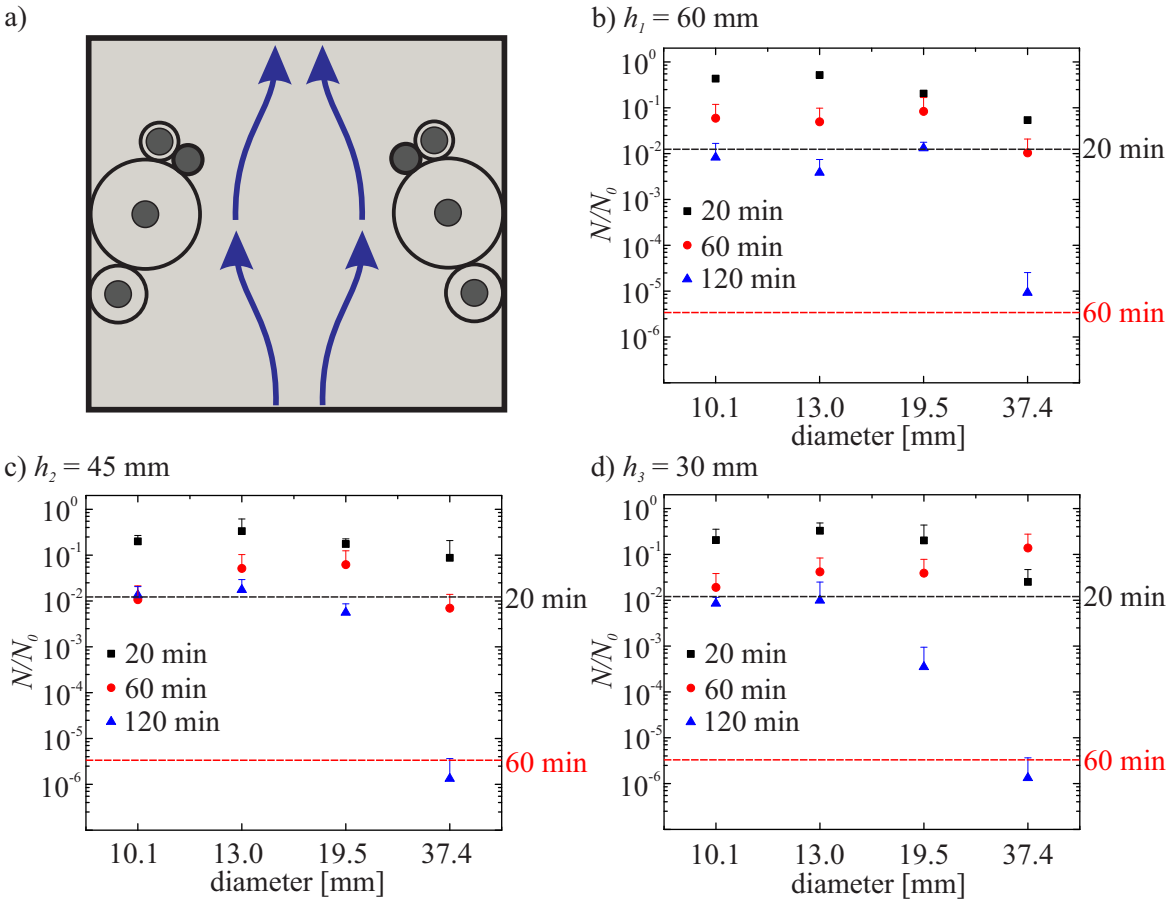

Figure 4.12: Inactivation of spore samples after 20 min, 60 min and 120 min plasma treatment using 3D barriers with different diameters $d_1 = 10.1$ mm, $d_2 = 13.0$ mm, $d_3 = 19.5$ mm and $d_4 = 37.4$ mm. The red dashed lines show the inactivation efficiency after 60 min without barrier and the black dashed line after 20 min, respectively. a) Treatment chamber with gas circulation with indirect gas flow (top view). b) Surviving rate using $h_1 = 60$ mm in dependence of the diameter. c) Surviving rate using $h_2 = 45$ mm in dependence of the diameter. c) Surviving rate using $h_3 = 30$ mm in dependence of the diameter.

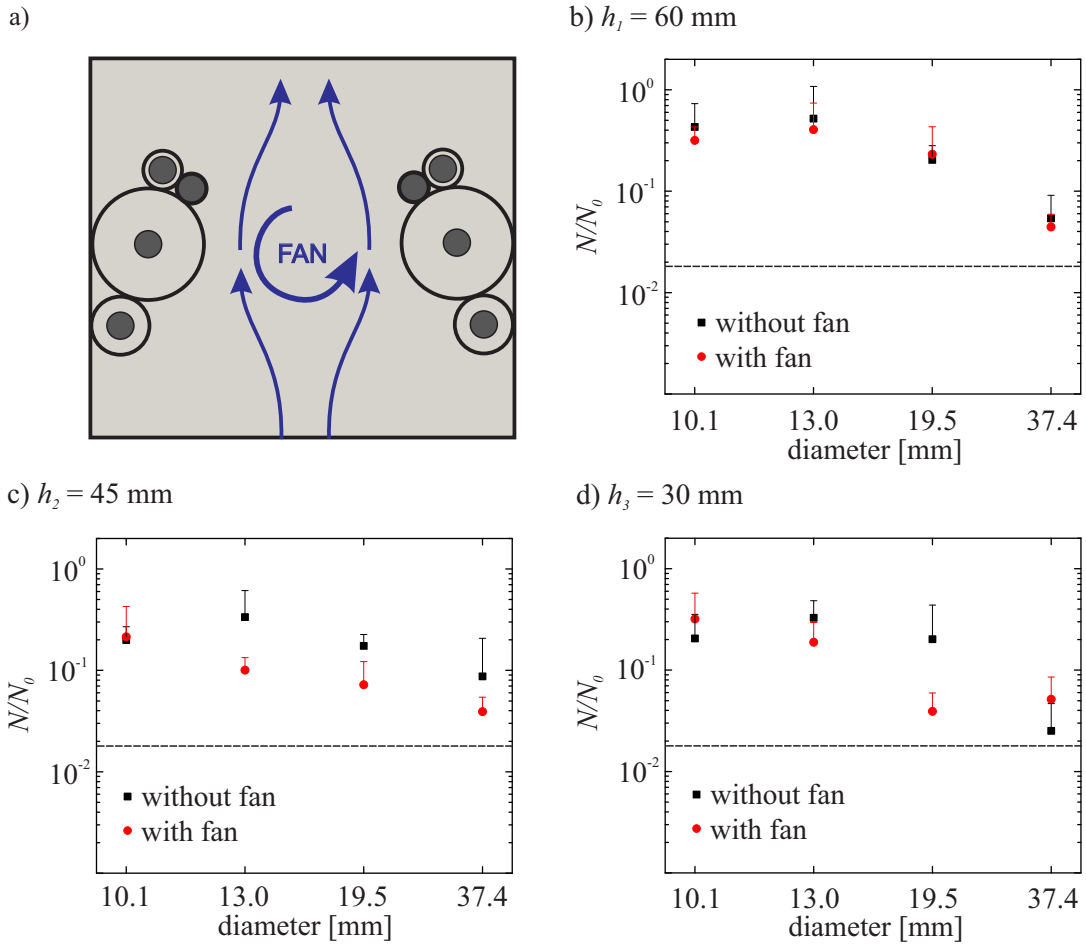

Figure 4.13: Inactivation of spore samples after 20 min plasma treatment using 3D barriers (with and without fan) with different diameters $d_1 = 10.1$ mm, $d_2 = 13.0$ mm, $d_3 = 19.5$ mm and $d_4 = 37.4$ mm. The black dashed lines show the inactivation efficiency after $t = 20$ min without barrier. a) Treatment chamber with gas circulation using an additional fan (top view). b) Surviving rate using $h_1 = 60$ mm in dependence of the diameter. c) Surviving rate using $h_2 = 45$ mm in dependence of the diameter. c) Surviving rate using $h_3 = 30$ mm in dependence of the diameter.

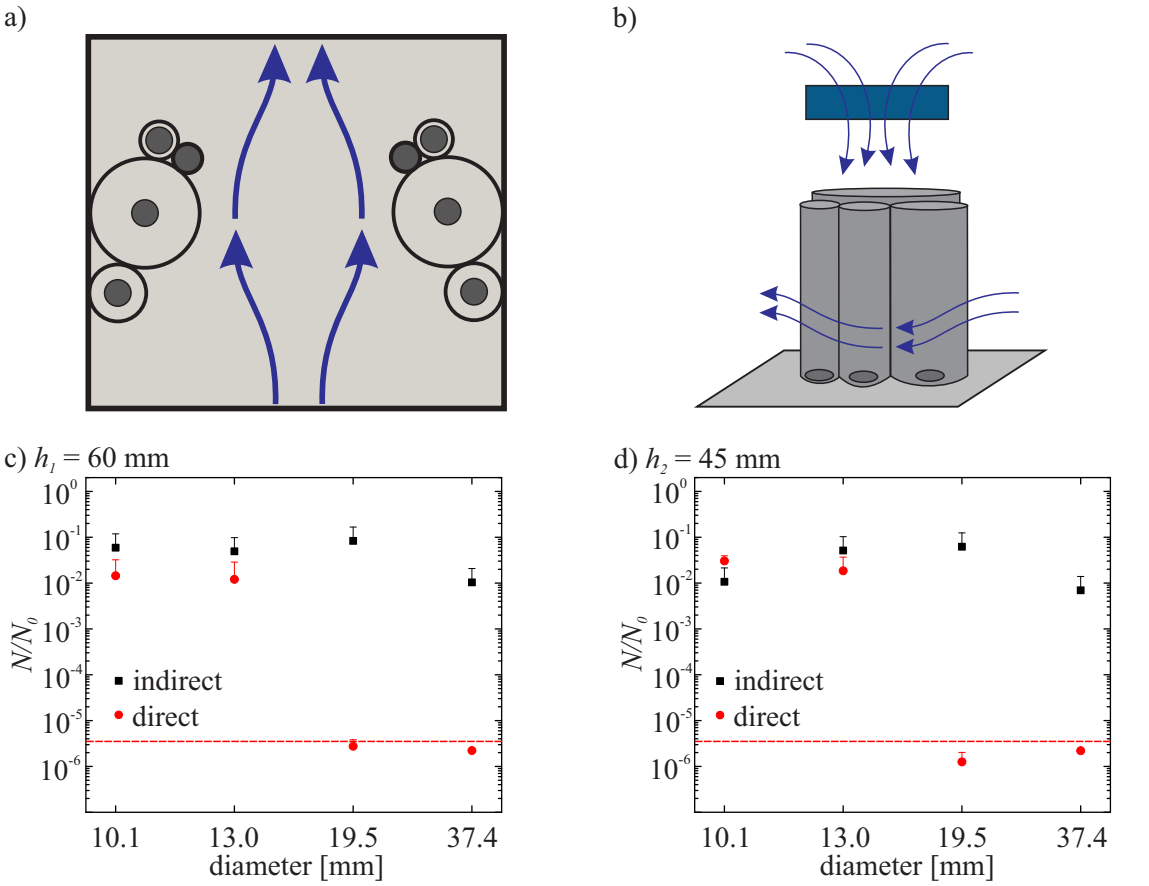

Figure 4.14: Plasma treatment ($t = 60$ min) of 3D barriers using an indirect and direct gas flow. The red dashed lines represent the inactivation efficiency after $t = 60$ min without barrier. a) Indirect treatment (top view). b) Direct treatment (side view) in the middle of the treatment chamber. c) Surviving rate using $h_1 = 60$ mm in dependence of the diameter. d) Surviving rate using $h_2 = 45$ mm in dependence of the diameter.

barriers (mean value of Fig. 4.9) after 20 min treatment time. Fig. 4.13 b) shows, that the use of a fan has no influence to the inactivation efficiency for the highest tube $h_1 = 60$ mm. In addition, Fig. 4.13 c) and d) show a slight increase of the inactivation efficiency. The investigations with a gas circulation inside the treatment chamber indicate, that the use of the fan minimal increases the inactivation efficiency, for h_2 and h_3, but not for h_1.

4.3.3 Direct Treatment Using 3D Barriers with Fan

In order to increase the inactivation efficiency, the 3D barriers with the spore samples were positioned directly under the fan. In addition the gas flow of the fan was oriented downwards to the samples. The plasma treatment was executed for $t = 60$ min. Fig. 4.14 a) shows the top view of the treatment chamber with 3D barriers for the indirect treatment and Fig. 4.14 b) illustrates a side view of a direct treatment, where the tubes are placed directly under the

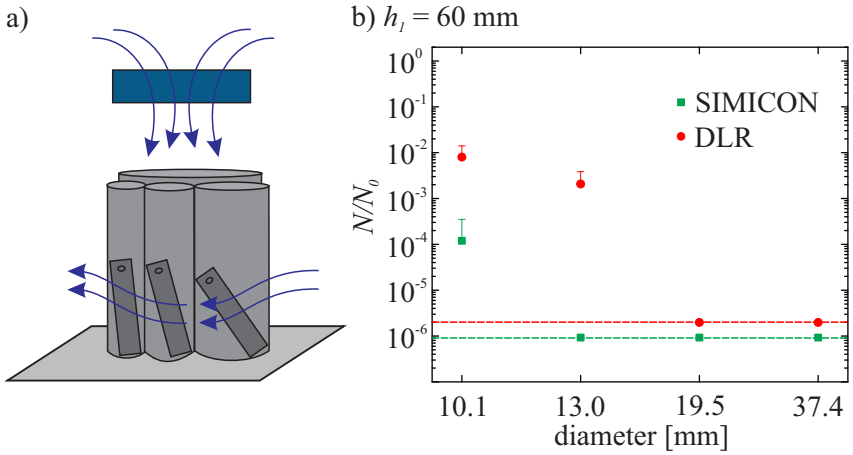

Figure 4.15: Plasma treatment ($t = 60$ min) using 3D barriers $h_1 = 60$ mm and direct gas flow. The red dashed line shows the detection limit of the survival rate for the DLR samples and the green dashed line the detection limit for the SIMICON samples. a) Direct treatment (side view) in the middle of the treatment chamber. b) Surviving rate of SIMICON bio indicators and self plated *B. atrophaeus*.

fan. The surviving rates of the indirect and direct treatment for $t = 60$ min are illustrated in Fig. 4.14 c) for $h_1 = 60$ mm and in Fig. 4.14 d) for $h_2 = 45$ mm. The dashed line represents the mean value of the surviving rate without barrier for $t = 60$ min. Note that no investigations for the lowest height h_3 were executed as we assume that samples in the lowest height are easier to inactivate than h_1 and h_2. The presented data shows no significant differences in the inactivation efficiency for the lowest diameters $d_1 = 10.1$ mm and $d_2 = 13.0$ mm for both heights h_1 and h_2. However, the survival rates of h_1 and h_2 for the diameters $d_3 = 19.5$ mm and $d_4 = 37.4$ mm are close to the detection limit and comparable with the inactivation efficiency without the use of a barrier. These results indicate that the inactivation efficiency using 3D barriers of the afterglow treatment could be improved significantly by a directly applied gas stream.

The microbiological investigations in chapter 4.2.2 revealed a higher robustness for the self plated DLR samples than the purchased SIMICON samples. In order to investigate the inactivation efficiency we analysed the inactivation efficiency of the direct application for SIMICON and self prepared spore samples in the highest tubes h_1. To take into account that the SIMICON samples have to be placed upright because of their geometry, the DLR samples were plated on sterilised stainless steel targets from SIMICON with the same initial number of spores per target. Fig. 4.15 a) illustrates the SIMICON targets placed in the stainless steel tubes below the fan. The survival rates of the SIMICON and DLR spores are presented in Fig. 4.15 b) for different diameters of h_1. The red dashed line presents the detection limit of the survival rate for the DLR samples and the green dashed line the detection limit for SIMICON samples.

The results show that the purchased bio indicators of SIMICON are easier to inactivate for h_1 than the DLR samples. In detail, the SIMICON bioindicators reach the detection limit for $d_2 = 13.0\,\text{mm}$, $d_3 = 19.5\,\text{mm}$ and $d_4 = 37.4\,\text{mm}$, while $d_1 = 10.1\,\text{mm}$ shows a survival rate of $N/N_0 \sim 1.2 \times 10^{-4}$. In addition, the results of the DLR spores on the SIMICON targets confirm the results of Fig. 4.14 c) for the direct treatment of DLR samples on stainless steel discs. The investigations indicate that the plated DLR-spores are more robust to the plasma treatment than the purchased bioindicators from SIMICON. The differences between SIMICON and DLR samples are discussed in the following chapter 4.3.4. In conclusion, the direct application of the gas flow using a fan is beneficial for the inactivation of 3D objects.

4.3.4 SEM Images of Multilayers and Treated Spore Samples

The previous microbiological investigations show differences in the treatment of the purchased bioindicaters with *B. atrophaeus* from SIMICON GmbH and the self plated spore suspensions from DLR. Therefore, spore samples were analysed with a scanning electron microscope (SEM) in order to observe differences from manufacturing processes. The investigation was executed with a SEM system at DLR Köln (SEM, ZEISS Merlin, Germany). Pre-coating of the sample was not required, the operating voltage was 1 kV and the working distance WD $> 2.5\,\text{mm}$. Furthermore, the SEM microscope operates in high vacuum with $\sim 10^{-6}\,\text{mbar}$. It is assumed that this vacuum has no influence to the spores [40, 190, 200].

Fig. 4.16 shows SEM images for SIMICON bioindicators a) and for DLR samples b). The image of the SIMICON sample allows to easily identify the spores of $\sim 1\,\mu\text{m}$ size. Furthermore, the spores are partly spread over the surface of the stainless steel target and some of the spore are agglomerated in clusters. The analysis of the DLR samples revealed that some of the spores are also spread over the surface, while other ones are accumulated. Furthermore, the DLR spores are hardly to identify because of a huge amount of residuals cover the spore layers. Probably, the residuals consist of cell debris from the sporulation process or medium contents of the spore solution. Nevertheless, the presence of residuals in the self plated DLR spore samples explains the lower inactivation efficiency of the plasma treatment for these samples. When the microorganisms are covered by residuals the reactive gas components need a longer time to interact with the spore coat. Since the aim is to sterilise spacecraft components, the initial number of microorganisms on the surface is supposed to be low which improves the inactivation efficiency of the plasma treatment.

Further SEM images were done to analyse the influence of the plasma treatment to the spore samples *B. atrophaeus*. Therefore, six SIMICON bioindicators were treated for 30 min in the PACA, while three of the samples were analysed using SEM and the other ones were used to identify the survival number of the spores. The analysis of the survival number showed, that all spores were inactivated during the measurement. In Fig. 4.17 SEM images of an untreated a) and treated b) SIMICON bioindicator are illustrated. Both images show agglomerations

a) SIMICON *B. atrophaeus*

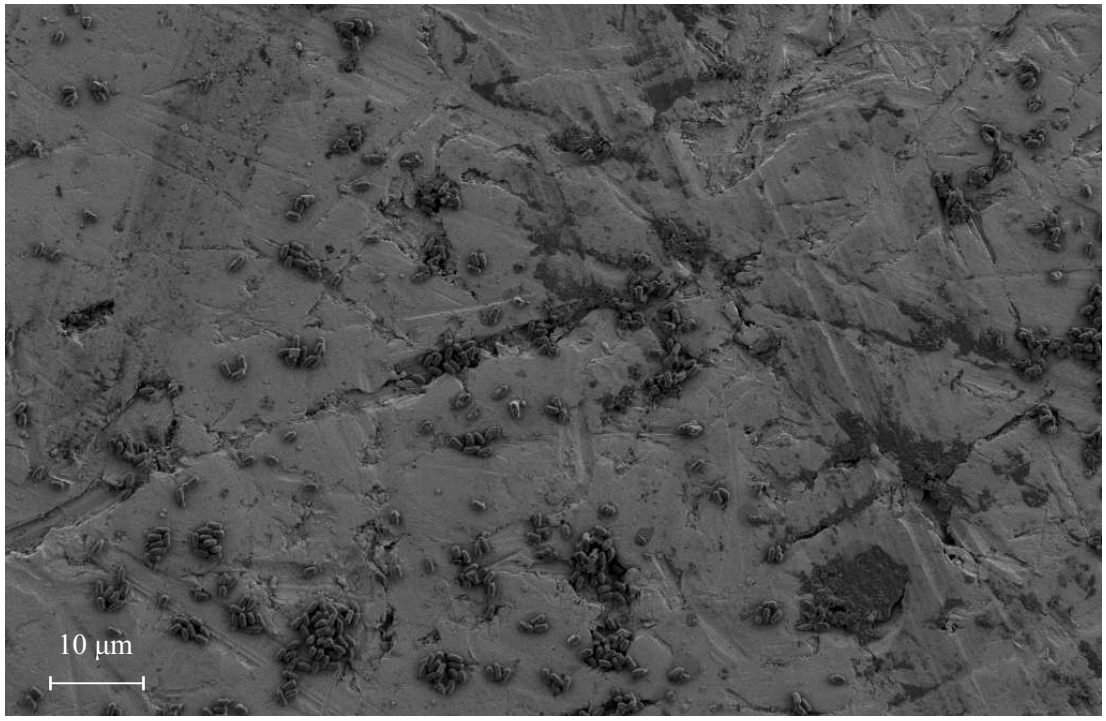

b) DLR *B. atrophaeus*

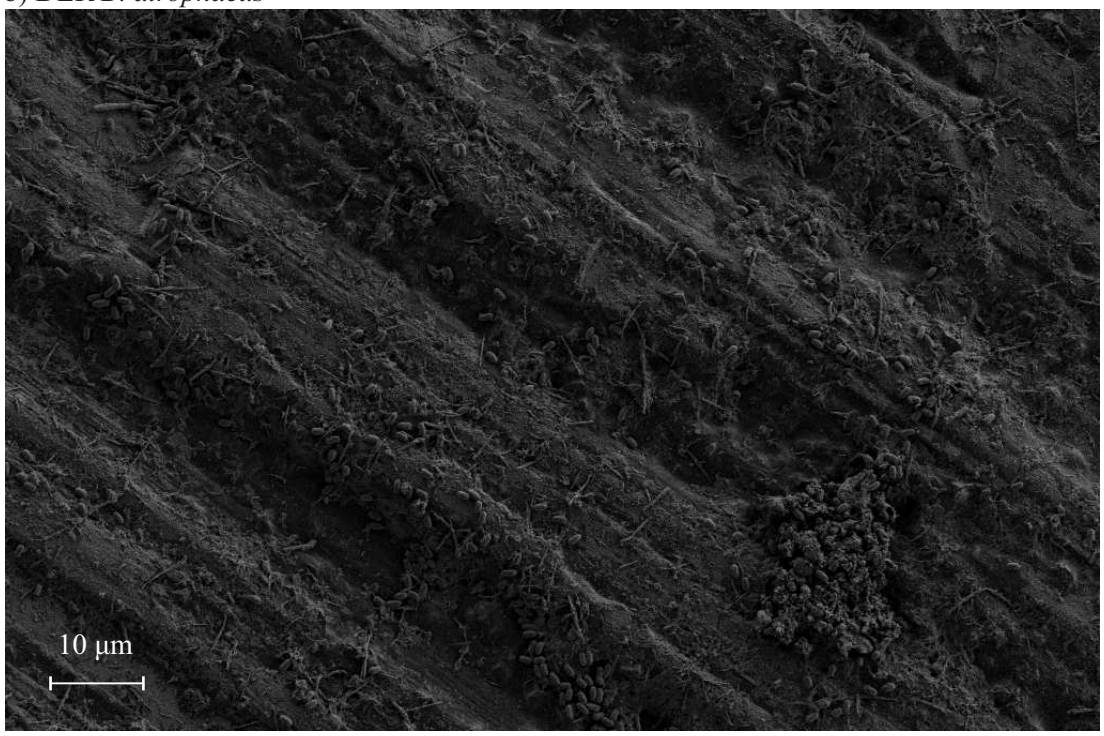

Figure 4.16: SEM images of *B. atrophaeus* of a) SIMICON and b) DLR samples.

a) untreated *B. atrophaeus*

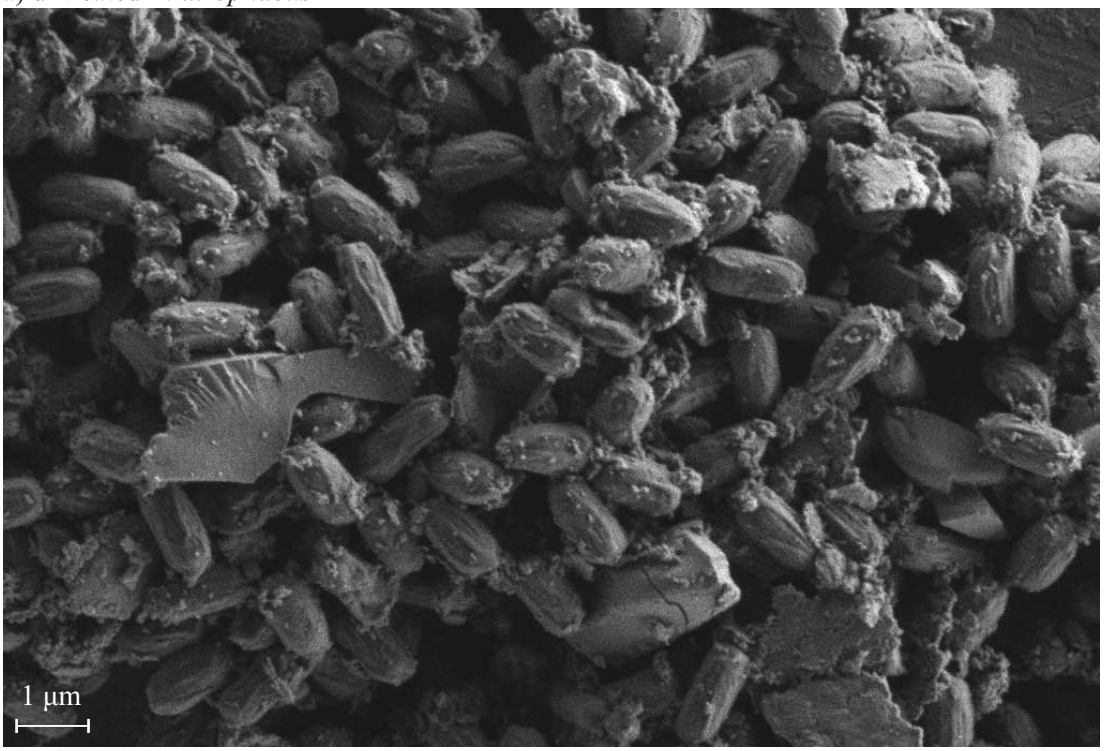

b) 30 min plamsa treatment *B. atrophaeus*

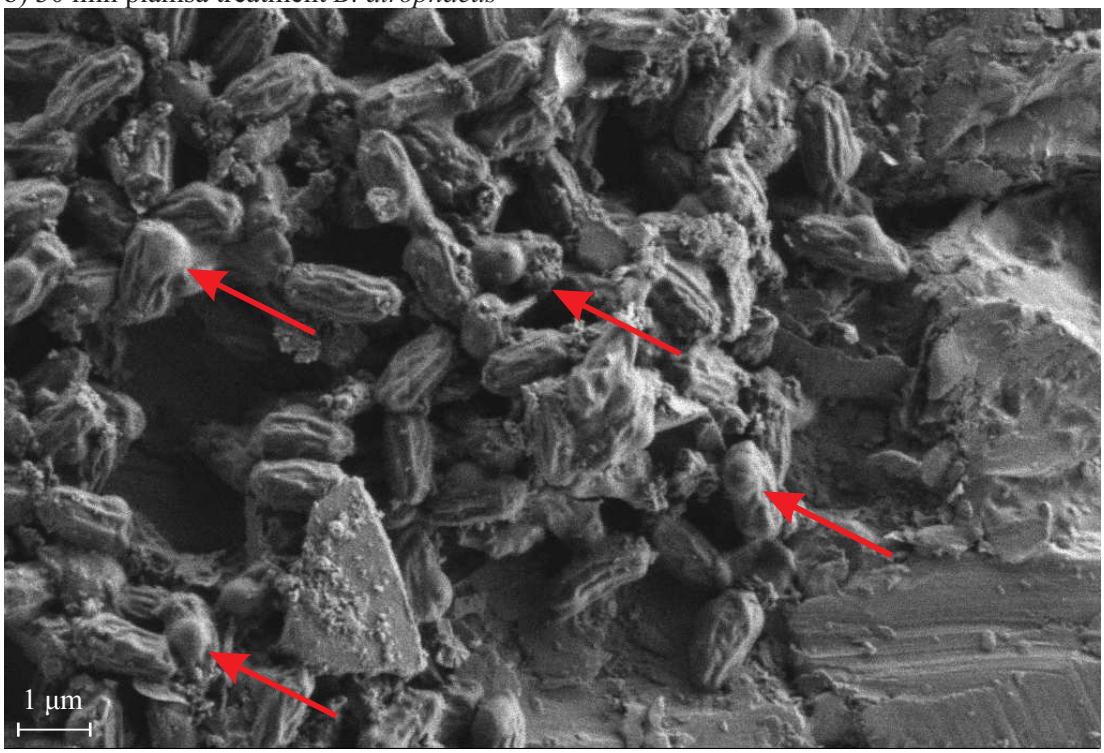

Figure 4.17: SEM images of SIMICON bioindicators. a) Untreated *B. atrophaeus*. b) 30 min plasma treatment of *B. atrophaeus*.

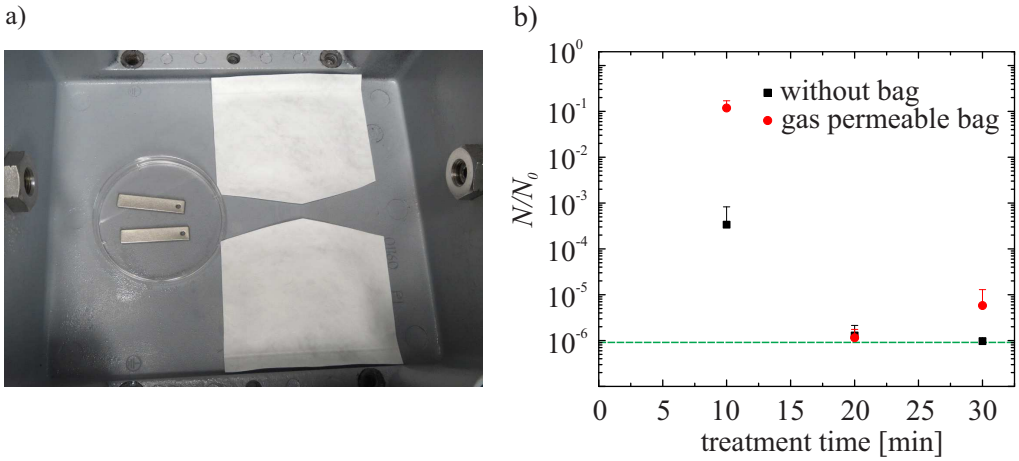

Figure 4.18: Investigation of the influence of a gas permeable packing. a) Treatment of spore samples without and with a gas permeable bag. b) Surviving rate of spore samples without and with a gas permeable bag, as a function of treatment time. The dashed line marks the detection limit.

of the spores, which was also visible in a lower magnification in Fig. 4.16 a). This confirms the theory in chapter 4.1.4 that the spores are not homogeneously spread over the surface but form spore-clusters which leads to longer plasma treatment times. The analysis of Fig. 4.17 a) and b) show a visible change on the surface of the spores, caused by the plasma treatment. Fig. 4.17 a) shows the untreated *B. atrophaeus* with a typical surface structure as described in Plomp *et al.* [27]. The surface of the treated spores in Fig. 4.17 b) has a higher roughness with longitudinal wrinkles. Some of the spores showed vesicles on the surface which are marked with red arrows. The images point out, that the plasma treatment affect the surface of the spores, but that the spores could still be identified when they are not detectable anymore by the microbiological evaluation protocol.

4.3.5 Samples Packed in Tyvek

In order to investigate the applicability of the plasma treatment for sterilisation techniques, we analysed the inactivation efficiency of the PACA for bioindicators in sealed bags. The purchased SIMICON samples are delivered in a separately gas permeable bag of Tyvek®. Tyvek®, made of high density polyethylene (DuPont) is widely used for packaging of sterilised equipment, because it provides a physical barrier and thus a resistance of microbiological penetration, which helps to maintain the sterility of the packed product. In addition it is compatible with low temperature oxidative gaseous sterilisation methods [40, 201]. To investigate the influence of the Tyvek® packing to the plasma treatment, two packed and two unpacked spore sample were treated at once. This experiment was repeated three times and the microbiological evaluation of chapter 4.2.1 was executed. Fig. 4.18 a) illustrates the treatment of packed an unpacked spore samples of SIMICON. The mean values of the surviving rates for

$t = 10\,\text{min}$, $t = 20\,\text{min}$ and $t = 30\,\text{min}$ are presented in Fig. 4.18 b). The dashed green line marks the mean value of the detection limit. The error bars for the investigation of the inactivation were calculated using error propagation with standard deviations of the measurement series. They are presented only upwards to improve the readability of the semi logarithmic view. The results show, that the survival rate for $t = 20\,\text{min}$ is higher for packed spore samples compared to unpacked spore samples. After 20 min plasma treatment, the survival rates for all treated samples were close to the detection limit which corresponds to a 6 log reduction. The mean value of the surviving rate after 30 min shows again higher values for the packed samples, while the unpacked samples are still reduced to the detection limit. We assume that the variation at 30 min are due to manufacturing variations of the spore samples which could influence the inactivation efficiency. Nevertheless after 30 min the packed spore samples show still a surviving rate of $N/N_0 \sim 5.8 \times 10^{-6}$. Our results agree with previous investigations of Wintenberg *et al.* [202] and Schnabel *et al.* [203], which also showed a successful inactivation of spores using plasma through gas permeable bags. The investigations of bioidicators in gas permeable bags indicate that the afterglow inactivation technology could be used for already packed samples. This allows to easily maintain the sterility after the sterilisation procedure.

4.4 Summary

The microbiological investigations in this chapter confirm that the plasma afterglow circulation apparatus could successfully inactivate bacterial endospores of *B. atrophaeus*. In detail the inactivation was executed in different treatment volumes, where the treatment in the largest treatment chamber of 2.6 l achieve a 4.6 log reduction after 30 min treatment time. The results suggest, that the treatment volume can be increased for the decontamination of large components, by increasing the treatment time. Furthermore, the use of additional electrodes would increase the production of reactive species, which allows to operate in large volumes with adequate treatment times. Thus, the use of additional electrodes or longer treatment times provides a cost-efficient enlargement of the apparatus. The investigations using 3D barriers for the plasma treatment show, that it is still possible to inactivate bacterial endospores in 3D objects, but that the efficiency of the treatment is reduced. The increase of the treatment time and the use of a directed gas flow reveal an enhancement of the inactivation efficiency. The measurements show differences in the inactivation efficiency in dependence of the used spore samples (SIMICON or DLR). SEM investigations of the spore samples show that the manufacturing process could have a huge impact on the quality of the spore samples. Although it is possible to inactivate the DLR samples, the residuals on the surface hinder the plasma treatment. In addition, it was possible to observe morphology changes of *B. atrophaeus* after the plasma treatment, which sustains the assumption, that the plasma treatment damages the surface of the microorganisms. Furthermore, the investigations

prove the successful inactivation of spore samples, packed in gas permeable bags of Tyvek®, which is beneficial to maintain the sterilisation degree. In conclusion, the microbiological investigations in this chapter show that the PACA using CAP technology provides a useful technique to inactivate endospores in different treatment volumes and to decontaminate 3D objects when a direct gas flow is used or the treatment time is adjusted.

Chapter 5

Material Compatibility Tests

In order to evaluate the cold atmospheric plasma (CAP) technology as an alternative decontamination method for planetary protection applications, the treatment has to be compatible with various materials used for explorations on planets or moons. In the following chapter, the influence of the plasma afterglow treatment to different materials is analysed using microscopic analysis, contact angle measurements and photoemission spectroscopy (XPS) to determine visible changes and variations of the chemical composition. The investigations were performed before and after the plasma treatment for the materials copper, brass, aluminium, stainless steel, polyoxymethylen (POM), polytetrafluorethylen (PTFE), epoxy, silicon and polyimide. The details of the examined materials are listed in Table 5.1.

5.1 Microscopic Analysis

At first, visible changes of the material samples were analysed before and after the plasma treatment to identify the influence of the plasma treatment. To investigate delayed alterations of the materials, sample images were analysed, immediately, 24 h and 7 days after the plasma treatment. For the investigations, copper, brass, aluminium, stainless steel, POM, PTFE,

Material Target	Description
copper	OF (oxygen free) CW008A (Gemmel Metalle, Fürth)
aluminium	AlZnMgCu1.5, EN AW-7075 (Gemmel Metalle, Fürth)
brass	CuZn37, CW508L (Gemmel Metalle, Fürth)
stainless steel	V2A, 1.4301 (LTO GmbH, Bielefeld)
POM	POM-C (Gemmel Metalle, Fürth)
epoxy	(Carbotec, Aachen, Conrad)
PTFE	(Beichler & Grünenwald GmbH, Löchgau)
silicon	Si-Wafer p-type (100) (Siegert Wafer, Aachen)
polymide	Kapton tape (42-020-00xx, Eurostat, Singapore)

Table 5.1: Materials for material compatibility tests.

epoxy, silicon and polyimide were treated in the setup (presented in Fig. 2.1), using the 2.6 l treatment chamber volume. The treatment was executed for low (approx. 40 % RH) and high (approx. 90 % RH) humidity conditions using the plasma parameters of $U = 6.0\,\mathrm{kV}$, $f = 10\,\mathrm{kHz}$ and $Q = 3.5\,\mathrm{l/min}$. The images of copper, brass and aluminium samples were taken with low magnification (DigiMicro Profi, dnp) to demonstrate the changes of the surface due to the plasma treatment. The material samples of POM, epoxy, polyimide, PTFE, silicon and stainless steel were investigated with a 100x magnification, using a Keyence digital microscope (VHZ100R, Keyence, Germany).

Fig. 5.1 shows images of copper, brass and aluminium samples, which were treated for $t = 60\,\mathrm{min}$ with 40 % and 90 % RH. The images reveal striking differences between the plasma treatment for low and high humidity conditions, especially for copper and brass. Note, that the visible round spots are remnants of the water droplets from the contact angle measurements, see chapter 5.2. It is assumed, that the surface interacts with the water droplets, so that the position of the droplet is visible. For copper under high humidity conditions, the appearance changes from a shiny red/brown surface before plasma treatment to a darker and matt surface, several days after the plasma treatment. For low humidity conditions, the copper sample shows blue areas, which most likely occur due to the interaction of nitric acid and copper to form coppernitrate. This colour change is not visible for samples which are treated under high humidity conditions. The observation is consistent with the spectroscopic analysis, which reveals low HNO_3 concentrations for high humidity conditions. In addition to copper, the surface of the brass samples shimmered green directly after the plasma treatment using low humidity and showed surface changes with dark areas. The colour change is however hardly visible in the figure due to the camera's exposure parameters. Nevertheless, this colour change can also be explained by the formation of coppernitrate, under the presence of HNO_3, as brass partly consists of copper. For high humidity conditions, brass and copper samples show a darker surface than before the plasma treatment. Aluminium reveals no blue colour after the plasma treatment, but shows also a slight change in the surface appearance. Under low humidity conditions the surface reveals some dark/brown structures and under high humidity conditions isolated brown points are visible. The observed deposits with a brown colour are most likely nitrogen residuals on the surface. In general, copper, brass and aluminium are non-noble metals, which preferential react with oxygen, while copper and aluminium could also form stable chemical compounds with nitrates. The formation of oxide and nitrate compounds on the sample surface explain the colour changes of the sample surfaces. However, the formation of oxide layers could also provide a chemical protection for further oxidation processes, which is known as the passivation of metals [204]. For a detailed analysis of the surface, the plasma treated samples were measured, using XPS spectroscopy (in chapter 5.3).

In contrast to copper, brass and aluminium, the plasma treated samples of POM, epoxy,

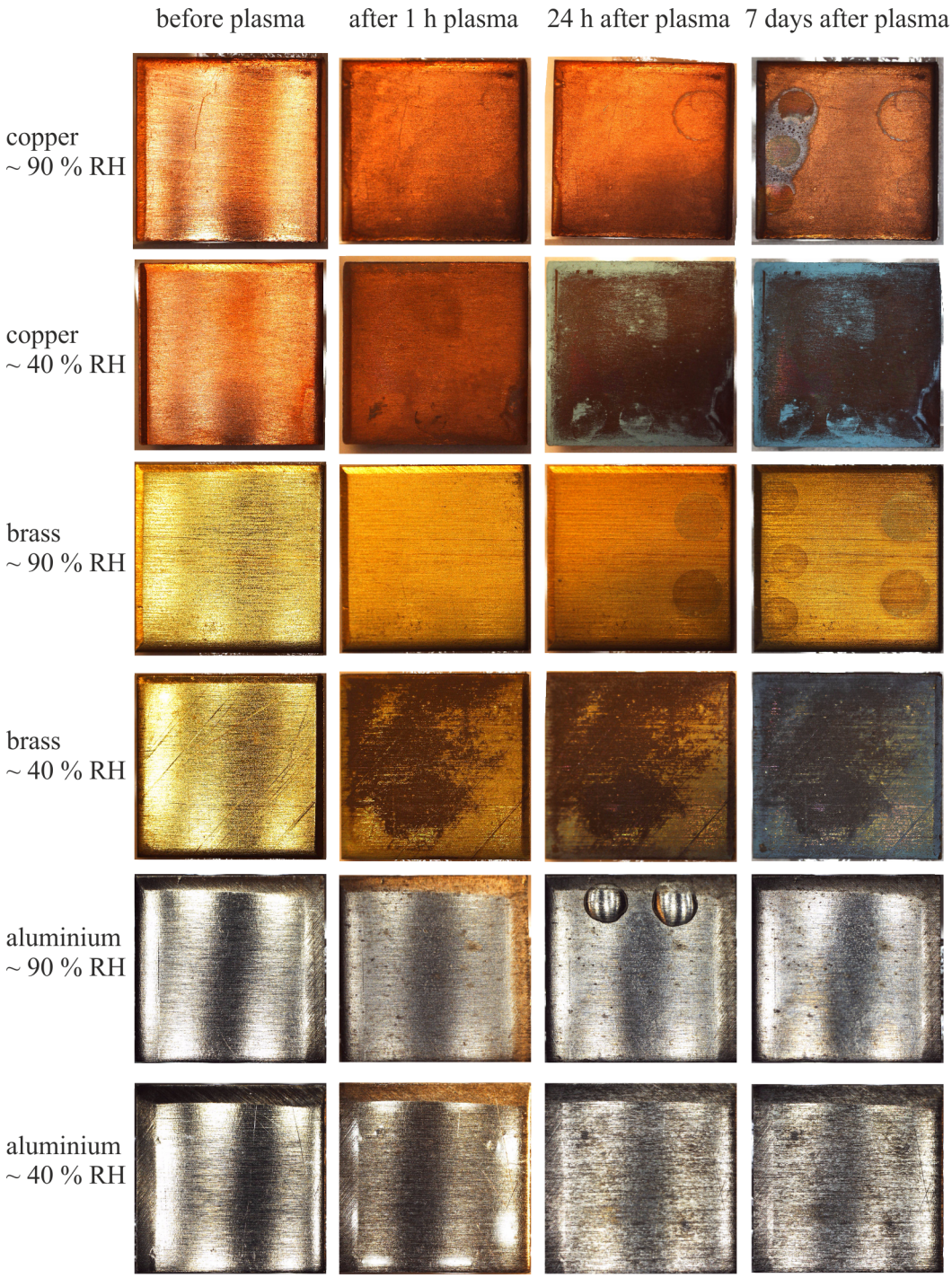

Figure 5.1: Illustration of the visual observation of copper, brass and aluminium before and after the plasma afterglow treatment for 40 % and 90 % relative humidity.

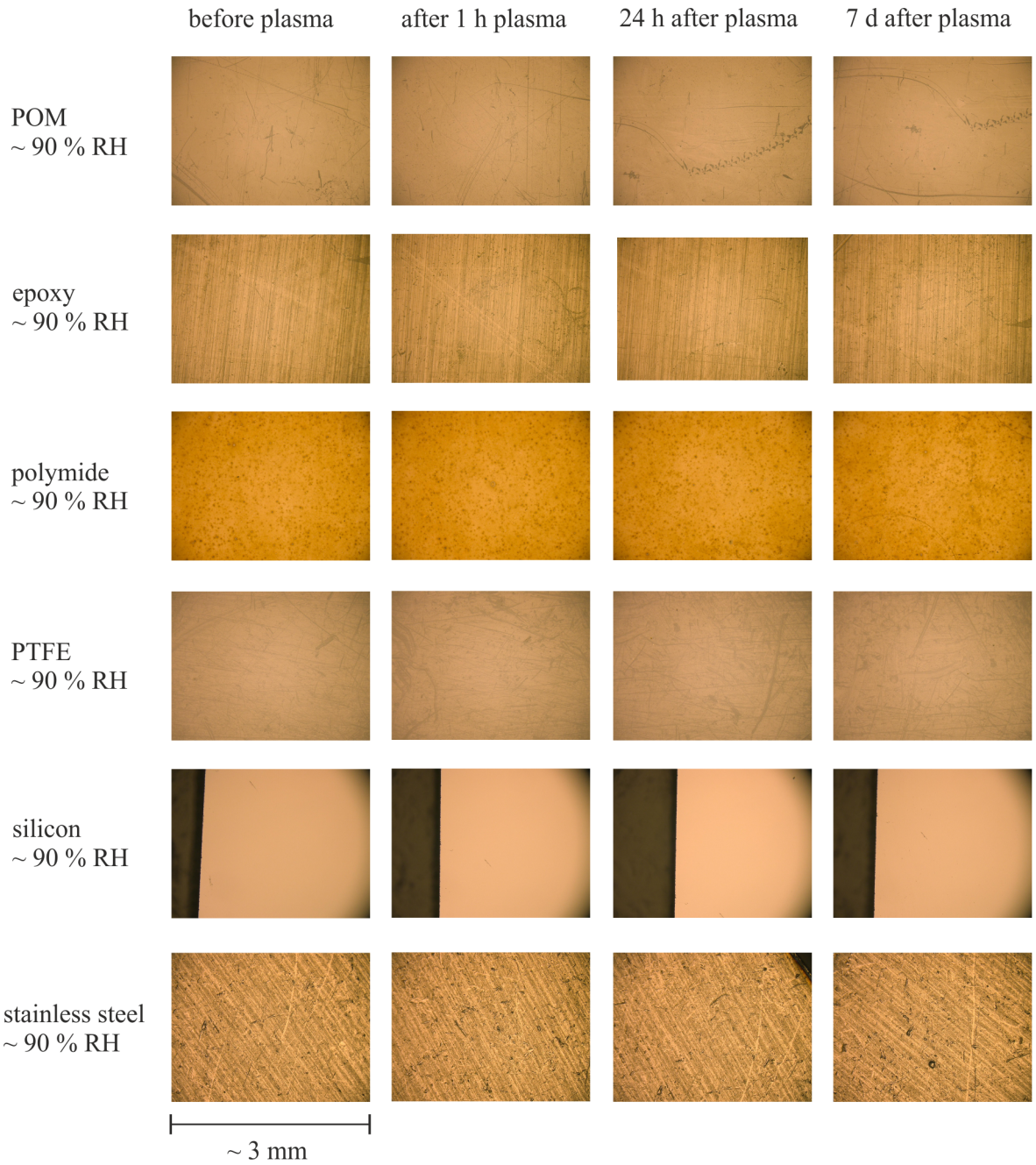

Figure 5.2: Illustration of the visual observation of POM, epoxy, polymide, PTFE, silicon and stainless steel before and after the plasma afterglow treatment under $\sim 90\,\%$ RH.

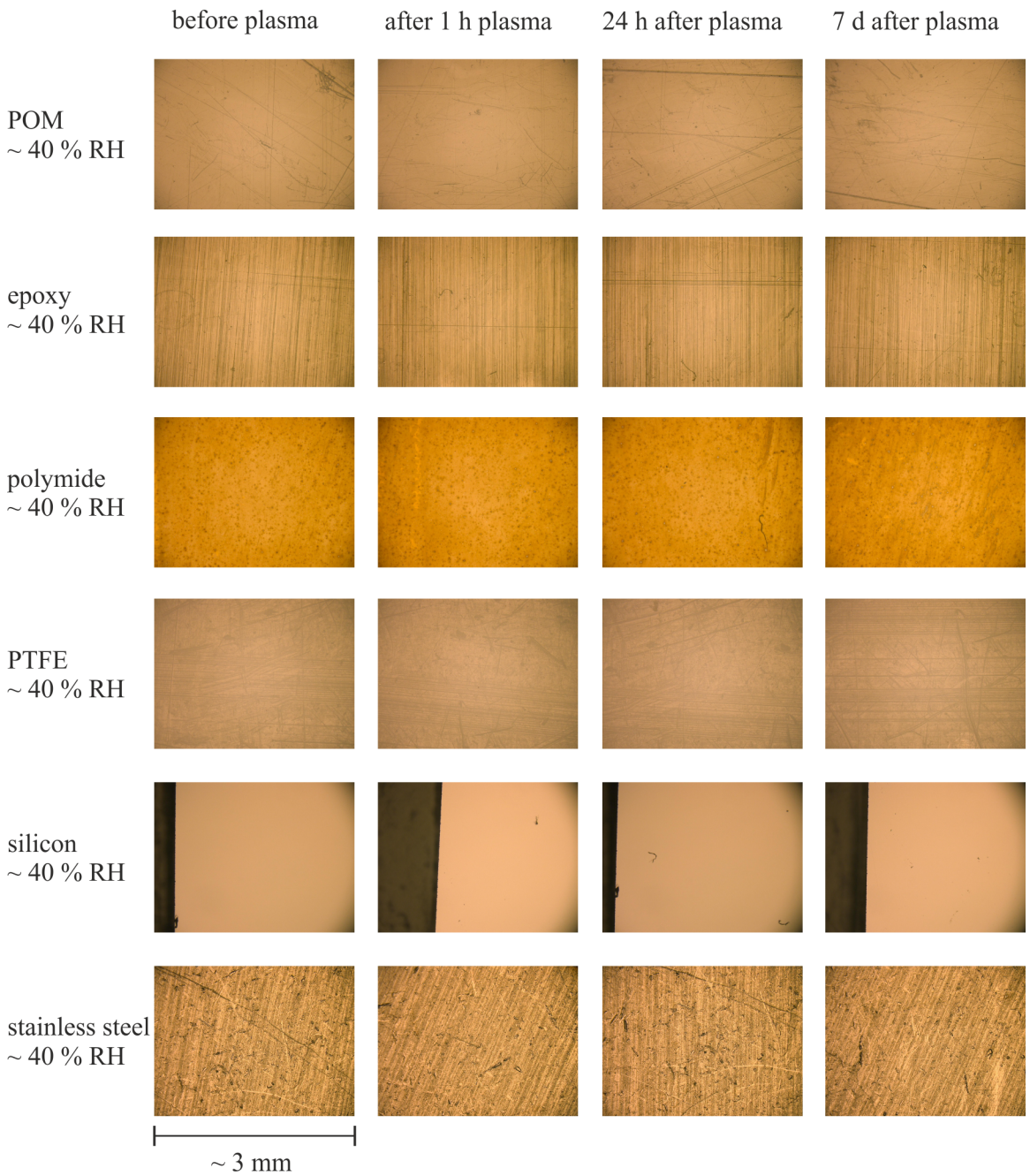

Figure 5.3: Illustration of the visual observation of POM, epoxy, polymide, PTFE, silicon and stainless steel before and after the plasma afterglow treatment under $\sim 40\,\%$ RH.

polymide, PTFE, silicon and stainless steel show no visible changes of the surface, as presented in Fig. 5.2 for $t = 30\,\text{min}$ and $\sim 90\,\%$ RH. Note, that silicon and stainless steel also develop natural oxide layers on the surface, which prevents the surface from further oxidation processes [204–206]. The visible changes in the structure are caused by different imaging positions of the samples.

Fig. 5.3 shows exemplary images of samples which were treated for $t = 30\,\text{min}$ and low humidity conditions of $\sim 40\,\%$ RH. Similar to Fig. 5.2, the samples show no visible changes of the surface after the plasma treatment. In addition, no visible differences of the plasma treatments are observed for low and high humidity conditions. Note, that for these materials also images for a plasma treatment of $t = 60\,\text{min}$ were investigated, but are not shown here, as they provide no additional results. In general, POM, PTFE, polymide, silicon and stainless steel are materials, which do not favourable react with oxygen. Thus, the surface of these materials show no alteration by the plasma treatment.

The microscopic investigations indicate that non-noble metals like copper, brass and aluminium are influenced by the plasma treatment in contrast to POM, epoxy, polymide, PTFE, silicon and stainless steel, which show no visible alteration for both humidity conditions. The visual observations indicate that the plasma treatment is compatible with materials, which do not favourable reacts with oxygen and NO_x molecules. Note, that silicon and stainless steel have native protecting oxide layers on the surface, which prevent further oxidation processes. In general, the treatment under low humidity conditions seems to influence the materials more than under high humidity conditions, which is explained by the higher HNO_3 and O_3 concentration in the circulating gas.

5.2 Contact Angle Measurements

In the present work, contact angle (CA) measurements are discussed to investigate possible surface modification by the plasma treatment. In general, wetting was first investigated by Thomas Young in 1805 [207, 208] and describes the behavior of a liquid, when the liquid contacts a solid. The contact angle measurement is one of the important tools to analyse the wettability of solid surfaces [207]. When a liquid not completely wet a surface, it forms a contact angle θ with the surface. The shape of a liquid drop on a homogeneous surface is influenced by the surface energy of the solid [209]. Fig. 5.4 illustrates different contact angles of a sessile drop on a surface. Fig. 5.4 a) shows a water droplet on an hydrophilic surface, b) on a surface without favourable wetting behavior and c) on an hydrophobic surface. The observation of the CA of a water droplet allows to identify if a solid surface is hydrophilic (CA: $\theta < 90°$) or hydrophobic (CA: $\theta > 90°$). The relation between the CA and the interface tensions of a liquid drop on an ideal solid surface is described by Young's equation [208, 210]:

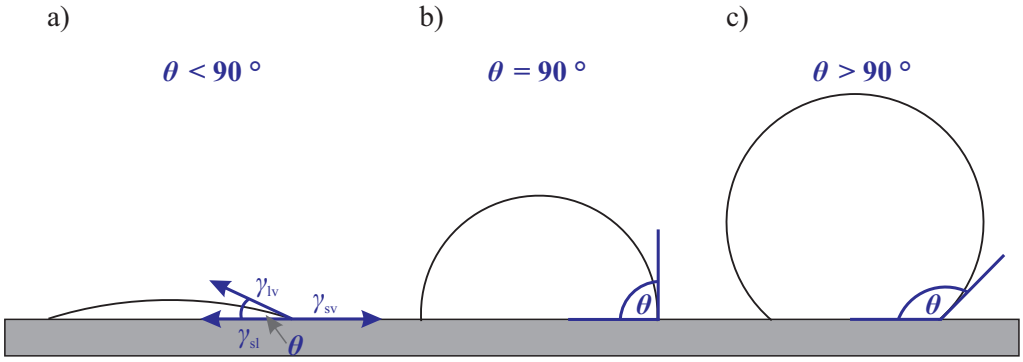

Figure 5.4: Schematic representation of a contact angle of a sessile water droplet on a surface (adapted from [210]). a) $\theta < 90°$ (hydrophilic). b) $\theta = 90°$. a) $\theta > 90°$ (hydrophobic).

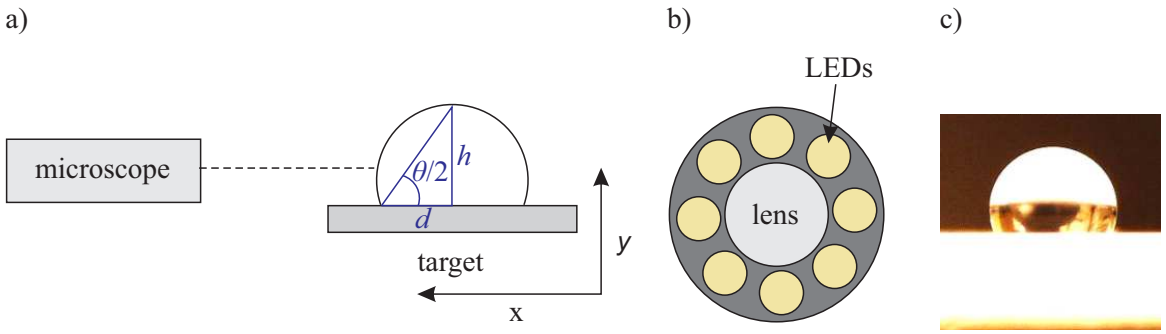

Figure 5.5: a) Schematic illustration of the contact angle measurement. b) Schematic view of the USB microscope lens, which is surrounded by eight LEDs to illuminate the sessile drop on the target. c) Exemplary picture of a water droplet on a PTFE target.

$$\gamma_{\mathrm{lv}}\cos(\theta) = \gamma_{\mathrm{sv}} - \gamma_{\mathrm{sl}}, \tag{5.1}$$

where θ denotes Young's contact angle and γ_{lv}, γ_{sv} and γ_{sl} the interface tensions of liquid-vapour, solid-vapour and solid-liquid, respectively [210]. The literature says, that if the surface tension of a liquid is below the surface energy of the solid, the wettability is high [211]. In addition, the surface energy could consist of polar and dispersion components. The polar components are caused by the interaction of permanent dipoles with other permanent dipoles or induced dipoles. The disperse components are caused by Van der Waals interactions. It is assumed that polar dominated solids interact favourable with polar dominated liquids and vice versa [212–214].

The CA was investigated by using a sessile water droplet on the target surface. A schematic illustration of the contact angle measurement is presented in Fig. 5.5 a). For the calculation of the contact angle, the $\theta/2$ method was used. For this method, it is assumed, that the sessile drop is a part of a sphere, so that the contact angle θ is calculated by the

following equation [210]:

$$\frac{\theta}{2} = \tan^{-1}\left(\frac{h}{d}\right). \tag{5.2}$$

Here, d is the radius and h is the height of the drop.

The contact angle measurements in the present work were executed, using a compact USB microscope (DigiMicro Profi, dnp). Therefore, a drop of approximately 1 µl was placed on the target surface. Afterwards, the position of the microscope was aligned to the droplet. The target including droplet was positioned on a $x - y$ variable table. This allowed to adjust the position of the droplet and the microscope in that way, that a sharp picture with a centred droplet was taken. Fig. 5.5 b) shows the lens of the microscope surrounded by 8 LEDs to illuminate the target. An exemplary image of the sessile water droplet on the PTFE surface is presented in Fig. 5.5 c).

In order to investigate the changes of the contact angle by the plasma treatment, the measurements were executed three times per sample, while the CA for one sample, is given by the mean value of three measured droplets. In detail, water (bidest, Carl Roth GmbH, Germany) was used as a test liquid for the examination. The total surface tension of water is $\gamma_{\mathrm{lv}} = 72.8\,\mathrm{mN/m}$ and consists of a polar ($\gamma_{\mathrm{lv}}^{\mathrm{p}} = 50.1\,\mathrm{mN/m}$) and a dispersion ($\gamma_{\mathrm{lv}}^{\mathrm{d}} = 22.7\,\mathrm{mN/m}$) component, while the polar component dominates.
The contact angle was measured for materials using plasma treatment times of $t = 0\,\mathrm{min}$, $t = 30\,\mathrm{min}$ and $t = 60\,\mathrm{min}$ and 40 % and 90 % RH. Afterwards, the measurement of the contact angle was repeated 24 h and 7 days after the treatment.

The measured contact angles of sessile water droplets are shown in Fig. 5.6 for the treated material samples using $t = 0\,\mathrm{min}$, $t = 30\,\mathrm{min}$ and $t = 60\,\mathrm{min}$, as well as $\sim 90\,\%$ RH and $\sim 40\,\%$ RH, respectively.

Fig. 5.6 presents the contact angle for a) PTFE, b) silicon, c) polymide, d) aluminium, e) stainless steel, f) brass, g) epoxy, h) POM and i) copper, before and after (immediate, 24 h and 7 days) the plasma treatment. The data in Fig. 5.6 a) confirm that the wettability of PTFE is not influenced by the plasma treatment. In addition, silicon, polymide, stainless steel, epoxy and POM reveal a slight decrease of the contact angle, (increased hydrophilic surface) and a recovery of the wettability after the plasma treatment. For silicon, polymide, stainless steel and POM, the treatment with 90 % RH and 60 min shows the lowest contact angle. Epoxy shows the smallest contact angle for 40 % RH, while no difference between 30 min and 60 min treatment time is observed.

The decrease of the contact angle of polymers by the plasma treatment and thus the increase of wettability could be explained by the plasma stimulated formation of polar groups, such as hydroxyl and carboxyl groups [39, 211]. The presence of polar groups could increase the surface energy of the solid and thus reduce the contact angle [39, 211]. The observation that the lowest contact angle of the polymers (POM and polymide) was detected under high humidity condition, agrees with the notion, that the OH concentration increases with an

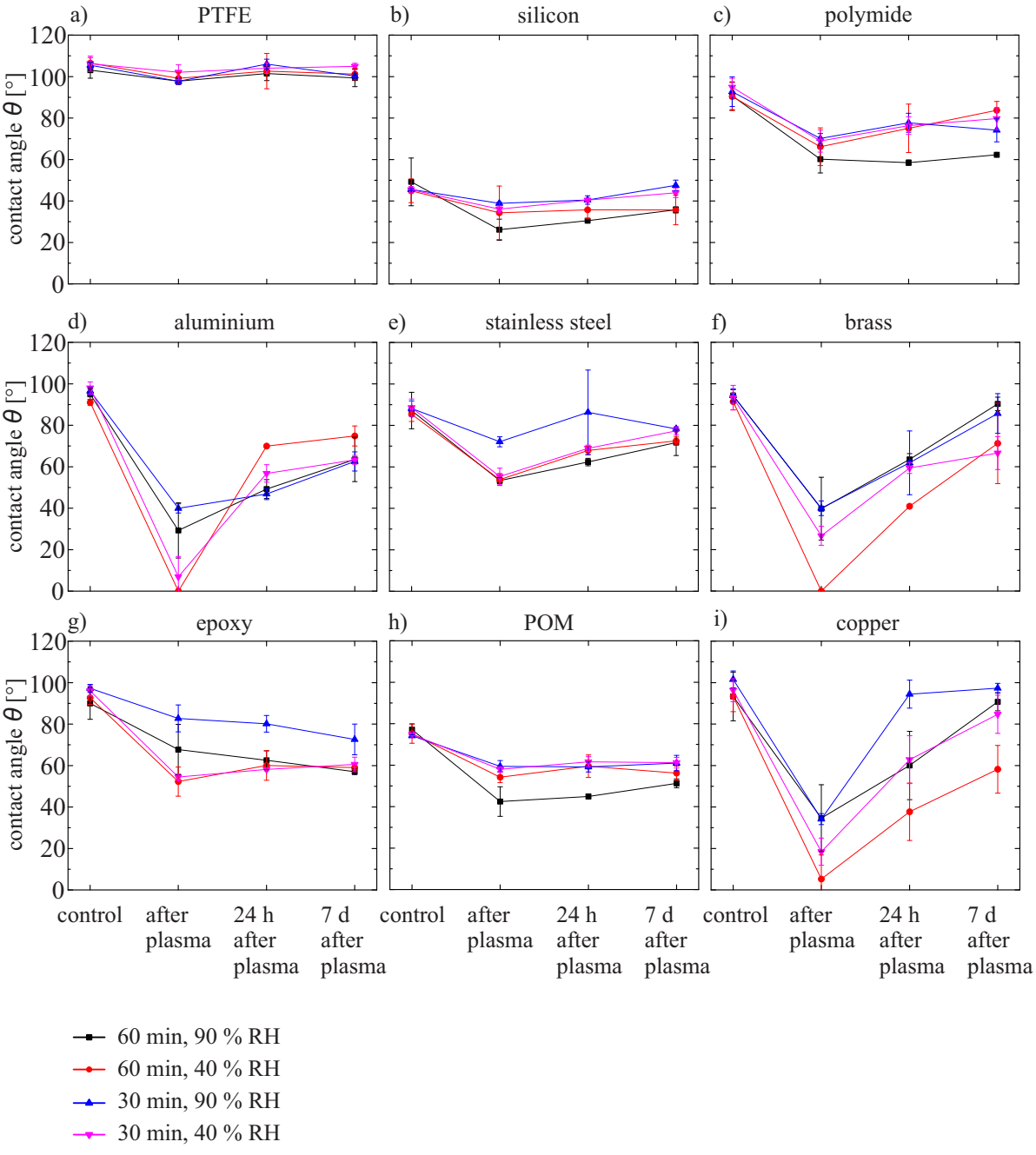

Figure 5.6: Contact angles for plasma afterglow treated materials under different conditions for $t = 30\,\text{min}$ and $t = 60\,\text{min}$ plasma treatment and 40 % and 90 % relative humidity. The contact angles are shown before and after (immediate, 24 h and 7 days) the plasma treatment for a) PTFE b) silicon c) polyimide d) aluminium e) stainless steel f) brass g) epoxy h) POM i) copper.

increase of the humidity. However, most of the plasma activated heavy particles interact only on the surface with the polymers [39].

Furthermore, the metals like aluminium, copper and brass, showed the highest reaction to the plasma afterglow treatment. For these materials, the contact angle is more influenced under low humidity conditions. In detail, the CA decreases for aluminium using 90 % RH and $t = 60$ min, from $\theta = 95°$ to $\theta = 30°$ and for 40 % RH from $\theta = 91°$ to $\theta = 0°$. Copper shows, comparable to brass, a decrease for 90 % RH and $t = 60$ min from $\theta = 101°$ to $\theta = 35°$ and for 40 % RH from $\theta = 93°$ to $\theta = 5°$. The enhanced decrease of the contact angles for 40 % RH is explained by increased amounts of HNO_3 and O_3, which was already discussed in chapter 3.5. Huang *et al.* [215] reported in their study that copper shows a superhydrophilic surface ($\theta < 10°$) when cupric oxide CuO is observed. Consecutively, the presented results in this chapter suggests that the oxidation is responsible of the decrease of the CA for copper, brass and aluminium. The enhanced surface wettability caused by the plasma treatment shows a recovery already after 24 h, which is called as the *aging effect*. Canal *et al.* [216] explain the reduction of the wettability by the decrease of hydrophilic groups on the surface and assume a reorientation of these groups towards the bulk phase of the material. Furthermore, they reported, that other factors, such as surface contamination from the environment, post-treatment oxidation or migration of contaminants to the surface could also contribute to the recovery of the hydrophilic surface. This aging effect could be found in the presented results in Fig. 5.6, which could be explained by the reorientation of hydrophilic groups for the plastic materials and for the metals by further oxidation and migration of contaminants to the surface.

In summary, the data show, that the contact angle changes dramatically for favourable oxidising metals like copper, brass and aluminium, while the CA of PTFE was not influenced by the treatment. Furthermore, copper, brass and aluminium were more affected for low humidity conditions of ~ 40 % RH. This result confirms the observations of the visible analysis in chapter 5.1, which show changes in the appearance of the materials copper, brass and aluminium, while the remaining materials show no alteration after the plasma treatment. For additional analysis of the surface changes, XPS investigations were done and presented in chapter 5.3.

5.3 XPS Measurements

X-Ray Photoelectron Spectroscopy (XPS) provides a useful tool to investigate the elemental composition of a solid sample surface [217]. The XPS spectroscopy uses X-rays to release electrons from the surface and measures the kinetic energy of these electrons. This technique is based on the photoelectric effect and was invented by Siegbahn and his group [218]. The measurement of the energy spectra allows to identify intensity peaks, which are characteristic

for the electronic structure of atoms. Furthermore, the ejected electrons in the sample could undergo energy loss processes, so that they do not show a concrete intensity peak. These electrons lead to a background signal in the XPS spectrum, while the emitted electrons without loss build a photoelectric peak above the background [217]. For a detailed XPS analysis, it is crucial to consider the influence of the background. For better understanding, the background and photoelectric peaks are marked in Fig. 5.7, which shows the XPS spectrum for untreated and treated PTFE samples.

For the analysis of the XPS spectrum it is necessary to respect further side effects, like the presence of Auger electrons. The Auger electrons could be ejected for example, when an electron from an L shell fills the unoccupied position of a K shell. This leads to a release of a photon which eject an other electron from an L shell, named as the Auger electron [219], which contribute to the KLL peak. In the presented spectra, Auger peaks are labelled as KLL and LLM. Note, that hydrogen cannot be analysed by XPS analysis [220]. More detailed information about XPS spectroscopy could be found in the literature [218, 221–223].

For the investigations, XPS spectroscopy was executed by Dr. Joachim Sann at the Physikalisch-Chemisches Institut (Justus-Liebig Universität) in Gießen. Therefore, copper, brass, aluminium, stainless steel, POM, PTFE, silicon and epoxy were treated for 60 minutes under high ($\sim 90\,\%$ RH) and low humidity ($\sim 40\,\%$ RH) conditions using $U = 6.0\,\mathrm{kV}$, $f = 10\,\mathrm{kHz}$ and $Q = 3.5\,\mathrm{l/min}$ and send to Gießen for the XPS analysis. Note, that the XPS analysis were executed more than one week after the plasma treatment. Furthermore, the polymide samples (tape) could not be analysed by XPS analysis, because of the incompatibility of the sample-tape-glue with the XPS vacuum ($p \sim 10^{-8}\,\mathrm{mbar}$). The samples were analysed using a XPS VersaProbe II (Physical Electronics GmbH) and monochromatic Al Kα radiation with 1486.6 eV as an appropriate X-ray source. The scan-step size was set to 0.8 eV. The software casaXPS was used for the evaluation of the spectral data.

In the following, XPS energy spectra are presented and the influence of the plasma treatment to the samples is discussed. For XPS analysis a direct comparison of the peak areas are not recommended due to variations of the electron detection. The casa XPS software provides a tool to calculate the percentage of the atomic concentrations on the sample surface, which can be used as a measure for comparison of the various samples [217].

The presented spectra show the detected electron intensity as a function of the electron binding energy. In Fig. 5.7, 5.8 and 5.9 the XPS analysis for plasma treated and untreated PTFE, silicon and POM samples are shown. The data show no significant influence of the plasma treatment to the respective samples for both humidity conditions. The results for silicon, PTFE and POM agree with the observations in chapter 5.2, which show a minor influence of the plasma treatment to the contact angle measurements. The investigations of the percentage atomic concentrations of silicon, PTFE and POM by casaXPS reveal no significant changes and are not shown here.

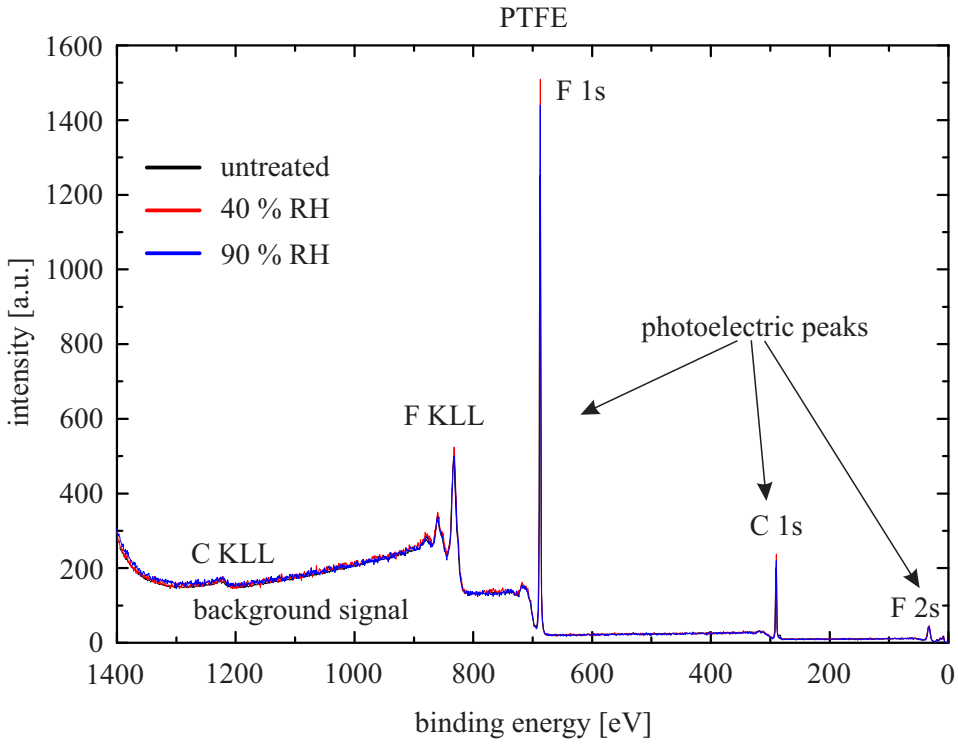

Figure 5.7: XPS spectra for untreated and plasma treated (high and low humidity conditions) PTFE samples.

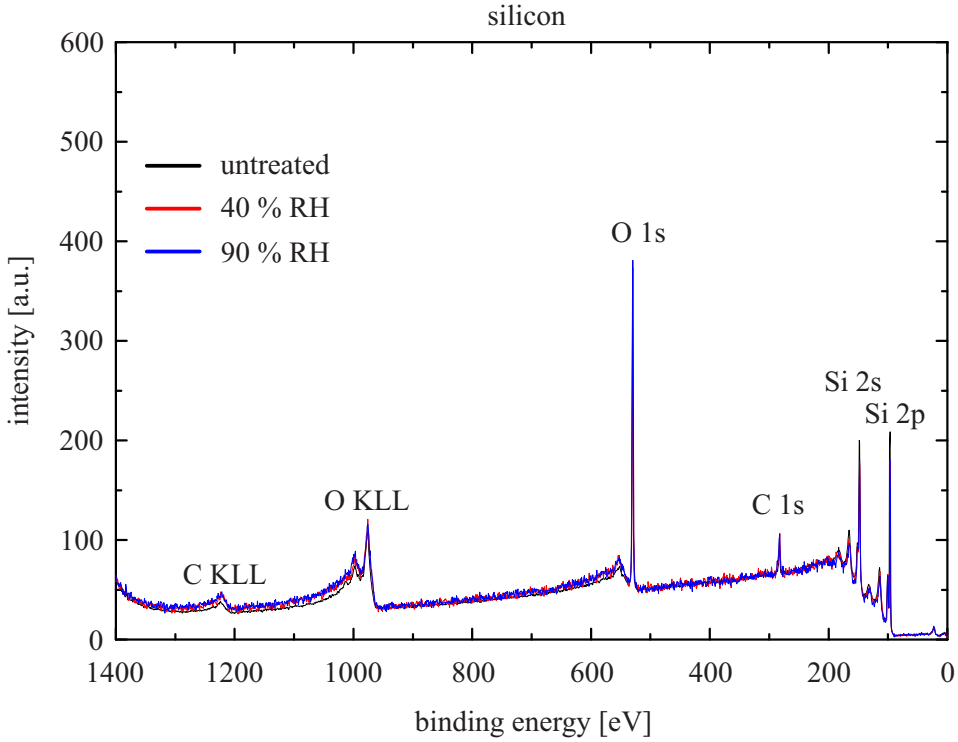

Figure 5.8: XPS spectra for untreated and plasma treated (high and low humidity conditions) silicon samples.

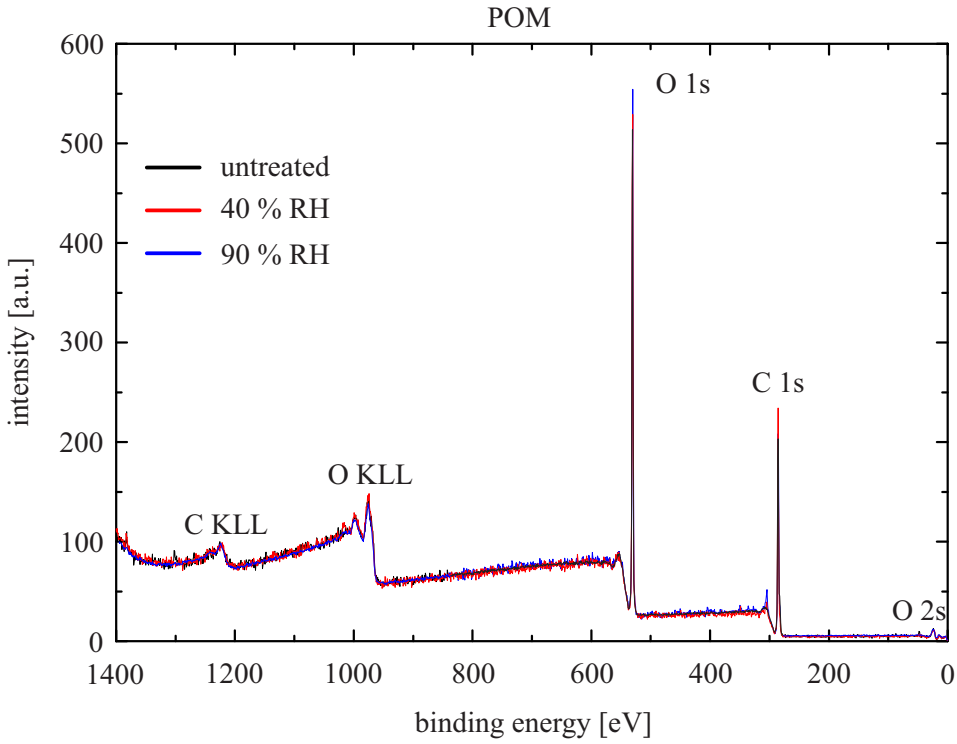

Figure 5.9: XPS spectra for untreated and plasma treated (high and low humidity conditions) POM samples.

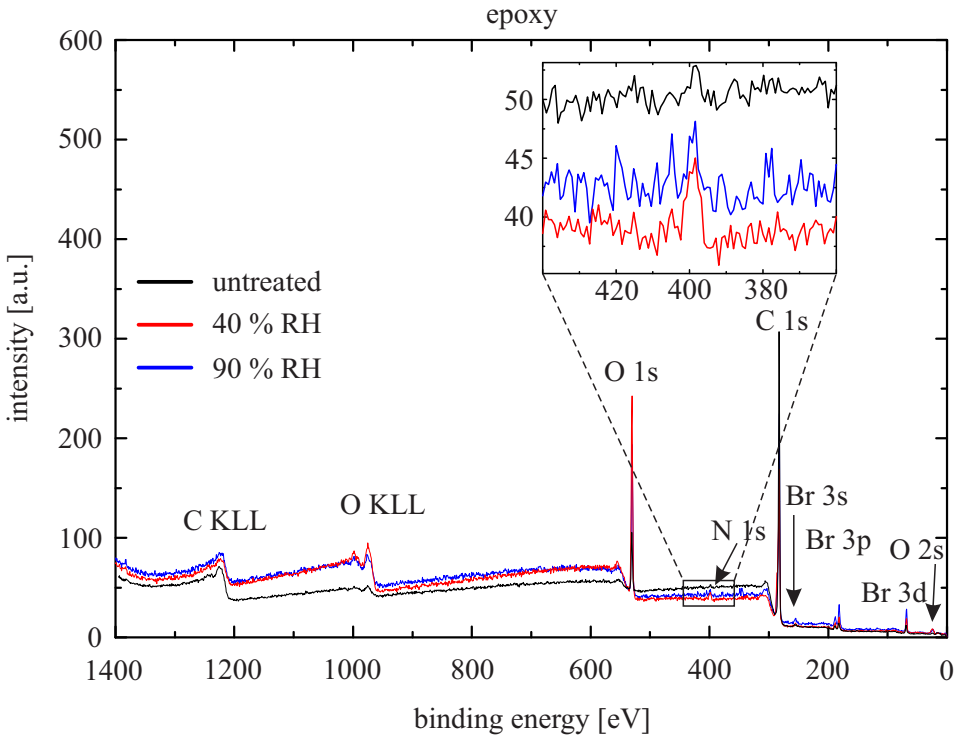

Figure 5.10: XPS spectra for untreated and plasma treated (high and low humidity conditions) epoxy samples. The inset illustrates a magnification of the N 1s peak.

Sample	O 1s	C 1s	N 1s	Br 3p
untreated epoxy	6.65	92.44	0.40	0.51
epoxy 40 %RH	25.68	71.20	1.71	1.41
epoxy 90 %RH	19.34	77.07	1.05	2.54

Table 5.2: Calculated percentage of atomic concentrations by casaXPS for untreated and plasma treated epoxy samples.

The contact angle measurements in chapter 5.2 show only a minor influence of the plasma treatment to the epoxy samples. In Fig. 5.10 the XPS spectra for untreated and plasma treated epoxy samples under high and low humidity conditions are illustrated. In total, there are only small visible variations in the spectrum. In particular, the O 1s peak intensity and the N 1s peak intensity are increased after the plasma treatment for both humidity conditions. A more detailed statement is possible by using the percentage atomic concentrations, which were calculated by the casaXPS software, shown in Table 5.2. The data show an increase of the oxygen and nitrogen amount on the sample surface, while the increase is higher under low humidity conditions. This result agrees with the observations in chapter 3, where the amount of reactive oxygen and nitrogen species are higher for low humidity conditions. In addition, the carbon concentration is reduced by the plasma treatment. This could be due to the relative increase of the oxygen amount on the surface by the plasma treatment or to a release of C atoms from the sample surface by reactions with the afterglow species. The release of C atoms from epoxy supports the observations in chapter 3, where an increase of HCHO and CO_2 molecules was detected during the plasma treatment. Since the electrode casing of the PACA is made of POM and PTFE, the generation of HCHO and CO_2 likely origins from these materials. However, POM and PTFE showed no alterations by the afterglow treatment, but the effect may occur when the materials are located close to the plasma region, so that also more reactive species and charged particles would interact with these materials.

The microscopic and contact angle measurements point out that the plasma treatment influences the surface of the copper samples. In Fig. 5.11 the XPS spectra for treated and untreated copper samples are illustrated. Fig. 5.11 a) shows that the background signal is different, which could be explained by surface variations of the samples. The difference is not caused by the plasma treatment but complicate the interpretation of the results. Fig. 5.11 b) also illustrates a magnified version of the XPS spectra around 950 eV, which refers to the observable Cu peaks in the spectrum. The measurement shows additional intensity peaks after the plasma treatment which indicates, that Cu is present in different states after the plasma treatment, for example Cu(II) as reported by Biesinger *et al.* [224]. Additionally, Fig. 5.11 c) shows some variations in the peak shape of Cu, which could be due to a change in the state of Cu. In addition to Cu, the N 1s peak shows a shift to higher binding energies, which indicates that nitrogen is also present in an other oxidation state. These results supports the notion that coppernitrate is formed and the amount of oxygen increases on the surface.

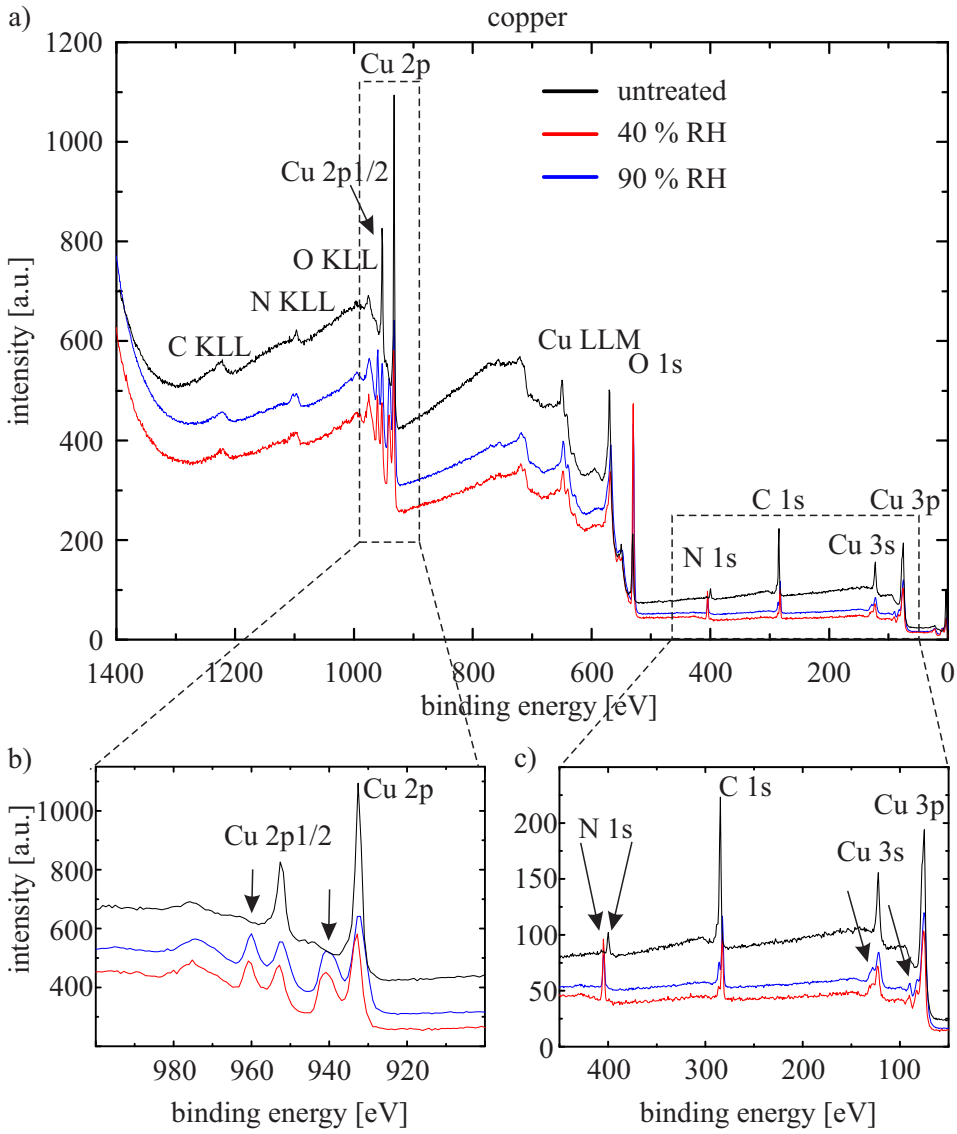

Figure 5.11: a) XPS spectra for untreated and plasma treated (high and low humidity conditions) copper samples. b) Magnification of the XPS spectra between $1000 - 900\,\text{eV}$. c) Magnification of XPS spectra between $450 - 50\,\text{eV}$.

Further investigations should be performed to analyse the detailed chemical variation on the copper surface to identify the formation of coppernitrate. The calculated percentage atomic concentrations are shown in Table 5.3. These results support the assumption, that the amount

Sample	O 1s	C 1s	N 1s	Cu 2p
untreated copper	26.38	59.48	4.17	9.98
copper 40 % RH	55.26	25.10	10.17	9.48
copper 90 % RH	53.80	28.57	6.15	11.48

Table 5.3: Calculated percentage of atomic concentrations by casaXPS for untreated and plasma treated copper samples.

of O and N atoms is increased on the copper surface after the plasma treatment. Similar to epoxy, the increase of O and N is higher for low humidity conditions.

In Fig. 5.12 and 5.13 the XPS spectra of plasma treated and untreated aluminium and brass samples are shown. Similar to the copper sample, the samples show a strong variance in the background signal which complicates the interpretation of the results. However, similar to the copper sample in Fig. 5.11, the shift of the N 1s peak to higher binding energies indicates that N atoms are present in other oxidation states. The calculated percentage atomic concentrations for aluminium and brass are shown in Table 5.4 and Table 5.5.

Sample	O 1s	C 1s	Mg 1s	Zn 2p	Al 2p	Cu 2p
untreated aluminium	47.44	25.91	1.51	0.27	24.80	0.07
aluminium 40 % RH	59.26	24.39	0.79	0.09	15.47	
aluminium 90 % RH	55.56	24.56	3.22	0.54	16.12	

Table 5.4: Calculated percentage of atomic concentrations by casaXPS for untreated and plasma treated aluminium samples.

Sample	O 1s	C 1s	N 1s	Cu 2p	Zn 2p
untreated brass	25.08	62.57	8.09	3.75	0.51
brass 40 % RH	56.37	26.21	8.79	4.46	4.17
brass 90 % RH	52.75	27.12	5.89	4.59	9.65

Table 5.5: Calculated percentage of atomic concentrations by casaXPS for untreated and plasma treated brass samples.

For the aluminium samples the casaXPS software could not calculate an appropriate value for N and Cu. Nevertheless, the results for aluminium indicate the amount of oxygen increases slightly, but not in this amount as for copper. This could be explained by the fact, that aluminium often has a natural oxide layer which impedes further corrosion [225]. The results for brass in Table 5.5 show a similar trend like the copper sample in Table 5.3, which is based on the fact, that copper is a component of brass.

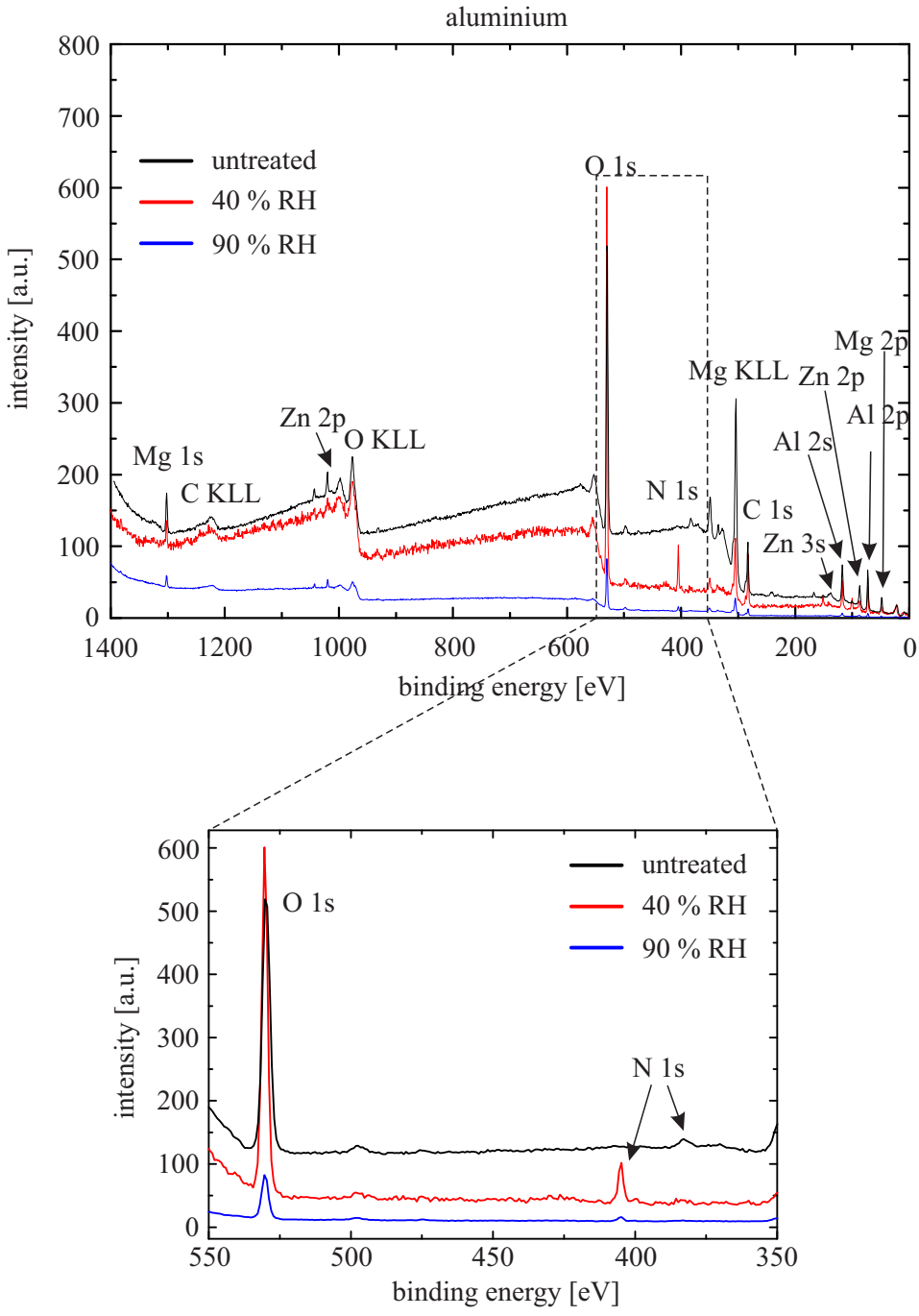

Figure 5.12: XPS spectra for untreated and plasma treated (high and low humidity conditions) aluminium samples. The magnification shows a shift of the N 1s peak.

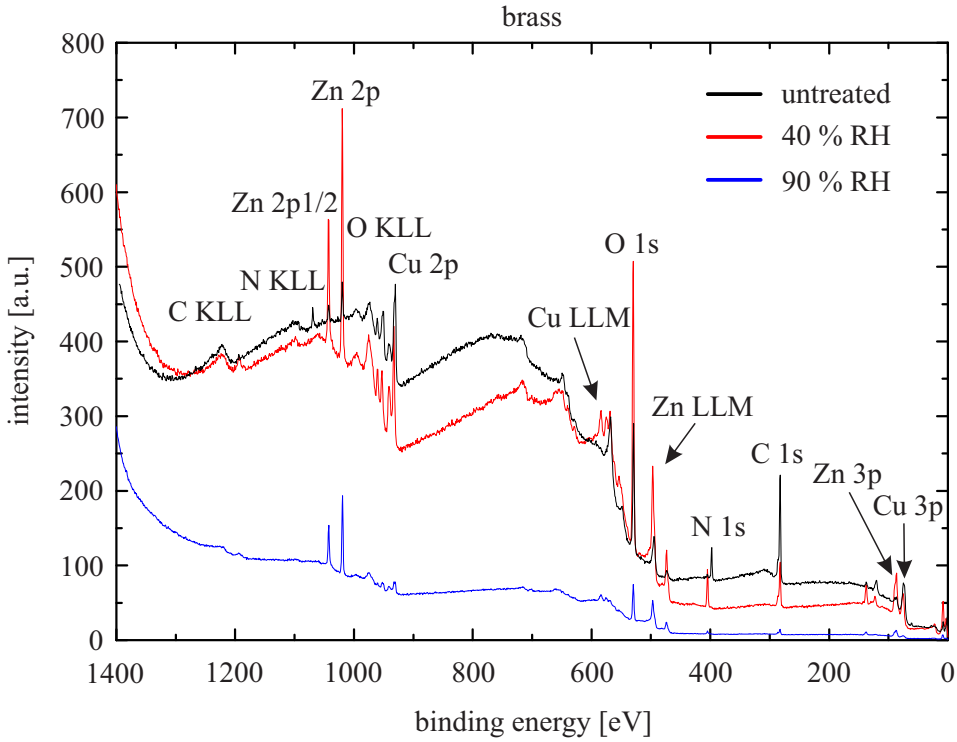

Figure 5.13: XPS spectra for untreated and plasma treated (high and low humidity conditions) brass samples.

Fig. 5.14 illustrates the detected XPS spectra for untreated and plasma treated stainless steel samples. Similar to copper and aluminium, the background signal differs for the samples, but the analysis of the spectrum shows no shift for the N 1s intensity peak. To investigate an influence of the plasma treatment, the calculated percentage atomic concentrations are analysed, shown in Table 5.6. The data show a slight increase of the O and N molecules after

Sample	O 1s	C 1s	N 1s	Fe 2p	Cr 2p	Ni 2p
untreated stainless steel	30.29	58.93	0.80	7.72	2.17	0.09
stainless steel 40 % RH	40.82	51.49	3.34	3.00	1.35	
stainless steel 90 % RH	35.68	61.29	1.58	1.46		

Table 5.6: Calculated percentage of atomic concentrations by casaXPS for untreated and plasma treated stainless steel samples.

the plasma treatment, while the increase is higher for the low humidity conditions. Compared to copper, brass and aluminium, stainless steel surface shows a minor reaction to the plasma treatment.

In summary, the plastic materials POM, epoxy and PTFE, as well as silicon and stainless steel, show a negligible change of the chemical composition of the surface after the plasma treatment. This agrees with the observations of the contact angle measurements. Further-

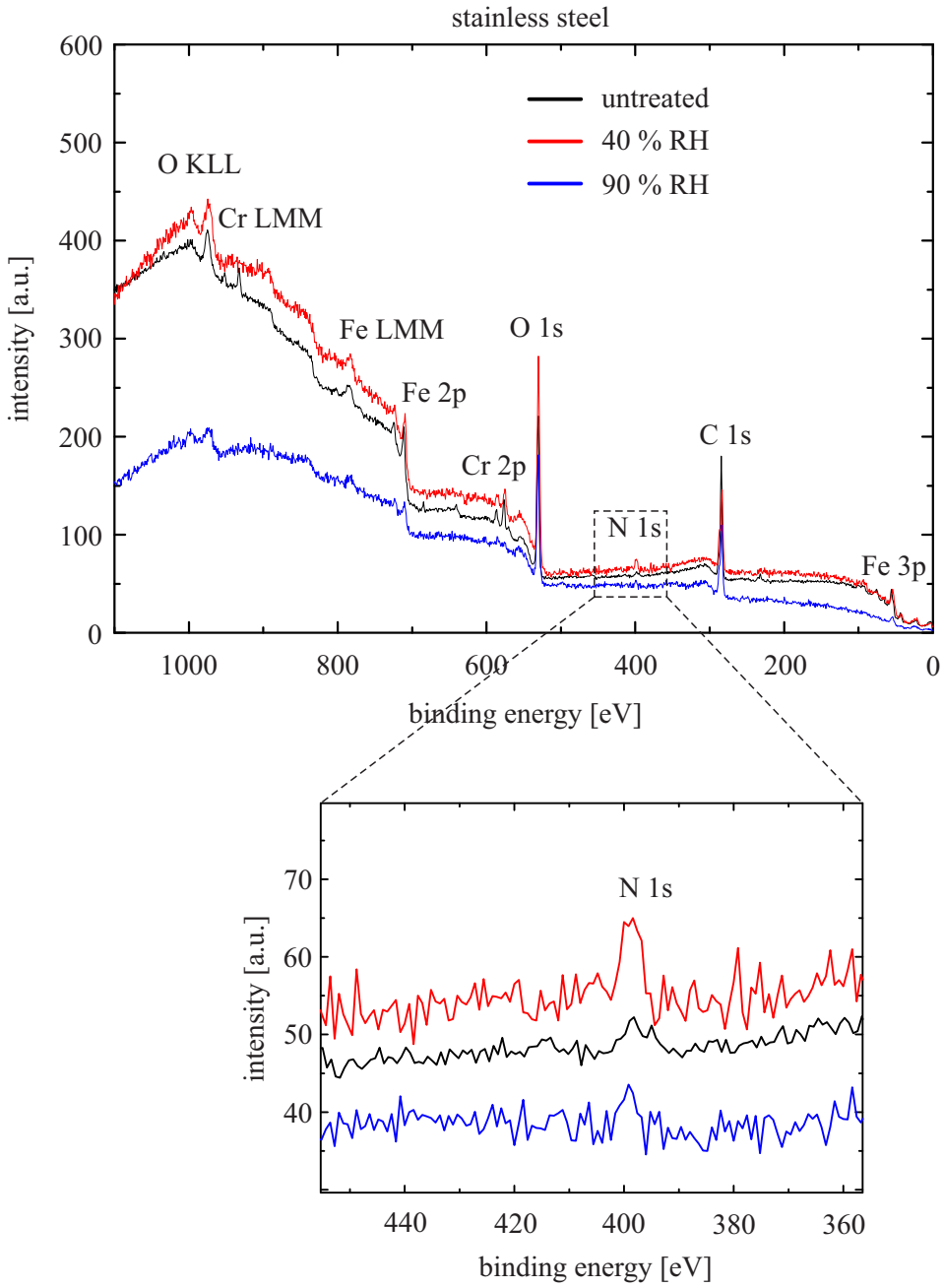

Figure 5.14: XPS spectra for untreated and plasma treated (high and low humidity conditions) stainless steel samples. The magnification shows no shift of the N 1s peak.

more, copper, brass and aluminium show the strongest change in the chemical composition of the surface which also supports the observation that the surface of these materials shows colour changes in chapter 5.1 and changes of the surface wettability in chapter 5.2. Additionally, higher humidity conditions lead to reduced reactions with the sample surfaces compared to low humidity conditions.

5.4 Summary

Material compatibility tests of the plasma afterglow treatment were performed for copper, brass, aluminium, PTFE, POM, epoxy, polymide, silicon and stainless steel. The visual analysis shows the alteration of metals like aluminium, copper and brass by the plasma treatment. Under low humidity conditions, copper and brass develop a blue colour on the surface, which indicates the formation of coppernitrate caused by the presence of HNO_3. Furthermore, aluminium shows a brown colour on some of the treated samples, which can be due to the reaction with NO_x molecules. The observations of copper, brass and aluminium go along with the contact angle measurements, which identify the biggest changes for low humidity conditions. Except of PTFE, all tested materials show an increased wettability (contact angle decrease), which indicates that polar molecules or oxygen are accumulated on the surfaces. This effect recovers after a few days, which agrees with the literature [15, 215, 216]. In contrast to copper, brass and aluminium, the plastic materials show only a slight variance in the wettability of the surface by the plasma treatment. In addition, stainless steel and silicon are minimal affected by the treatment.

The visual and wettability investigations are supported by the XPS analysis of the sample surfaces. The XPS analysis, show minor changes in the chemical surface composition of PTFE, POM, epoxy and silicon and suggest that these materials are negligible influenced by the plasma treatment. However, the favourable oxidising materials like copper, brass and aluminium show a strong reactivity to the plasma treatment under low humidity conditions. This reactivity decreases for high humidity conditions due to reduced concentrations of O_3, N_2O and HNO_3. Furthermore, the XPS analysis show a change of the oxidation states of nitrogen and copper, which indicates the reaction of RONS with the surface. In agreement with the contact angle measurements, the XPS investigations reveal the highest surface concentration of oxygen and nitrogen for the plasma treatment under low humidity conditions.

In conclusion, the executed investigations propose a high humidity treatment for microbial inactivation and the use of not favourable oxidising materials. Further investigations of copper, aluminium and brass are recommended to analyse the reaction depth of the afterglow species into deeper surface layers of these materials.

Chapter 6

Conclusion and Outlook

This thesis aims at the application of the CAP technology for the decontamination of spacecraft equipment, motivated by the international planetary protection policies. For this purpose, a new plasma afterglow circulation apparatus (PACA) was developed, which is based on a surface micro-discharge (SMD) plasma source. The PACA was characterised for different plasma conditions by executing spectroscopic investigations of the reactive afterglow species, by investigations of the inactivation efficiency using various treatment volumes and 3D barriers and by executing material compatibility tests. The combination of these three different research focuses and the mutual confirmation of the results lead to an improved fundamental understanding of the chemical reaction processes and afterglow composition of the used plasma decontamination method.

In chapter 2 the PACA and the corresponding electrode system based on the SMD technology was introduced. The special geometry of the apparatus and the SMD electrode provide an afterglow circulation and a resulting plasma boosting associated with an enhancement of the reactive afterglow species concentration. In detail, the PACA enables to change the treatment volume, the gas flow and the adaption of the operating humidity condition. Due to the circulation of the afterglow, the long-living reactive species interact with the target in a distance to the plasma discharge region, with the consequence that charged particles, short-living species and UV light do not participate in the interaction.

In chapter 3, the spectroscopic characterisation of the plasma afterglow composition was presented to enhance the understanding of the afterglow reactivity and the complexity of the reaction mechanisms. For the investigations, the distribution of the ozone concentration, the influence of the humidifier, the gas flow rate, the humidity condition, the power consumption and the use of artificial gases were studied. In general, the spectroscopic analysis shows that the generation of O_3, N_2O, NO_2, HCHO and HNO_3 depends on the operating conditions. The investigations of the ozone distribution and of the humidifier indicate, that ozone is negligibly influenced by passing the humidifier water. However, the afterglow composition for high humidity conditions supports the theoretical assumptions that the increase of H_2O molecules

changes the chemical pathways in the discharge region which leads to a reduced formation of O_3, HCHO and N_2O molecules. Reduced amounts of reactive nitrogen and oxygen molecules for high humidity conditions were consistent with the results for the material compatibility in chapter 5.

The studies of the afterglow composition in dependence to the gas flow rate show an increase of the afterglow species by the reduction of the gas flow, due to the reduction of recombination processes and the increase of the residence time of the molecules in the discharge region. The investigations of the afterglow composition for different humidity conditions depict unexpected results in addition to the reduction of HCHO, O_3 and N_2O by increasing humidity. In detail, the detected HNO_3 concentration strongly depends on the humidity conditions, due to condensation of HNO_3 within the PACA. These findings are supported by the results from chapter 5. The investigations of the afterglow composition reveal the proportionality of the O_3, N_2O, HCHO and HNO_3 production to the power consumption and that the PACA operated in an ozone dominated regime and not in a NO_x dominated one. In general, the power consumption varies with the humidity condition, gas composition and treatment time. For future investigations, the use of a higher power consumption would allow to analyse the gas composition for a NO_x dominated afterglow composition. These investigations could improve the understanding of the transformation from the O_3 dominating mode to the NO_x dominating mode.

Furthermore, a NO_2 formation originated by HNO_3 molecules was found for the afterglow composition, after the extinction of the plasma and the reduction of O_3. In addition, ozone quenching processes were observed as a result from NO_x compounds in the PACA. More detailed studies are required to investigate the critical behavior of gaseous and condensed HNO_3 in terms of different humidity conditions. It could be beneficial to perform theoretical simulations of the plasma afterglow generation to enhance the understanding of the important reaction processes and to confirm the experimental findings of the presented work.

In addition, the use of different carrier gases in the PACA shows, that the afterglow chemistry changes by the modulation of the gas composition, which provides interesting subjects for future investigations of the PACA. In detail, the investigation of the NO_2 generation after the plasma extinction could provide additional insights in the reaction processes. With the developed PACA and the embedded spectroscopic measuring tools for the afterglow composition, the ideal platform was build to perform a manifold of novel plasma experiments. To realise a reproducible plasma treatment procedure, the spectroscopic analysis of the afterglow composition can be used as a monitoring parameter to identify environmental influences and alterations of the PACA.

To evaluate the PACA as an innovative apparatus for microbiological inactivation, the plasma treatment of *Bacillus atrophaeus* was executed and discussed in chapter 4. In summary, the bacterial endospores were successfully inactivated using different treatment chamber

volumes of 0.54 l, 1.8 l and 2.6 l. The investigations show a 4.4 log reduction after $t = 30$ min in the largest treatment chamber. In addition, the inactivation of *B. atrophaeus* samples, using 3D barriers, points out the necessity to extend the treatment time. However, the direct application of a gas flow by using an additional fan inside the treatment chamber, improves the inactivation efficiency for the treatment of 3D objects. The investigations with gas permeable packages for *B. atrophaeus* samples prove the inactivation of the target through a diffusion barrier. This is beneficial for the decontamination of already packed samples and to maintain the degree of sterility after the decontamination process. The results of the microbiological investigations suggest the use of the PACA as an efficient inactivation apparatus and build the foundation for a successful up-scaling of the PACA, in order to decontaminate large 3D objects. In future research the focus of multiple plasma electrodes would enable to increase the treatment chamber volume to decontaminate large objects. For the evaluation of the PACA decontamination process in terms of planetary protection requirements, additional bacterial endospores have to be investigated to prove the wide applicability of the presented inactivation method.

To test the influence of the PACA treatment on sensitive materials, the compatibility of the plasma treatment was analysed for a broad range of materials (copper, brass, aluminium, silicon, POM, PTFE, polymide, stainless steel and epoxy) in chapter 5 to simulate the interaction with spacecraft materials. The observations of visible changes of copper, brass and aluminium due to oxidation processes were confirmed by contact angle and XPS measurements. The contact angle measurements show a strong increase of the wettability directly after the plasma treatment, but also a wettability recovery after several days. Furthermore, the results reveal that the materials are more influenced for low humidity conditions, due to the increase of reactive oxygen and nitrogen species, which were evidenced by spectroscopic analysis in chapter 3. For the copper, brass and aluminium samples, the XPS spectra indicate changes of the oxidation states of copper and nitrogen atoms, which is a hint for the reaction of HNO_3 with the copper surface. The remaining material samples silicon, POM, PTFE, polymide, stainless steel and epoxy show only a minor reaction to the plasma treatment and are thus suitable for further plasma decontamination experiments.

In conclusion, this thesis provides a detailed analysis of a newly designed PACA in order to inactivate bacterial endospores in and on complex objects. The broad research focus significantly improves the understanding of the afterglow reaction processes for different ambient conditions, operating with a SMD electrode at ambient air. For future decontamination experiments, the results of the presented work suggest the use of high humidity conditions to maximise the inactivation efficiency and to provide a compatible plasma treatment for a broad range of materials. The results further show the necessity to analyse the afterglow compositions after the plasma-on phase to gain insight into the complexity of the reaction processes and the need to monitor the power consumption and the afterglow composition

during the decontamination process. The use of these characterisation methods provides the basis to verify the PACA as an evaluated decontamination method in terms of planetary protection application. In general, the up-scaling and evaluation of the PACA for the decontamination of spacecraft equipment will open many additional application and research fields for the PACA utilisation in space and on earth, such as wastewater treatment, emission control, deodorisation, agriculture and food processing.

LIST OF ABBREVIATIONS

APPJ atmospheric pressure plasma jet

AC alternating current

BSA bovine serum albumin

CAP cold atmospheric plasma

cfu colony forming units

COSPAR Committee on Space Research

DBD dielectric barrier discharge

DBGD dielectric barrier grating discharge

DC direct current

DHMR dry heat microbial reduction

DLR Deutsches Zentrum für Luft- und Raumfahrt

D-value decimal reduction value

ECSS European Cooperation for Space Standardisation

ESA European Space Agency

FE-DBD floating electrode dielectric barrier discharge

FTIR Fourier Transformation Infrared

ICSU International Council of Scientific Unions

IPA isopropylic alcohol

MRSA methicillin-resistant *Staphylococcus aureus*

NASA National Aeronautics and Space Administration

OAUGDP one atmosphere uniform glow discharge plasma

SEM Scanning Electron Microscopy

SMD surface micro-discharge

UV ultraviolet light

PACA plasma afterglow circulation apparatus

PBS phosphate buffered saline

PET polyethylen

PFA Perfluoraloxy alkanes

PTFE Polytetrafluorethylen

POM Polyoxymethylene

RF radio frequency

RH relative humidity

VHP vapour hydrogen peroxide

XPS X-Ray Photoelectron Spectroscopy

WD working distance

Appendix A

Inactivation Studies

Plasma Source	**Target**	**Reference**	
corona discharge (pin to plate)	yeasts, vegetative bacteria, bacterial endospores	Scholtz *et al.* [64] 2010	
corona discharge (pulsed)	*E. coli* human tooth canal	Bussiahn *et al.* [65] 2010	
corona discharge (in water)	vegetative bacteria bacterial endospores	Joubert *et al.* [66] 2012	
corona discharge (jet and indirect)	food packaging microorganisms on food	Lee/Nthenge *et al.* [68, 69]	
glow discharge	*Pseudomonas fluorescens*	Laroussi *et al.* [75] 1996	
glow discharge (OAUGDP)	bacteria, bacterial endospores, yeast and bacterial viruses	Montie *et al.* [76] 2000	
glow discharge (APPJ)	*Demodex folliculorum*	Daeschlein *et al.* [87] 2010	
glow discharge (APPJ)	*Bacillus atrophaeus*	Lim *et al.* [88] 2007	
glow discharge (APPJ)	sensitive materials *E. coli* and *B. atrophaeus*	Weltmann *et al.* [83, 89] 2007/2008	
DBD	*B. subtilis* *Aspergillus niger*	Trompeter *et al.* [99]	
DBD (FE-DBD)	*Staphylococci, Streptococci* and *Candida* species of yeast	Fridman *et al.* [97] 2007	
DBD (direct mode)	*D. radiodurans* planetary protection	Cooper *et al.* [50] 2009	
DBD (DBGD)	*E. coli*	Gallagher *et al.* [102] 2007	
DBD (direct)	etching of polimers and *B. subtilis*	Kuzminova *et al.* [103] 2017	
DBD	food products	review of Liao *et al.* [105] 2017	
DBD	*E. coli*, *Listeria*	Lu *et al.* [109] 2014	

Table A.1: Overview of studies for inactivation of microorganism using corona discharges, glow discharges and DBDs.

Appendix B

FTIR Reference Spectra

This appendix lists the used reference spectra of the individual gas components, which were used to interpret the detected FTIR absorption spectra. Note, that the Calcmet software uses the reference spectra to calculate the individual concentration of the gas components. The Figures B.9 and B.10 show reference spectra for different FTIR parameters. Nevertheless, these spectra were used to qualitatively interpret the detected absorption spectra.

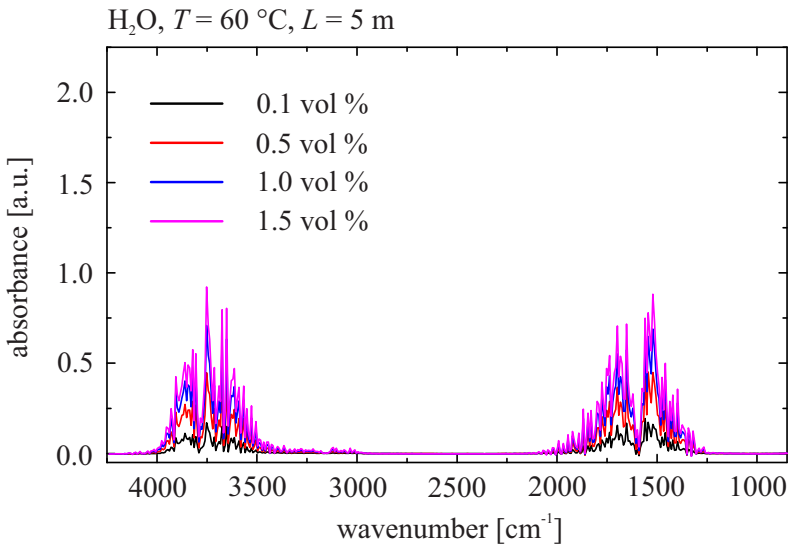

Figure B.1: H_2O reference spectra for 0.1, 0.5 1.0 and 1.5 vol %.

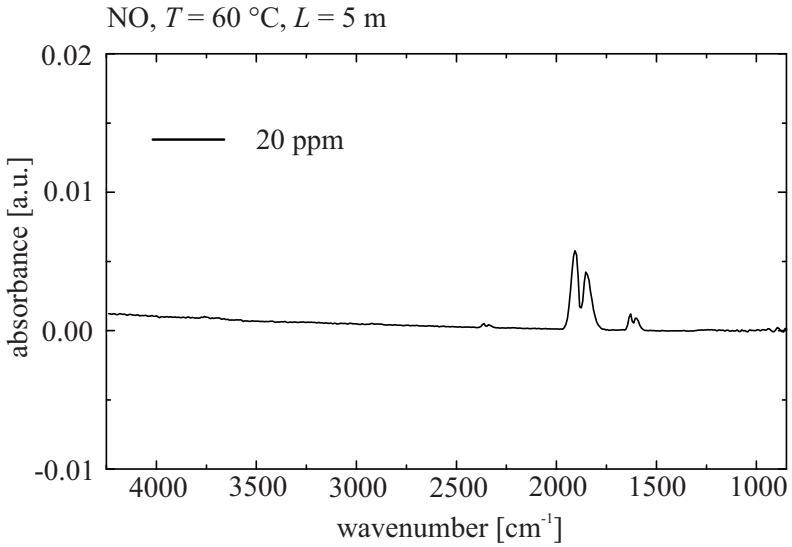

Figure B.2: Reference spectrum for 20 ppm NO.

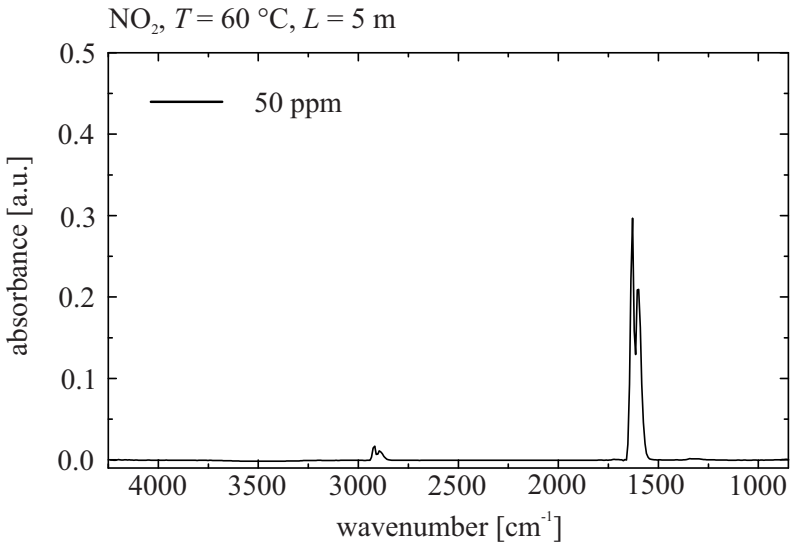

Figure B.3: Reference spectrum for 50 ppm NO_2.

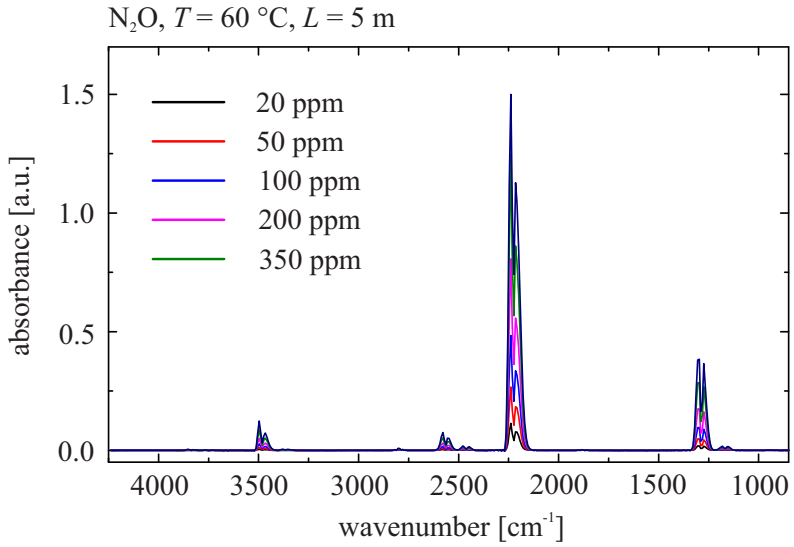

Figure B.4: N_2O reference spectra for 20 ppm, 50 ppm, 100 ppm, 200 ppm and 350 ppm.

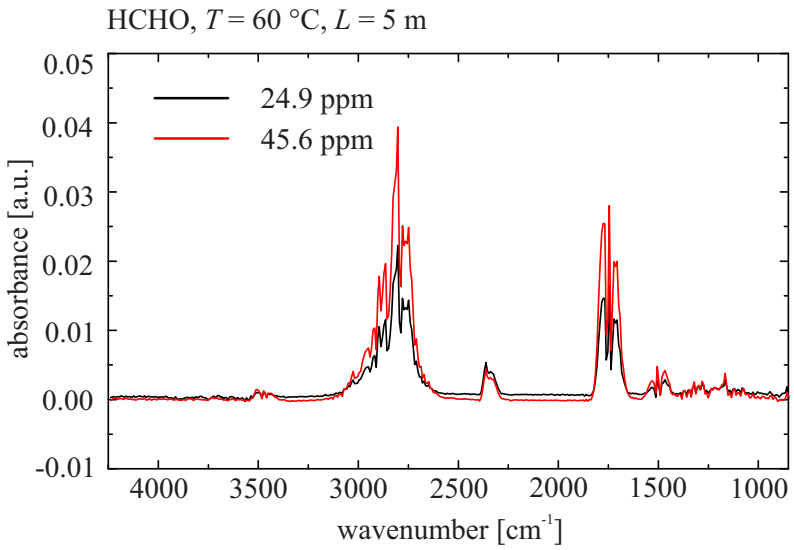

Figure B.5: HCHO reference spectra for 24.9 and 45.6 ppm.

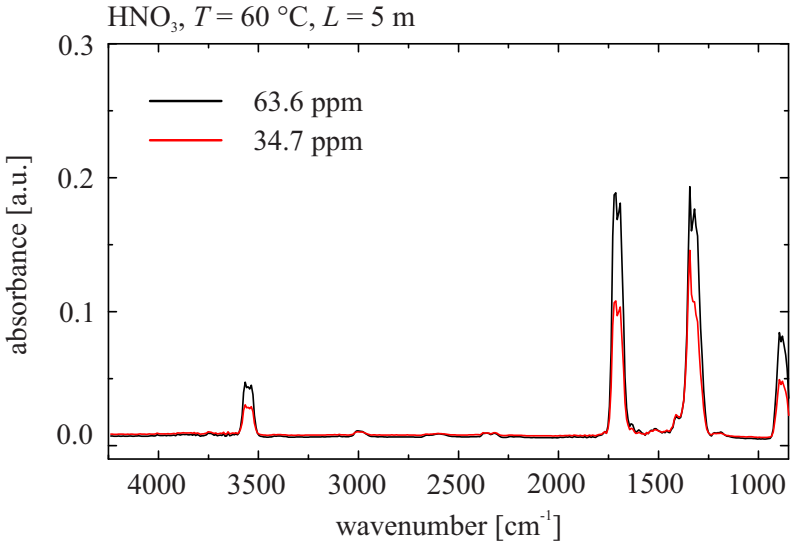

Figure B.6: HNO_3 reference spectra for 34.7 and 63.6 ppm.

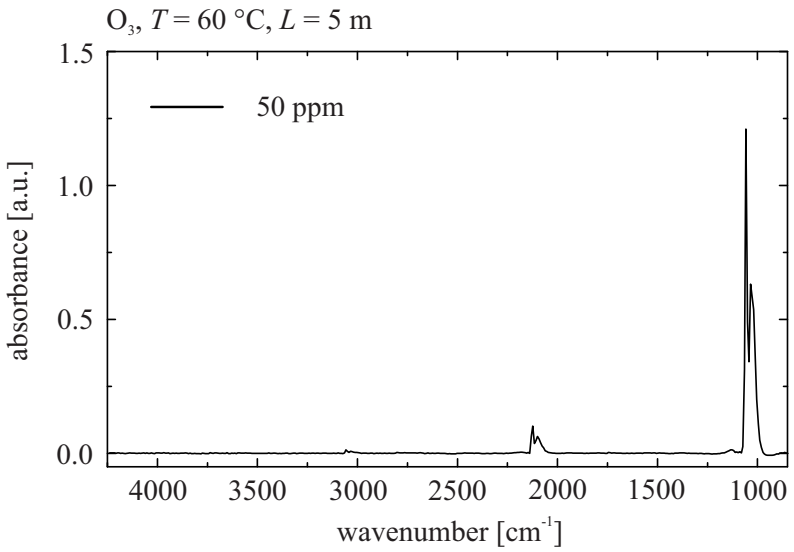

Figure B.7: Reference spectrum for 50 ppm O_3.

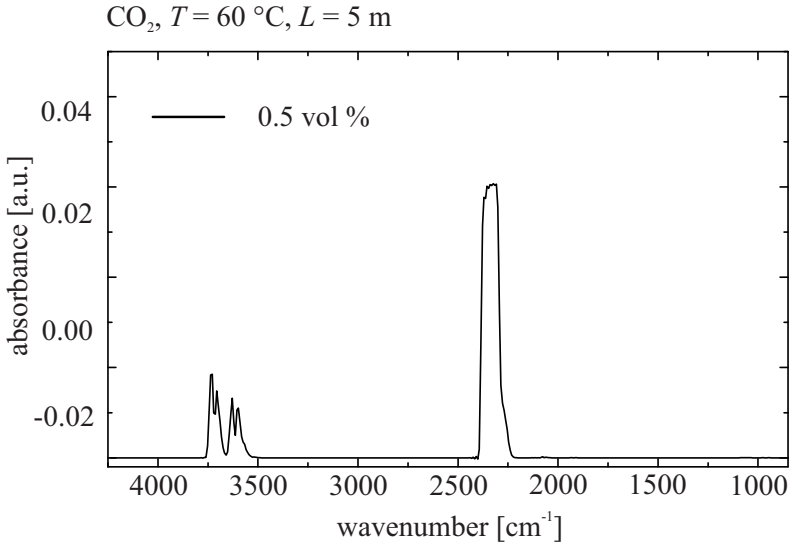

Figure B.8: Reference spectrum for 0.5 vol % CO_2.

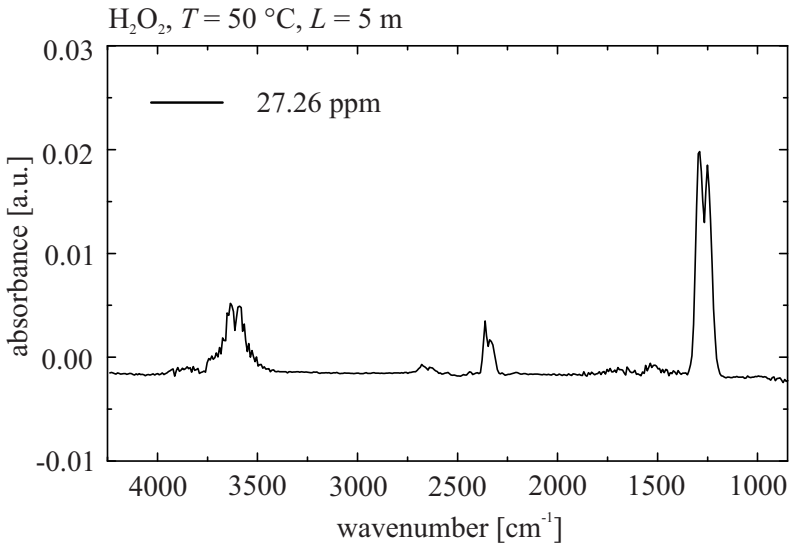

Figure B.9: Reference spectrum for 27.26 ppm H_2O_2 using $T = 50°C$ and $L = 5\,m$.

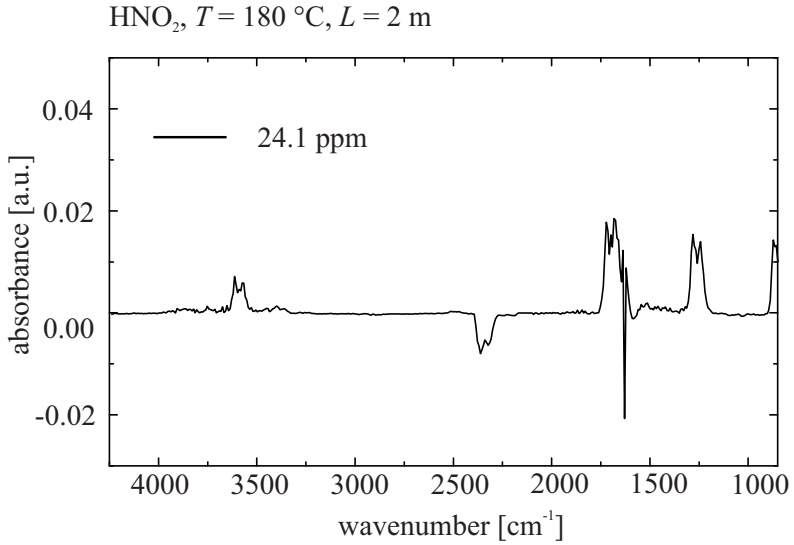

Figure B.10: Reference spectrum for 24.1 ppm HNO_2 using $T = 180°C$ and $L = 2\,m$.

Bibliography

[1] G. Kminek and V. Conley, "COSPAR's planetary protection policy," *COSPAR*, 2017.

[2] T. Pottage, S. Macken, K. Giri, J. T. Walker, and A. M. Bennett, "Low-temperature decontamination with hydrogen peroxide or chlorine dioxide for space applications," *Applied and Environmental Microbiology*, vol. 78, p. 4169, 2012.

[3] C. Moissl-Eichinger, P. Rettberg, and R. Pukall, "The first collection of spacecraft-associated microorganisms: A public source for extremotolerant microorganisms from spacecraft assembly clean rooms," *Astrobiology*, vol. 12, p. 1024, 2012.

[4] J. D. Rummel, "From planetary quarantine to planetary protection: A NASA and international story," *Astrobiology*, vol. 19, p. 624, 2019.

[5] A. Frick, R. Mogul, P. Stabekis, C. A. Conley, and P. Ehrenfreund, "Overview of current capabilities and research and technology developments for planetary protection," *Advances in Space Research*, vol. 54, p. 221, 2014.

[6] P. Rettberg, A. M. Anesio, V. R. Baker, J. A. Baross, S. L. Cady, E. Detsis, C. M. Foreman, E. Hauber, G. G. Ori, D. A. Pearce, N. O. Renno, G. Ruvkun, B. Sattler, M. P. Saunders, D. H. Smith, D. Wagner, and F. Westall, "Planetary protection and mars special regions - A suggestion for updating the definition," *Astrobiology*, vol. 16, p. 119, 2016.

[7] P. Rettberg, A. Antunes, J. Brucato, P. Cabezas, G. Collins, A. Haddaji, G. Kminek, S. Leuko, S. McKenna-Lawlor, C. Moissl-Eichinger, J.-L. Fellous, K. Olsson-Francis, D. Pearce, E. Rabbow, S. Royle, M. Saunders, M. Sephton, A. Spry, N. Walter, R. Wimmer Schweingruber, and J.-C. Treuet, "Biological contamination prevention for outer solar system moons of astrobiological interest: What do we need to know?," *Astrobiology*, vol. 19, p. 1, 2019.

[8] C. Moissl-Eichinger, A. K. Auerbach, A. J. Probst, A. Mahnert, L. Tom, Y. Piceno, G. L. Andersen, K. Venkateswaran, P. Rettberg, S. Barczyk, R. Pukall, and G. Berg, "Quo vadis? Microbial profiling revealed strong effects of cleanroom maintenance and

routes of contamination in indoor environments," *Scientific Reports*, vol. 5, p. 9156, 2015.

[9] M. Stieglmeier, P. Rettberg, S. Barczyk, M. Bohmeier, R. Pukall, R. Wirth, and C. Moissl-Eichinger, "Abundance and diversity of microbial inhabitants in european spacecraft-associated clean rooms," *Astrobiology*, vol. 12, p. 572, 2012.

[10] C. Moissl-Eichinger, R. Pukall, A. J. Probst, M. Stieglmeier, P. Schwendner, M. Mora, S. Barczyk, M. Bohmeier, and P. Rettberg, "Lessons learned from the microbial analysis of the herschel spacecraft during assembly, integration, and test operations," *Astrobiology*, vol. 13, p. 1125, 2013.

[11] K. Koskinen, P. Rettberg, R. Pukall, A. Auerbach, L. Wink, S. Barczyk, A. Perras, A. Mahnert, D. Margheritis, G. Kminek, and C. Moissl-Eichinger, "Microbial biodiversity assessment of the european space agency's exomars 2016 mission," *Microbiome*, vol. 5, p. 143, 2017.

[12] P. Schwendner, C. Moissl-Eichinger, S. Barczyk, M. Bohmeier, R. Pukall, and P. Rettberg, "Insights into the microbial diversity and bioburden in a south american spacecraft assembly clean room," *Astrobiology*, vol. 13, p. 1140, 2013.

[13] D. L. Nuding, R. V. Gough, K. J. Venkateswaran, J. A. Spry, and M. A. Tolbert, "Laboratory investigations on the survival of bacillus subtilis spores in deliquescent salt mars analog environments," *Astrobiology*, vol. 17, p. 997, 2017.

[14] M. Müller, T. Shimizu, S. Binder, P. Rettberg, J. L. Zimmermann, G. E. Morfill, and H. Thomas, "Plasma afterglow circulation apparatus for decontamination of spacecraft equipment," *AIP Advances*, vol. 8, p. 105013, 2018.

[15] S. Shimizu, S. Barczyk, P. Rettberg, T. Shimizu, T. Klaempfl, J. L. Zimmermann, T. Hoeschen, C. Linsmeier, P. Weber, G. E. Morfill, and H. M. Thomas, "Cold atmospheric plasma – A new technology for spacecraft component decontamination," *Planetary and Space Science*, vol. 90, p. 60, 2014.

[16] G. Horneck, P. Rettberg, G. Reitz, J. Wehner, U. Eschweiler, K. Strauch, C. Panitz, V. Starke, C. Baumstark-Khan, G. Horneck, P. Rettberg, G. Reitz, J. Wehner, U. Eschweiler, K. Strauch, C. Panitz, V. Starke, and C. Baumstark-Khan, "Protection of bacterial spores in space, a contribution to the discussion on panspermia," *Origins of Life and Evolution of the Biosphere*, vol. 31, p. 527, 2001.

[17] G. Drews, *Mikrobiologie: Die Entdeckung der unsichtbaren Welt*. Heidelberg: Springer, 2010.

[18] W. L. Nicholson, N. Munakata, G. Horneck, H. J. Melosh, and P. Setlow, "Resistance of bacillus endospores to extreme terrestrial and extraterrestrial environments," *Microbiology and Molecular Biology Reviews*, vol. 64, p. 548, 2000.

[19] A. Driks, "Bacillus subtilis spore coat," *Microbiology and Molecular Biology Reviews*, vol. 63, p. 1, 1999.

[20] J. Jeon, *Surface micro-discharge (SMD) - Analysis of the antimicrobial effect and the plasma chemistry.* PhD thesis, Ludwig-Maximillians-Universität München, München, 2014.

[21] A. D. Grossman, "Genetic networks controlling the initiation of sporulation and the development of genetic competence in bacillus subtilis," *Annual Review of Genetics*, vol. 29, p. 477, 1995.

[22] B. Setlow, A. E. Cowan, and P. Setlow, "Germination of spores of bacillus subtilis with dodecylamine," *Journal of Applied Microbiology*, vol. 95, p. 637, 2003.

[23] P. Stragier and R. Losick, "Molecular genetics of sporulation in bacillus subtilis," *Annual Review of Genetics*, vol. 30, p. 297, 1996.

[24] M. Cortesão, F. M. Fuchs, F. M. Commichau, P. Eichenberger, A. C. Schuerger, W. L. Nicholson, P. Setlow, and R. Moeller, "Bacillus subtilis spore resistance to simulated mars surface conditions," *Frontiers in Microbiology*, vol. 10, p. 333, 2019.

[25] C. Moissl-Eichinger, C. Cockell, and P. Rettberg, "Venturing into new realms? Microorganisms in space," *FEMS Microbiology Reviews*, vol. 40, p. 722, 2016.

[26] S. R. Sella, B. P. Guizelini, L. P. Vandenberghe, A. B. Medeiros, and C. R. Soccol, "Bioindicator production with bacillus atrophaeus' thermal-resistant spores cultivated by solid-state fermentation," *Applied Microbiology and Biotechnology*, vol. 82, p. 1019, 2009.

[27] M. Plomp, T. J. Leighton, K. E. Wheeler, M. E. Pitesky, and A. J. Malkin, "Bacillus atrophaeus outer spore coat assembly and ultrastructure," *Langmuir : The ACS Journal of Surfaces and Colloids*, vol. 21, p. 10710, 2005.

[28] A. O. Henriques and C. P. Moran, "Structure, assembly, and function of the spore surface layers," *Annual Review of Microbiology*, vol. 61, p. 555, 2007.

[29] D. L. Popham, J. Helin, C. E. Costello, and P. Setlow, "Analysis of the peptidoglycan structure of bacillus subtilis endospores," *Journal of Bacteriology*, vol. 178, p. 6451, 1996.

[30] P. Setlow, "Mechanisms for the prevention of damage to DNA in spores of bacillus species," *Annual Review of Microbiology*, vol. 49, p. 29, 1995.

[31] R. Moeller, P. Setlow, G. Horneck, T. Berger, G. Reitz, P. Rettberg, A. J. Doherty, R. Okayasu, and W. L. Nicholson, "Roles of the major, small, acid-soluble spore proteins and spore-specific and universal DNA repair mechanisms in resistance of bacillus subtilis spores to ionizing radiation from X rays and high-energy charged-particle bombardment," *Journal of Bacteriology*, vol. 190, p. 1134, 2008.

[32] A. Debus, "The european standard on planetary protection requirements," *Research in Microbiology*, vol. 157, p. 13, 2006.

[33] ECSS-Q-ST-70-56C, "ECSS-Q-ST-70-56C Vapour phase bioburden reduction for flight hardware," *European Cooperation for Space Standardization*, 2013.

[34] ECSS-Q-ST-70-57C, "ECSS-Q-ST-70-57C Dry heat bioburden reduction for flight hardware," *European Cooperation for Space Standardization*, 2013.

[35] ECSS-Q-ST-70-53C, "ECSS-Q-ST-70-53C Materials and hardware compatibility tests for sterilization processes," *European Cooperation for Space Standardization*, 2008.

[36] D. E. Pugel, J. D. Rummel, and C. Conley, "Brushing your spacecraft's teeth: A review of biological reduction processes for planetary protection missions," *Aerospace Conference, 2017 IEEE*, p. 1, 2017.

[37] H. M. Mott-Smith, "History of "plasmas"," *Nature*, vol. 233, p. 219, 1971.

[38] A. Piel, *Plasma Physics: An Introduction to Laboratory, Space, and Fusion Plasmas*. Heidelberg: Springer International Publishing, 2 ed., 2017.

[39] A. Fridman, *Plasma chemistry*. Cambridge: Cambridge University Press, 2012.

[40] T. Klämpfl, *Cold atmospheric plasma decontamination against nosocomial bacteria*. PhD thesis, Technischen Universität München, München, 2014.

[41] U. Stroth, *Plasmaphysik: Phänomene, Grundlagen, Anwendungen*. Wiesbaden: Vieweg+Teubner Verlag, 2011.

[42] A. Fridman, A. Chirokov, and A. Gutsol, "Non-thermal atmospheric pressure discharges," *Journal of Physics D: Applied Physics*, vol. 38, p. R1, 2005.

[43] H.-E. Wagner, R. Brandenburg, K. V. Kozlov, A. Sonnenfeld, P. Michel, and J. F. Behnke, "The barrier discharge: Basic properties and applications to surface treatment," *Vacuum*, vol. 71, p. 417, 2003.

[44] L. Bárdos and H. Baránková, "Cold atmospheric plasma: Sources, processes, and applications," *Thin Solid Films*, vol. 518, p. 6705, 2010.

[45] C. Hertwig, N. Meneses, and A. Mathys, "Cold atmospheric pressure plasma and low energy electron beam as alternative nonthermal decontamination technologies for dry food surfaces: A review," *Trends in Food Science & Technology*, vol. 77, p. 131, 2018.

[46] J. Ehlbeck, U. Schnabel, M. Polak, J. Winter, T. von Woedtke, R. Brandenburg, T. von dem Hagen, and K.-D. Weltmann, "Low temperature atmospheric pressure plasma sources for microbial decontamination," *Journal of Physics D: Applied Physics*, vol. 44, p. 013002, 2011.

[47] A. Schutze, J. Y. Jeong, S. E. Babayan, J. Park, G. S. Selwyn, and R. F. Hicks, "The atmospheric-pressure plasma jet: A review and comparison to other plasma sources," *IEEE Transactions on Plasma Science*, vol. 26, p. 1685, 1998.

[48] P. Puligundla and C. Mok, "Inactivation of spores by nonthermal plasmas," *World Journal of Microbiology & Biotechnology*, vol. 34, p. 143, 2018.

[49] K. Stapelmann, M. Fiebrandt, M. Raguse, P. Awakowicz, G. Reitz, and R. Moeller, "Utilization of low-pressure plasma to inactivate bacterial spores on stainless steel screws," *Astrobiology*, vol. 13, p. 597, 2013.

[50] M. Cooper, G. Fridman, D. Staack, A. F. Gutsol, V. N. Vasilets, S. Anandan, Y. I. Cho, A. Fridman, and A. Tsapin, "Decontamination of surfaces from extremophile organisms using nonthermal atmospheric-pressure plasmas," *IEEE Transactions on Plasma Science*, vol. 37, p. 866, 2009.

[51] G. Isbary, T. Shimizu, Y.-F. Li, W. Stolz, H. M. Thomas, G. E. Morfill, and J. L. Zimmermann, "Cold atmospheric plasma devices for medical issues," *Expert Review of Medical Devices*, vol. 10, p. 367, 2013.

[52] M. G. Kong, G. Kroesen, G. Morfill, T. Nosenko, T. Shimizu, J. van Dijk, and J. L. Zimmermann, "Plasma medicine: An introductory review," *New Journal of Physics*, vol. 11, p. 115012, 2009.

[53] T. Shimizu, J. L. Zimmermann, and G. E. Morfill, "The bactericidal effect of surface micro-discharge plasma under different ambient conditions," *New Journal of Physics*, vol. 13, p. 023026, 2011.

[54] S. Lerouge, M. R. Wertheimer, and L. Yahia, "Plasma sterilization: A review of parameters, mechanisms, and limitations," *Plasmas and Polymers*, vol. 6, p. 175, 2001.

[55] M. Laroussi, "Sterilization of contaminated matter with an atmospheric pressure plasma," *IEEE Transactions on Plasma Science*, vol. 24, p. 1188, 1996.

[56] G. Fridman, M. Peddinghaus, M. Balasubramanian, H. Ayan, A. Fridman, A. Gutsol, and A. Brooks, "Blood coagulation and living tissue sterilization by floating-electrode dielectric barrier discharge in air," *Plasma Chemistry and Plasma Processing*, vol. 26, p. 425, 2006.

[57] G. E. Morfill, T. Shimizu, B. Steffes, and H.-U. Schmidt, "Nosocomial infections - A new approach towards preventive medicine using plasmas," *New Journal of Physics*, vol. 11, p. 115019, 2009.

[58] B. Eliasson and U. Kogelschatz, "Modeling and applications of silent discharge plasmas," *IEEE Transactions on Plasma Science*, vol. 19, p. 309, 1991.

[59] J.-S. Chang, P. A. Lawless, and T. Yamamoto, "Corona discharge processes," *IEEE Transactions on Plasma Science*, vol. 19, p. 1152, 1991.

[60] S. Pekárek, "DC corona discharge ozone production enhanced by magnetic field," *The European Physical Journal D*, vol. 56, p. 91, 2010.

[61] E. Sysolyatina, A. Mukhachev, M. Yurova, M. Grushin, V. Karalnik, A. Petryakov, N. Trushkin, S. Ermolaeva, and Y. Akishev, "Role of the charged particles in bacteria inactivation by plasma of a positive and negative corona in ambient air," *Plasma Processes and Polymers*, vol. 11, p. 315, 2014.

[62] R. Cramariuc, A. Tudorache, M. E. Popa, E. Branduse, L. Nisiparu, A. Mitelut, M. O. Turtoi, and L. Fotescu, "Corona discharge in electroporation of cell membranes," *Journal of Physics: Conference Series*, vol. 142, p. 012062, 2008.

[63] G.-A. Shin and M. D. Sobsey, "Reduction of norwalk virus, poliovirus 1, and bacteriophage MS2 by ozone disinfection of water," *Applied and Environmental Microbiology*, vol. 69, p. 3975, 2003.

[64] V. Scholtz, J. Julák, and V. Kříha, "The microbicidal effect of low-temperature plasma generated by corona discharge: Comparison of various microorganisms on an agar surface or in aqueous suspension," *Plasma Processes and Polymers*, vol. 7, p. 237, 2010.

[65] R. Bussiahn, R. Brandenburg, T. Gerling, E. Kindel, H. Lange, N. Lembke, K.-D. Weltmann, T. von Woedtke, and T. Kocher, "The hairline plasma: An intermittent negative dc-corona discharge at atmospheric pressure for plasma medical applications," *Applied Physics Letters*, vol. 96, p. 143701, 2010.

[66] V. Joubert, C. Cheype, J. Bonnet, D. Packan, J.-P. Garnier, J. Teissié, and V. Blanckaert, "Inactivation of bacillus subtilis var. niger of both spore and vegetative forms by means of corona discharges applied in water," *Water Research*, vol. 47, p. 1381, 2013.

[67] D. Dobrynin, G. Friedman, A. Fridman, and A. Starikovskiy, "Inactivation of bacteria using DC corona discharge: Role of ions and humidity," *New Journal of Physics*, vol. 13, p. 1, 2011.

[68] T. Lee, P. Puligundla, and C. Mok, "Corona discharge plasma jet inactivates foodborne pathogens adsorbed onto packaging material surfaces," *Packaging Technology and Science*, vol. 30, p. 681, 2017.

[69] A. Kilonzo-Nthenge, S. Liu, S. Yannam, and A. Patras, "Atmospheric cold plasma inactivation of salmonella and escherichia coli on the surface of golden delicious apples," *Frontiers in Nutrition*, vol. 5, p. 120, 2018.

[70] Z. Chang, C. Yao, and G. Zhang, "Non-thermal equilibrium atmospheric pressure glow-like discharge plasma jet," *Plasma Science and Technology*, vol. 18, p. 17, 2016.

[71] A. v. Engel, R. Seeliger, and M. Steenbeck, "Über die Glimmentladung bei hohen Drucken," *Zeitschrift für Physik*, vol. 85, p. 144, 1933.

[72] A. Bogaerts, E. Neyts, R. Gijbels, and J. van der Mullen, "Gas discharge plasmas and their applications," *Spectrochimica Acta Part B: Atomic Spectroscopy*, vol. 57, p. 609, 2002.

[73] J. R. Roth, S. Nourgostar, and T. A. Bonds, "The one atmosphere uniform glow discharge plasma (OAUGDP)- A platform technology for the 21st century," *IEEE Transactions on Plasma Science*, vol. 35, p. 233, 2007.

[74] J. R. Roth, P. P. Tsai, C. Liu, M. Laroussi, and P. D. Spence, "One atmosphere uniform glow discharge plasma," *U.S. Patent: 5,414,324*.

[75] M. Laroussi, "Sterilization of contaminated matter with an atmospheric pressure plasma," *IEEE Transactions on Plasma Science*, vol. 24, p. 1188, 1996.

[76] T. C. Montie, K. Kelly-Wintenberg, and J. R. Roth, "An overview of research using the one atmosphere uniform glow discharge plasma (OAUGDP) for sterilization of surfaces and materials," *IEEE Transactions on Plasma Science*, vol. 28, p. 41, 2000.

[77] T. Akitsu, H. Ohkawa, M. Tsuji, H. Kimura, and M. Kogoma, "Plasma sterilization using glow discharge at atmospheric pressure," *Surface and Coatings Technology*, vol. 193, p. 29, 2005.

[78] H. Okawa and T. Akitsu, "Bactericidal characteristics and material conformity of atmospheric-pressure glow discharge," *Plasma Medicine*, vol. 4, p. 37, 2014.

[79] J. A. Daseco, K. G. Pabelina, M. A. T. Siringan, and H. J. Ramos, "Comparative study on the use of different metal electrodes in low-pressure glow discharge plasma sterilization," *Plasma Medicine*, vol. 4, p. 1, 2014.

[80] S. E. Babayan, J. Y. Jeong, A. Schütze, V. J. Tu, M. Moravej, G. S. Selwyn, and R. F. Hicks, "Deposition of silicon dioxide films with a non-equilibrium atmospheric-pressure plasma jet," *Plasma Sources Science and Technology*, vol. 10, p. 573, 2001.

[81] A. Schutze, J. Y. Jeong, S. E. Babayan, J. Park, G. S. Selwyn, and R. F. Hicks, "The atmospheric-pressure plasma jet: A review and comparison to other plasma sources," *IEEE Transactions on Plasma Science*, vol. 26, p. 1685, 1998.

[82] K.-D. Weltmann, E. Kindel, R. Brandenburg, C. Meyer, R. Bussiahn, C. Wilke, and T. von Woedtke, "Atmospheric pressure plasma jet for medical therapy: Plasma parameters and risk estimation," *Contributions to Plasma Physics*, vol. 49, p. 631, 2009.

[83] K.-D. Weltmann, R. Brandenburg, T. von Woedtke, J. Ehlbeck, R. Foest, M. Stieber, and E. Kindel, "Antimicrobial treatment of heat sensitive products by miniaturized atmospheric pressure plasma jets (APPJs)," *Journal of Physics D: Applied Physics*, vol. 41, p. 194008, 2008.

[84] R. Foest, E. Kindel, A. Ohl, M. Stieber, and K.-D. Weltmann, "Non-thermal atmospheric pressure discharges for surface modification," *Plasma Physics and Controlled Fusion*, vol. 47, p. B525, 2005.

[85] M. Laroussi, M. G. Kong, G. Morfill, W. Stolz, *Plasma medicine: Applications of low-temperature gas plasmas in medicine and biology.* Cambridge: Cambridge University Press, 2012.

[86] S. Reuter, T. von Woedtke, and K.-D. Weltmann, "The kINPen—a review on physics and chemistry of the atmospheric pressure plasma jet and its applications," *Journal of Physics D: Applied Physics*, vol. 51, p. 233001, 2018.

[87] G. Daeschlein, S. Scholz, A. Arnold, T. von Woedtke, E. Kindel, M. Niggemeier, K.-D. Weltmann, and M. Junger, "In vitro activity of atmospheric pressure plasma jet (APPJ) plasma against clinical isolates of demodex folliculorum," *IEEE Transactions on Plasma Science*, vol. 38, p. 2969, 2010.

[88] J.-P. Lim, H. S. Uhm, and S.-Z. Li, "Influence of oxygen in atmospheric-pressure argon plasma jet on sterilization of bacillus atrophaeous spores," *Physics of Plasmas*, vol. 14, p. 093504, 2007.

[89] R. Brandenburg, J. Ehlbeck, M. Stieber, T. v. Woedtke, J. Zeymer, O. Schlüter, and K.-D. Weltmann, "Antimicrobial treatment of heat sensitive materials by means of atmospheric pressure Rf-driven plasma jet," *Contributions to Plasma Physics*, vol. 47, p. 72, 2007.

[90] J.-W. Lackmann and J. E. Bandow, "Inactivation of microbes and macromolecules by atmospheric-pressure plasma jets," *Applied Microbiology and Biotechnology*, vol. 98, p. 6205, 2014.

[91] M. Laroussi, "Low-temperature plasma jet for biomedical applications: A review," *IEEE Transactions on Plasma Science*, vol. 43, p. 703, 2015.

[92] B. Eliasson, W. Egli, and U. Kogelschatz, "Modelling of dielectric barrier discharge chemistry," *Pure and Applied Chemistry*, vol. 66, p. 1275, 1994.

[93] U. Kogelschatz, B. Eliasson, and W. Egli, "Dielectric-barrier discharges. Principle and applications," *Le Journal de Physique IV*, vol. 07, p. C4 47, 1997.

[94] N. Gherardi, G. Gouda, E. Gat, A. Ricard, and F. Massines, "Transition from glow silent discharge to micro-discharges in nitrogen gas," *Plasma Sources Science and Technology*, vol. 9, p. 340, 2000.

[95] U. Kogelschatz, B. Eliasson, and W. Egli, "From ozone generators to flat television screens: History and future potential of dielectric-barrier discharges," *Pure and Applied Chemistry*, vol. 71, p. 1819, 1999.

[96] S. U. Kalghatgi, G. Fridman, M. Cooper, G. Nagaraj, M. Peddinghaus, M. Balasubramanian, V. N. Vasilets, A. F. Gutsol, A. Fridman, and G. Friedman, "Mechanism of blood coagulation by nonthermal atmospheric pressure dielectric barrier discharge plasma," *IEEE Transactions on Plasma Science*, vol. 35, p. 1559, 2007.

[97] G. Fridman, A. D. Brooks, M. Balasubramanian, A. Fridman, A. Gutsol, V. N. Vasilets, H. Ayan, and G. Friedman, "Comparison of direct and indirect effects of non-thermal atmospheric-pressure plasma on bacteria," *Plasma Processes and Polymers*, vol. 4, p. 370, 2007.

[98] W. Siemens, "Über die elektrostatische Induction und die Verzögerung des Stroms in Flaschendrähten," *Annalen der Physik und Chemie*, vol. 178, p. 66, 1857.

[99] F.-J. Trompeter, W. J. Neff, O. Franken, M. Heise, M. Neiger, S. Liu, G. J. Pietsch, and A. B. Saveljew, "Reduction of bacillus subtilis and aspergillus niger spores using nonthermal atmospheric gas discharges," *IEEE Transactions on Plasma Science*, vol. 30, p. 1416, 2002.

[100] G. Fridman, A. Shereshevsky, M. M. Jost, A. D. Brooks, A. Fridman, A. Gutsol, V. Vasilets, and G. Friedman, "Floating electrode dielectric barrier discharge plasma in air promoting apoptotic behavior in melanoma skin cancer cell lines," *Plasma Chemistry and Plasma Processing*, vol. 27, p. 163, 2007.

[101] S. G. Joshi, M. Cooper, A. Yost, M. Paff, U. K. Ercan, G. Fridman, G. Friedman, A. Fridman, and A. D. Brooks, "Nonthermal dielectric-barrier discharge plasma-induced inactivation involves oxidative DNA damage and membrane lipid peroxidation in escherichia coli," *Antimicrobial Agents and Chemotherapy*, vol. 55, p. 1053, 2011.

[102] M. J. Gallagher, N. Vaze, S. Gangoli, V. N. Vasilets, A. F. Gutsol, T. N. Milovanova, S. Anandan, D. M. Murasko, and A. A. Fridman, "Rapid inactivation of airborne bacteria using atmospheric pressure dielectric barrier grating discharge," *IEEE Transactions on Plasma Science*, vol. 35, p. 1501, 2007.

[103] A. Kuzminova, T. Kretková, O. Kylián, J. Hanuš, I. Khalakhan, V. Prukner, E. Doležalová, M. Šimek, and H. Biederman, "Etching of polymers, proteins and bacterial spores by atmospheric pressure DBD plasma in air," *Journal of Physics D: Applied Physics*, vol. 50, p. 135201, 2017.

[104] R. Brandenburg, "Dielectric barrier discharges: progress on plasma sources and on the understanding of regimes and single filaments," *Plasma Sources Science and Technology*, vol. 27, p. 079501, 2018.

[105] X. Liao, D. Liu, Q. Xiang, J. Ahn, S. Chen, X. Ye, and T. Ding, "Inactivation mechanisms of non-thermal plasma on microbes: A review," *Food Control*, vol. 75, p. 83, 2017.

[106] D. Butscher, D. Zimmermann, M. Schuppler, and P. Rudolf von Rohr, "Plasma inactivation of bacterial endospores on wheat grains and polymeric model substrates in a dielectric barrier discharge," *Food Control*, vol. 60, p. 636, 2016.

[107] H. I. Yong, H.-J. Kim, S. Park, A. U. Alahakoon, K. Kim, W. Choe, and C. Jo, "Evaluation of pathogen inactivation on sliced cheese induced by encapsulated atmospheric pressure dielectric barrier discharge plasma," *Food Microbiology*, vol. 46, p. 46, 2015.

[108] A. Berardinelli, F. Pasquali, C. Cevoli, M. Trevisani, L. Ragni, R. Mancusi, and G. Manfreda, "Sanitisation of fresh-cut celery and radicchio by gas plasma treatments in water medium," *Postharvest Biology and Technology*, vol. 111, p. 297, 2016.

[109] H. Lu, S. Patil, K. M. Keener, P. J. Cullen, and P. Bourke, "Bacterial inactivation by high-voltage atmospheric cold plasma: Influence of process parameters and effects on cell leakage and DNA," *Journal of Applied Microbiology*, vol. 116, p. 784, 2014.

[110] T. Maisch, T. Shimizu, A. Mitra, J. Heinlin, S. Karrer, Y.-F. Li, G. Morfill, and J. L. Zimmermann, "Contact-free cold atmospheric plasma treatment of deinococcus radiodurans," *Journal of Industrial Microbiology and Biotechnology*, vol. 39, p. 1367, 2012.

[111] T. Shimizu, Y. Sakiyama, D. B. Graves, J. L. Zimmermann, and G. E. Morfill, "The dynamics of ozone generation and mode transition in air surface micro-discharge plasma at atmospheric pressure," *New Journal of Physics*, vol. 14, p. 103028, 2012.

[112] V. I. Gibalov and G. J. Pietsch, "Dynamics of dielectric barrier discharges in different arrangements," *Plasma Sources Science and Technology*, vol. 21, p. 024010, 2012.

[113] N. Mastanaiah, J. A. Johnson, and S. Roy, "Effect of dielectric and liquid on plasma sterilization using dielectric barrier discharge plasma," *PloS ONE*, vol. 8, p. e70840, 2013.

[114] K. Oehmigen, M. Hähnel, R. Brandenburg, C. Wilke, K.-D. Weltmann, and T. von Woedtke, "The role of acidification for antimicrobial activity of atmospheric pressure plasma in liquids," *Plasma Processes and Polymers*, vol. 7, p. 250, 2010.

[115] M. Hähnel, T. von Woedtke, and K.-D. Weltmann, "Influence of the air humidity on the reduction of bacillus spores in a defined environment at atmospheric pressure using a dielectric barrier surface discharge," *Plasma Processes and Polymers*, vol. 7, p. 244, 2010.

[116] T. G. Klämpfl, G. Isbary, T. Shimizu, Y.-F. Li, J. L. Zimmermann, W. Stolz, J. Schlegel, G. E. Morfill, and H.-U. Schmidt, "Cold atmospheric air plasma sterilization against spores and other microorganisms of clinical interest," *Applied and Environmental Microbiology*, vol. 78, p. 5077, 2012.

[117] J. Jeon, T. G. Klaempfl, J. L. Zimmermann, G. E. Morfill, and T. Shimizu, "Sporicidal properties from surface micro-discharge plasma under different plasma conditions at different humidities," *New Journal of Physics*, vol. 16, p. 103007, 2014.

[118] J. L. Zimmermann, K. Dumler, T. Shimizu, G. E. Morfill, A. Wolf, V. Boxhammer, J. Schlegel, B. Gansbacher, and M. Anton, "Effects of cold atmospheric plasmas on adenoviruses in solution," *Journal of Physics D: Applied Physics*, vol. 44, p. 505201, 2011.

[119] J. L. Zimmermann, T. Shimizu, V. Boxhammer, and G. E. Morfill, "Disinfection through different textiles using low-temperature atmospheric pressure plasma," *Plasma Processes and Polymers*, vol. 9, p. 792, 2012.

[120] J. Mandler, S. Moritz, S. Binder, T. Shimizu, M. Müller, M. H. Thoma, and J. L. Zimmermann, "Disinfection of dental equipmentinactivation of enterococcus mundtii

on stainless steel and dental handpieces using surface micro-discharge plasma," *Plasma Medicine*, vol. 7, p. 407, 2017.

[121] S. Ikawa, K. Kitano, and S. Hamaguchi, "Effects of pH on bacterial inactivation in aqueous solutions due to low-temperature atmospheric pressure plasma application," *Plasma Processes and Polymers*, vol. 7, p. 33, 2010.

[122] C. Timmons, K. Pai, J. Jacob, G. Zhang, and L. M. Ma, "Inactivation of salmonella enterica, shiga toxin-producing escherichia coli, and listeria monocytogenes by a novel surface discharge cold plasma design," *Food Control*, vol. 84, p. 455, 2018.

[123] T. Shimizu, V. Lachner, and J. L. Zimmermann, "Surface microdischarge plasma for disinfection," *Plasma Medicine*, vol. 7, p. 175, 2017.

[124] A. N. Kontaratos, "On the functional dependence of townsend's first ionization coefficient," *Applied Scientific Research*, vol. 12, p. 27, 1965.

[125] J. M. Meek, *Electrical breakdown of gases*. Chichester: Wiley, 1978.

[126] K. H. Wagner, "Die Entwicklung der Elektronenlawine in den Plasmakanal, untersucht mit Bildverstärker und Wischverschluß," vol. 189, p. 465, 1966.

[127] K. T. A. L. Burm, "Calculation of the townsend discharge coefficients and the paschen curve coefficients," *Contributions to Plasma Physics*, vol. 47, p. 177, 2007.

[128] H. Raether, "Zur Entwicklung von Kanalentladungen," *Archiv für Elektrotechnik*, vol. 34, p. 49, 1940.

[129] H. Raether, "Die Entwicklung der Elektronenlawine in den Funkenkanal," *Zeitschrift für Physik*, vol. 112, p. 464, 1939.

[130] L. B. Loeb and J. M. Meek, "The mechanism of spark discharge in air at atmospheric pressure. I," *Journal of Applied Physics*, vol. 11, p. 438, 1940.

[131] A. A. Kulikovsky, "Positive streamer in a weak field in air: A moving avalanche-to-streamer transition," *Physical Review E*, vol. 57, p. 7066, 1998.

[132] A. J. Palmer, "A physical model on the initiation of atmospheric–pressure glow discharges," *Applied Physics Letters*, vol. 25, p. 138, 1974.

[133] U. Kogelschatz, "Dielectric-barrier discharges: Their history, discharge physics, and industrial applications," *Plasma Chemistry and Plasma Processing*, vol. 23, p. 1, 2003.

[134] V. I. Gibalov and G. J. Pietsch, "The development of dielectric barrier discharges in gas gaps and on surfaces," *Journal of Physics D: Applied Physics*, vol. 33, p. 2618, 2000.

[135] J. T. Herron and D. S. Green, "Chemical kinetics database and predictive schemes for nonthermal humid air plasma chemistry. Part II. Neutral species reactions," *Plasma Chemistry and Plasma Processing*, vol. 21, p. 459, 2001.

[136] L. W. Sieck, J. T. Heron, and D. S. Green, "Chemical kinetics database and predictive schemes for humid air plasma chemistry. Part I: Positive ion–molecule reactions," *Plasma Chemistry and Plasma Processing*, vol. 20, p. 235, 2000.

[137] Y. Sakiyama and D. B. Graves, "Efficient modeling of atmospheric pressure surface micro-discharge plasma chemistry," *Plasma Sources Science and Technology*, vol. 22, p. 012003, 2013.

[138] Y. Sakiyama, D. B. Graves, H.-W. Chang, T. Shimizu, and G. E. Morfill, "Plasma chemistry model of surface microdischarge in humid air and dynamics of reactive neutral species," *Journal of Physics D: Applied Physics*, vol. 45, p. 425201, 2012.

[139] D. B. Graves, "The emerging role of reactive oxygen and nitrogen species in redox biology and some implications for plasma applications to medicine and biology," *Journal of Physics D: Applied Physics*, vol. 45, p. 263001, 2012.

[140] B. Eliasson, M. Hirth, and U. Kogelschatz, "Ozone synthesis from oxygen in dielectric barrier discharges," *Journal of Physics D: Applied Physics*, vol. 20, p. 1421, 1987.

[141] S. Pekárek, "Experimental study of surface dielectric barrier discharge in air and its ozone production," *Journal of Physics D: Applied Physics*, vol. 45, p. 075201, 2012.

[142] U. Kogelschatz, B. Eliasson, and M. Hirth, "Ozone generation from oxygen and air: Discharge physics and reaction mechanisms," *Ozone: Science & Engineering*, vol. 10, p. 367, 1988.

[143] M. J. Pavlovich, H.-W. Chang, Y. Sakiyama, D. S. Clark, and D. B. Graves, "Ozone correlates with antibacterial effects from indirect air dielectric barrier discharge treatment of water," *Journal of Physics D: Applied Physics*, vol. 46, p. 145202, 2013.

[144] X. Zhang, B. J. Lee, H. G. Im, and M. S. Cha, "Ozone production with dielectric barrier discharge: Effects of power source and humidity," *IEEE Transactions on Plasma Science*, vol. 44, p. 2288, 2016.

[145] D. Yuan, C. Ding, Y. He, Z. Wang, S. Kumar, Y. Zhu, and K. Cen, "Characteristics of dielectric barrier discharge ozone synthesis for different pulse modes," *Plasma Chemistry and Plasma Processing*, vol. 37, p. 1165, 2017.

[146] S. Yao, Z. Wu, J. Han, X. Tang, B. Jiang, H. Lu, S. Yamamoto, and S. Kodama, "Study of ozone generation in an atmospheric dielectric barrier discharge reactor," *Journal of Electrostatics*, vol. 75, p. 35, 2015.

[147] C. v. Sonntag and U. v. Gunten, *Chemistry of ozone in water and wastewater treatment: From basic principles to applications*. London: IWA Publishing, 2012.

[148] U. Kogelschatz and P. Baessler, "Determination of nitrous oxide and dinitrogen pentoxide concentrations in the output of air-fed ozone generators of high power density," *Ozone: Science & Engineering*, vol. 9, p. 195, 1987.

[149] T. Andrews, "VII. On the volumetric relations of ozone, and the action of the electrical discharge on oxygen and other gases," *Philosophical Transactions of the Royal Society of London*, vol. 150, p. 113, 1860.

[150] R. Dorai and M. J. Kushner, "A model for plasma modification of polypropylene using atmospheric pressure discharges," *Journal of Physics D: Applied Physics*, vol. 36, p. 666, 2003.

[151] M. Capitelli, C. M. Ferreira, B. F. Gordiets, and A. I. Osipov, *Plasma Kinetics in Atmospheric Gases*, vol. 31 of *Springer Series on Atomic, Optical, and Plasma Physics*. Berlin and Heidelberg: Springer, 2000.

[152] J. Köritzer, *Biophysical effects of cold atmospheric plasma on glial tumor cells*. PhD thesis, Ludwig-Maximilians-Universität München, München, 2013.

[153] G. E. Morfill, M. G. Kong, and J. L. Zimmermann, "Focus on plasma medicine," *New Journal of Physics*, vol. 11, p. 115011, 2009.

[154] E. C. Y. Inn and Y. Tanaka, "Absorption coefficient of ozone in the ultraviolet and visible regions," *Journal of the Optical Society of America*, vol. 43, p. 870, 1953.

[155] R. D. Hudson, "Critical review of ultraviolet photoabsorption cross sections for molecules of astrophysical and aeronomic interest," *Reviews of Geophysics and Space Physics*, vol. 9, p. 305, 1971.

[156] M. Griggs, "Absorption coefficients of ozone in the ultraviolet and visible regions," *The Journal of Chemical Physics*, vol. 49, p. 857, 1968.

[157] P. M. Skrabal, *Spektroskopie: Eine methodenübergreifende Darstellung vom UV- bis zum NMR-Bereich*, vol. 8355. Zürich: UTB GmbH, 1 ed., 2009.

[158] J. Orphal and K. Chance, "Ultraviolet and visible absorption cross-sections for hitran," *Journal of Quantitative Spectroscopy and Radiative Transfer*, vol. 82, p. 491, 2003.

[159] R. Sander, "Compilation of henry's law constants (version 4.0) for water as solvent," *Atmospheric Chemistry and Physics*, vol. 15, p. 4399, 2015.

[160] A. C. Edwards, P. S. Hooda, and Y. Cook, "Determination of nitrate in water containing dissolved organic carbon by ultraviolet spectroscopy," *International Journal of Environmental Analytical Chemistry*, vol. 80, p. 49, 2001.

[161] E. J. Hart, K. Sehested, and J. Holoman, "Molar absorptivities of ultraviolet and visible bands of ozone in aqueous solutions," *Analytical Chemistry*, vol. 55, p. 46, 2002.

[162] N. B. Colthup, L. H. Daly, and S. E. Wiberley, *Introduction to infrared and Raman spectroscopy*. New York: Academic Press, 2. ed. ed., 1975.

[163] Gasmet Technologies Oy, *CX-series FTIR gas analyser - Instruction and operating manual*, E.1.8 ed., 2011.

[164] G. P. Basmer, *Theorie der FT-IR Spektroskopie: Gasmet FT-IR Analysator Calcmet Software*, 2004. Available: https://www.ffb.kit.edu/392.php [Accessed: June 2019].

[165] G. Hohlneicher, I. Kautz, J. Wolf, "Einführung in die Infrarotspektroskopie," *Universität zu Köln, Lehrstuhl für Physikalische Chemie*, 1993. Available: http://-www.uni-koeln.de/math-nat-fak/phchem/meerholz/teaching/pdf/fv02scripta.pdf [Accessed: June 2019].

[166] C. A. Cantrell, J. A. Davidson, A. H. McDaniel, R. E. Shetter, and J. G. Calvert, "Infrared absorption cross sections for N_2O_5," *Chemical Physics Letters*, vol. 148, p. 358, 1988.

[167] M. Hołub, "On the measurement of plasma power in atmospheric pressure DBD plasma reactors," *International Journal of Applied Electromagnetics and Mechanics*, vol. 39, p. 81, 2012.

[168] T. C. Manley, "The electric characteristics of the ozonator discharge," *Transactions of The Electrochemical Society*, vol. 84, p. 83, 1943.

[169] K. G. Kostov, R. Y. Honda, L. Alves, and M. E. Kayama, "Characteristics of dielectric barrier discharge reactor for material treatment," *Brazilian Journal of Physics*, vol. 39, p. 322, 2009.

[170] S. Grundmann and C. Tropea, "Experimental damping of boundary-layer oscillations using DBD plasma actuators," *International Journal of Heat and Fluid Flow*, vol. 30, p. 394, 2009.

[171] J. Kriegseis, B. Möller, S. Grundmann, and C. Tropea, "Capacitance and power consumption quantification of dielectric barrier discharge (DBD) plasma actuators," *Journal of Electrostatics*, vol. 69, p. 302, 2011.

[172] M. J. Pavlovich, D. S. Clark, and D. B. Graves, "Quantification of air plasma chemistry for surface disinfection," *Plasma Sources Science and Technology*, vol. 23, p. 065036, 2014.

[173] A. Aydogan and M. D. Gurol, "Application of gaseous ozone for inactivation of bacillus subtilis spores," *Journal of the Air & Waste Management Association*, vol. 56, p. 179, 2006.

[174] K. Ishizaki, N. Shinriki, and H. Matsuyama, "Inactivation of bacillus spores by gaseous ozone," *Journal of Applied Bacteriology*, vol. 60, p. 67, 1986.

[175] W. Demtröder, *Experimentalphysik 1: Mechanik und Wärme*. Berlin, Heidelberg: Springer-Verlag, 8 ed., 2018.

[176] D. Gardoni, A. Vailati, and R. Canziani, "Decay of ozone in water: A review," *Ozone: Science & Engineering*, vol. 34, p. 233, 2012.

[177] C. Weschler, A. T. Hodgson, and J. D. Wooley, "Indoor chemistry: ozone, volatile organic compounds, and carpets," *Environmental Science and Technology*, vol. 26, p. 2371, 1992.

[178] Z. S. Can and M. Gurol, "Formaldehyde formation during ozonation of drinking water," *Ozone: Science & Engineering*, vol. 25, p. 41, 2003.

[179] T. Salthammer, S. Mentese, and R. Marutzky, "Formaldehyde in the indoor environment," *Chemical Reviews*, vol. 110, p. 2536, 2010.

[180] J. D. McClurkin, D. E. Maier, and K. E. Ileleji, "Half-life time of ozone as a function of air movement and conditions in a sealed container," *Journal of Stored Products Research*, vol. 55, p. 41, 2013.

[181] C. Douat, S. Hübner, R. Engeln, and J. Benedikt, "Production of nitric/nitrous oxide by an atmospheric pressure plasma jet," *Plasma Sources Science and Technology*, vol. 25, p. 025027, 2016.

[182] E. J. Baek, H. M. Joh, S. J. Kim, and T. H. Chung, "Effects of the electrical parameters and gas flow rate on the generation of reactive species in liquids exposed to atmospheric pressure plasma jets," *Physics of Plasmas*, vol. 23, p. 073515, 2016.

[183] A. A. Abdelaziz, T. Ishijima, N. Osawa, and T. Seto, "Quantitative analysis of ozone and nitrogen oxides produced by a low power miniaturized surface dielectric barrier discharge: Effect of oxygen content and humidity level," *Plasma Chemistry and Plasma Processing*, vol. 39, p. 165, 2019.

[184] C. E. Mortimer and U. Müller, *Chemie: Das Basiswissen der Chemie.* Stuttgart: Thieme, 10 ed., 2010.

[185] V. S. Sugur, "Problems in storage and handling of red fuming nitric acid," *Defence Science Journal*, vol. 33, p. 331, 1983.

[186] S. Lerouge, M. R. Wertheimer, R. Marchand, M. Tabrizian, and L. Yahia, "Effect of gas composition on spore mortality and etching during low–pressure plasma sterilization," *Journal of Biomedical Materials Research*, vol. 51, p. 128, 2000.

[187] R. H. Hansen, J. V. Pascale, T. De Benedictis, P.M. Rentzepis, "Effect of atomic oxygen on polymers," *Journal of Polymer Science*, vol. 1965, p. 2205.

[188] A. V. Pipa and J. Ropcke, "Analysis of the mid-infrared spectrum of the exhaust gas from an atmospheric pressure plasma jet (APPJ) working with an argon–air mixture," *IEEE Transactions on Plasma Science*, vol. 37, p. 1000, 2009.

[189] J. Jeon, T. M. Rosentreter, Y. Li, G. Isbary, H. M. Thomas, J. L. Zimmermann, G. E. Morfill, and T. Shimizu, "Bactericidal agents produced by surface micro-discharge (SMD) plasma by controlling gas compositions," *Plasma Processes and Polymers*, vol. 11, p. 426, 2014.

[190] S. Moreau, M. Moisan, M. Tabrizian, J. Barbeau, J. Pelletier, A. Ricard, and L. Yahia, "Using the flowing afterglow of a plasma to inactivate bacillus subtilis spores: Influence of the operating conditions," *Journal of Applied Physics*, vol. 88, p. 1166, 2000.

[191] A. Schmidt, "Plasmasterilisation für Raumfahrtanwendungen - Plasma sterilization for space applications," Master's thesis, Justus-Liebig-Universität Gießen, Gießen, 2019.

[192] K. A. Woedtke T, "The limits of sterility assurance," *GMS Krankenhaushygiene Interdisziplinar*, vol. 3, p. 1, 2008.

[193] H. Shintani and A. Sakudo, eds., *Gas plasma sterilization in microbiology: Theory, applications, pitfalls and new perspectives.* Norfolk: Caister Academic Press, 2016.

[194] M. Carrera, R. O. Zandomeni, J. Fitzgibbon, and J.-L. Sagripanti, "Difference between the spore sizes of bacillus anthracis and other bacillus species," *Journal of Applied Microbiology*, vol. 102, p. 303, 2007.

[195] M. Raguse, M. Fiebrandt, K. Stapelmann, K. Madela, M. Laue, J.-W. Lackmann, J. E. Thwaite, P. Setlow, P. Awakowicz, and R. Moeller, "Improvement of biological indicators by uniformly distributing bacillus subtilis spores in monolayers to evaluate enhanced spore decontamination technologies," *Applied and Environmental Microbiology*, vol. 82, p. 2031, 2016.

[196] H. Shintani, "Current mistaken interpretation of microbiological data on gas plasma sterilization," *Pharmaceutical Regulatory Affairs*, vol. 4, p. 1, 2015.

[197] K. Reineke, K. Langer, C. Hertwig, J. Ehlbeck, and O. Schlüter, "The impact of different process gas compositions on the inactivation effect of an atmospheric pressure plasma jet on bacillus spores," *Innovative Food Science & Emerging Technologies*, vol. 30, p. 112, 2015.

[198] H. van Bokhorst-van de Veen, H. Xie, E. Esveld, T. Abee, H. Mastwijk, and M. Nierop Groot, "Inactivation of chemical and heat-resistant spores of bacillus and geobacillus by nitrogen cold atmospheric plasma evokes distinct changes in morphology and integrity of spores," *Food Microbiology*, vol. 45, p. 26, 2015.

[199] A. D. Russell, "Bacterial spores and chemical sporicidal agents," *Clinical Microbiology Reviews*, vol. 3, p. 99, 1990.

[200] J. Opretzka, J. Benedikt, P. Awakowicz, J. Wunderlich, and A. v. Keudell, "The role of chemical sputtering during plasma sterilization of bacillus atrophaeus," *Journal of Physics D: Applied Physics*, vol. 40, p. 2826, 2007.

[201] DuPont, *Sterilization Pouches of Tyvek Feature Outstanding Microbial Barrier*, 2019. Available: http://www.dupont.com/products-and-services/packaging-materials-solutions/pharmaceutical-packaging/brands/tyvek-sterile-packaging/uses-and-applications/protective-clean-peel-pouches.html [Accessed: June 2019].

[202] K. Kelly-Wintenberg, T. C. Montie, C. Brickman, J. R. Roth, A. K. Carr, K. Sorge, L. C. Wadsworth, and P. P. Y. Tsai, "Room temperature sterilization of surfaces and fabrics with a one atmosphere uniform glow discharge plasma," *Journal of Industrial Microbiology and Biotechnology*, vol. 20, p. 69, 1998.

[203] U. Schnabel, M. Andrasch, K.-D. Weltmann, J. Ehlbeck, "Inactivation of microorganisms in tyvek packaging by microwave plasma processed air," *Global Journal of Biology, Agriculture & Health Science*, vol. 4, p. 185, 2015.

[204] H. Gerischer, "Passivität der Metalle," *Angewandte Chemie*, vol. 70, p. 285, 1958.

[205] A. G. Aberle, "Surface passivation of crystalline silicon solar cells: A review," *Progress in Photovoltaics: Research and Applications*, vol. 8, p. 473, 2000.

[206] J. Albers, *Grundlagen integrierter Schaltungen: Bauelemente und Mikrostrukturierung*. München: Carl-Hanser-Verlag, 2007.

[207] T. Zhao and L. Jiang, "Contact angle measurement of natural materials," *Colloids and Surfaces B: Biointerfaces*, vol. 161, p. 324, 2018.

[208] Thomas Young, "An essay on the cohesion of fluids," *Philosophical Transactions of the Royal Society of London*, vol. 95, p. 65, 1805.

[209] A. Ulman, *An introduction to ultrathin organic films: From Langmuir-Blodgett to self-assembly*. Burlington: Elsevier Science, 1991.

[210] Y. Yuan and T. R. Lee, "Contact angle and wetting properties," *Surface Science Techniques. Springer Series in Surface Sciences*, vol. 2013, p. 3.

[211] Y. C. Liu and D. N. Lu, "Surface energy and wettability of plasma-treated polyacrylonitrile fibers," *Plasma Chemistry and Plasma Processing*, vol. 26, p. 119, 2006.

[212] D. K. Owens and R. C. Wendt, "Estimation of the surface free energy of polymers," *Journal of Applied Polymer Science*, vol. 13, p. 1741, 1969.

[213] Krüss GmbH, *Two-Component Surface Energy Characterization as a Predictor of Wettability and Dispersability - Application report: AR213e*, 2000. Available: https://www.kruss-scientific.com/fileadmin/user_upload/website/literature-/kruss-ar213-en.pdf [Accessed: June 2019].

[214] M. Quitzau, M. Wolter, V. Zaporojtchenko, H. Kersten, and F. Faupel, "Modification of polyethylene powder with an organic precursor in a spiral conveyor by hollow cathode glow discharge," *The European Physical Journal D*, vol. 58, p. 305, 2010.

[215] D.-J. Huang and T.-S. Leu, "Fabrication of high wettability gradient on copper substrate," *Applied Surface Science*, vol. 280, p. 25, 2013.

[216] C. Canal, R. Molina, E. Bertran, and P. Erra, "Wettability, ageing and recovery process of plasma-treated polyamide 6," *Journal of Adhesion Science and Technology*, vol. 18, p. 1077, 2004.

[217] Casa Software Ltd, *CasaXPS Manual 2.3.15*, 2009. Available: http://www.-casaxps.com/ebooks/OrangeBookRev1.3ebook.pdf [Accessed: May 2019].

[218] K. M. Siegbahn, "Nobel lecture: Electron spectroscopy for atoms, molecules and condensed matter," *The Nobel Foundation*, 1981.

[219] K. Levsen, "Physikalische Methoden in der Chemie: ESCA," *Chemie in unserer Zeit*, vol. 10, p. 48, 1976.

[220] N. Stojilovic, "Why can't we see hydrogen in x-ray photoelectron spectroscopy?," *Journal of Chemical Education*, vol. 89, p. 1331, 2012.

[221] S. Hüfner, *Photoelectron spectroscopy: Principles and applications*. Springer-Verlag Berlin Heidelberg, 3 ed., 2003.

[222] M. Henzler and W. Göpel, *Oberflächenphysik des Festkörpers*. Teubner Studienbücher Physik, Wiesbaden: Vieweg+Teubner Verlag, 1991.

[223] D. A. Shirley, "High-resolution x-ray photoemission spectrum of the valence bands of gold," *Physical Review B*, vol. 5, p. 4709, 1972.

[224] M. C. Biesinger, L. W. Lau, A. R. Gerson, and R. S. Smart, "Resolving surface chemical states in XPS analysis of first row transition metals, oxides and hydroxides: Sc, Ti, V, Cu and Zn," *Applied Surface Science*, vol. 257, p. 887, 2010.

[225] H. Ardelean, C. Fiaud, P. Marcus, "Enhanced corrosion resistance of magnesium and its alloys through the formation of cerium (and aluminium) oxide surface films," *Materials and Corrosion*, vol. 52, p. 889, 2001.

Acknowledgements

Da die Anfertigung meiner Doktorarbeit ohne die Hilfe zahlreicher Personen nicht möglich gewesen wäre, möchte ich mich an dieser Stelle nochmal herzlich bei allen beteiligten Personen bedanken.
Zuerst möchte ich mich bei meinem Doktorvater Prof. Gregor Morfill für die Betreuung und Unterstützung meiner Doktorarbeit bedanken. Ich möchte mich insbesondere für die hilfreichen Anregungen und Diskussionen bedanken, die mir während meiner Zeit stets weitergeholfen und mir einen neuen Blick auf meine Arbeit ermöglicht haben.
Mein Dank geht auch an Prof. Markus Thoma für seine Unterstützung und für die Begutachtung dieser Arbeit.
Ich möchte mich besonders bei Dr. Hubertus Thomas bedanken, der mir die Möglichkeit und das Vertrauen geben hat meine Doktorarbeit am Deutschen Zentrum für Luft- und Raumfahrt anzufertigen und der mich stets mit hilfreichen Korrekturen und Diskussionen unterstützt hat.
Danke auch an Dr. Julia Zimmermann und den terraplasmaniern für ihre Zusammenarbeit und für die sanfte Eingewöhnung in die bayrische Kultur. Ohne Julia hätte ich es vermutlich nicht bis zum DLR geschafft!
Ich bedanke mich bei Dr. Petra Rettberg für die tatkräftige Unterstützung und für ihre Hilfe bei diversen biologischen und raumfahrtrelevanten Fragestellungen.
Ich möchte mich vielmals bei Dr. Matthias Kolbe und Mareike Wegener für ihre tatkräftige Unterstützung und Hilfe bei den REM Aufnahmen bedanken. Ebenso bedanke ich mich bei Dr. Joachim Sann und Sandra Moritz für die Durchführung und Unterstützung bei den XPS Messungen.
Ein großer Dank geht außerdem an Alisa Schmidt für die tolle und produktive Zusammenarbeit und für Ihr bewundernswertes Durchhaltevermögen an heißen Labortagen.
Nicht zu vergessen gilt mein Dank der gesamten Arbeitsgruppe *Komplexe Plasmen*, die mir eine schöne und unvergessliche Zeit am DLR ermöglicht hat. Besonders zu erwähnen sind dabei meine Bürokollegen Erich, Alex und Ingo, die mir stets mit Rat und Tat zur Seite standen und immer für einen unterhaltsamen Ausgleich gesorgt haben. Zusätzlich möchte ich mich bei Claudius, Peter, Daniel und Christina bedanken für Ihre Ideen und tatkräftige Unterstützung bei diversen Problemen, die dank ihrer Hilfe doch noch gelöst werden konnten.
Ich danke allen Kölnern Institutsdoktoranden, für die unterhaltsamen Abende an Doktoran-

dentagen und für die freundliche Aufnahme am Kölner Standort und die Einführung in den Kölner Karneval.
Ein besonderer Dank gilt meiner Familie, insbesondere meinen Eltern Lothar und Ulli und meiner Schwester Lena. Ohne ihre Unterstützung und motivierenden Zusprüche ("*Arbeit ist ein schwerer Beruf*") wären mein Studium und die Doktorarbeit nicht denkbar gewesen. Ich verspreche euch, Land ist in Sicht!
Ich möchte mich außerdem herzlich bei meinem Patenonkel Michael bedanken, der mich während meines Studiums und meiner Doktorarbeit immer unterstützt hat und ohne den dieser Weg nicht möglich gewesen wäre.
Zuletzt möchte ich ganz besonders meiner besseren Hälfte Stefan danken. Danke für deine großartige und tatkräftige Unterstützung und dass du mich schon so lange begleitest. Insbesondere bedanke ich mich für deine Hartnäckigkeit, sich stets ein Päuschen zu gönnen, getreu deinem Lebensmotto "*Ein guter Gaul springt nicht höher als er muss!*".